# *Structural studies at megabar static pressures in application to mineral physics and material science*

Doctoral Thesis

submitted to obtain the academic degree of Doctor of Natural Sciences

(Dr. rer. nat.)

of the Bayreuth Graduate School of Mathematical and Natural Sciences (BayNAT)

of the University of Bayreuth

***Saiana Khandarkhaeva***

from *Ulan-Ude (Russian Federation)*

Bayreuth, 2022

This doctoral thesis was prepared at the Laboratory of Crystallography (Material Physics and Technology at Extreme Conditions Group) and the Bavarian Research Institute of Experimental Geochemistry and Geophysics (BGI) at the University of Bayreuth from 05/2017 until 04/2022and was supervised by Prof. Dr. Dr. h. c. Leonid Dubrovinsky and Prof. Dr. Dr. h. c. Natalia Dubrovinskaia.

This is a full reprint of the thesis submitted to obtain the academic degree of Doctor of Natural Sciences (Dr. rer. nat.) and approved by the Bayreuth Graduate School of Mathematical and Natural Sciences (BayNAT) of the University of Bayreuth.

Date of submission: 16.05.2022

Date of defence: 02.09.2022

Acting director: Prof. Dr. Hans Keppler

Doctoral committee:

| | |
|---|---|
| Prof. Dr. Dr. h. c. Leonid Dubrovinsky | (reviewer) |
| Prof. Dr. Dan Frost | (reviewer) |
| PD. Dr. Catherine McCammon | (chairman) |
| PD. Dr. Gerd Steinle-Neumann | |

# Zusammenfassung

Hochdruck-Hochtemperatur-Studien (HPHT) sind entscheidend für das Verständnis der Mineralogie, Petrologie, Dynamik und der chemischen Zusammensetzung erdinnerer Mineralien, von Himmelskörpern und extrasolaren Planeten. Den HPHT-Bedingungen ausgesetzt, kann Festkörpermaterie nicht nur strukturelle Umwandlungen erfahren, sondern auch Änderungen der physikalischen Eigenschaften wie Optik, elektronische Zustände, Magnetismus, thermische und elektrische Leitfähigkeit usw. zeigen. Jüngste methodologische Entwicklungen in der Hochdruckforschung haben den Fokus auf ein neues Gebiet gelenkt - die Synthese und Charakterisierung neuartiger Verbindungen mit exotischer Kristallchemie und physikalischen Eigenschaften. Die Fülle der neu entdeckten Materialien untermauert die signifikante Rolle dieses neuen Forschungszweiges.

Lasergeheizte Diamantstempelzellen (LHDACs) die es ermöglichen einen weiten P,T-Phasenraum abzudecken sind das leistungsstärkste Werkzeug um die Synthese dieser neuen Materialien zu bewerkstelligen. In-situ Einkristall-Röntgenbeugung (SCXRD) ist ein ideales Instrument um direkte und eindeutige Informationen über die atomare Anordnung als auch über die chemische Zusammensetzung kristalliner Materie zu erhalten. Die Kombination von LHDAC mit SCXRD und sowie die Erhöhung der Druck-Temperatur-Bedingungen, die in Materialstudien erreichbar sind, erweitern unser Wissen über das Materialverhalten unter extremen Bedingungen.

Diese Dissertation fasst methodologische Entwicklungen zusammen die darauf abzielen die LHDAC-Leistung als auch die experimentellen Strategien der SCXRD-Datenerfassung bei Multimegabar-Drücken zu verbessern. Weiterhin werden Ergebnisse zahlreicher Experimente, die an verschiedenen chemischen Systemen durchgeführt wurden, die für die Geo- und Materialwissenschaften relevant sind und zu einer Reihe origineller und wichtiger Erkenntnisse geführt haben, zusammengefasst.

Im ersten Teil dieser Arbeit werden die Entwicklung und Erprobung sekundärer Diamtantstempel beleuchtet, die mit einem fokussierten Ionenstrahl (FIB) aus einer Einkristall-Diamantplatte geformt wurden. Wir haben die Effizienz von Diamantstempel unterschiedlicher Geometrien zur Druckmultiplikation in verschiedenen Betriebsmodi bewertet: als einzelner sekundärer Diamantstempel oder als Paar in der zweistufigen DAC (dsDAC)-Anordnung. Das

Maximum der erreichbaren Drücke in DACs mit einem einzigen Eindringkörper schien unabhängig von der Größe und Form des Sekundärambosses zu sein. Die Ambosse des modifizierten toroidalen Designs ermöglichten jedoch eine Zunahme des Probenvolumens, was die Qualität der XRD-Daten erheblich verbesserte.

Im Rahmen der Methodenentwicklung haben wir einen neuartigen Submikrometer-Fokussieraufbau für die Hochdruck-Röntgenkristallographie an der Extreme-Condition-Beamline P02.2 bei PETRA III, DESY (Hamburg, Deutschland) installiert und in Betrieb genommen. Wir haben die Fähigkeit des neuen Aufbaus zur erfolgreichen Durchführung von SCXRD-Studien bei ultrahohen Drücken durch Testläufe an mikrometergroßen Kalibrierungsproben demonstriert, gefolgt von Strukturstudien von Fe-haltigem Silikat-Perowskit $(Mg_{0.91(2)}Fe_{0.09(2)})SiO_3$ und neuartiges orthorhombisches Hochdruckpolymorph von $Fe_3O_4$ ($\gamma$-$Fe_3O_4$) bei Drücken über 150 GPa.

Die an Magnetit bei Drücken bis ~80 GPa und Temperaturen bis ~5000 K durchgeführten Experimente führten yu der Entdeckung der $Fe_3O_4$-Polymorphe – $\gamma$-$Fe_3O_4$ mit einer orthorhombischen Kristallstruktur vom Typ $Yb_3S_4$ und $\delta$-$Fe_3O_4$ mit einer modifizierten Th3P4 Struktur. Weiterhin wurde festgestellt, dass $Fe_3O_4$, das über ~75 GPa unter Druck gesetzt und über ~2000 K erhitzt wird, chemisch instabil wird und eine Reihe von Selbstredox- oder Zersetzungsreaktionen durchläuft. Unter den chemischen Produkten dieser Prozesse fanden wir hcp-Fe und zwei exotische Eisenoxide – $Fe_5O_7$ und $Fe_{25}O_{32}$, beide mit ungewöhnlichen Zusammensetzungen und Kristallstrukturen.

Ein bedeutender Teil dieser Dissertation widmet sich der Untersuchung von Kristallstrukturen von neuartigen Metallcarbiden, die in LHDACs synthetisiert wurden. Insbesondere bisher unbekannte Rhenium-Kohlenstoff (Re-C)-Verbindungen bildeten sich aufgrund direkter chemischer Reaktionen der Diamantstempel mit den benutyten Rheniumdichtungen bei Drücken von etwa 200 GPa nach gepulster Lasererwärmung. Unter Verwendung des nanofokussierten Synchrotron-Röntgenstrahls erhielten wir SCXRD-Daten und ermittelten Kristallstrukturen und chemische Zusammensetzungen von vier Phasen: $Re_2C$, $ReC_2$, ReC, $ReC_{0.2}$ – und enthüllten die unerwartet reichhaltige Chemie des Re-C-Systems bei Drücken von mehreren Megabar.

Die Kristallstrukturen von Ca-C-Verbindungen, *Immm*-$CaC_2$ (HP-$CaC_2$) und $Ca_3C_7$, zeigten komplexe polyanionische Kohlenstoffeinheiten – deprotonierte Polyacen-ähnliche bzw. para-Poly(indenoinden)-ähnliche Nanobänder. Die Synthese dieser Phasen wurde in LHDACs im Druckbereich von 40-150 GPa realisiert. Basierend auf experimentellen XRD-Daten und theoretischen Berechnungen haben wir die Natur der chemischen Bindung analysiert und das Kompressionsverhalten synthetisierter Verbindungen ermittelt.

Schließlich wurde die Methodik der Synthese und Untersuchung neuartiger Verbindungen im Terapascal-Druckbereich in einem laserbeheizten dsDACs am Re-N-System veranschaulicht. Die vollständigen chemischen und strukturellen Charakterisierungen der $Re_7N_3$- und $ReN_{0.2}$-Feststoffe wurden in-situ mittels SCXRD an der Material Science Beamline ID11 der ESRF (Grenoble, Frankreich) realisiert, was eindeutig die Möglichkeit beweist, Hochdruckkristallographie innerhalb des Terapascal-Regimes auszudehnen.

## Summary

High-pressure high-temperature (HPHT) studies are crucial for understanding the mineralogy, petrology, dynamics, and chemistry of materials inside the Earth, celestial bodies, and extrasolar planets. Exposed to the HPHT conditions, solid state matter might not only undergo structural transformations but also reveal changes in physical properties such as optics, electronic states, magnetism, thermal- and electrical conductivity, etc. Although the mineral physics studies remain the mainstream of high-pressure research, recent methodological developments have driven the focus into a new area - the synthesis and characterization of novel compounds with exotic crystal chemistry and physical properties. The plethora of discovered phases validates the importance of pursuing this new research path.

Laser-heated diamond anvil cells (LHDACs), enabling to cover the widest *P,T*-range, is the most powerful tool to reach the HPHT conditions required for the synthesis of novel . The *in situ* high-pressure single-crystal X-ray diffraction (SCXRD) is an ideal instrument, providing direct and unequivocal information on both the atomic arrangement and chemical composition of crystalline matter. Combination of LHDAC technique with SCXRD and pushing up pressure-temperature conditions achievable in structural studies extend our knowledge of materials behavior at extremes.

This thesis summarizes methodological developments aiming at improving both the LHDAC performance and the experimental strategies of the SCXRD data collection at multimegabar pressures. It also presents the results of numerous experiments performed on different chemical systems relevant for geo- and material sciences that led to a number of original and important findings.

The first part of the presented research is dedicated to the testing of the secondary stage anvils shaped with the focused ion beam (FIB) from the single-crystal diamond plate. We evaluated the efficiency of anvils of different designs for pressure multiplication in different modes of operations: as a single indenter or as a pair of anvils in the double-stage DAC (dsDAC) assembly. The maximum of achievable pressures in DACs with a single indenter appeared to be independent on the size and shape of the secondary anvil. However, the anvils of modified toroidal design enabled a gain in the sample volume that significantly improved the quality of XRD data.

In the scope of methodological development, we installed and commissioned a novel sub-micron focusing setup for high-pressure X-ray crystallography at the extreme condition beamline P02.2 at PETRA III, DESY (Hamburg, Germany). We have demonstrated the capability of the new setup to successfully perform SCXRD studies at ultra-high pressures by test runs conducted on micron-sized calibration samples, followed by structural studies of Fe-bearing silicate perovskite $(Mg_{0.91(2)}Fe_{0.09(2)})SiO_3$, and novel orthorhombic high-pressure polymorph of $Fe_3O_4$ (*i.e.* γ-$Fe_3O_4$ ) at pressures above 150 GPa.

The experiments conducted on magnetite at pressures up to ~80 GPa and temperatures up to ~5000 K revealed the two hitherto unknown $Fe_3O_4$ polymorphs –γ-$Fe_3O_4$ with the orthorhombic $Yb_3S_4$-type structure and δ-$Fe_3O_4$ with the modified $Th_3P_4$-type structure. We also found that $Fe_3O_4$, pressurized above ~75 GPa and heated above ~2000 K, becomes chemically unstable and undergoes a series of self-redox or decomposition reactions. Among the chemical products of these processes, we found *hcp*-Fe and two exotic iron oxides - $Fe_5O_7$ and $Fe_{25}O_{32}$, both with unusual compositions and crystal structures.

A significant part of the thesis is dedicated to studies of crystal structures of novel metal carbides synthesized in LHDACs. In particular, hitherto unknown rhenium-carbon (Re-C) compounds formed due to direct chemical reactions of the diamond anvils with the rhenium gasket at pressures of about 200 GPa after pulsed laser-heating. Using the nano-focused synchrotron X-ray beam, we obtained SCXRD data and established crystal structures and chemical compositions of four phases: $Re_2C$, $ReC_2$, ReC, $ReC_{0.2}$ - uncovering the unexpectedly rich chemistry of the Re-C system at multimegabar pressures.

The crystal structures of Ca-C compounds, *Immm*-$CaC_2$ (HP-$CaC_2$) and $Ca_3C_7$, revealed complex poly-anionic carbon entities - deprotonated polyacene-like and para-poly(indenoindene)-like nanoribbons, respectively. The synthesis of these phases was realized in LHDACs in the pressure range of 40-150 GPa. Based on experimental XRD data and theoretical calculations we analysed the nature of chemical bonding and established the compressional behaviour of synthesized compounds.

Finally, the methodology of the synthesis and study of novel compounds at terapascal pressure range in a laser-heated dsDACs was exemplified on the Re-N system. The full chemical and structural characterizations of $Re_7N_3$ and $ReN_{0.2}$ solids were realized *in situ* by means of

SCXRD at Material Science Beamline ID11 at ESRF (Grenoble, France), unambiguously proving the possibility to extend high-pressure crystallography to the terapascal regime within the multi-grain samples.

# Acknowledgements

First and foremost, I would like to thank my supervisors: Prof. Dr. Leonid Dubrovinsky and Prof. Dr. Natalia Dubrovinskaia for the many things they taught me over the last five years. Being a newcomer in the field of high-pressure high-temperature science I've gained a lot and will be always grateful for their patient guidance, encouraging, endless optimism and a great scientific atmosphere in our group. Thank you very much for all the support and inspiration, that you give to me personally and to us all.

First three years of my study I have spent in BGI and would like to thank Prof. Hans Keppler, Prof. Tomoo Katsura, and Prof. Dan Frost for providing an excellent environment for collaborative work. I would like to thank the administrative and technical staff of BGI, Petra Buchert, Janina Potzel, Anna Dinius, Detlef Krausse, Stefan Übelhack, Sven Linhardt, Raphael Njul and Trenz Ulrike for their help in corresponding problems. Specially, I would like to express my gratitude to Dorothea Wiesner for her kind patience and support during my learning.

Also I would like to thank all the members of the Laboratory of Crystallography for a warm and friendly atmosphere for scientific work. Special thanks to Prof. Dr. Sander van Smaalen and Dr. Andreas Schönleber for helpful discussions on the laboratory seminars, the laboratory secretary Denis Kelk-Huth, who helped me with many of administrative problems and questions.

I highly appreciate the staff of P02.2 (Petra III), IDD-13 (APS) and ID11 (ESRF) beamlines for the invaluable help during our experiments: Dr. Hanns-Peter Liermann, Dr. Vitali Prakapenka, Dr. Carlotta Giacobbe, Dr. Eleanor Lawrence Bright, Dr. Jonathan Wright, Dr. Pavel Sedmak. Also, I would like to acknowledge all members of P02.2 beamline, kindly hosted me last year. Many thanks for our fruitful discussions and a pleasant environment in the team.

There are no words that can express all of my gratitude to my friends and comrades: Egor Koemets, Iulia Koemets, Artem Chanyshev, Alexandra Chanysheva, Dmitry Druzhbin, Alexander Kurnosov, Anna Kurnosova, Alena Aslandukova, Andrii Aslandukov, Dmitry Bondar, Yiqing Yin, Stella Chariton, Anna Pakhomova, Georgios Aprillis, Sumith Abeykoon, Serena Dominijanni, Denis Vasiukov, Daniil Kudryavtsev, Johannes Meusburger. Thank you all for the joyful time we spent together, your kindness, help and support.

I'm truly grateful to the people, who significantly helped me during this work, being not only good friends but also great teachers and advisors: Dr. Maxim Bykov, Dr. Elena Bykova, Dr.

Konstantin Glazyrin, Dr. Dominique Laniel, Dr. Sergey Ovsyannikov, Dr. Thomas Meier. Additionally, I would like to thank Dr. Thomas Meier for translating the Summary of this thesis into German.

One should be always grateful to the first teacher in his life. Hereby, I would like to thank Alexander Glebovich Cherkov for showing me the beauty and excitement of scientific journey. Thank you very much!

I would like to thank my parents Zinaida Khazheeva and Evgenii Khandarkhaev, my sister Elena Bagaeva and her children Irina, Tatiana and Pavel, for their endless love and support, for many of warm things said in difficult times, for guiding me on my first, but the most important steps in my life.

I would like to express my special gratitude to the most patient and understanding person, the best friend and colleague, my husband Timofey Fedotenko. Thank you for always being on my side.

# Table of content

# Chapter 1 Introduction

A great number of scientific disciplines including geophysics, geochemistry, mineralogy, material sciences and engineering is interested in study of solid state matter exposed to extreme conditions. Being the fundamental thermodynamic variables, pressure (*P*) and temperature (*T*) significantly affect on the state of matter, determining a variety of material properties. Therefore, the in situ characterization of materials at moderated *P, T*-conditions is of a great importance for scientific community.

Among the number of high-pressure devices, diamond anvils cells can provide the capability to reach the widest range of pressures and temperatures, covering the conditions of entire Earth's interior (*1*). Recently, the diamond anvil cell has been popularized, becoming the only one device enabling to achieve static pressures as high as 1 TPa (*2*), simulating the conditions of the planetary bodies with masses significantly exceeding the mass of the Earth. Similarly, the expansion of the pressure and temperature limits gains a lot in the fields of material science and condensed-matter physics, enabling the discovery of novel material with unique physical properties, such as superconductivity, ultra-hardness, ultra-incompressibility, high-energy density, etc. (*3*–*6*)

## 1.1 Methodological aspects of diamond anvil cell operating at multimegabar pressure range

The design of DACs went through long iterative and incremental development aimed at achieving higher and higher pressures. Currently, the double-stage DAC (dsDAC) design is used to tackle multimegabar pressures (*2*, *7*–*11*). The dsDACs implement the secondary anvils in the pressure chamber of a conventional DAC to enable pressure multiplication due to the further force transfer to the even smaller area of the culet of the secondary anvil. Initially, secondary anvils in dsDACs were produced of isotropic material, nanocrystalline diamond (NCD) (*7*), which is supposed to overcome the limits related to the low fracture toughness and brittleness of conventional single-crystalline anvils. Following this breakthrough, the assemblies of synthetic nano-polycrystalline diamond (NPD) secondary anvils were introduced (*9*, *10*). However, certain

drawbacks of NCD or NPD anvils, e.g. opacity and high luminescence, remained unsolved, which complicates spectroscopic measurements in DACs.

Few years ago DACs with so-called toroidal design (tDACs) were introduced (*12*, *13*). Using FIB, the profile of the primary single-crystal anvils was modified, featuring a circumference cavity on the culet and a summit (a tip) in its center, which works as a secondary anvil, when the DAC is assembled. In tDACs pressures of ~500 GPa have been achieved and the authors suggested that there is still a potential for a further pressure increase through adjusting the size and the slope of the cavity of the toroidal anvil. These new tDACs were used for synchrotron infrared absorption spectroscopy studies of dense solid hydrogen at 80 K and ~400 GPa (*14*). However, the preparation of the tDAC cell remained laborious and often resulted in failure on external anvils.

The developments described above and the ongoing discussion of capabilities of various ultra-HP DAC techniques call for systematic testing of the performance of secondary anvils of different designs. Using FIB, we manufactured various types of secondary anvils from commercially available single-crystal diamond plates (AlmaxEasy Lab) and investigated their efficiency for pressure multiplication.

## 1.2 Methodological aspects of structural studies at multimegabar pressure range

The higher the pressures, the more challenging are synthesis and diffraction studies in DACs become, even if we consider the dedicated high-pressure beamlines at synchrotron facilities, where the X-ray beam can be focused down to 2–3 μm in diameter. At pressures exceeding 150 GPa, the size of the sample is of only about 10 μm or even less, while the single-crystalline grains of the reaction product(s) are often of submicron size. This results in a drastic worsening of the signal-to-noise ratio in collected diffraction data. Also a parasitic contribution from gasket material significantly decreases the quality of data, when the sample chamber becomes smaller upon compression. Only a submicron focusing of the X-ray beam can provide suitable conditions to collect SCXRD data at multi-megabar pressures. Also a very precise sample alignment system with a small sphere of confusion in necessary to obtain SCXRD of suitable quality. Indeed, submicron-size samples, have to stay illuminated by the X-ray beam upon rotation of ±38º or higher angles. Thus, only a combination of precise motorization solutions with the sub-micron

beam capability of an instrument enables successful experiments. Below we present new developments at the Extreme Conditions Beamline (P02.2, PETRA III, DESY, Germany) (*15*) that enable considerable improvements for data collection at very high pressures and for small scattering volumes.

## 1.3 Structural diversity and chemical transformations of magnetite at HPHT

Understanding the behavior of natural iron-bearing systems at high- and ultra-high pressures and temperatures relevant to the deep planetary interiors requires knowledge of the phase relations in chemically simple systems such as Fe–O.

Due to its importance as geomaterial, magnetite ($Fe_3O_4$) was intensively investigated at high pressures. Upon compression up to ~25 GPa at room temperature, it undergoes structural phase transition to a "post-spinel phase"(*16*). The transition is associated with significant changes of magnetic and electrical properties(*17–19*). Decades of highly controversial history of structural studies of post-spinel $Fe_3O_4$ phase ended up with the general consensus that it adopts the $CaTi_2O_4$-type structure (*20–23*). Another phase transformation of $Fe_3O_4$ was reported upon laser heating (between approximately 1500 to 2000 K) at pressures from 64 to 73 GPa (*23*, *24*). Powder X-ray diffraction data were interpreted as formation of an orthorhombic phase with the $CaFe_2O_4$-type structure. However, assignment of a space group and interpretation of the diffraction data remain ambiguous and call for further investigations.

The stability of $Fe_3O_4$ at high pressure is a widely debated problem. It is especially important due to (at least) two reasons: (a) buffers involving magnetite (or its high-pressure polymorphs) are expected to control many processes in Earth's interiors, including diamonds formation (*25*, *26*); (b) magnetite (together with hematite and some other iron-bearing minerals) is a major component of banded iron formations (BIFs) which, as believed, have been subducted into Earth's mantle and may thus play a significant role in the planetary oxygen cycle (*20*, *27*). Lazor et al.(*28*) predicted breakdown of $Fe_3O_4$ into FeO and $Fe_2O_3$ at ~50 GPa based on thermodynamic calculations. It was noted that at these conditions post-spinel $Fe_3O_4$ phase has lower density than the assemblage of cubic $Fe_xO$ and $Rh_2O_3$-II-structured ι-$Fe_2O_3$ (*28*). However, justification of this hypothesis is strongly dependent on equations of state used for volume

determination of relevant phases and exact composition of $Fe_xO$ component. Moreover, in the case of ferric spinels, like $Fe_3O_4$, this scenario could be inconclusive due to partial reduction of $Fe^{3+}$ to $Fe^{2+}$ during the high-pressure high-temperature treatment (*21*). Indeed, according to a recent report[4], laser heating of $Fe_3O_4$ at ~80 GPa and 2950 K leads to the formation of $Fe_{25}O_{32}$, a phase, containing more ferrous iron than the starting material(*20*).

Summarizing the brief overview of the state-of-the-art, there are two main problems associated with the behavior of $Fe_3O_4$ at high-pressures and high-temperatures: (a) not all possible phases of $Fe_3O_4$ as well as their crystal structures (and crystal chemistry) are established, and (b) chemical stability of the oxide is insufficiently studied, as PT conditions of its decomposition and products of reactions have not been fully characterized. This motivated us to conduct HPHT studies of $Fe_3O_4$ up to pressures ~80 GPa and temperatures up to 5000 K performed in LHDACs.

## 1.4 Re-C system at multimegabar pressure regime

Rhenium (Re) belongs to the group VII of transition metals with a half filled *d*-band. It does not undergo any structural transformation up to at least ~660 GPa, resembling the same hexagonal close packed (*hcp*) structure (*7*, *29*). Rhenium is ductile but has high bulk and shear moduli, and a high melting point of ~3453 K (*30*, *31*). Due to these reasons, rhenium has been used as a gasket material for studies under ultra-high pressures in DAC.

The range of currently achievable static pressures has been extended to ~1000 GPa (*2*) due to implementation of double-stage diamond anvil cells (dsDAC) and to ~600 GPa with toroidal type anvils (tDAC) (*12*, *13*). In order to achieve such extreme pressures, the linear size of samples and sample chambers should be drastically decreased. At pressures above ~150 GPa, a pressure chamber's diameter (made of precompressed Re foil) is usually smaller than 50 μm, and in dsDACs above 300 GPa it is less than 10 μm. Meanwhile, the size of a laser beams in typical laser heating (LH) setups used in DAC experiments varies from 15 to 50 μm at FWHM (*32*, *33*). As a result, irradiation of, at least the edge of a Re-gasket, by the laser beam during laser heating becomes unavoidable and may lead to a chemical reaction between Re and carbon of the diamond anvils. Awareness of these reactions is also of a primary interest for the development of the methodology of ultra-high pressure high temperature experiments, in which Re gaskets are

commonly used. Below we report on the *in situ* study of novel Re-C compounds formed after pulsed laser heating in DACs at about 200 GPa.

## 1.5 Novel calcium carbides synthesized in LHDACs

Richness of carbon chemistry and the existence of the vast number of organic compounds in nature are due to unlimited carbon catenation. However, known metal carbides contain the simplest carbon anions: isolated carbon atoms $C^{4-}$or $[C_2]^{2-}$-dumbbells ($CaC_2$, $SrC_2$, $BaC_2$, $YC_2$, $LaC_2$, $La_2C_3$, $CeC_2$, $TbC_2$, $YbC_2$, and $LuC_2$ (*34–37*)) and linear trimers $[C_3]^{4-}$ ($Mg_2C_3$, $Me_4C_7$ (Me = Y, Ho, Er, Tm, Lu), $Sc_3C_4$ , and $Ln_3C_4$ (Ln = Ho - Lu) (*38–41*), which have the same carbon skeleton as methane, acetylene, and allene. HPHT conditions might alter the bonding patterns in carbides, leading to new compounds with unusual structural units and interesting properties. Considering that for the binary systems Mg-C (*42*), Ca-C (*43*), Y-C (*44*), and La–C(*45*) *ab initio* structure search predicts the formation of unusual metal carbides with exotic $[C_4]$, $[C_5]$ units, $[C_6]$ rings, graphitic carbon sheets, and a number of structural transitions, studying them under compression might enable exploring the catenation of carbon.

Calcium carbides have been in focus of high-pressure research during recent years. $CaC_2$ is of a particular interest, as it is characterised by rich polymorphism. Three polymorphs of $CaC_2$ known at ambient conditions (*46*) ($CaC_2$-I, $CaC_2$-II, $CaC_2$-III) feature common for acetylides $[C_2]$-dumbbells, but carbon starts to polymerize at relatively low pressures, and at about 7 GPa $CaC_2$ transforms into a metallic phase (space group *Cmcm*) featuring 1D zig-zag polymeric carbon chains, as established using Raman spectroscopy and X-ray diffraction (*47*). Theory predicts further structural transformations in $CaC_2$ upon pressure increase coupled with the progressive polymerization of carbon atoms. According to calculations by Li et al. (*48*), above 20 GPa the structure of $CaC_2$ should have $P\bar{1}$ symmetry and contain infinite carbon strips built of interconnected pairs of fused five-member rings. This phase should be thermodynamically stable up to 37 GPa (*48*). Above this pressure, according to the calculation, metallic $P\bar{1}$ -$CaC_2$ transforms into metallic *Immm*-$CaC_2$ (*48*, *49*), in which carbon atoms are polymerized to form infinite quasi-1D ribbons built of fused 6-member rings. The latter prediction is of a particular interest, as the suggested carbon catenation in *Immm*-$CaC_2$ (*48*, *49*) resembles deprotonated polyacene-like

nanoribbons. So far, experimental studies of Ca-C system were limited by ~20 GPa, and the effect of pressure induced polymerization of carbon is poorly understood. This motivates us to perform a systematic investigation of Ca-C systems by means of single-crystal X-ray diffraction in LHDACs in wide pressure and temperature ranges: from 40 GPa to 150 GPa and up to ~2500 K.

## 1.6 Material synthesis and characterization at terapascal pressures

Latest developments in the diamond anvil cell technique, and, particularly, the invention of double-stage and toroidal diamond anvil cells (ds-DACs and t-DACs) (*7*, *12*, *13*), enabled a breakthrough in the synthesis of materials and studying structure-properties relations at high and ultra-high pressures. Solving and refining the crystal structures of solids synthesized directly from pure elements in laser-heated conventional DACs (*4*, *6*, *50–53*) at pressures up to about two megabar (*51*, *54*) became possible due to the synergy of expertise in both - generating multimegabar pressures (*2*, *7*, *8*) and in SCXRD at ultra-high pressures, which were pioneered a few years ago (*55*, *56*). Since HPHT synthesis has become a well-established technique for materials discovery, extending investigations to the TPa regime has been desired for a long time.

To achieve the desired pressures, we combined toroidal (*12*, *13*) and double-stage (*2*, *7*, *8*) anvils design. The full structural and chemical characterization on novel compounds was performed *in situ* using single-crystal X-ray diffraction in LHDACs at pressures close to 1 TPa.

# Chapter 2 Methods and instruments

## 2.1 Generation of the high pressures using the diamond anvil cells

### 2.1.1 Working principles of the diamond anvil cells

High-pressure high-temperature (HPHT) studies are crucial for understanding the mineralogy, petrology, dynamics, and chemistry of materials inside the Earth, celestial bodies, and extrasolar planets. Solid state matter exposed to the HPHT is able not only to undergo phase transitions but also exhibit unexpected chemistry, like not known at ambient conditions stoichiometry or chemical reactions. The study of the properties, structural transitions and chemical behavior of materials exposed to extreme pressures is of a great importance for geo- and materials sciences, potentially leading to the discovery of novel materials with unique properties and different technological applications.

The simplest definition of pressure is: $P = \frac{F}{A}$, where $F$ is the force applied perpendicularly to the surface, and $A$ is the area of this surface. According to this relation, there are two main methods, which are used to apply static high pressure to the sample: either by to maximizing the applied force; or by reducing the size of the area, on which force is being applied. The first approach is used in concept of piston cylinder (*57*) and multi anvil apparatuses(*58*), where large and/or massive devices are focused to maximize the applied force on relatively large samples (from ~ 0.1 cm to ~1 cm in linear dimensions). The opposite approach of decreasing the sample's volume is implemented in diamond anvil cells (DACs) technique, where the typical linear size of sample is about 10-100 μm. Invented in 1959 (*59*), the DAC became one of the most powerful tool to the generate static high pressures. Among the number of high-pressure devices, DACs can provide the capability to reach the widest range of pressures, covering the conditions of entire Earth's interior (*60*). Recently, the diamond anvil cell has been popularized, becoming the only one device enabling to achieve static pressures as high as 1 TPa (*2*), simulating the conditions of the planetary bodies with masses significantly exceeding the mass of the Earth.

The transparency of diamonds in a large range of energies of electromagnetic radiation enables to probe samples *in situ* at extreme conditions by different analytical methods, such as X-ray diffraction (XRD) (*56*), X-ray transmission microscopy (XRTM) (*61*), nuclear magnetic

resonance (NMR) (*62*), Raman (*63*), Mossbauer (*64*) and X-ray absorption spectroscopies (*65*) and other techniques based on optical measurements (*66*, *67*).

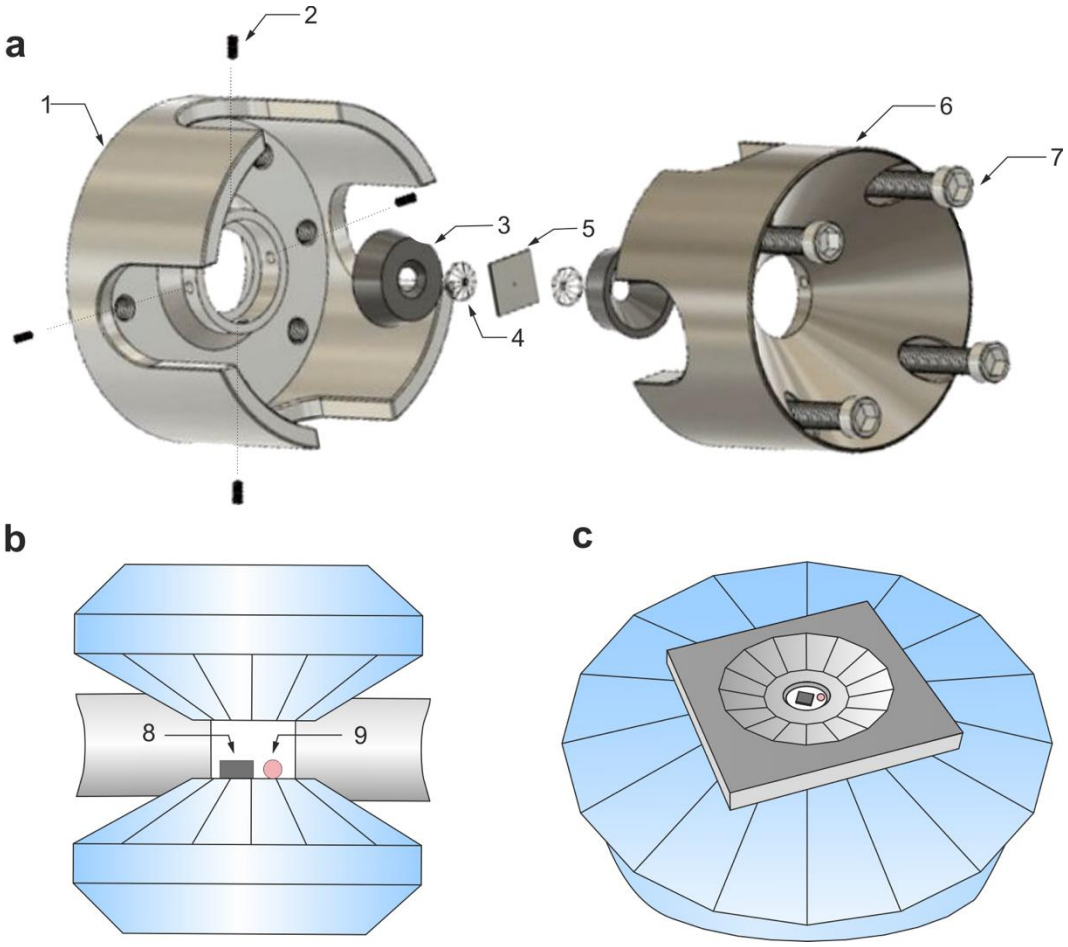


*Figure 2.1.1. .A design of BX-90 diamond anvil cell: (a) – Schematic illustration of DAC; (b) – a cross-section and a top view (c) schemes of the loaded sample chamber. 1 – Outer cylinder part of the cell, 2 – setscrews, used for the alignment of the diamond anvils (for simplicity are shown only for cylinder part); 3 – diamond supporting seats, 4 – diamond anvils, 5 – metallic gasket, 6 – inner piston part; 7 – screws for generating the loading force; 8 –.sample; 9 – pressure marker.*

Many different designs of DAC were invented over the last decades. There are some types of cells, which are commercially available from Diacell, Almax easyLab and Syntek companies; also several designs were invented in research institutions (Merrill-Basset 3-pin DAC (*1*), BX90 and BX90 mini (*68*), Mao-Bell-type DAC (*69*), Le Toullec type DAC (*70*), ETH-type DAC (*71*)).

The majority of studies presented in a current thesis, are performed in a BX90 type of DACs(*68*), which were designed and fabricated in Bayerisches Geoinstitut (BGI, Bayreuth, Germany), thus, the basic principles of device's operation will be described based on this type of cells (Figure 2.1.1).

The BX90 DAC consists of the metal body, equipped by couple of seats, on which diamond anvils are precisely aligned, and metallic gasket with a circular hole squeezed in between these anvils. Seats are generally made of ultra-hard materials (e.g. tungsten carbide) and serve to transfer the load from mechanically driven external body to the diamond anvils.

The metallic gasket with circular hole is compressed between the two diamond tips to form cylindrically shaped sample chamber. Typically, metallic gaskets are made of chemically inert at ambient conditions metals or alloys, mainly all the gaskets, used in presented below studies were made of rhenium, a 5d transition metal, which has a high bulk (above 350 GPa) and shear (above 180 GPa) moduli and melting point—3453 K (*72*).

The diamond anvils are typically made of polished single crystals of diamonds oriented according to the (100)-direction of the highest strength. The combination of the geometrical shape of the diamond cut, the shape of the seat, and the aperture of the metallic body are crucial parameters. For experiments, involving *in situ* single crystal X-ray diffraction, large aperture Boehler-Almax diamond anvils and seats are necessary. The choice of the culet size was adjusted, according to the desired pressure range, since the usage of diamond anvils with smaller culets is required to extend achievable pressure range.

### 2.1.2 Diamond anvils with modified design

In order to reach higher and higher pressures the design of DACs went through number stages of development. At the moment conventional DACs with beveled diamond anvils work up to ~450 GPa, but further pressure increase is limited by the yield strength of single-crystal diamond (*73–75*). The collapse of the diamond anvils under compression in the [001] direction is usually provoked by the cleavage along the {110} planes.

Currently, to reach multimegabar pressures, the interest has switched to so-called double-stage DAC (dsDAC) design. The dsDACs implements secondary anvils in the pressure chamber of a conventional DAC to enable pressure multiplication due to the further force transfer to even smaller area of the culet of the secondary anvil (Figurea). Experiments in dsDACs with secondary anvils made of an isotropic material, nanocrystalline diamond (*7*) (NCD), demonstrated a possibility to conduct XRD studies up to ~750 GPa (*8*) and later enabled achieving static pressures as high as 1 TPa (*2*). NCD semiballs with the grain size of 2-15 nm and 10-20 μm in diameter were used in these experiments.

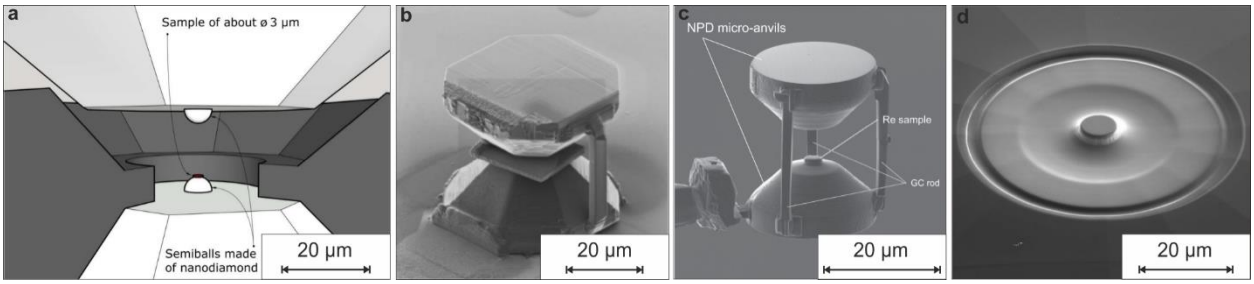


*Figure 2.1.2. Diamond anvil cell with modified design, aiming the operation at multimegabar pressures. (a) – A schematic illustration of dsDAC assembly, made of NCD semi-spheres, introduced by Dubrovinsky et al.* (*7*)*; (b) and (c) – dsDACs, shaped from NPD plates, using the focused ion beam* (*9, 10*)*; (d) – a design of toroidal diamond anvil, proposed by Jenei et al.* (*12*)*.*

Following the first breakthrough, secondary micro-anvils have been produced using focus ion beam (FIB) milling from other materials, for example, synthetic nano-polycrystalline diamond (*9*) (NPD) with a grain size of ~100 nm (Figure 2.1.2b, c). The reported maximum of achieved pressures was over 300 GPa with the culet size of the secondary anvil of 3 μm (*9*). The reduction of a grain size of NPD to ~10 nm enabled to ~600 GPa (*10*), as determined based on the equation of state (EoS) of rhenium reported in ref. (*7*) (or ~430 GPa, according to ref. (*29*)). Nevertheless, the synthesis of NCD balls in a large volume press and selection of the balls suitable for ultra-high-pressure experiments remain laborious. Another drawback of NCD or NPD is that they are opaque and highly luminescent that complicates spectroscopic measurements.

Recently, DACs with so-called toroidal anvils (tDACs) (Figure 2.1.2d) were introduced (*12*, *13*). Using FIB, the profile of the primary anvils is modified, so that the culet features a

circumference cavity and a summit (a tip) in its center with a diameter of ~15-25 μm. When two anvils are forced together, the shape of the cavity resembles a toroid and the sample is squeezed between the tips. The toroidal cavity accommodates gasket material and reduces its outflow from the center. It also helps to decrease the magnitude of the shear stresses in the anvils themselves. Upon compression, conventional anvils undergo a convex deformation, when the pressure chamber gets a shape of a convex lens. Eventually, the deformation leads to the failure of anvils. In the toroidal design this effect can be partially compensated due to complex stress distribution, and tDACs sustain higher pressures than DACs with conventional anvils. In tDACs pressures of ~500 GPa have been achieved (*12*, *13*), and the authors suggested that there is still a potential for a further pressure increase through adjusting the size and the slope of the cavity of the toroidal anvil.

## 2.1 Pressure transmitting media

The diamond anvils cell is uniaxial compression device, the stress along the loading directions is always larger than the stresses in the gasket plane. Non-isotropic compression of the sample leads to the appearance of high shear strains and often results in the broadening of the diffraction reflections. To maintain hydrostatic or quasihydrostatic compression in the DAC, a pressure-transmitting medium is normally employed. The pressure transmitting media (PTM) fills the sample chamber and surrounds the sample providing the isotropic distribution of stress.

The best pressure-transmitting media are light noble gases He and Ne. They are highly inert and stable over a wide pressure range, and have a relatively high solidification pressure ~10-15 GPa (*76*). In addition, light inert gases have a low X-ray absorption and give a low background, thus, have an additional advantage for X-ray diffraction studies in DACs.

Some alkali metal halides (e.g. NaCl, KCl, LiF, etc.) are often used as PTM if a thermal insulation of the samples in high-pressure high-temperature studies is needed. In experiments aiming the synthesis of novel materials PTM can also serve as a reactant and source of light elements for chemical reactions. In these cases, $O_2$ and $N_2$ gases can be loaded cryogenically; or liquid paraffin oil and/or $BH_3NH_3$ solid can be added to the sample chamber manually.

In the present thesis different PTMs were used. The gaseous ones (Ne and $N_2$) were loaded in a gas-loading system developed and installed in Bayerisches Geoinstitut (*77*). A DAC was placed inside the pressure vessel, later the gas was pumped into the vessel up to ~1.2 kbar. Once external gas pressure was released, the DAC was closed by manual tightening of the screws in the piston-driving mechanism.

## 2.2 Pressure determination

*In-situ* determination of the pressure inside the sample chamber plays the most important role in DAC experiments. There are several common pressure determination methods based on the use of different calibrants. The first one is the usage of pressure marker, the material with a well-known response on applied pressure. It can be loaded into the DAC along with the sample and probe with analytical techniques.

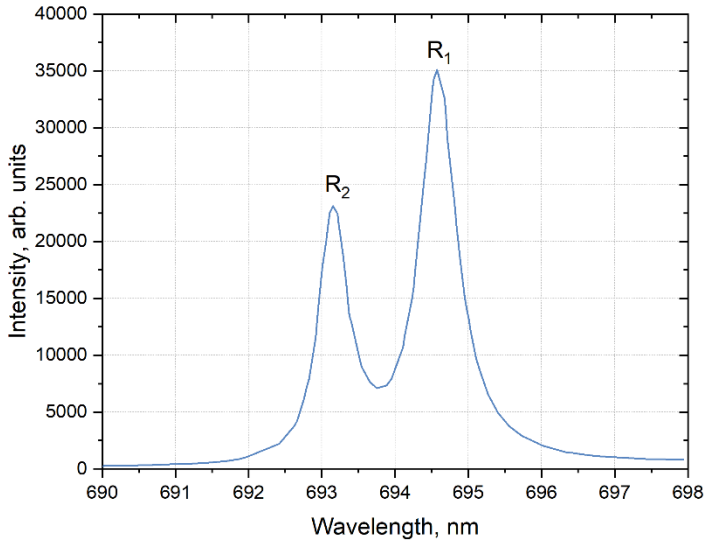


*Figure 2.2.1. Ruby florescence spectrum*

Pressure dependence of the ruby (Cr-doped $Al_2O_3$) fluorescence is the one of the way to precisely determine pressures in the experiments up to 100 GPa (*78*). Exposed to the laser light, a

ruby crystal with produces fluorescence signal, which can be detected using optical spectrometer. The following equation describes the relationship between the central position of the ruby R1 spectral peak with respect to the pressure (*79*):

$$P(\,GPa) = A \cdot \frac{\Delta\lambda}{\lambda_0} \cdot \left[1 + B \cdot \left(\frac{\Delta\lambda}{\lambda_0}\right)\right] \qquad \textit{Equation. 2.2-1}$$

where A and B are the calibration constants (A=1.87(1)·103, B=5.5) and $\lambda_0$ is the position of R1 peak (Figure 2.2.2) at ambient pressure; $\Delta\lambda$ is the relative shift of R1 peak at pressure $P$ (*79*). Usually, the intensity of the ruby fluorescence signal decreases with increasing of pressure, thus, experiments at multimegabar pressures require other calibrants. Also, one needs to avoid potential involvement of ruby in chemical reactions during high-temperature experiments. Therefore, in our own work we used the ruby fluorescence technique only at ambient temperature experiments.

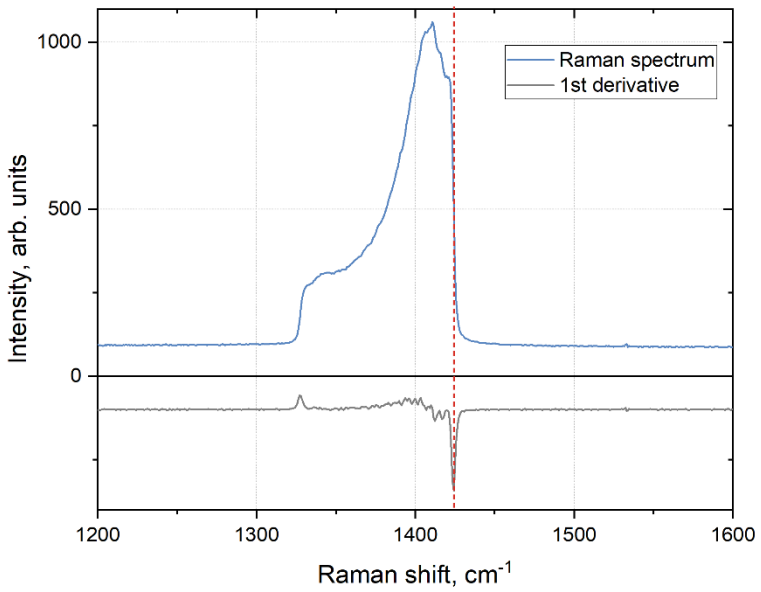


*Figure 2.2.2. Raman spectrum of the diamond anvil under stress and its 1st order derivative. Red dashed line indicates the position of the high-wavenumber edge.*

An alternative method of spectroscopic determination of pressure is a pressure dependence of the first-order Raman mode of the diamond culet (*80*). At the center of the culet, stress of diamond anvil correlates with the high-wavenumber edge of the Raman band in the following way:

$$P(GPa) = K_0\left(\frac{\Delta v}{v_0}\right)\left[1 + \frac{1}{2}(K_0' - 1)\left(\frac{\Delta v}{v_0}\right)\right] \qquad \textit{Equation 2.2-2}$$

where $K_0 = 547$ and $K_0' = 3.75$ are calibration constants, $v_0$ is the position of the high-wavenumber Raman edge at ambient pressure and $\Delta v$ is the difference between positions at ambient and measured pressures. The position of the edge is defined as a local minimum of the its 1st order derivative (Figure 2.2.2). This method is less accurate comparing to Ruby fluorescence measurements, however, it doesn't affect on chemical clearance of the system.

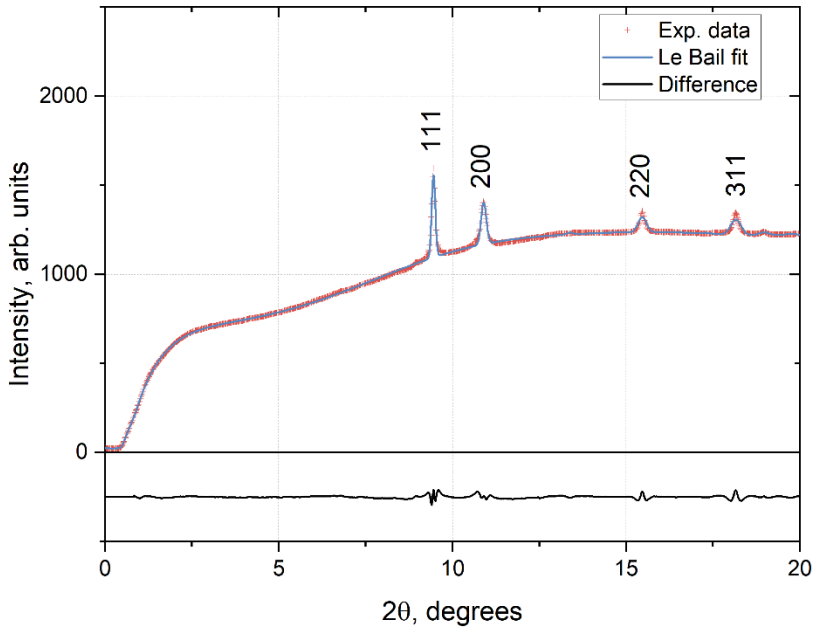


*Figure 2.2.3. Powder XRD pattern of solid Ne at 78.2 GPa with indexed reflections used for calculation of the unit cell volume. The pressure is determined from EoS of solid Ne* (*81*).

*In-situ* X-Ray diffraction is the most precise technique to measure the pressure inside the DAC. Pressure marker, a material with the well-known equation of state (EOS), can be loaded into the DAC along with the sample and probed by X-rays. The pressure marker is supposed to be a chemically inert compound with high crystal symmetry and with an absence of pressure-induced phase transitions. Often the flakes of Au–metal are used as pressure gauges in high-pressure high-temperature studies, since they can also act as a heat absorber (*81*); in some studies pressure could be determined by the diffraction signal, coming from metallic (e.g. rhenium) gasket (*29*, *82*). One

could also use the PTM as a pressure gauge if it has a well-established equation of state in a desired range of pressures (Figure 2.2.3).

In the present thesis, the combination of several techniques of pressure determination methodologies were used. Typically, spectroscopic approach was used for preliminary estimations, XRD data and EoS of Ne or Re were used for more accurate measurements.

## 2.3 Equations of state

The equation of state of a system describes the relationship between volume (V), pressure (P), and temperature (T) through the bulk modulus and thermal expansion. All equations of state, used in this thesis were measured at constant (ambient) temperature – 293 K. There are several types of analytical isothermal EOSes (*83*, *84*). The third order Birch-Murnaghan EOS (Equation 2.4-1) is one of the most common among them, and it was mainly used in the present thesis (*84*). According to this equation, pressure-volume dependence of matter at constant temperature can be described by bulk modulus ($K_0 = -V \cdot (\partial P / \partial V)$) and its pressure derivatives (particularly, $K' = \partial K / \partial P$). This "finite strain EoS" is derived from the assumption that the strain energy of a solid undergoing compression can be expressed as a Taylor series in the finite Eulerian strain $f_E$ (Equation 2.3-1). Expressions for the 2nd-order Birch-Murnaghan EoS can be obtained by setting K'= 4 in (Equation 2.3-2).

$$P(GPa) = \frac{3K_0}{2} \cdot \left[\left(\frac{V_0}{V}\right)^{\frac{7}{3}} - \left(\frac{V_0}{V}\right)^{\frac{5}{3}}\right] \cdot \left\{1 - \frac{3}{4}(4 - K') \cdot \left[\left(\frac{V_0}{V}\right)^{\frac{2}{3}} - 1\right]\right\} \qquad \textit{Equation 2.3-1}$$

$$f_E = \frac{1}{2}\left[\left(\frac{V}{V_0}\right)^{-\frac{2}{3}} - 1\right] \qquad \textit{Equation 2.3-2}$$

However, the finite-strain Birch-Murnaghan EoS doesn't accurately represent the volume variation of most solids under very high compression ($\frac{V}{V_0} < 0.6$). Thus, Vinet et al. derived an EoS from a generalized inter-atomic potential $f_V$ (Equation 2.3-3) (*83*). The final expression of Vinet EoS is given in Equation 2.3-4:

$$f_V = 1 - \left(\frac{V}{V_0}\right)^{\frac{1}{3}} \qquad \textit{Equation 2.3-3}$$

$$P(GPa) = 3K_0 \cdot \left(\frac{V}{V_0}\right)^{-\frac{2}{3}} \left[1 - \left(\frac{V}{V_0}\right)^{\frac{1}{3}}\right] \cdot \exp\left\{\frac{3}{2}(K' - 1) \cdot \left[1 - \left(\frac{V}{V_0}\right)^{\frac{1}{3}}\right]\right\} \qquad \textit{Equation 2.3-4}$$

This definition of $f_V$ means that $f_V$ = 0 at P = 0; $f_V$ increases with positive quantity with increasing pressure. It follows the conventions in the definition of magnitude and sign of Eulerian finite strain $f_E$. In this work, we used Eosfit7c software (*85*) to fit experimental *PV*-data in order to define the equations of state of the phases of interest.

## 2.4 Generation of high-temperatures inside the diamond anvil cells

Heating is an important part of DAC experiments, especially if studies are aimed at the modeling of processes that occur in deep planetary interiors. Temperatures as high as ~1000 K can be generated by electrical resistive heating. However, at higher temperatures a graphitization of the diamond anvils occurs, which often leads to the experiment's failure. The transparency of diamonds in a large range of energies of electromagnetic radiation is one of the significant advantages of the DAC technique. It allows to precisely focus a high power laser on the tiny sample, exposed to high pressures inside the DAC sample chamber (*86*). The choice of laser wavelengths depends on the absorption characteristics of the sample: $CO_2$ based infrared ($\lambda$ = 10.6 μm) and Nd:YAG near-infrared lasers (NIR, $\lambda$ ~ 1064 nm) are the most common in high-pressure science. NIR lasers beam are usually used to heat visibly non-transparent materials such as metals, alloys, and various transition metal bearing oxides.

A portable double-sided laser-heating setup with *in situ* temperature determination was used in described below experiments (*87*). This system allows to heat the sample from both sides using a tightly focused (up to 5 μm in diameter at FWHM) NIR laser beam. The setup allows precise heating of samples at pressures above 200 GPa and could be combined with synchrotron beamline equipment.

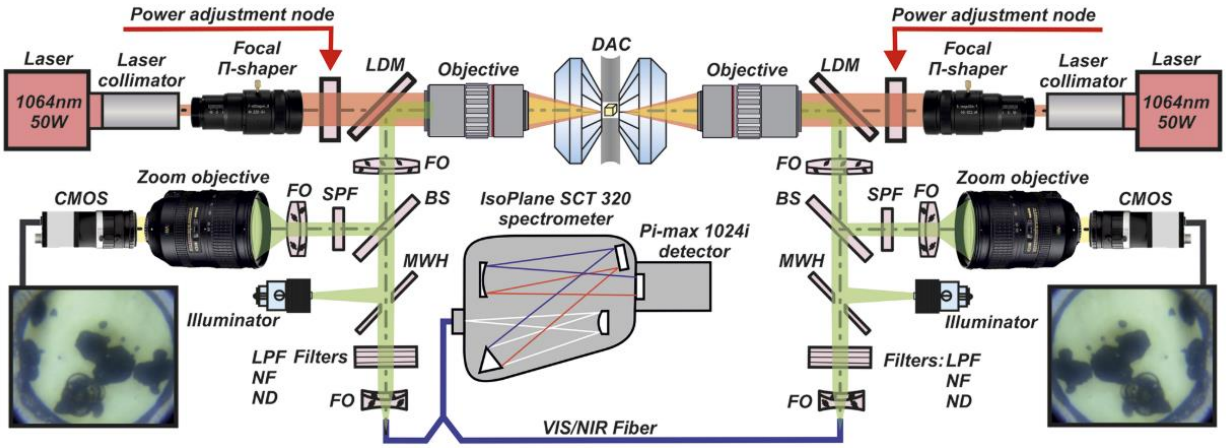


*Figure 2.4.1. A principal scheme of double-sided laser-heating setup used in the present thesis. LDMs are the long-pass dichromic mirrors; FOs are the focusing optics; BSs are 50/50 beam splitters; SPFs are the short-pass filters with a cutoff at 800 nm; CMOS are the cameras for optical observation; MWHs are the mirrors with a hole; LPFs are the long-pass filters with a cut-on wavelength of 550 nm; NFs are the notch filters for 1064 nm, and NDs are neutral density filters. The illustration is modified after ref.* (*87*).

## 2.5 Raman spectroscopy

Raman spectroscopy is a spectroscopic technique based on the inelastic scattering of monochromatic optical radiation on the irradiated sample.

When light interacts with matter, nearly all of the photons are scattered elastically (Rayleigh scattering) without the loss of energy ($E = E_0$, Figure *2.5.1*). However, a very small percentage (~10-6 %) of the incident light is scattered inelastically and a loss (i.e. $E > E_0$, Stokes Raman scattering) or gain (i.e. $E < E_0$, anti-Stokes Raman scattering) of energy occurs.

In the case of Rayleigh scattering, an incident light of energy $E_0$ and frequency $\nu_0$ , interacts with a molecule and excites the cloud of electrons from the ground level to a "virtual level. This "virtual" state is unstable, therefore, photons return to the ground level. Since there is no loss of energy in this process, and Rayleigh scattering has the same energy and frequency ($E_0$, $\nu_0$) as the incident light (i.e. elastic scattering). The Stokes Raman scattering occurs when the electron cloud absorbs a part of the incident radiation and falls to a vibrational level (i.e. an excited level) instead

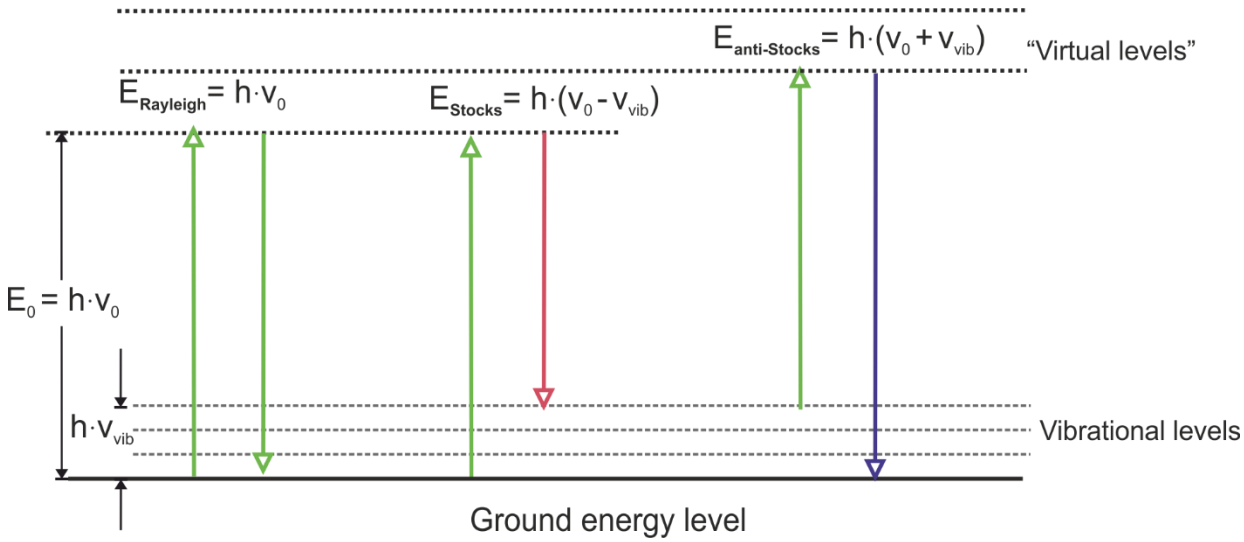


*Figure 2.5.1. The principle scheme of Rayleigh and Raman scattering processes. A molecule excited from the ground level to the virtual state with absorption of the photon and fall back with photon emission correspondingly. The excitation energy is $E_0 = h\nu_0$ is the energy of incident photon, h is the Planck's constant and $\nu_{vib}$ is the frequency corresponds to molecular vibrations.*

of the ground one. In this case, the Stokes Raman scattering has lower energy than the incident light. Anti-Stokes Raman scattering happens when the incident light meets the electron cloud already in a vibrational state. The cloud gets excited to the "virtual level" and then falls back to the ground level having more energy than the incident light. The intensity ratio between the Stokes and anti-Stokes scattering depends on the population of vibrational levels described by Boltzmann's law. Therefore, at ambient temperature the Stokes component is dominant in the inelastic spectra and often the only one considered. The frequency of Raman peak is associated to the certain molecular or lattice vibration s, e.g. symmetric or asymmetric stretching or bending.

In this work, the Raman studies of the samples were performed using LabRam systems equipped He-Ne (632 nm) laser source. He-Ne laser operates in continuous mode with a constant power of 50 mW. Raman spectra were collected in the region 200 –4000 $cm^{-1}$ with a resolution of 0.5 $cm^{-1}$.

## 2.6 Focused ion beam technique

The scanning electron microscopy (SEM) is a type of microscopy technique that visualize the sample surface by scanning it with a tightly focused beam of high-energy electrons. The electrons interact with the sample, producing different types of signals that contain information about the surface topography and its composition.

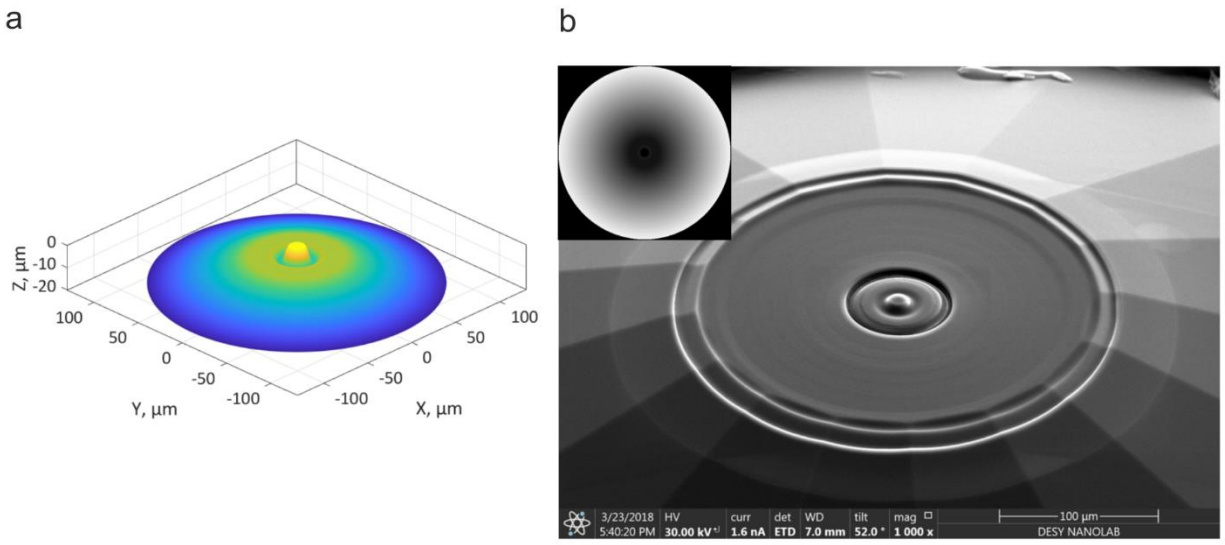


*Figure 2.6.1. An example of FIB-prepared sample. (a) A 3D model of the toroidal tip; (b) SEM image of thetoroidal diamond anvil, the insert shows a bitmap patter, used for milling.*

Unlike to SEM, FIB setup uses a focused beam of Ga-ions, which allows to machine the surface of the sample according to desired pattern. In the present work we used FIB machines **(**Scios DualBeam system, FEI Deutschland GmbH) installed at Bayerisches Geoinstitut (BGI, Bayreuth, Germany) and at DESY Nanolab (Hamburg, Germany). For production of secondary stage anvils, a 3D model of desired shape was programmed using the MATLAB software. The simulated milling profile was saved as a 2D 24-bit grey-scale RGB bitmap. The value of blue color corresponds to the milling time; any value of green color, different from 0 open the Ga-beam shutter. The milling was performed under the acceleration voltage of 30 kV with the Ga ion current

of varying from 1 nA to 30 nA. The Si-application mode was used for the estimation of dwelling time and the doze of Ga-ions.

## 2.7 X-ray diffraction in DACs

### 2.7.1 Basic principles

Established at the beginning of an 20$^{th}$ century, the X-ray diffraction (XRD) technique became one of the most widely used analytical techniques to reveal information about the crystal structure, chemical composition, and physical properties of materials (*88*). The development of powerful X-ray sources, sensitive detectors, and the possibility to perform experiments in different sample environments, which significantly expanded the scientific opportunities. (*89–91*).

The diffraction occurs as a result of elastic scattering of incoming electromagnetic waves by scattering objects if they are ordered with characteristic repeating features, comparable to the wavelength of incident radiation. In the case of solid-state matter, the scattering objects are electrons of atoms, that are ordered in a 3D periodic structure with interatomic distances comparable to the wavelength of X-ray beam. Assuming atoms are arranged in layers (planes) with a constant spacing between them, the reflected X-rays scattered from atomic planes interfere constructively only if the difference between path lengths of the two waves equal to an integer number ($n$) of wavelengths (Figure 3.4.1). Thus, the diffraction conditions for the crystalline materials are described according to the Bragg's law (or Wulff-Bragg's condition) (*92*):

$$2d \cdot sin\,(\theta) = n\lambda \qquad \textit{Equation 2.7-1}$$

where $d$ – is an interplanar in the family of *hkl* crystallographic planes, $\theta$ – the incident angle of X-rays with the wavelength $\lambda$, $n$ denotes the reflection order (integer number).

The crystalline matter causes an incident X-rays to be diffracted into specific directions defined by the its structure. By measuring the angles and intensities of diffracted radiation, it is possible to solve the inverse problem: to establish the three-dimensional distribution of electronic density within the crystal. Later, one can determine the atomic positions and extract information about interatomic distances, crystallographic disorder and other valuable properties of solids.

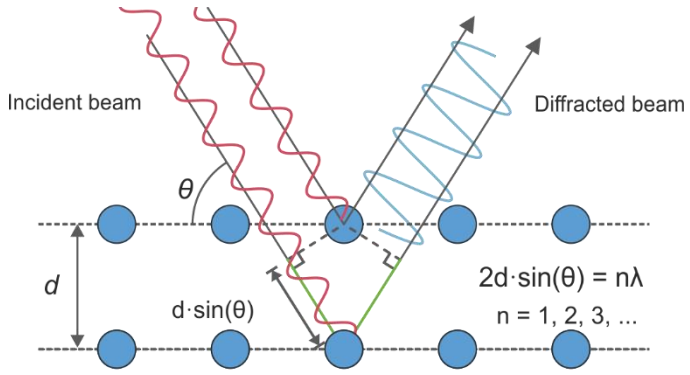


*Figure 2.4.1. Schematic illustration of Bragg's law. Incident X-rays approach the family of hkl planes and diffracted X-ray beam, scattered on the lower plane traverses an extra path with the length of* $2d \cdot sin(\theta)$. *Constructive interference occurs when the difference in the path length equals to an integer number of the wavelength.*

### 2.7.2 Powder and single-crystal X-ray diffraction

Traditionally, the XRD is divided into two approaches: powder and single-crystal. Powder X-ray diffraction is based on working with powders (a mixture of fine grains) of crystalline material. Possessing the random orientations, a portion of crystallites fulfills the Bragg's law and produces a diffraction signal, known as Debye-Scherrer rings (Figure 2.7.1a). Defining the *d*-spacings of the diffraction peaks, one could identify the phase and determine its lattice parameters.

Unfortunately, this approach experiences difficulties if the new phases are present in the sample. In the case of powder XRD a direct structure solution is almost impossible due to the loss of data on the reciprocal vectors. The single-crystal XRD is more advanced technique. Typical single-crystal XRD patterns contains a number of diffraction spots at a certain distance between each other (Figure 2.7.1b). Since the Bragg conditions for a given *d*-spacing and a wavelength would be meet only at the defined θ-angles, the crystal should be irradiated in different orientations with respect to incident beam, thus, all the reflections would be properly measured. The main advantage of SCXRD over the powder XRD is the possibility to obtain a direct information on the atomic arrangement within the unit cell (crystal structure) since it is carried in the intensities of Bragg reflections.

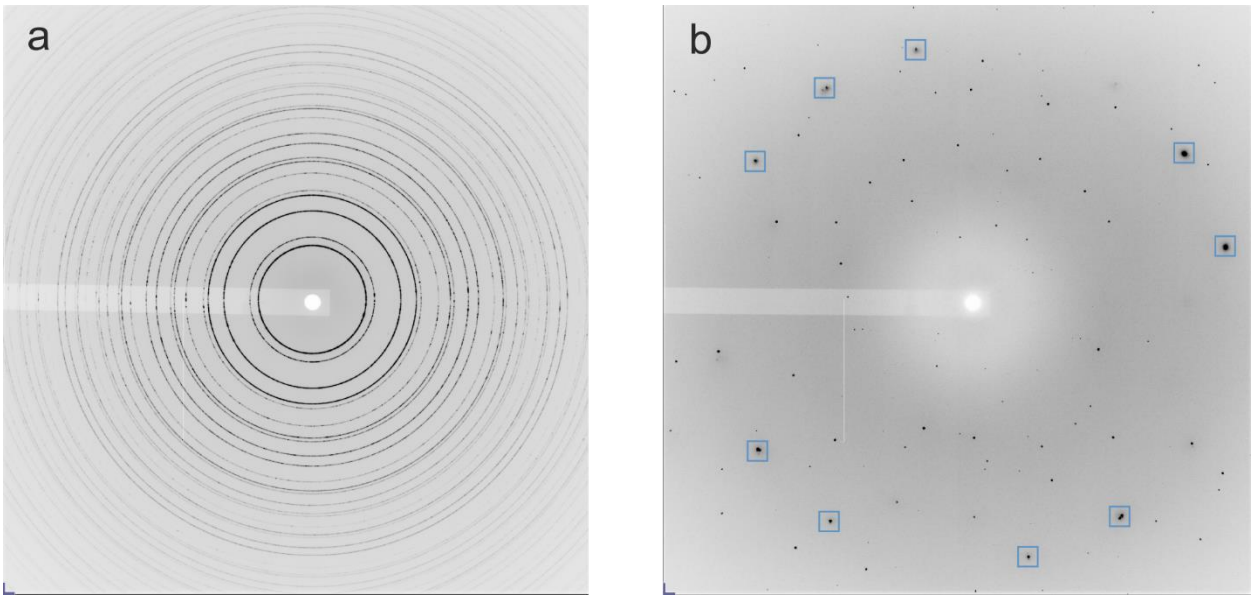


*Figure 2.7.1. Example of X-ray diffraction images produced by a powder (a) and a single crystal sample (b). The blue rectangles on (b) highlight the intense reflections of the diamond anvil. The Debye-Scherrer rings on (a) correspond to $CeO_2$ powder sample. Non-highlighted spots on (b) are the Bragg reflections from the enstatite crystal.*

## 2.8 X-ray diffraction data collection in diamond anvil cells at synchrotron facilities

### 2.8.1 X-ray diffraction studies in DACs: advantages and limitations

In comparison with diffraction studies at ambient conditions, the implementation of XRD technique in diamond anvil cell experiments experiences some difficulties. First, the sample environment gives an additional XRD signal; parasitic scattering comes from diamond anvils, metallic gasket, the solidified PTM. Second, the metallic body of a DAC shadows more than 60% of the diffraction reflections, worsening the diffraction statistics on the collected data. Third, the size of a sample in routine DAC experiments (up to 100 GPa) is usually about 10-20 μm. In experiments at multimegabar pressures, the samples' linear dimensions do not exceed 3-5 μm. Materials synthesized in a DAC after laser heating usually are represented as multi-phased mixtures of single-crystalline grains, often of submicron size (Figure 2.8.1). Thus, only a combination of precise motorization system with the micron or submicron-sized X-ray beam

provides the capability to perform successful XRD experiments in LHDACs at ultra-high pressures.

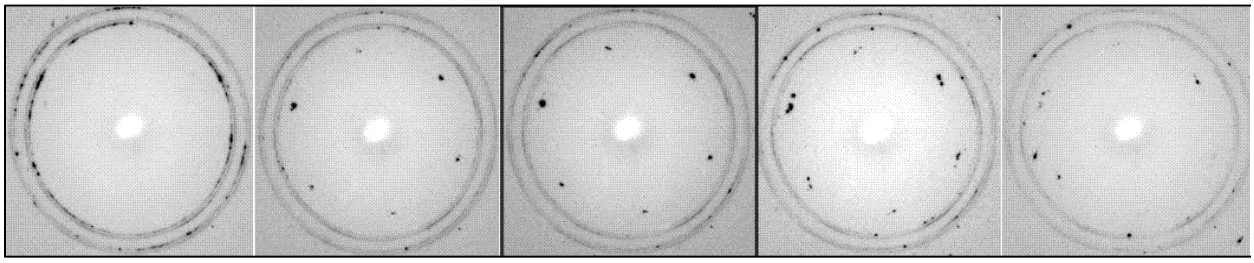

*Figure 2.8.1. A part of 2.5×0.5 μm² from 2D XRD map (20×20 μm²), recorded with step 0.5 μm in both directions. Typical linear size of sample is about 1 μm. Peaks are sharp and strong on the central frame, but they become lower or ever totally disappear 1 μm away from central position. Sample in dsDAC at pressure 200(5) GPa after pulsed laser heating.*

### 2.8.2 Alignment of a DAC on the goniometer

Proper alignment of the sample in DAC is essential for collecting high-quality XRD data. The general alignment procedure is usually based on the absorption of X-rays. When the DAC is being moved by *y*- and *z*-motors, in plane perpendicular to the direction of the beam (Figure 2.8.2a), the intensity of the X-ray beam is recorded by the diode (Figure 2.8.2b). The resulted absorption curve has a characteristic profile when the beam passes through the indented part of the gasket and the sample chamber. The center of the gasket is then defined from the absorption curves obtained for *y*- and *z*-scans.

A position of DAC on the rotation axis is defined from the triangulation procedure. If ω axis is initially aligned with the primary beam (Figure 2.8.2-2a, b), the alignment along the *x*-direction should be performed by scanning the sample in horizontal direction at two different ω positions (-ω and ω).

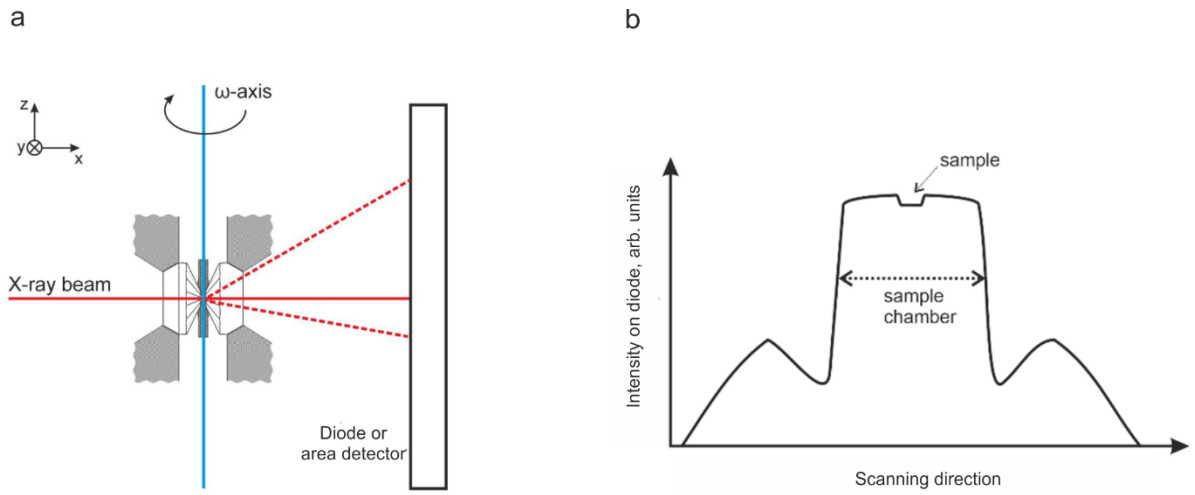


*Figure 2.8.2-1. XRD studies in DAC on synchrotron facilities. (a) – the geometry of experiment; (b) - an example of absorption profile, obtained during the alignment procedure.*

The correction must be applied with the *x*-translation motor above the ω-axis using the formula: $\Delta x_{high} = \frac{d}{\sin\omega}$. In case, when ω axis is initially not aligned with respect to primary beam (Figure 2.8.2-2.c, d) additional *y*-corrections must be. Thus, a third scan at position ω=0 is required. In this case, the correction for *x*-position is defined as: $\Delta x_{high} = \frac{d_1+d_2}{2\cdot\sin\omega}$ and *y*-corrections should be applied as following: $\Delta y_{low} = \frac{d_2-d_1}{4\cdot\sin^2\frac{\omega}{2}}$, $\Delta y_{high} = -\Delta y_{low}$ – for both *y*-motors below and above axis of rotation. The alignment procedure should be repeated until the absolute value of any correction is less than a size of X-ray beam. The full alignment procedure should be performed after each possible displacement of the DAC, e.g. after a manual pressure increase or after laser heating, when the DAC could be moved during annealing or cooling cycles.

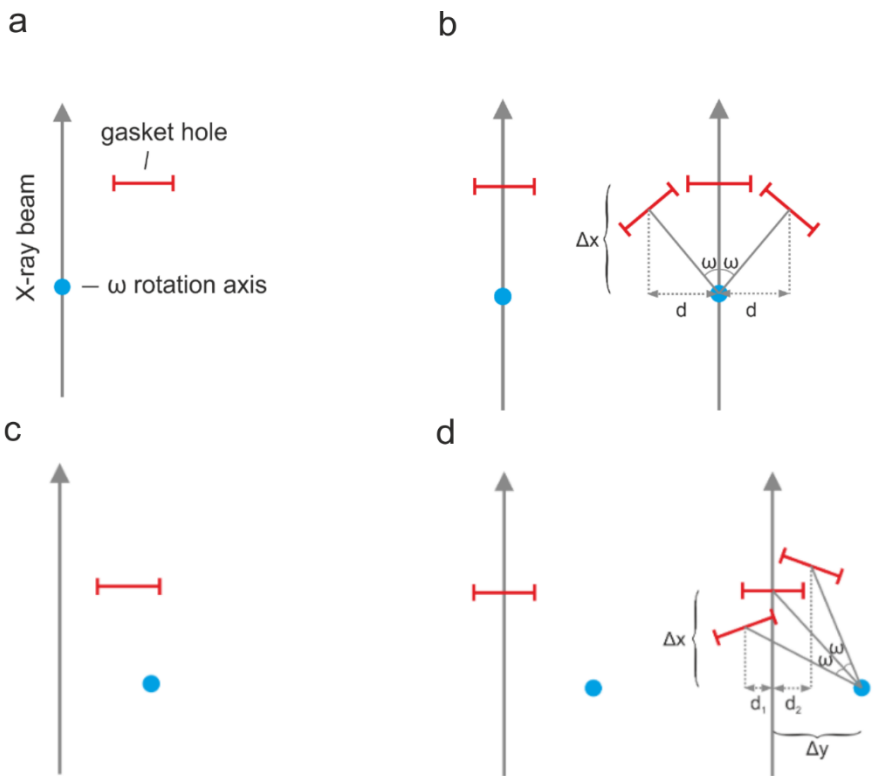


*Figure 2.8.2-2. Typical process of sample centering in the projection along the z-axis. (a) - ω-axis is aligned with primary beam; gasket hole is away from the primary beam. (b) - After several scans in the plane perpendicular to the primary beam direction the gasket hole is aligned with the beam. DAC is rotated around the ω-axis. Two horizontal scans at –ω and ω positions are performed in order to determine the distance between the centers to define x-correction. (c) - Second possible state: both gasket hole and ω-axis are away from the primary beam. (d) - After several scans in the plane perpendicular to the primary beam direction the gasket hole is aligned with the beam, ω-axis is away. DAC is rotated around the ω axis. Three horizontal scans at –ω, 0 and ω positions are performed in order to determine the distance between the centers of the gasket. Correction of x- and both y-motors (above and below axis of rotation) should be applied.*

### 2.8.3 Two-dimensional X-ray imaging maps

In an LHDAC experiments, the sample often represents the multigrain assemblage of crystallites, which sometimes belong to different phases. To find the best spot for the SCXRD data collection, or to obtain the information about the distribution of different phases, one could collect a 2D map of diffraction images.

The user set-ups a script that moves sample by small steps in *y*- and *z*-directions, and on each step it collects a XRD image with or without ω-oscillations. Later, this set of images could be analyzed manually in DIOPTAS program (50). Or it could be imported in XDI (51) software which builds a contrast maps based on the intensity of selected region of interest defined as particular *d*-spacing, for this user needs to find the unique non-overlapping diffraction peaks of the phase of interest.

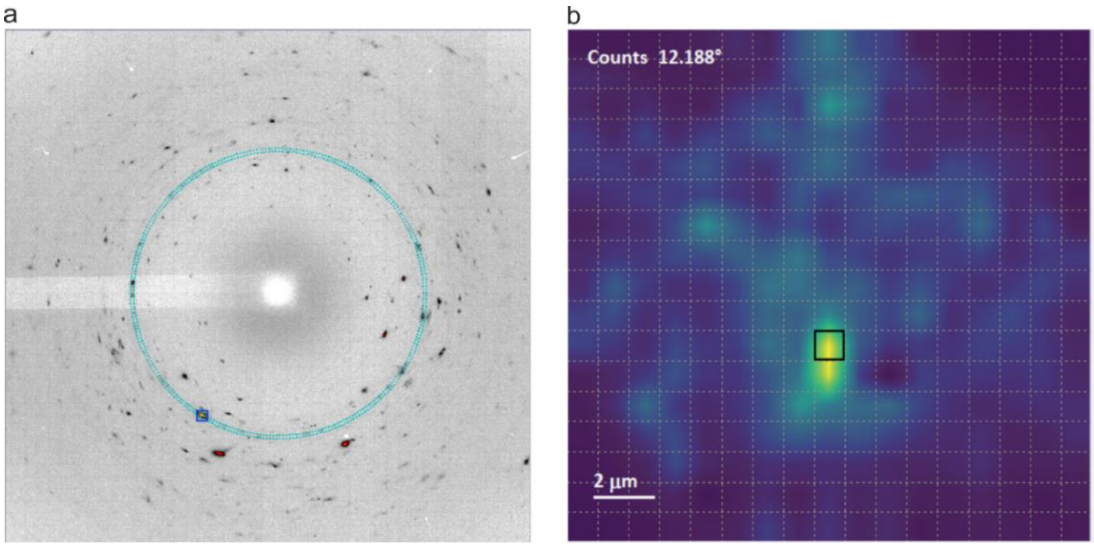


*Figure 2.8.3. Analysis of 2D map X-ray showing the localization of the phase of interest in the pressure chamber. (a) - A typical diffraction image, revealing the presence of single crystalline grain, suitable for SCXRD studies. (b) - A reconstructed X-ray image of the sample chamber (17×17 µm², 1 µm step size), showing the position, where diffraction peaks of unidentified phase are the most intense.*

### 2.8.4 Data processing

In case of powder diffraction studies, calibration of instrument model and integration of diffraction patterns were made in the DIOPTAS software (*93*) using $CeO_2$ powder standard (NIST SRM 674b). In this thesis integrated patterns from powder XRD experiments were processed using the Le Bail technique implemented in JANA2006 program (*94*).

The SCXRD data analysis, including the indexing of diffraction peaks, data integration, frame scaling, and absorption correction, was performed using CrysAlisPro software package(*95*). A crystal of orthoenstatite $(Mg_{1.93},Fe_{0.06})(Si_{1.93},Al_{0.06})O_6$ (space group *Pbca*, *a*=8.8117(2) Å,

*b*=5.18320(10) Å, *c*=18.2391(3) Å) was used as a calibration standard for refinement of the instrumental parameters of the diffractometer (the sample-to-detector distance, the detector's origin, offsets of the goniometer angles and rotations of the X-ray beam and the detector around the instrument axis). In general, the treatment of SCXRD data includes several steps:

*1) Peak hunting*

A peak hunting procedure starts with *ph s* command, it extracts the intensities and coordinates of peaks from experimental diffraction frames. After the input of a proper ω-angular range, the extraction algorithm should be chosen: automatic, traditional (when user himself defines the threshold for the intensities and the area size of diffraction peaks), smart or 3D. Further, the software reconstructs the position of peaks in a reciprocal space. The resulting list of peaks can be reviewed via *pt e* command that shows a table with a Miller indices *hkl* , *xyz* coordinates and experimental intensities of each Bragg's reflection. By default, software uses an orientation matrix of calibrant to derive Miller indices, they would be modified in further steps. The file containing information of all diffraction peaks might be saved using *wd t* command under the *.tabbin format. Later one could upload the peak table into opened CrysAlis project via *rd t* command.

2) *Unit cell finding*

The next task for the user is to find a unit cell of the phase of interest. This can be done via manual inspection of all reflections in the reciprocal space viewer, invoked by pt ewald command. The basic algorithms of peak hunting do not recognize the parasitic diffraction from diamonds, gasket, dead pixels of the detector, and contribution of powder diffraction arcs originated from PTM. It leads to the high contamination of the reciprocal space, worsening the procedure of data processing (Figure. 2.8.4a). However, the recent development of the "cleaning algorithm" by Dr. M. Bykov and Dr. E. Koemets significantly simplified the SCXRD data analysis. Once initial cleaning is done, one could manually select the reflections which should build a 3-dimensional lattice in the reciprocal space and apply an automatic indexing procedure with *um ttt* command (Figure. 2.8.4b, c). At this step, the software defines the orientation matrix of single-crystalline grain, which later could be derived by *ty u* command. The obtained unit cell should be refined against the whole batch of the reflections with *um i* command. Usually, the search of the starting peaks for the unit cell finding is a complex task, especially in the case of laser-heated samples, containing a huge amount of crystallites. The newest development in high-pressure

crystallography, the DAFi software completely solves a task of searching for regular lines forming the unit cell in case of multi-grain samples (Figure. 2.8.4d).

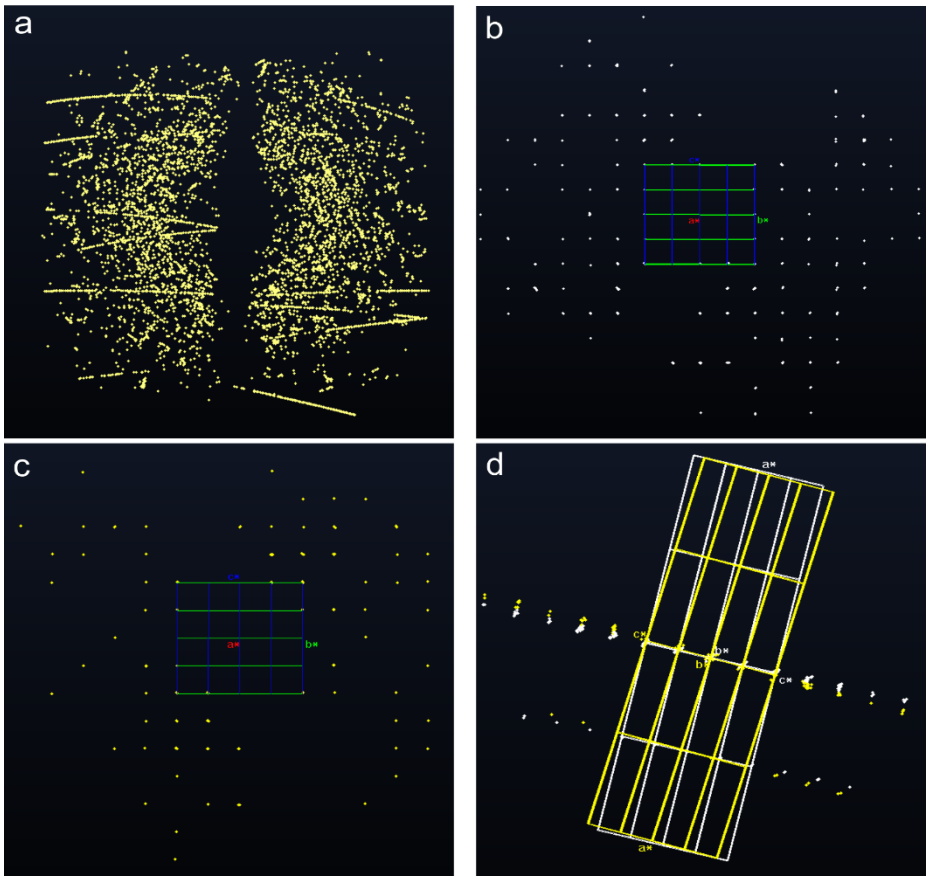


*Figure. 2.8.4. The results of the peak search reconstruction and indexing in the reciprocal space using CrysAlisPro for the case of sample laser-heated at 200(5) GPa and 3000(300) K. (a) - An example of initial dataset (a) in a reciprocal space; (b) and (c) - a separate presentation of each of two single-crystallinedomains observed in this dataset, (d) – a mutual rotation of these domains around b*-axis. The dots represent the reflections, colored cells – orientation and unit cells.*

### *3) Data reduction*

For the given orientation matrix (UB-matrix), the precise extraction of Bragg's peaks intensities could be initialized with *dc proffit* command. CrysAlisPro predicts the positions of the reflections based on the UB-matrix and integrates their intensities, taking into account reflection's

shape and the background level. Analyzing the systematic absences, the software suggests a space group and the user inspects the quality of the data by inspecting the frame scaling curve and confidence values reported by program: $R_\sigma$ and $F_{obs}^2/\sigma_{int}(F_{obs}^2)$ and the quality of merging intensities of the symmetry-equivalent reflections $R_{int}$. These values are derived as follows:

$$R_{int} = \frac{\sum|F_{obs}^2 - \langle F_{obs}^2\rangle|}{\sum|F_{obs}^2|} \qquad \textit{Equation 2.8-1}$$

$$R_\sigma = \frac{\sum[\sigma_{int}(F_{obs}^2)]}{\sum[F_{obs}^2]} \qquad \textit{Equation 2.8-2}$$

$$\sigma_{int}(F_{obs}^2) = \sqrt{\frac{\sum\left(F_{obs}^2 - \langle F_{obs}^2\rangle\right)^2}{n}} \qquad \textit{Equation 2.8-3}$$

where the summations are taken over all input reflections for which more than one symmetry equivalent is averaged; $F_{obs}^2$ is intensity corrected for Lorentz-polarization, $\langle F_{obs}^2\rangle$ is its mean value over all measured equivalents; $n$ – is the number of redundant reflections. If the one is not satisfied with the quality of integration, it is possible to run the process again adjusting several variables, which influence the treatment of detector images: background correction, masking of reflections, integration range, etc.

*4) Data finalization*

The last step to be made in a CrysAlis software is a data finalization. The user checks again the error factors, systematic absences and defines the proper space group. CrysAlis writes down files containing information on the performed data reduction. Among them, the most important are standard reflection and instruction files recognizable with the various structure-solution software packages: file of types *.hkl*, *.cif-od*, *.cif* and *.ins.*

*5) Structure solution and refinement*

The files generated in the previous step further are imported into structure solution software. In this thesis the JANA2006 (*94*) and Olex2(*96*) were used.

The structure solution is a process using intensities of collected reflections for calculation of atomic positions and thermal parameters. The diffracted X-rays carry not only the information on the reciprocal vectors but also information on the electronic density distribution within the unit

cell of a sample. The intensities of Bragg reflections ($I_{hkl}$) are proportional to the square of structure factor ${F_{hkl}}^2$ with the respect to the following formula:

$$ {F_{hkl}}^2 = \frac{I_{hkl}}{k \cdot L_p \cdot A} \qquad \textit{Equation 2.8-4} $$

where $k$ is a scale factor, $L_p$ is Lorentz-polarization correction, $A$ is a transmission factor; those are related as special corrections.

The structure factor contains information regarding the types of atoms and their positions within the unit cell:

$$ \mathbf{F}_{hkl} = F_{hkl} \cdot \exp(i\alpha_{hkl}) = $$
$$ = \sum_j f_j \cdot \exp\left[-B_j \cdot \left(\frac{sin\theta}{\lambda}\right)^2\right] \exp\left[2\pi i \cdot \left(hx_j + ky_j + lz_j\right)\right] \qquad \textit{Equation 2.8-5} $$

where the summing is made for the atoms within the unit cell; $x_j$, $y_j$, $z_j$ are the coordinates of the $j^{\text{th}}$ atom; $f_j$ is the scattering factor of the $j^{\text{th}}$ atom; $\alpha_{hkl}$ is the phase of the diffracted beam; $B_j$ is a $B$-factor directly related to the mean square isotropic displacement of the $j^{\text{th}}$ atom; $\theta$ is the scattering angle and $\lambda$ is the X-ray wavelength.

The electron density ($\rho_{xyz}$) then could be derived by applying the inverse Fourier transformation resulting in the following equation:

$$ \rho_{xyz} = \frac{1}{V}\sum_{hkl} \boldsymbol{F}_{hkl} \cdot \exp\left[-2\pi i \cdot (hx + ky + lz)\right] \qquad \textit{Equation 2.8-6} $$

where $V$ is a unit cell volume.

Indeed, it is possible to determine the electronic density and, therefore, positions of all the atoms. Based on a set of experimental structural amplitudes, ${F_{hkl}}^2$, the structure solution process could be described as a calculation of atomic coordinates and atomic thermal displacement parameters. Unfortunately, the experimental values of ${F_{hkl}}^2$ are real numbers, while $F_{hkl}$ required for calculation of electronic density is a complex function. Therefore, a direct determination of $\alpha_{hkl}$ phase is impossible. This issue is called a “phase problem”. However, it could be overcome with automated phasing procedures such as the Patterson synthesis, direct methods, heavy-atom methods, charge flipping algorithms, dual-space methods and others that are implemented in various software (*94*, *97*, *98*). After applying one of these methods, the distribution of electronic

density might be established; and the starting structural model could be completed. In the next step, the structural model is being refined against the experimental dataset with a least-squares minimization variation of adjustable parameters (e.g. atomic coordinates, occupancies, anisotropic thermal displacement parameters).

The agreement between the model and experimental data is defined by *R*-factors, representing the quality of the refined structural model:

$$R_1 = \frac{\sum\left||F_{obs}| - |F_{calc}|\right|}{\sum|F_{obs}|} \qquad \textit{Equation 2.8-7}$$

$$wR_2 = \left[\frac{\sum w\left|F_{obs}^2 - F_{calc}^2\right|}{\sum wF_{obs}^2}\right]^{\frac{1}{2}} \qquad \textit{Equation 2.8-8}$$

where $F_{obs}$ –the observed structure factor amplitude, $F_{calc}$ – the calculated structure factor amplitude based on the model; and $w$ –weighting factor derived for each measured reflection based on its standard uncertainty.

# Chapter 3 Thesis synopsis

This part provides a short overview of the results presented in Chapters 4-7, that have been either published or prepared for submission to peer-review journals. In the Chapter 4 we report the results of methodological developments aiming the improvement of DAC performance at multimegabar pressures. Subsection 4.1 is dedicated to the tests of secondary stage anvils shaped with FIB from the single-crystal diamond plate. Using the Raman spectroscopy and synchrotron X-ray diffraction we evaluated the efficiency of anvils with different designs for pressure multiplication in dsDACs. Subsection 4.2 describes the newest developments at the extreme conditions beamline P02.2 (*15*) at PETRA III (Hamburg, Germany) enabling significant progress in data collection for samples, exposed to very high pressures with small scattering volumes. We optimized the procedure of the X-ray beam focusing down to submicron level and tested a new sample alignment system. Novel experimental setup allowed us to discover, particularly, a new high-pressure polymorph of $Fe_3O_4$ formed after laser-heating of $Fe_2O_3$ at pressures of ~200 GPa. In course of development and testing methodology of ultra-high pressure studies, we perform numerous experiments on different chemical systems relevant for geo- and material sciences and got number of important and sometimes unexpected results. Outcome of these experiments described in specific chapters. In Chapter 5 we report the results of additional studies devoted to $Fe_3O_4$ behavior at HPHT in laser-heated DAC. Our findings complement the phase diagram of $Fe_3O_4$ up to ~80 GPa and 5000 K, reveal the conditions of formation of two novel high-pressure $Fe_3O_4$ polymorphs and provide the information about chemical instability of magnetite at extreme conditions. These experiments demonstrate that HPHT treatment promotes the formation of ferric-rich Fe-O compounds from decomposition of $Fe_3O_4$, thus arguing for the possible involvement of magnetite in the deep oxygen cycle. Chapter 6 is dedicated to the investigations of crystal structures of novel metal carbides synthesized during laser-heating experiments in DACs. In the Subsection 6.1 we present the study of hitherto unknown Re-C compounds formed due to direct chemical reaction between the diamond anvil and rhenium gasket at pressures of about 200 GPa in pulsed laser-heated DAC. The awareness of these reactions is of primary interest for the development of the methodology for ultra-high-pressure high-temperature experiments, in which Re gaskets are widely used. Unexpectedly we uncover rich chemistry of Re-C system. Using the nano-focused synchrotron X-ray beam, we obtained single-crystal XRD data and established

crystal structures and chemical compositions of four phases: $Re_2C$, $ReC_2$, ReC, $ReC_{0.2}$. One of them, an orthorhombic $ReC_2$, possesses an unusual for any known metal carbides "honeycomb"–like arrangement of carbon atoms, suggesting an unusual mechanism of interaction between carbon atoms in inorganic solids at very high-pressures. In Subsection 6.2 we show unique examples of the formation of complex poly-anionic carbon entities in crystal structures of calcium carbides, synthesized in LHDACs: *Immm*-$CaC_2$ (HP-$CaC_2$) and $Ca_3C_7$. The structures of HP-$CaC_2$ and $Ca_3C_7$ contain deprotonated polyacene-like and para-poly(indenoindene)-like nanoribbons, respectively. Based on experimental XRD data and theoretical calculations we analyse the nature of chemical bonding and establish the compressional behaviour of synthesized compounds. Chapter 7 is devoted to the methodology of the synthesis and study of novel compounds at terapascal pressure range in a laser-heated dsDACs. Full chemical and structural characterizations of $Re_7N_3$ and $ReN_{0.2}$ solids were realized *in situ* by means of SCXRD at material science beamline ID11 at ESRF (Grenoble, France), demonstrating the possibility to extend high-pressure crystallography to the terapascal regime within the multi-grain samples.

## 3.1 Methodological developments in ultra-high pressure studies

### 3.1.1 Secondary anvils shaped from the single-crystal diamond plate

The recent developments in high-pressure science such as the implementation of secondary stage anvils (*7*, *9*, *10*) or the usage of toroidal DACs (*12*, *13*) enabled to reach the static high pressures as high as 1 TPa (*2*) and perform diffraction or spectroscopic studies of matter at ultra-high pressures. However, the ongoing discussions of the capabilities of various ultra-HP DAC techniques and their possible complications call for further systematic investigations shape and type of anvils on efficiency of pressure generation.

In this study, we tested the performance of secondary anvils of different designs in dsDACs. The anvils of conical frustum or disc shapes with flat or modified culet profiles (toroidal or beveled) were prepared by FIB-milling a Ia-type diamond plate, made of a (100)-oriented single crystals (Figure 3.1.1.-1).

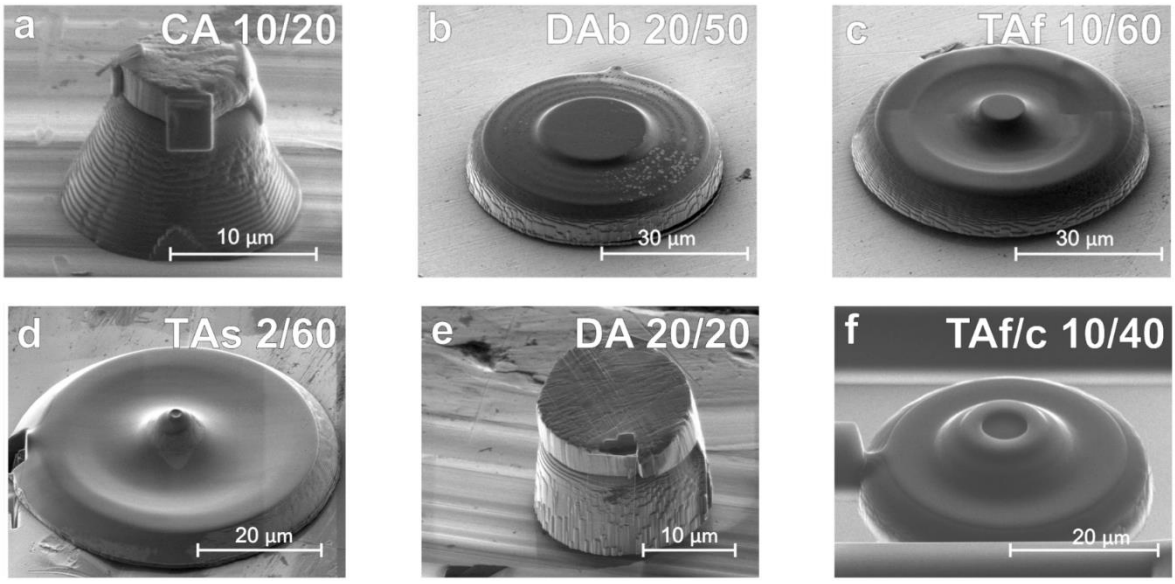


*Figure 3.1.1-1. SEM-images of secondary anvils shaped using FIB from a single-crystal diamond plate of the 10-µm thickness. (a) Conical frustum anvil with a disc-shaped Ir sample on top fixed by a deposited Pt layer; (b) beveled disc-shaped anvil (slope of 8˚); (c) toroidal anvil with the flat tip; (d) toroidal anvil with a hemispherical tip; (e) disc-shaped anvil with the Ir disc-shaped sample on top, fixed by a deposited Pt layer; (f) toroidal anvil with a flat culet featuring a cavity on top.*

Based on Raman spectroscopy and synchrotron XRD measurements we evaluated the efficiency of anvils for pressure multiplication in different modes of operation: as single indenters forced against the primary anvils, or as pairs of anvils forced together in a full dsDAC assembly. All types of secondary anvils performed well up to about ~250 GPa without failure of the primary anvils. The maximum achievable pressures in DACs with a single indenter appeared to be independent on the size and shape of the secondary anvil (Figure 3.1.1-2a). However, the anvils of modified toroidal design enabled a gain in the sample volume, which significantly improves the quality of XRD data, without a loss in pressure (Figure 3.1.1-2b). Feasibility tests confirm the pressure multiplication efficiency of paired assemblies if they are used in dsDACs.

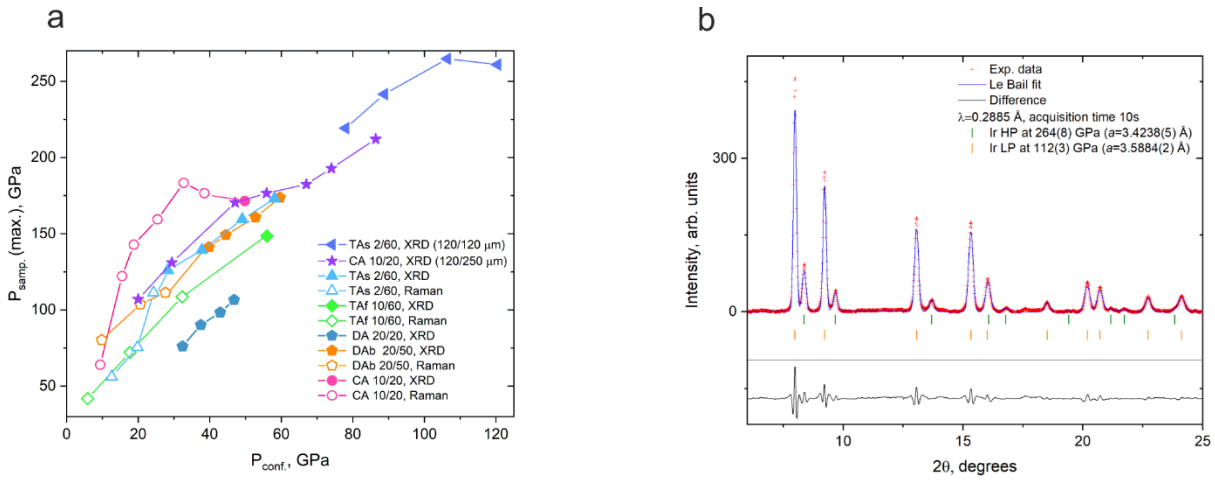


*Figure 3.1.1-2. The performance of secondary stage anvils acting as single indenters. (a) - The relationship between the maximum of achieved and confining pressures. Open and filled symbols are pressure values obtained from Raman spectroscopy and synchrotron XRD, respectively. Different colors designate types of indenters. (b) Example of Le Bail refinement using powder XRD data collected for toroidal anvil with hemispherical tip.*

### 3.1.2 Sub-micron focusing setup for high-pressure crystallography at P02 beam-line at PETRA III

One of the major challenges of structural studies at ultra-high pressures is the reduction of sample sizes, which often requires a very small size of the X-ray beam and high flux. Furthermore, micron-sized samples require the implementation of more precise and accurate sample positioning systems at dedicated high-pressure beamlines. Here we report the development of a sub-micron focusing setup at the general-purpose (GP) experiment table of the beamline P02.2 (*15*) at PETRA III, DESY (Hamburg, Germany). The new setup achieves sub-micron beam size 0.9x0.9 μm$^2$ at FWHM by usage of compound refractive lenses (CRLs) supplemented with a phase plate reducing the spherical aberrations of the CRLs. The implementation of a correcting phase plate also increases a photon flux and reduces the beam tails at the focal spot. In addition, we describe an improved sample positioning system with the implementation of a modern air bearing rotation

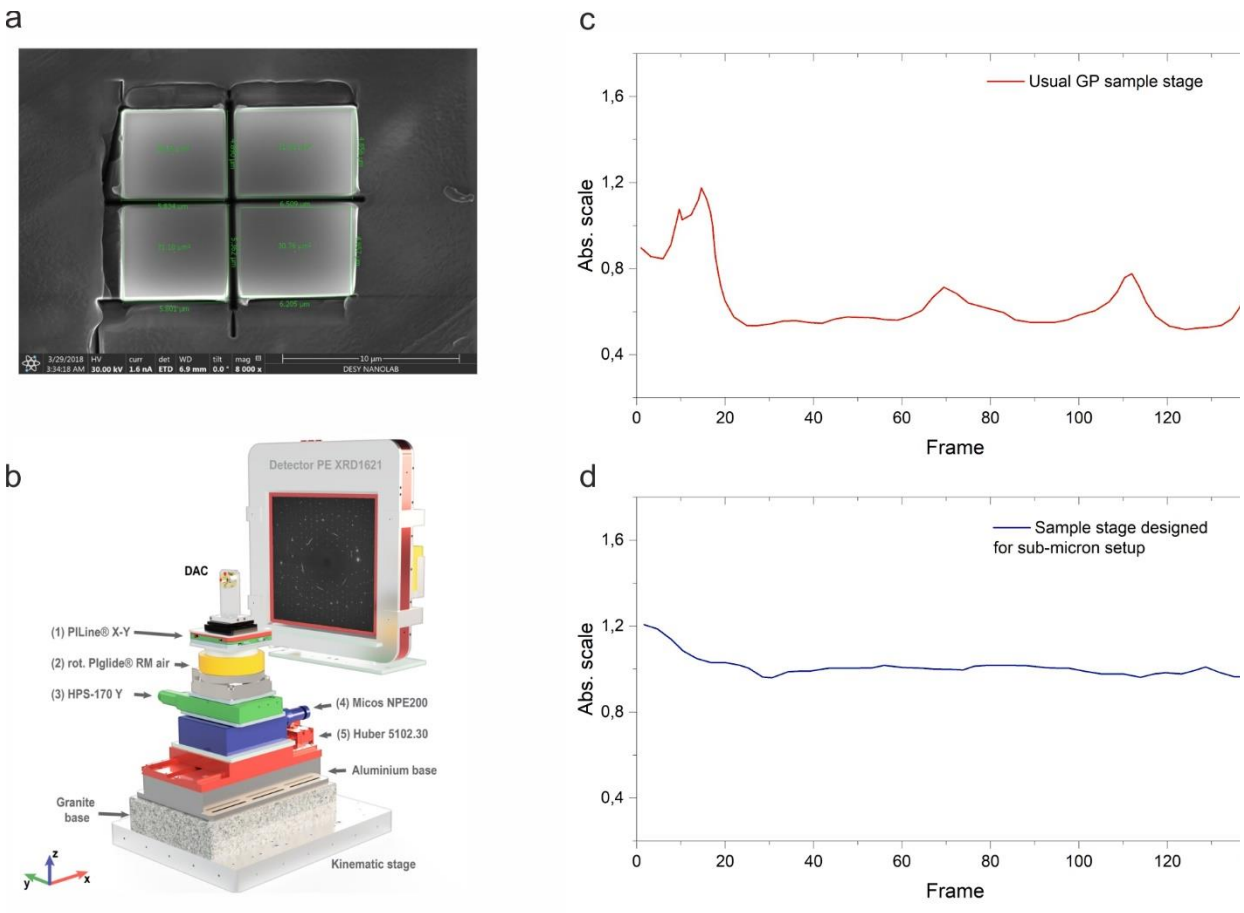


*Figure 3.1.2. Sub-micron focusing setup for high-pressure crystallography. (a) –calibration sample of orthoenstatite prepared by FIB; (b) - a schematic illustration of the designed "sub-micron" sample stack; (c) an output of empirical absorption correction applied for orthoenstatite sample, indicating the wobbling of omega motor used in standard sample stack of GP table; (d) – a scaling curve of calibration sample, applied to data, acquired using sub-micron sample stack, showing the excellent stability of goniometer during the data collection.*

stage operating in a combination with piezo actuator XY stages, enabling a spherical confusion on the order of a micron or below and a position accuracy of 0.1-0.2 μm (Figure 3.1.2b).

We demonstrate the capability of the new setup by performing a test runs using micron-size single crystals of $CoSb_3$ and $(Mg_{1.93}Fe_{0.06})(Si_{1.93},Al_{0.06})O_6$ prepared by FIB (Figure 3.1.2). Our studies, conducted at pressures above 150 GPa, reveal the capability of novel setup to successfully perform SCXRD studies at ultra-high pressures. The crystal structures of new orthorhombic high-pressure polymorph of $Fe_3O_4$ and Fe-bearing perovskite $(Mg_{0.91(2)}Fe_{0.09(2)})SiO_3$ were solved and refined in a multigrain matrix after laser-heating in diamond anvil cells. These state-of-the-art

examples highlight the full potential of the designed experimental setup with the application to high-pressure crystallographic studies.

## 3.2 High-pressure high-temperature behaviour of magnetite

In this part of the thesis we report the results of *in situ* HPHT synchrotron SCXRD studies of magnetite ($Fe_3O_4$) in laser heated diamond anvil cells. Magnetite is the oldest known magnetic mineral and archetypal mixed-valence oxide. However, despite its recognized role in deep Earth processes, the behaviour of magnetite at extreme conditions remains insufficiently studied. Our experiments conducted at pressures up to ~80 GPa and temperatures up to ~5000 K reveal two hitherto unknown $Fe_3O_4$ polymorphs, γ-$Fe_3O_4$ with the orthorhombic $Yb_3S_4$-type structure and δ-$Fe_3O_4$ with the modified $Th_3P_4$-type structure. The latter has never been predicted for iron oxides.

We also found that $Fe_3O_4$, pressurized above ~75 GPa and heated above ~2000 K, becomes chemically unstable and undergoes a series of self-redox or decomposition reactions. Among the chemical products of these processes we found *hcp*-Fe (*99*) and two exotic iron oxides with unusual compositions and crystal structures: $Fe_5O_7$ and $Fe_{25}O_{32}$ (*20*). The available single-crystal XRD data allow us to perform a complex analysis of the compressional behaviour of different iron oxide phases and analyse variations of the volumes of different Fe-O coordination polyhedra. We conclude that ferrous iron in prismatic oxygen environment in iron oxides does not undergo spin crossover up to at least 80 GPa, and ferric iron in oxygen octahedra transforms from the high to the low spin state above ~45 GPa if there is $Fe^{3+}/\Sigma Fe \geq 2/3$ in the oxide composition. Interestingly, that volumes of octahedra in $Fe_5O_7$ are found to be larger than predicted for pure $Fe^{3+}$, indicating a partial charge transfer between iron atoms in prismatic and octahedral sites.

Our results complement the phase diagram of $Fe_3O_4$ up to ~80 GPa and ~5000 K with two previously unknown phases. A chemical instability of $Fe_3O_4$ at conditions corresponding to the depth of over 1800 km indicates the significant changes in the Fe-O system at extreme conditions and provides an additional argument in favour of possible chemical heterogeneity of the Earth's lower mantle. Our experiments on $Fe_3O_4$ demonstrate that HPHT conditions promote formation of

ferric-rich Fe-O compounds, thus arguing for possible involvement of magnetite in the deep oxygen cycle.

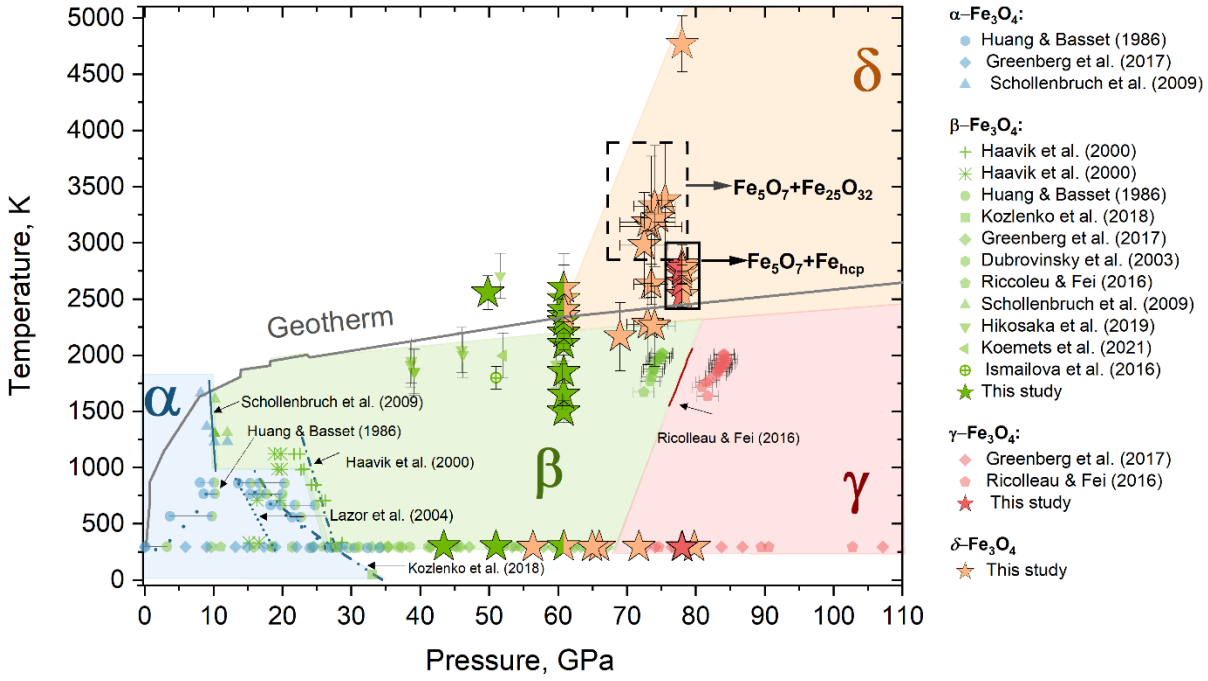


*Figure 3.2.1. Transformational phase diagram of $Fe_3O_4$ summarizing literature data and the results of the present study (plotted as stars). Literature data are obtained from references (21–23, 25, 26, 100–104).*

## 3.3 High-pressure high temperature synthesis of novel metal carbides

### 3.3.1 Crystal structures of rhenium carbides

In this subsection we report the results of *in situ* SCXRD studies of hitherto unknown Re-C compounds formed due to direct chemical reaction between diamond anvil and rhenium gasket in a pulsed laser heated DAC at pressures of about 200 GPa. Investigations of crystalline matter under such extreme conditions are very challenging; however, we managed to overcome technical difficulties associated with very small, micron-sized, samples, poor signal to noise ratio, and parasitic diffraction typical for high pressure experiments in DACs. We used nano-focused synchrotron X-ray beam at ID 11 beamline at ESRF (Grenoble, France) to obtain SCXRD data and established crystal structures and chemical compositions of four phases: $Re_2C$ (*30*, *105*), $ReC_2$,

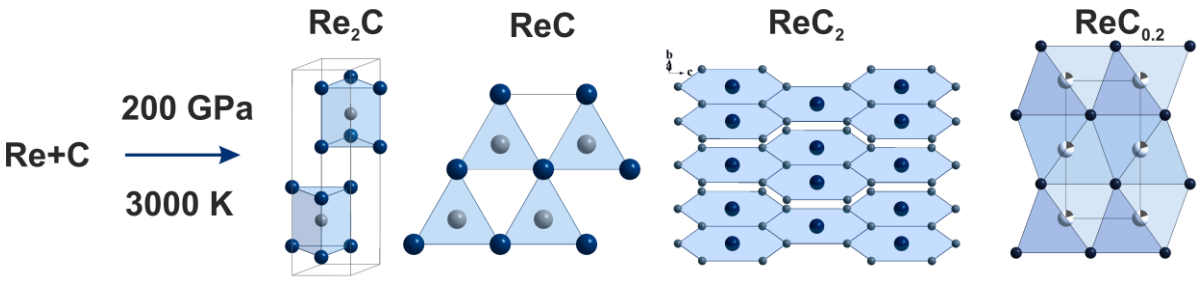


*Figure 3.3.1. Crystal structures of Re-C compounds observed in the present study at ~200 GPa: hP-$Re_2C$, WC-type structured ReC, $TiSi_2$-type structured oF-$ReC_2$; and B8-type structured interstitial solid solution $ReC_{0.2}$. Dark blue balls designate Re atoms; dark gray balls – carbon atoms, white balls with a dark gray sector symbolize a partial occupancy of the position by carbon atoms.*

ReC, $ReC_{0.2}$. Two of observed compounds - WC-structured ReC and orthorhombic $TiSi_2$-structured $ReC_2$ - have never been observed or predicted for the Re-C system. Orthorhombic $ReC_2$, possesses an unusual for carbides crystal structure. It is composed of "honeycomb-like" carbon nets, with unexpectedly long C-C distances (~1.758(3)-1.850(4) Å).

Apart of importance to material science, solid-state physics, and high-pressure chemistry, our findings have to be taken into account upon the planning experiments in laser-heated DACs at multimegabar pressures (as soon as Re is common material for gaskets, and diamond always can act as a source of carbon).

### 3.3.2 Crystal structures of calcium carbides

Known metal carbides contain the simplest carbon anions: isolated carbon atoms $C^{4-}$, $[C_2]^{2-}$-dumbbells and linear trimers $[C_3]^{4-}$, which are isostructural to methane, acetylene, and allene, respectively (*34–41*). However, *ab initio* calculations predict the pressure-induced changes in the bonding patterns of carbides, leading to formation of the exotic carbon poly-anions: $[C_4]$ chains, $[C_5]$ units, $[C_6]$ rings, and, eventually, graphitic carbon sheets (*42–45*)

In Subsection 7.2 we show the results of HPHT studies of $CaC_2$ in LHDACs performed using synchrotron SCXRD at pressures up to ~150 GPa and temperatures up to ~3000 K. Single crystals of $CaC_2$-I (*46*) were loaded into the BX-90 DAC with a paraffin oil, served as pressure-

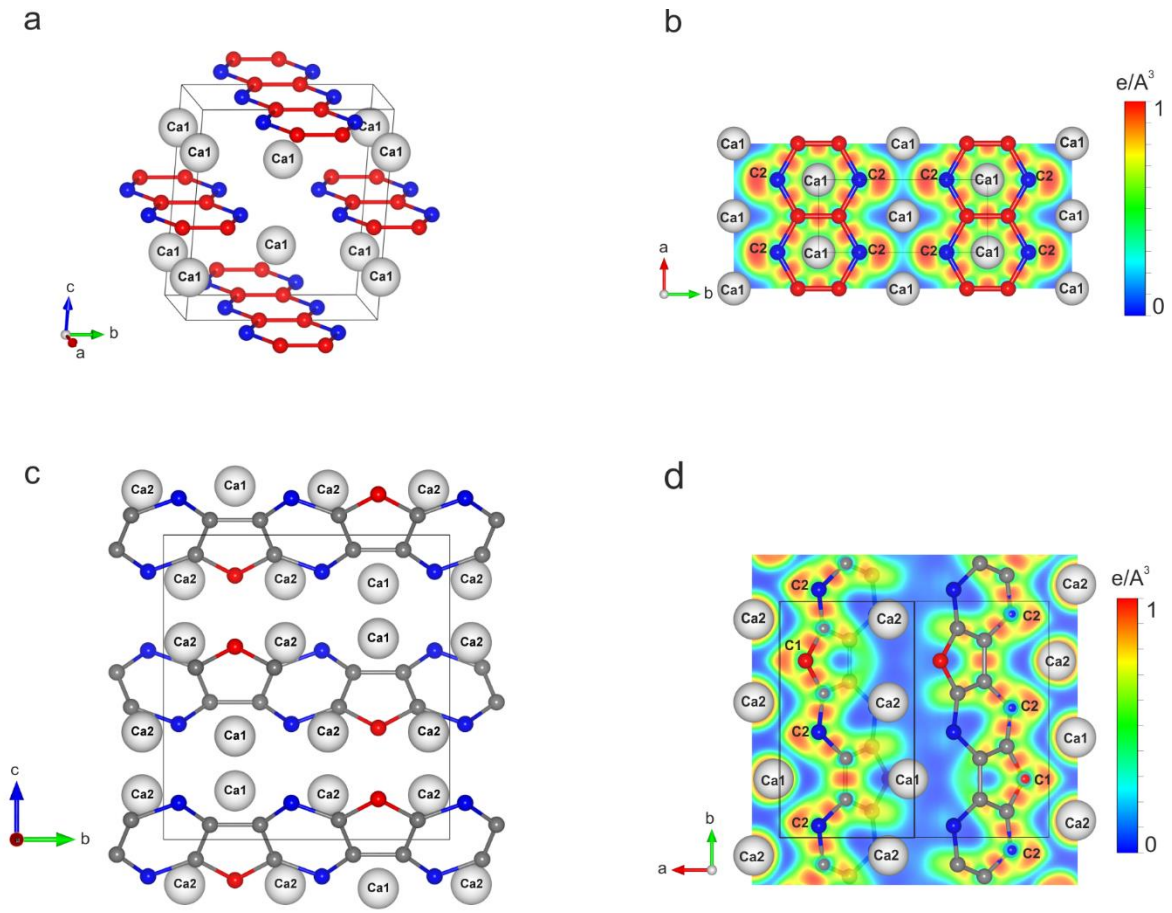


*Figure. 3.3.2. Crystal structures of novel calcium carbides, synthesized in present work. (a) –HP-$CaC_2$ (at 44(1) GPa), (b) –$Ca_3C_7$ (at 38(1) GPa) cross-sections of the calculated electron localization function (ELF) in projection high-lighting the deprotonated poly-acene(c) and para-poly-indenoindene(d) nanoribbons. Calcium atoms are shown as white spheres; grey, red and blue ones symbolize carbon atoms.*

transmitted medium. Laser heating was performed in a continuous mode using double-sided laser-heating setup at the BGI (*61*). For the first time, we observed the formation of predicted high-pressure polymorph of $CaC_2$ (HP- $CaC_2$), its crystal structure was solved and refined on the basis of experimental SCXRD data. Also we observed a novel $Ca_3C_7$ compound, which was never anticipated or observed before, with the orthorhombic crystal structure (space group *Pnma*), featuring infinite, fully deprotonated *para*-poly-indenoindene (*p*-PInIn)-like (*106*). Experimental results were supported by DFT calculations. Theoretically calculated crystal structures are in a perfect agreement with the experimentally determined ones.

## 3.4 High-pressure high-temperature synthesis at terapascal pressures

Theoretical modelling predicts very unusual structures and properties of materials at extreme pressure-temperature conditions(*107*, *108*). Hitherto, their synthesis and investigations above 200 GPa have been hindered by both the technical complexity of ultra-high-pressure experiments and the absence of relevant methods of materials' analysis *in situ*. Here we report on the methodology that was developed to enable experiments at static compression in terapascal regime with laser heating and on its application to the synthesis of a novel rhenium nitride, $Re_7N_3$, and a rhenium-nitrogen alloy at terapascal pressures a laser-heated dsDACs.

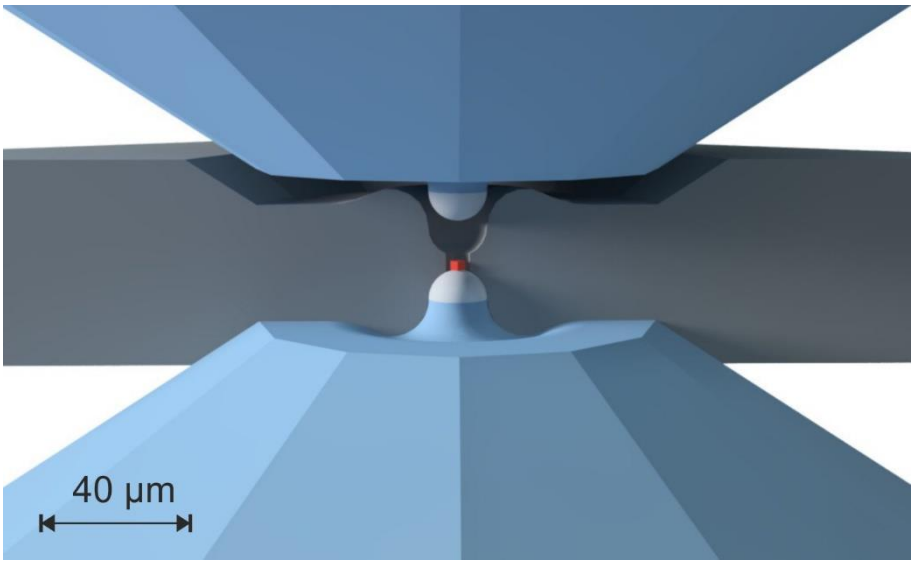


*Figure 3.4.1-1. A 3D presentation of diamond anvils featuring the toroidal profile with NCD semi-balls (white half-spheres) placed on the toroidal tip. External anvils are conventional Boehler-Almax type single-beveled diamonds with a 40-μm culet size. Sample is shown as red block.*

To achieve the desired pressures, we combined toroidal (*12*, *13*) and double-stage (*2*, *7*, *8*) anvils design: two semi-balls made of transparent NCD (*2*), were placed on the tip of the miniature toroidal culet. A few grains of a rhenium powder (99.995% purity, Merck Inc.) were placed into the pressure chamber, which was then filled with nitrogen ($N_2$) at about 1.4 kbar using the high-pressure gas-loading setup (*77*) at the Bayerisches Geoinstitut (BGI, Bayreuth, Germany) After

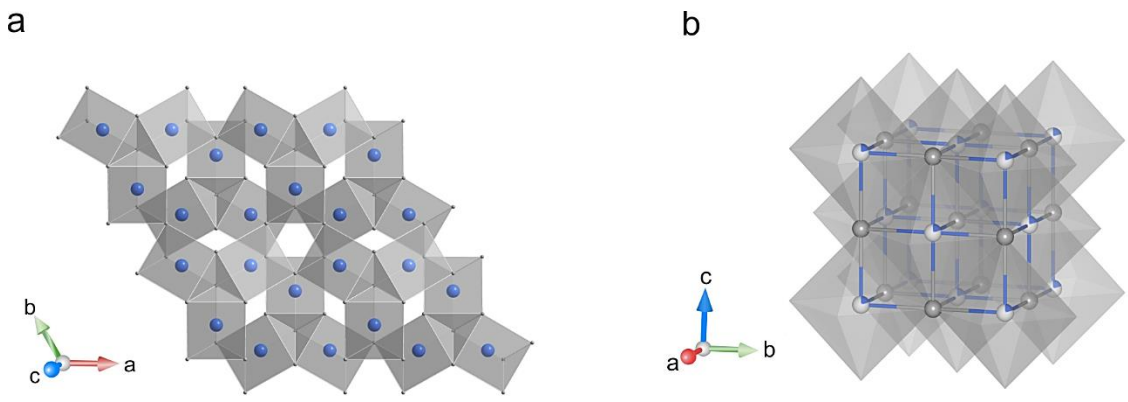


*Figure 3.4.2-2. Crystal structures of phases observed in laser-heated dsDACs at terapascal pressures. (a) - hexagonal $Re_7N_3$ at 905(5) GPa in dsDAC #1; (b) cubic (B1 NaCl-type structured) rhenium-nitrogen solid solution $ReN_{0.2}$ at 730(4) dsDAC #3. Rhenium atoms are shown as grey spheres and nitrogen atoms are shown as blue ones.*

pressurization of the cells to about 120-140 GPa on the first-stage anvils, the samples were laser heated. The dsDACs with temperature-quenched material were transported to ID11 at the ESRF (Grenoble, France) and investigated using both powder and single-crystal XRD. A rhenium-nitrogen alloy, and a novel rhenium nitride $Re_7N_3$ were synthesized in three different experiments in the Re-N system. Full chemical and structural characterizations of $Re_7N_3$ and $ReN_{0.2}$ solids were realized *in situ*, demonstrating the successful application of high-pressure crystallography methods to multi-grain samples, subjected to terapascal pressures. By extending experimental field of high-pressure synthesis and structural studies, our work paves the way towards discovering of new materials and observations of novel physical phenomena at extreme conditions.

## 3.5 List of manuscripts and statement of authors' contribution

1) S. Khandarkhaeva (SK), T. Fedotenko (TF), A. Krupp (AKr), K. Glazyrin (KG), W. Dong (WD), H.-P. Liermann (HPL), M. Bykov (MB), A. Kurnosov (AK), N. Dubrovinskaia (ND) and L. Dubrovinsky (LD), Testing the performance of secondary anvils shaped with focused ion beam from the single-crystal diamond for use in double-stage diamond anvil cells. *Rev. Sci. Instrum.* **93**, 033904 (2022), DOI:10.1063/5.0071786

SK., ND and LD designed and planed the experiments. SK, WD and MB prepared secondary stage anvils using the FIB. SK, AKr and AK assembled diamond anvil cells. SK and AKr performed Raman measurements. SK, TF, AKr, KG, HPL and LD performed synchrotron XRD studies. SK, LD and ND wrote the manuscript with contributions of all authors. SK contribution 90%.

2) K. Glazyrin (KG), S. Khandarkhaeva (SK), T. Fedotenko (TF), D. Laniel (DL), F. Seiboth (FS), A. Schropp (AS), J. Garrevoet (JG), D. Brückner (DB), G. Falkenberg (GF), A. Kubec (AK), C. David (CV), M. Wendt (MW), S. Wenz (SW), L. Dubrovinsky (LD), N. Dubrovinskaia (ND) and H.-P. Liermann (HPL). Sub-micron focusing setup for high-pressure crystallography at the Extreme Conditions Beamline of PETRA III. In press, *Journal of Synchrotron Radiation.*

KG, FS, AS, JG, DB, GF, AK, CV and HPL designed and implemented the setup of sub-micron focusing of X-ray beam. KG, MW SW designed a new sample positioning system. SK, TF, DL performed synchrotron XRD studies. SK analyzed SCXRD data. KG, SK, LD, ND and HPL wrote the manuscript with contributions of all authors. SK contribution in experiment results 90%.

3) S. Khandarkhaeva (SK), T. Fedotenko (TF), S. Chariton (SC), E. Bykova (EB), S. V. Ovsyannikov (SVO), K. Glazyrin (KG), H.-P. Liermann (HPL), V. Prakapenka (VP), N. Dubrovinskaia (ND) and L. Dubrovinsky (LD), Structural Diversity of Magnetite and Products of Its Decomposition at Extreme Conditions. *Inorg. Chem.* **61**, 1091–1101 (2022), DOI:10.1021/acs.inorgchem.1c03258.

SK, ND and LD designed and planed the experiments. SVO performed synthesis of $Fe_3O_4$ single-crystals in the large volume press. SK, TF, SC, KG, HPL, VP and LD performed synchrotron XRD

studies. SK, SC and EB analyzed SCXRD data. SK, LD and ND wrote the manuscript with contributions of all authors. SK contribution 75%.

4) S. Khandarkhaeva (SK), T. Fedotenko (TF), M. Bykov (MB), E. Bykova (EB), S. Chariton (SC), P. Sedmak (PS), K. Glazyrin (KG), V. Prakapenka (VP), N. Dubrovinskaia (ND), L. Dubrovinsky (LD), Novel Rhenium Carbides at 200 GPa. *Eur. J. Inorg. Chem.* **2020**, 2186–2190 (2020), DOI:10.1002/ejic.202000252.

SK, ND and LD designed and planed the experiments. SK, TF, MB, EB, SC, PS, KG, VP and LD performed synchrotron XRD studies. SK, MB, EB and LD. analyzed SCXRD data, SC performed synthesis of $Re_2C$ single-crystals in the large volume press. SK, LD and ND wrote the manuscript with contributions of all authors. SK contribution 75%.

5) S. Khandarkhaeva (SK), T. Fedotenko (TF), A. Aslandukova (AlA), M. Bykov (MB), D. Laniel (DL), A. Aslandukov (AnA), B. Winkler (BW), U. Ruschewitz (UR), C. Tobeck (CT), S. Chariton (SC), V. Prakapenka (VP), K. Glazyrin (KG), H.-P. Liermann (HPL), C. Giacobbe (CG), E. Lawrence Bright (ELB), N. Dubrovinskaia (ND) and L. Dubrovinsky (LD), High-pressure synthesis of $CaC_2$ and $Ca_3C_7$ with deprotonated polyacene- and para-poly(indenoindene)-like nanoribbons. To be submitted to *Nature Chemistry*.

SK and LD designed and planed the experiments. SK, TF, DL, AnA, SC, VP, KG, HPL, CG, EBL and LD performed synchrotron XRD studies. SK analyzed SCXRD data. SK, MB and LD interpreted the results. AlA performed theoretical calculations. BW performed theoretical calculation of Raman spectra. UR and CT synthesized $CaC_2$ samples. SK, LD and ND wrote the manuscript with corrections from MB and UR. SK contribution 75%.

6) L. Dubrovinsky (LD), S. Khandarkhaeva (SK), T. Fedotenko (TF), D. Laniel (DL), M. Bykov (MB), C. Giacobbe (CG), E. Lawrence Bright (EBL), P. Sedmak (PS), S. Chariton (SC), V. Prakapenka (VP), A. V. Ponomareva (AP), E. A. Smirnova (EAS), M. P. Belov (MPB), F. Tasnádi (FT), N. Shulumba (NS), F. Trybel (FT), Igor A. Abrikosov (IAA), N. Dubrovinskaia (ND). Materials synthesis at terapascal static pressures. In press, *Nature*.

LD and SK designed and planed the experiments. LD, SK and DL prepared diamond anvil cells of modified design. LD, SK, TF, DL, MB, CG, EBL, PS, SC, VP performed synchrotron XRD studies. SK and LD analyzed SCXRD data. AVP, EAS, MPB, FT, NS, FT, IAA performed

theoretical calculations. LD, ND and IAA wrote the manuscript with contribution form SK and all co- authors. SK contribution 45%.

# References


1. W. A. Bassett, High Pressure Research : An Diamond anvil cell , 50th birthday. *High Press. Res.* **29**, 163–186 (2009).

2. N. Dubrovinskaia, L. Dubrovinsky, N. A. Solopova, A. Abakumov, S. Turner, M. Hanfland, E. Bykova, M. Bykov, C. Prescher, V. B. Prakapenka, S. Petitgirard, I. Chuvashova, B. Gasharova, Y.-L. Mathis, P. Ershov, I. Snigireva, A. Snigirev, Terapascal static pressure generation with ultrahigh yield strength nanodiamond. *Sci. Adv.* **2**, e1600341 (2016).

3. E. Snider, N. Dasenbrock-Gammon, R. McBride, M. Debessai, H. Vindana, K. Vencatasamy, K. V. Lawler, A. Salamat, R. P. Dias, Room-temperature superconductivity in a carbonaceous sulfur hydride. *Nature*. **586**, 373–377 (2020).

4. M. Bykov, S. Chariton, H. Fei, T. Fedotenko, G. Aprilis, A. V. Ponomareva, F. Tasnádi, I. A. Abrikosov, B. Merle, P. Feldner, S. Vogel, W. Schnick, V. B. Prakapenka, E. Greenberg, M. Hanfland, A. Pakhomova, H.-P. Liermann, T. Katsura, N. Dubrovinskaia, L. Dubrovinsky, High-pressure synthesis of ultraincompressible hard rhenium nitride pernitride Re2(N2)(N2) stable at ambient conditions. *Nat. Commun.* **10**, 2994 (2019).

5. H. Gou, N. Dubrovinskaia, E. Bykova, A. A. Tsirlin, D. Kasinathan, W. Schnelle, A. Richter, M. Merlini, M. Hanfland, A. M. Abakumov, D. Batuk, G. Van Tendeloo, Y. Nakajima, A. N. Kolmogorov, L. Dubrovinsky, Discovery of a superhard iron tetraboride superconductor. *Phys. Rev. Lett.* **111**, 1–5 (2013).

6. M. Bykov, E. Bykova, G. Aprilis, K. Glazyrin, E. Koemets, I. Chuvashova, I. Kupenko, C. McCammon, M. Mezouar, V. Prakapenka, H.-P. Liermann, F. Tasnádi, A. V. Ponomareva, I. A. Abrikosov, N. Dubrovinskaia, L. Dubrovinsky, Fe-N system at high pressure reveals a compound featuring polymeric nitrogen chains. *Nat. Commun.* **9**, 1–8 (2018).

7. L. Dubrovinsky, N. Dubrovinskaia, V. B. Prakapenka, A. M. Abakumov, Implementation of micro-ball nanodiamond anvils for high-pressure studies above 6 Mbar. *Nat. Commun.* **3**, 1163–1167 (2012).

8. L. Dubrovinsky, N. Dubrovinskaia, E. Bykova, M. Bykov, V. Prakapenka, C. Prescher, K.

Glazyrin, H.-P. Liermann, M. Hanfland, M. Ekholm, Q. Feng, L. V Pourovskii, M. I. Katsnelson, J. M. Wills, I. A. Abrikosov, The most incompressible metal osmium at static pressures above 750 gigapascals. *Nature*. **525**, 226–229 (2015).

9. T. Sakai, T. Yagi, H. Ohfuji, T. Irifune, Y. Ohishi, N. Hirao, Y. Suzuki, Y. Kuroda, T. Asakawa, T. Kanemura, High-pressure generation using double stage micro-paired diamond anvils shaped by focused ion beam. *Rev. Sci. Instrum.* **86**, 033905 (2015).

10. T. Sakai, T. Yagi, T. Irifune, H. Kadobayashi, N. Hirao, T. Kunimoto, H. Ohfuji, S. Kawaguchi-Imada, Y. Ohishi, S. Tateno, K. Hirose, High pressure generation using double-stage diamond anvil technique: problems and equations of state of rhenium. *High Press. Res.* **38**, 107–119 (2018).

11. S. S. Lobanov, V. B. Prakapenka, C. Prescher, Z. Konôpková, H. P. Liermann, K. L. Crispin, C. Zhang, A. F. Goncharov, Pressure, stress, and strain distribution in the double-stage diamond anvil cell. *J. Appl. Phys.* **118** (2015), doi:10.1063/1.4927213.

12. Z. Jenei, E. F. O'Bannon, S. T. Weir, H. Cynn, M. J. Lipp, W. J. Evans, Single crystal toroidal diamond anvils for high pressure experiments beyond 5 megabar. *Nat. Commun.* **9**, 3563 (2018).

13. A. Dewaele, P. Loubeyre, F. Occelli, O. Marie, M. Mezouar, Toroidal diamond anvil cell for detailed measurements under extreme static pressures. *Nat. Commun.* **9**, 2913 (2018).

14. P. Loubeyre, F. Occelli, P. Dumas, Synchrotron infrared spectroscopic evidence of the probable transition to metal hydrogen. *Nature*. **577**, 631–635 (2020).

15. H.-P. Liermann, Z. Konôpková, W. Morgenroth, K. Glazyrin, J. Bednarčik, E. E. McBride, S. Petitgirard, J. T. Delitz, M. Wendt, Y. Bican, A. Ehnes, I. Schwark, A. Rothkirch, M. Tischer, J. Heuer, H. Schulte-Schrepping, T. Kracht, H. Franz, The Extreme Conditions Beamline P02.2 and the Extreme Conditions Science Infrastructure at PETRA III. *J. Synchrotron Radiat.* **22**, 908–924 (2015).

16. H.-K. Mao, T. Takahashi, W. A. Bassett, G. L. Kinsland, L. Merrill, Isothermal compression of magnetite to 320 KB. *J. Geophys. Res.* **79**, 1165–1170 (1974).

17. H. Mao, D. Virgo, P. M. Bell, High-pressure 57Fe Mossbauer data on the phase and

magnetic transitions ofmagnesioferrite (MgFe2O4), magnetite (Fe3O4), and hematite (Fe2O3). *Year B. Carnegie Inst. Washingt.* **76**, 522–525 (1977).

18. M. P. Pasternak, S. Nasu, K. Wada, S. Endo, High-pressure phase of magnetite. *Phys. Rev. B.* **50**, 6446–6449 (1994).

19. E. R. Morris, Q. Williams, Electrical resistivity of Fe 3 O 4 to 48 GPa: Compression-induced changes in electron hopping at mantle pressures. *J. Geophys. Res. Solid Earth*. **102**, 18139–18148 (1997).

20. E. Bykova, L. Dubrovinsky, N. Dubrovinskaia, M. Bykov, C. McCammon, S. V Ovsyannikov, H.-P. Liermann, I. Kupenko, A. I. Chumakov, R. Rüffer, M. Hanfland, V. Prakapenka, Structural complexity of simple Fe2O3 at high pressures and temperatures. *Nat. Commun.* **7**, 10661 (2016).

21. C. Haavik, S. Stølen, H. Fjellvåg, M. Hanfland, D. Häusermann, Equation of state of magnetite and its high-pressure modification: Thermodynamics of the Fe-O system at high pressure. *Am. Mineral.* **85**, 514–523 (2000).

22. L. S. Dubrovinsky, N. A. Dubrovinskaia, C. McCammon, G. K. Rozenberg, R. Ahuja, J. M. Osorio-Guillen, V. Dmitriev, H. P. Weber, T. Le Bihan, B. Johansson, The structure of the metallic high-pressure Fe3O4 polymorph: Experimental and theoretical study. *J. Phys. Condens. Matter*. **15**, 7697–7706 (2003).

23. E. Greenberg, W. M. Xu, M. Nikolaevsky, E. Bykova, G. Garbarino, K. Glazyrin, D. G. Merkel, L. Dubrovinsky, M. P. Pasternak, G. K. Rozenberg, High-pressure magnetic, electronic, and structural properties of MFe2O4 (M = Mg,Zn,Fe) ferric spinels. *Phys. Rev. B.* **95**, 195150 (2017).

24. A. Ricolleau, Y. Fei, Equation of state of the high-pressure Fe 3 O 4 phase and a new structural transition at 70 GPa. *Am. Mineral.* **101**, 719–725 (2016).

25. E. Huang, W. A. Bassett, Rapid determination of Fe 3 O 4 phase diagram by synchrotron radiation. *J. Geophys. Res.* **91**, 4697 (1986).

26. K. Hikosaka, R. Sinmyo, K. Hirose, T. Ishii, Y. Ohishi, The stability of Fe5O6 and Fe4O5 at high pressure and temperature. *Am. Mineral.* **104**, 1356–1359 (2019).

27. D. P. Dobson, J. P. Brodholt, Subducted banded iron formations as a source of ultralow-velocity zones at the core–mantle boundary. *Nature*. **434**, 371–374 (2005).

28. P. Lazor, O. N. Shebanova, H. Annersten, High-pressure study of stability of magnetite by thermodynamic analysis and synchrotron X-ray diffraction. *J. Geophys. Res. Solid Earth*. **109**, 1–16 (2004).

29. S. Anzellini, A. Dewaele, F. Occelli, P. Loubeyre, M. Mezouar, Equation of state of rhenium and application for ultra high pressure calibration. *J. Appl. Phys.* **115**, 043511 (2014).

30. E. A. Juarez-Arellano, B. Winkler, A. Friedrich, D. J. Wilson, M. Koch-Müller, K. Knorr, S. C. Vogel, J. J. Wall, H. Reiche, W. Crichton, M. Ortega-Aviles, M. Avalos-Borja, Reaction of rhenium and carbon at high pressures and temperatures. *Zeitschrift fur Krist.* **223**, 492–501 (2008).

31. R. Jeanloz, B. K. Godwal, C. Meade, Static strength and equation of state of rhenium at ultra-high pressures. *Nature*. **349**, 687–689 (1991).

32. I. Kupenko, L. Dubrovinsky, N. Dubrovinskaia, C. McCammon, K. Glazyrin, E. Bykova, T. B. Ballaran, R. Sinmyo, A. I. Chumakov, V. Potapkin, A. Kantor, R. Rüffer, M. Hanfland, W. Crichton, M. Merlini, Portable double-sided laser-heating system for Mössbauer spectroscopy and X-ray diffraction experiments at synchrotron facilities with diamond anvil cells. *Rev. Sci. Instrum.* **83**, 124501 (2012).

33. G. Aprilis, C. Strohm, I. Kupenko, S. Linhardt, A. Laskin, D. M. Vasiukov, V. Cerantola, E. G. Koemets, C. McCammon, A. Kurnosov, A. I. Chumakov, R. Rüffer, N. Dubrovinskaia, L. Dubrovinsky, Portable double-sided pulsed laser heating system for time-resolved geoscience and materials science applications. *Rev. Sci. Instrum.* **88**, 084501 (2017).

34. Louis E. Toth, *transition metal carbides and nitrides* (1971).

35. F. H. Spedding, K. Gschneidner, A. H. Daane, The Crystal Structures of Some of the Rare Earth Carbides. *J. Am. Chem. Soc.* **80**, 4499–4503 (1958).

36. T. Sakai, G. Y. Adachi, T. Yoshida, J. Shiokawa, Magnetic and electrical properties of

LaC2, CeC2, PrC2, NdC2, and SmC2. *J. Chem. Phys.* **75**, 3027–3032 (1981).

37. M. Atoji, R. C. Medrud, K. Gschneidner, A. H. Daane, R. E. Rundle, F. H. Spedding, K. Gschneidner, A. H. Daane, T. Sakai, G. Y. Adachi, T. Yoshida, J. Shiokawa, R. E. Rundle, N. C. Baenziger, A. S. Wilson, R. A. McDonald, Neutron diffraction studies of CaC2, YC2, LaC 2, CeC2, TbC2, YbC2, LuC 2, and UC2. *J. Chem. Phys.* **80**, 99–105 (1958).

38. V. Babizhetskyy, B. Kotur, V. Levytskyy, H. Michor, *Handbook on the Physics and Chemistry of Rare Earths* (Elsevier B.V., ed. 1, 2017), vol. 52.

39. H. Mattausch, T. Gulden, R. K. Kremer, J. Horakh, A. Simon, Carbide mit C34-- und C4_-Ionen, 1439–1443 (1994).

40. H. Fjellvaag, P. Karen, Crystal structure of magnesium sesquicarbide. *Inorg. Chem.* **31**, 3260–3263 (1992).

41. R. Pöttgen, W. Jeitschko, Sc3C4, a Carbide with C3 Units Derived from Propadiene. *Inorg. Chem.* **30**, 427–431 (1991).

42. T. A. Strobel, O. O. Kurakevych, D. Y. Kim, Y. Le Godec, W. Crichton, J. Guignard, N. Guignot, G. D. Cody, A. R. Oganov, Synthesis of β-Mg2C3: A monoclinic high-pressure polymorph of magnesium sesquicarbide. *Inorg. Chem.* **53**, 7020–7027 (2014).

43. Y. L. Li, S. N. Wang, A. R. Oganov, H. Gou, J. S. Smith, T. A. Strobel, Investigation of exotic stable calcium carbides using theory and experiment. *Nat. Commun.* **6**, 1–9 (2015).

44. X. Gao, Y. Jiang, R. Zhou, J. Feng, Stability and elastic properties of Y-C binary compounds investigated by first principles calculations. *J. Alloys Compd.* **587**, 819–826 (2014).

45. C. Su, J. Zhang, G. Liu, X. Wang, H. Wang, Y. Ma, Catenation of carbon in LaC2 predicted under high pressure. *Phys. Chem. Chem. Phys.* **18**, 14286–14291 (2016).

46. M. Knapp, U. Ruschewitz, Structural phase transitions in CaC2. *Chem. - A Eur. J.* **7**, 874–880 (2001).

47. L. Wang, X. Huang, D. Li, Y. Huang, K. Bao, F. Li, G. Wu, B. Liu, T. Cui, Pressure-induced structural transformation of CaC 2. *J. Chem. Phys.* **144**, 194506 (2016).

48. Y. L. Li, S. N. Wang, A. R. Oganov, H. Gou, J. S. Smith, T. A. Strobel, Investigation of

exotic stable calcium carbides using theory and experiment. *Nat. Commun.* **6**, 6974 (2015).

49. D. Benson, Y. Li, W. Luo, R. Ahuja, G. Svensson, U. Häussermann, Lithium and calcium carbides with polymeric carbon structures. *Inorg. Chem.* **52**, 6402–6406 (2013).

50. M. Bykov, E. Bykova, E. Koemets, T. Fedotenko, G. Aprilis, K. Glazyrin, H. P. Liermann, A. V Ponomareva, J. Tidholm, F. Tasnádi, I. A. Abrikosov, N. Dubrovinskaia, L. Dubrovinsky, High-Pressure Synthesis of a Nitrogen-Rich Inclusion Compound ReN8·x N2 with Conjugated Polymeric Nitrogen Chains. *Angew. Chemie - Int. Ed.* **57**, 9048–9053 (2018).

51. M. Bykov, S. Khandarkhaeva, T. Fedotenko, P. Sedmak, N. Dubrovinskaia, L. Dubrovinsky, Synthesis of FeN 4 at 180 GPa and its crystal structure from a submicron-sized grain. *Acta Crystallogr. Sect. E Crystallogr. Commun.* **74**, 1392–1395 (2018).

52. M. Bykov, K. V. Yusenko, E. Bykova, A. Pakhomova, W. Kraus, N. Dubrovinskaia, L. Dubrovinsky, Synthesis of Arsenopyrite-Type Rhodium Pernitride RhN 2 from a Single-Source Azide Precursor. *Eur. J. Inorg. Chem.* **2019**, 3667–3671 (2019).

53. M. Bykov, S. Chariton, E. Bykova, S. Khandarkhaeva, T. Fedotenko, A. V. Ponomareva, J. Tidholm, F. Tasnádi, I. A. Abrikosov, P. Sedmak, V. Prakapenka, M. Hanfland, H. Liermann, M. Mahmood, A. F. Goncharov, N. Dubrovinskaia, L. Dubrovinsky, High-Pressure Synthesis of Metal–Inorganic Frameworks Hf 4 N 20 ·N 2 , WN 8 ·N 2 , and Os 5 N 28 ·3 N 2 with Polymeric Nitrogen Linkers. *Angew. Chemie*. **132**, 10407–10412 (2020).

54. S. Khandarkhaeva, T. Fedotenko, M. Bykov, E. Bykova, S. Chariton, P. Sedmak, K. Glazyrin, V. Prakapenka, N. Dubrovinskaia, L. Dubrovinsky, Novel Rhenium Carbides at 200 GPa. *Eur. J. Inorg. Chem.* **2020**, 2186–2190 (2020).

55. E. Bykova, thesis, University of Bayreuth (2015).

56. N. Dubrovinskaia, L. Dubrovinsky, Crystallography taken to the extreme. *Phys. Scr.* **93**, 062501 (2018).

57. F. R. Boyd, J. L. England, Apparatus for phase-equilibrium measurements at pressures up to 50 kilobars and temperatures up to 1750°C. *J. Geophys. Res.* **65**, 741–748 (1960).

58. N. Kawai, S. Endo, The Generation of Ultrahigh Hydrostatic Pressures by a Split Sphere Apparatus. *Rev. Sci. Instrum.* **41**, 1178–1181 (1970).

59. J. C. Jamieson, A. W. Lawson, N. D. Nachtrieb, New Device for Obtaining X-Ray Diffraction Patterns from Substances Exposed to High Pressure. *Rev. Sci. Instrum.* **30**, 1016–1019 (1959).

60. B. Li, C. Ji, W. Yang, J. Wang, K. Yang, R. Xu, W. Liu, Z. Cai, J. Chen, H. Mao, Diamond anvil cell behavior up to 4 Mbar. *Proc. Natl. Acad. Sci.* **115**, 1713–1717 (2018).

61. T. Fedotenko, L. Dubrovinsky, G. Aprilis, E. Koemets, A. Snigirev, I. Snigireva, A. Barannikov, P. Ershov, F. Cova, M. Hanfland, N. Dubrovinskaia, Laser heating setup for diamond anvil cells for in situ synchrotron and in house high and ultra-high pressure studies. *Rev. Sci. Instrum.* **90**, 104501 (2019).

62. T. Meier, S. Khandarkhaeva, S. Petitgirard, T. Körber, A. Lauerer, E. Rössler, L. Dubrovinsky, NMR at pressures up to 90 GPa. *J. Magn. Reson.* **292**, 44–47 (2018).

63. M. I. Eremets, Megabar high-pressure cells for Raman measurements. *J. Raman Spectrosc.* **34**, 515–518 (2003).

64. G. Aprilis, C. Strohm, I. Kupenko, S. Linhardt, A. Laskin, D. M. Vasiukov, V. Cerantola, E. G. Koemets, C. McCammon, A. Kurnosov, A. I. Chumakov, R. Rüffer, N. Dubrovinskaia, L. Dubrovinsky, Portable double-sided pulsed laser heating system for time-resolved geoscience and materials science applications. *Rev. Sci. Instrum.* **88**, 084501 (2017).

65. S. Petitgirard, G. Spiekermann, C. Weis, C. Sahle, C. Sternemann, M. Wilke, Miniature diamond anvils for X-ray Raman scattering spectroscopy experiments at high pressure. *J. Synchrotron Radiat.* **24**, 276–282 (2017).

66. Z. Konôpková, R. S. McWilliams, N. Gómez-Pérez, A. F. Goncharov, Direct measurement of thermal conductivity in solid iron at planetary core conditions. *Nature*. **534**, 99–101 (2016).

67. T. Fedotenko, D. S. Souza, S. Khandarkhaeva, L. Dubrovinsky, N. Dubrovinskaia, Isothermal equation of state of crystalline and glassy materials from optical measurements

in diamond anvil cells. *Rev. Sci. Instrum.* **92**, 063907 (2021).

68. I. Kantor, V. Prakapenka, A. Kantor, P. Dera, A. Kurnosov, S. Sinogeikin, N. Dubrovinskaia, L. Dubrovinsky, BX90: A new diamond anvil cell design for X-ray diffraction and optical measurements. *Rev. Sci. Instrum.* **83**, 125102 (2012).

69. H. K. Mao, P. M. Bell, in *Carnegie Institution Washington Yearbook* (Carnegie Institution Washington, Washington DC, 1978), pp. 904–908.

70. R. Letoullec, J. P. Pinceaux, P. Loubeyre, The membrane diamond anvil cell: A new device for generating continuous pressure and temperature variations. *High Press. Res.* **1**, 77–90 (1988).

71. R. Miletich, D. R. Allan, W. F. Kuhs, in *High-temperature and high-pressure crystal chemistry* (The Mineralogical Society of America, Washington DC, 2001).

72. H. O. Pierson, *Handbook of refractory carbides and nitrides* (NOYES PUBLICATION, Westwood, New Jersey, USA, 1996).

73. Y. Akahama, N. Hirao, Y. Ohishi, A. K. Singh, Equation of state of bcc-Mo by static volume compression to 410 GPa. *J. Appl. Phys.* **116**, 1–6 (2014).

74. Y. Akahama, H. Kawamura, Pressure calibration of diamond anvil Raman gauge to 410 GPa. *J. Phys. Conf. Ser.* **215**, 012195 (2010).

75. A. L. Ruoff, H. Xia, H. Luo, Y. K. Vohra, Miniaturization techniques for obtaining static pressures comparable to the pressure at the center of the earth: X-ray diffraction at 416 GPa. *Rev. Sci. Instrum.* **61**, 3830–3833 (1990).

76. A. Jayaraman, Diamond anvil cell and high-pressure physical investigations. *Rev. Mod. Phys.* **55**, 65–108 (1983).

77. A. Kurnosov, I. Kantor, T. Boffa-Ballaran, S. Lindhardt, L. Dubrovinsky, A. Kuznetsov, B. H. Zehnder, A novel gas-loading system for mechanically closing of various types of diamond anvil cells. *Rev. Sci. Instrum.* **79**, 045110 (2008).

78. K. Syassen, Ruby under pressure. *High Press. Res.* **28**, 75–126 (2008).

79. G. Shen, Y. Wang, A. Dewaele, C. Wu, D. E. Fratanduono, J. Eggert, S. Klotz, K. F.

Dziubek, P. Loubeyre, O. V. Fat'yanov, P. D. Asimow, T. Mashimo, R. M. M. Wentzcovitch, Toward an international practical pressure scale: A proposal for an IPPS ruby gauge (IPPS-Ruby2020). *High Press. Res.* **40**, 299–314 (2020).

80. Y. Akahama, H. Kawamura, Pressure calibration of diamond anvil Raman gauge to 310GPa. *J. Appl. Phys.* **100**, 043516 (2006).

81. Y. Fei, A. Ricolleau, M. Frank, K. Mibe, G. Shen, V. Prakapenka, High-Pressure Geoscience Special Feature: Toward an internally consistent pressure scale. *Proc. Natl. Acad. Sci.* **104**, 9182–9186 (2007).

82. C. S. Zha, W. A. Bassett, S. H. Shim, Rhenium, an in situ pressure calibrant for internally heated diamond anvil cells. *Rev. Sci. Instrum.* **75**, 2409–2418 (2004).

83. P. Vinet, J. Ferrante, J. H. Rose, J. R. Smith, Compressibility of solids. *J. Geophys. Res.* **92**, 9319 (1987).

84. F. Birch, Finite Elastic Strain of Cubic Crystals. *Phys. Rev.* **71**, 809–824 (1947).

85. J. Gonzalez-Platas, M. Alvaro, F. Nestola, R. Angel, EosFit7-GUI : a new graphical user interface for equation of state calculations, analyses and teaching. *J. Appl. Crystallogr.* **49**, 1377–1382 (2016).

86. W. A. Bassett, Diamond anvil cell, 50th birthday. *High Press. Res.* **29**, 163–186 (2009).

87. T. Fedotenko, L. Dubrovinsky, G. Aprilis, E. Koemets, A. Snigirev, I. Snigireva, A. Barannikov, P. Ershov, F. Cova, M. Hanfland, N. Dubrovinskaia, Laser heating setup for diamond anvil cells for in situ synchrotron and in house high and ultra-high pressure studies. *Rev. Sci. Instrum.* **90**, 104501 (2019).

88. G. Hildebrandt, The discovery of the diffraction of X-rays in crystals — a historical review. *Cryst. Res. Technol.* **28**, 747–766 (1993).

89. C. Stan, C. Beavers, M. Kunz, N. Tamura, X-Ray diffraction under extreme conditions at the Advanced Light Source. *Quantum Beam Sci.* **2**, 4 (2018).

90. I.-E. Benrabah, H. P. Van Landeghem, F. Bonnet, F. Robaut, A. Deschamps, Use of space-resolved in-situ high energy X-ray diffraction for the characterization of the compositional

dependence of the austenite-to-ferrite transformation kinetics in steels. *Quantum Beam Sci.* **4**, 1 (2019).

91. X. Ou, J. Li, F. Zheng, P. Wu, Q. Pan, X. Xiong, C. Yang, M. Liu, In situ X-ray diffraction characterization of $NiSe_2$ as a promising anode material for sodium ion batteries. *J. Power Sources*. **343**, 483–491 (2017).

92. M. Ladd, R. Palmer, *Structure Determination by X-ray Crystallography* (Springer US, Boston, MA, 2013; http://link.springer.com/10.1007/978-1-4614-3954-7).

93. C. Prescher, V. B. Prakapenka, DIOPTAS : a program for reduction of two-dimensional X-ray diffraction data and data exploration. *High Press. Res.* **35**, 223–230 (2015).

94. V. Petříček, M. Dušek, L. Palatinus, Crystallographic Computing System JANA2006: General features. *Zeitschrift für Krist. - Cryst. Mater.* **229**, 345–352 (2014).

95. O. D. Rigaku, CrysAlisPro Software System, Version 1.171. 38.41 l, Rigaku Coorporation (2015).

96. O. V. Dolomanov, L. J. Bourhis, R. J. Gildea, J. A. K. Howard, H. Puschmann, OLEX2 : a complete structure solution, refinement and analysis program. *J. Appl. Crystallogr.* **42**, 339–341 (2009).

97. G. M. Sheldrick, SHELXT - Integrated space-group and crystal-structure determination. *Acta Crystallogr. Sect. A Found. Crystallogr.* **71**, 3–8 (2015).

98. W. Clegg, A. J. Blake, J. M. Cole, J. S. O. Evans, P. Main, S. Parsons, D. J. Watkin, *Crystal Structure Analysis* (Oxford University Press, 2009; https://oxford.universitypressscholarship.com/view/10.1093/acprof:oso/9780199219469.001.0001/acprof-9780199219469).

99. L. S. Dubrovinsky, S. K. Saxena, F. Tutti, S. Rekhi, T. LeBehan, In Situ X-Ray Study of Thermal Expansion and Phase Transition of Iron at Multimegabar Pressure. *Phys. Rev. Lett.* **84**, 1720–1723 (2000).

100. K. Schollenbruch, A. B. Woodland, D. J. Frost, F. Langenhorst, Detecting the spinel–post-spinel transition in Fe 3 O 4 by in situ electrical resistivity measurements. *High Press. Res.*

**29**, 520–524 (2009).

101. D. P. Kozlenko, L. S. Dubrovinsky, S. E. Kichanov, E. V. Lukin, V. Cerantola, A. I. Chumakov, B. N. Savenko, Magnetic and electronic properties of magnetite across the high pressure anomaly. *Sci. Rep.* **9**, 4464 (2019).

102. V. Cerantola, E. Bykova, I. Kupenko, M. Merlini, L. Ismailova, C. McCammon, M. Bykov, A. I. Chumakov, S. Petitgirard, I. Kantor, V. Svitlyk, J. Jacobs, M. Hanfland, M. Mezouar, C. Prescher, R. Rüffer, V. B. Prakapenka, L. Dubrovinsky, Stability of iron-bearing carbonates in the deep Earth's interior. *Nat. Commun.* **8**, 15960 (2017).

103. L. Ismailova, E. Bykova, M. Bykov, V. Cerantola, C. McCammon, T. Boffa Ballaran, A. Bobrov, R. Sinmyo, N. Dubrovinskaia, K. Glazyrin, H.-P. Liermann, I. Kupenko, M. Hanfland, C. Prescher, V. Prakapenka, V. Svitlyk, L. Dubrovinsky, Stability of Fe,Al-bearing bridgmanite in the lower mantle and synthesis of pure Fe-bridgmanite. *Sci. Adv.* **2**, e1600427 (2016).

104. E. Koemets, T. Fedotenko, S. Khandarkhaeva, M. Bykov, E. Bykova, M. Thielmann, S. Chariton, G. Aprilis, I. Koemets, K. Glazyrin, H.-P. Liermann, M. Hanfland, E. Ohtani, N. Dubrovinskaia, C. McCammon, L. Dubrovinsky, *Eur. J. Inorg. Chem.*, in press, doi:10.1002/ejic.202100274.

105. E. A. Juarez-Arellano, B. Winkler, A. Friedrich, L. Bayarjargal, V. Milman, J. Yan, S. M. Clark, Stability field of the high-(P, T) Re2C phase and properties of an analogous osmium carbide phase. *J. Alloys Compd.* **481**, 577–581 (2009).

106. M. Di Giovannantonio, Q. Chen, J. I. Urgel, P. Ruffieux, C. A. Pignedoli, K. Müllen, A. Narita, R. Fasel, On-Surface Synthesis of Oligo(indenoindene). *J. Am. Chem. Soc.* **142**, 12925–12929 (2020).

107. P. F. McMillan, Chemistry at high pressure. *Chem. Soc. Rev.* **35**, 855 (2006).

108. R. J. Needs, C. J. Pickard, Perspective: Role of structure prediction in materials discovery and design. *APL Mater.* **4**, 053210 (2016).

# Chapter 4.1. Testing the performance of secondary anvils shaped with focused ion beam from the single-crystal diamond for use in double-stage diamond anvil cells

*Saiana Khandarkhaeva[1,2a)], Timofey Fedotenko[2], Alena Krupp[1], Konstantin Glazyrin[3], Weiwei Dong[3], Hanns-Peter Liermann[3], Maxim Bykov[1*], Alexander Kurnosov[1], Natalia Dubrovinskaia[2,6] and Leonid Dubrovinsky[1]*

[1]*Bayerisches Geoinstitut, University of Bayreuth, Universitätstraße 30, 95440 Bayreuth, Germany*

[2]*Material Physics and Technology at Extreme Conditions, Laboratory of Crystallography, University of Bayreuth, Universitätstraße 30, 95440 Bayreuth, Germany*

[3]*Deutsches Elektronen-Synchrotron, Notkestraße 85, 22607 Hamburg, Germany*

[6]*Theoretical Physics Division, Department of Physics, Chemistry and Biology (IFM), Linköping University, SE-581 83, Linköping, Sweden*

*a) Author to whom correspondence should be addressed: saiana.khandarkhaeva@uni-bayreuth.de*

**Current address: Geophysical Laboratory, Carnegie Institution of Washington, 5251 Broad Branch Road NW, 20015 Washington, District of Columbia, USA*

*Rev. Sci. Instrum.* **2022**, *93* (3), 033904. https://doi.org/10.1063/5.0071786.

## Abstract

The success of high-pressure research relies on the inventive design of pressure-generating instruments and materials used for their construction. In this study, the anvils of conical frustum or disc shapes with flat or modified culet profiles (toroidal or beveled) were prepared by milling an Ia-type diamond plate made of a (100)-oriented single crystal using the focused ion beam (FIB). Raman spectroscopy and synchrotron X-ray diffraction (XRD) were applied to evaluate the efficiency of the anvils for pressure multiplication in different modes of operation: as single indenters forced against the primary anvil in diamond anvil cells (DACs), or as pairs of anvils forced together in double-stage diamond anvil cells (dsDACs). All types of secondary anvils

performed well up to about 250 GPa. The pressure multiplication factor of single indenters appeared to be insignificantly dependent on the shape of the anvils and their culets' profiles. The enhanced pressure multiplication factor found for pairs of toroidally shaped secondary anvils makes this design very promising for ultra-high-pressure experiments in dsDACs.

## Introduction

The impact of high-pressure (HP) studies on fundamental physics, chemistry, and especially on Earth and planetary sciences, is enormous. Solids exposed to high pressures reveal numerous complex phenomena, such as metal-to-insulator transitions(*1*, *2*), high temperature superconductivity(*3–5*), and new "super"-states of matter(*6–8*). Even at moderated pressure-temperature (PT) conditions fully unexpected chemical bonding and stoichiometry can be observed(*9*). Nowadays, high-pressure high-temperature (HPHT) synthesis has become a well-established technique, which enables discoveries of novel materials with unique physical properties(*10–12*). Among all of apparatuses used for static pressure generation, diamond anvil cells (DACs) are the most efficient, providing the widest span of achievable PT conditions. The transparency of diamond in a large range of energies of electromagnetic radiation enables probing the samples *in situ* at extreme conditions by different analytical methods, such as X-ray diffraction (XRD), X-ray transmission microscopy (XRTM), Raman, nuclear magnetic resonance (NMR), Mossbauer, X-ray absorption spectroscopies and many of other techniques based on optical measurements. (*13–22*)

The design of DACs went through long iterative and incremental development aimed at achieving higher and higher pressures. At the moment conventional DACs with bevelled diamond anvils work up to ~ 450 GPa, but further pressure increase is limited by the yield strength of single-crystal diamond(*23–25*). Being the hardest and strongest of known materials, diamond is brittle, its fracture toughness is relatively low, and hardness is anisotropic(*26*, *27*). Collapse of the diamond anvils under compression in the [001] direction is usually provoked by the cleavage along the {110} planes.

Currently, to tackle multimegabar pressures, the interest has switched to so-called double-stage DAC (dsDAC) design(*28–31*). The dcDACs implement secondary anvils in the pressure

chamber of a conventional DAC to enable pressure multiplication due to the further force transfer to even smaller area of the culet of the secondary anvil. Experiments in dsDACs with secondary anvils made of an isotropic material, nanocrystalline diamond(*28*) (NCD), first demonstrated a possibility of XRD studies up to ~750 GPa(*32*) and later enabled beating static pressures as high as 1 TPa(*29*). NCD semiballs of only a dozen microns in diameter (with a grain size of 2-15 nm) were used in these experiments as secondary anvils. Following the first breakthrough, secondary micro-anvils have been produced using focus ion beam (FIB) milling from other materials, for example, synthetic nano-polycrystalline diamond(*30*) (NPD) with a grain size of ca. 100 nm. The reported maximum of achieved pressures was over 300 GPa with the culet size of the secondary anvil of 3 μm(*30*). Use of NPD with a grain size reduced down to ~10 nm enabled achieving ~600 GPa(*31*), as determined based on the equation of state (EoS) of rhenium reported by Dubrovinsky et al. (2012)(*28*) (or ~430 GPa, according to the Re EoS of Anzellini et al. (2014)(*33*)). Such pressures are comparable to those reported in experiments with NCD semiballs as secondary anvils(*28*),(*32*). Nevertheless, the HPHT synthesis of NCD balls in a large volume press and selection of the balls suitable for ultra-HP experiments remain laborious. Another drawback of NCD or NPD is that they are opaque and highly luminescent that complicates spectroscopic measurements.

Recently, DACs with so-called toroidal anvils (tDACs)(*34*, *35*) were introduced. Using FIB, the profile of the primary anvils is modified, so that the culet features a circumference cavity and a summit (a tip) in its center with a diameter of ~15-25 μm, which works as a secondary anvil, when the DAC is assembled. When two anvils are forced together, the shape of the cavity resembles a toroid and the sample is squeezed between the tips. The toroidal cavity accommodates gasket (or sample) material and reduces its outflow from the center. It also helps to decrease the magnitude of the shear stresses in the anvils themselves. Upon compression, conventional anvils undergo a convex deformation, when the pressure chamber gets a shape of a convex lens. Eventually, the deformation leads to the failure of anvils. In the toroidal design this effect can be partially compensated due to complex stress distribution, and tDACs sustain higher pressures than DACs with conventional anvils. In tDACs pressures of ~500 GPa have been achieved(*34*, *35*), and the authors suggested that there is still a potential for a further pressure increase through adjusting the size and the slope of the cavity of the toroidal anvil. These new tDACs were used for

synchrotron infrared absorption spectroscopy studies of dense solid hydrogen at 80 K and ~400 GPa.(*36*)

The developments described above and the ongoing discussion of capabilities of various ultra-HP DAC techniques call for systematic testing of the performance of secondary anvils of different designs. Here, using FIB, we manufactured various types of secondary anvils from commercially available single-crystal diamond plates (AlmaxEasy Lab) and investigated their efficiency for pressure multiplication. Our results are described in detail below.

## Methods

*Fabrication of secondary anvils*

Secondary anvils were prepared by FIB milling of single-crystal diamond plates with a thickness of 10 μm using the FIB machines (Scios DualBeam system, FEI Deutschland GmbH) installed at Bayerisches Geoinstitut (BGI, Bayreuth, Germany) and at DESY Nanolab (Hamburg, Germany). Each time a 3D model was programmed using the MATLAB software. The simulated milling profile was saved as a 2D 24-bit grey-scale RGB bitmap. The milling was performed under the acceleration voltage of 30 kV with the Ga ion current of 15-30 nA. A recess with a depth of ~0.5 μm on toroidal anvils with a semispherical tip was made at 30 kV and 1nA.

*dsDAC preparation*

The BX-90(*37*) type DACs were used in the most of experiments. The culets of primary anvils were either of 120 or 250 μm in diameter. The primary sample chambers were formed by pre-indenting rhenium gaskets to the thickness of 12-13 μm and by drilling a hole with a diameter of ~120 μm in the center of the indentation. Paraffin oil was used as a pressure transmitting medium (PTM). Iridium, gold (99.9% purity, purchased from Sigma Aldrich), or their mixtures were used as both samples and pressure markers in X-ray diffraction studies. Thin pellets of these metals were prepared by pressurizing their powders, which then were placed upon the secondary-stage anvil either in the chamber of the FIB instrument, or using a micromanipulator (Micro Support Co. Ltd.).

*Pressure determination*

Raman spectra from the primary or secondary diamond anvils were recorded using the LabRam system equipped with a He-Ne laser source (λ=632 nm) at the BGI. The size of the laser beam is 2 μm in diameter. The pressure was determined on the position of the high-frequency edge of the $A_{1g}$ diamond Raman mode according to the calibration of Akahama and Kawamura (2010)(*24*).

The 3rd order Birch–Murnaghan equations of state of Ir ($V_0$=56.56(4) Å$^3$, $K_0$=341(10) GPa, and K´=4.7(3); Yusenko et al. (2019)(*38*)) and Au ($V_0$=67.850(4) Å$^3$, $K_0$=167 GPa, and K´=5.77(2); Fei et al. (2007)(*39*)) were utilized to determine pressure on the basis of XRD data using the EOSfit7c software(*40*).

*X-ray diffraction*

Synchrotron XRD studies were conducted at beamline P02.2 (Petra III, DESY Hamburg, Germany) with either (a) a submicron X-ray beam (0.8x0.8 μm$^2$ at FWHM, focused with a system using compound refractive lenses, the wavelength λ=0.4853 Å) or (b) a micron-size beam (2x2 μm$^2$ at FWHM, focused with Kirkpatrick–Baez mirrors, λ=0.2885 Å). Diffraction images were recorded on a Perkin Elmer XRD1621 flat panel detector. Calibration of the instrument model, as well as the integration of diffraction patterns, were made using the DIOPTAS(*41*) software with the $CeO_2$ powder standard (NIST SRM 674b). 2D X-ray diffraction imaging was made using XDI program(*42*). The lattice parameters and the unit cell volumes of Au and Ir were obtained through the LeBail method applied to the powder XRD data using JANA2006 program(*43*).

## Results and discussions

*Performance of secondary anvils used as single indenters forced against the primary anvil of a DAC*

The secondary anvils of different sizes and forms (conical frustum- or disc-shaped) with flat or modified culet profiles (toroidal or bevelled) (Figure 1) were prepared by FIB milling of an Ia-type diamond plate made of an (100)-oriented single crystal as described above in *Methods*. All

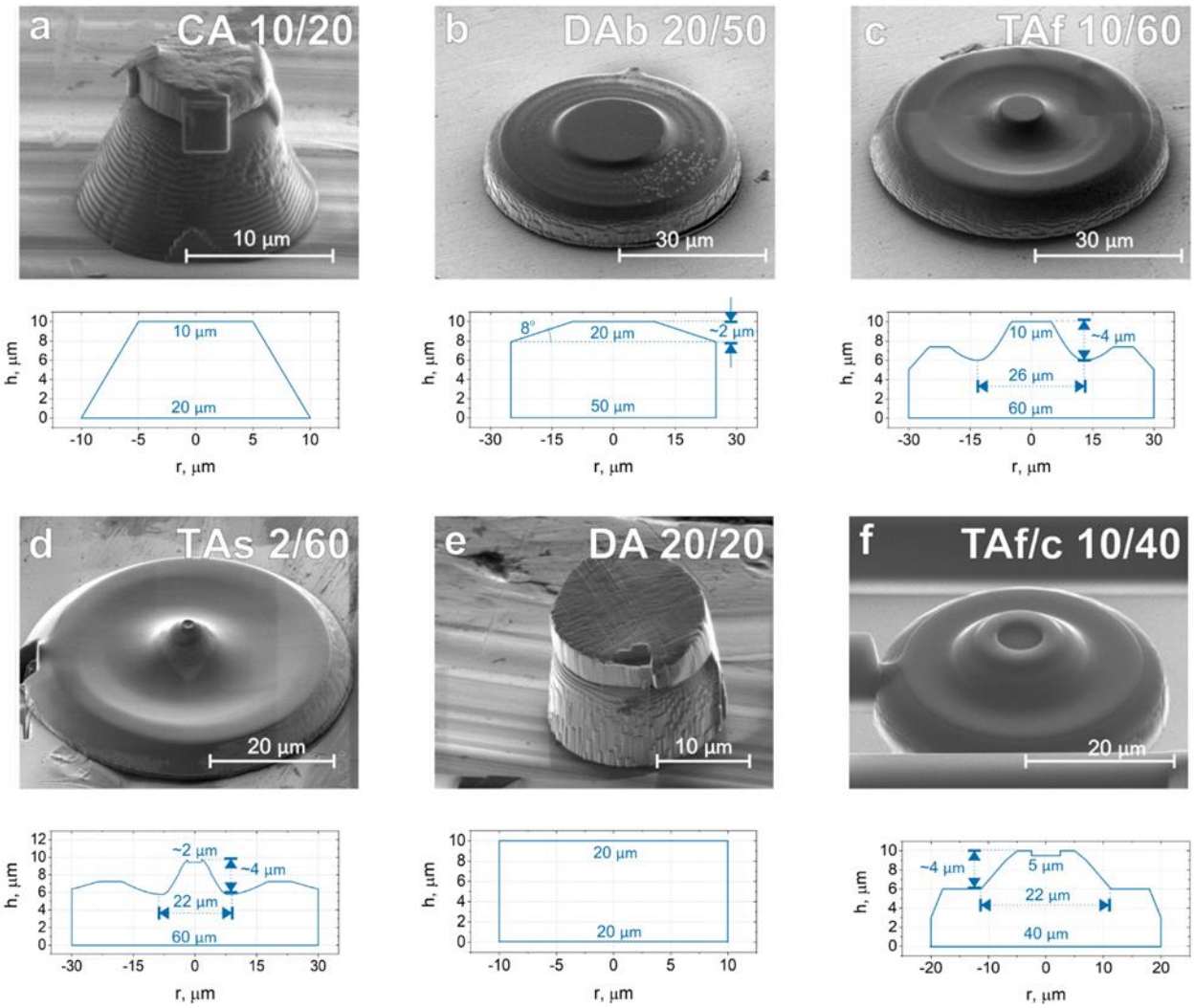


***Figure 1.*** *SEM images of secondary anvils shaped using FIB from a single-crystal diamond plate of the 10-µm thickness. (a) Conical frustum anvil CA 10/20 with a disc-shaped Ir sample on top fixed by a deposited Pt layer; (b) bevelled disc-shaped anvil DAb 20/50 (slope of 8˚); (c) toroidal anvil TAf 10/60; (d) toroidal anvil TAs 2/60 with a hemispherical tip (the spherical diameter is of ~2 µm; the cavity on the top with a depth of ~0.5 µm was made to increase the amount of the sample in the pressure chamber; (e) disc-shaped anvil DA 20/20 with the Ir disc-shaped sample on top, fixed by a deposited Pt layer; (f) toroidal anvil TAf/c 10/40 with a flat culet featuring a cavity of ~5 µm in diameter and ~0.5 µm in depth . Cross-sections of the anvils provided below each image show the dimensions of the anvils and the profiles of their culets.*

anvils had the same height of 10 µm defined by the thickness of the diamond plate from which they were prepared. A list of all anvils fabricated and tested in this study is provided in Table 5.1.

***Table 1**: List of secondary anvils fabricated and tested in this study as single indenters. All anvils had the same height of 10 µm defined by the thickness of the diamond plate, from which they were prepared.*

| Secondary anvil designation (anvil name) | Design of secondary anvils | Top diameter (culet size), µm | Bottom diameter, µm | Figure number for anvil's image |
|---|---|---|---|---|
| CA 10/20 | Conical frustum Anvil | 10 | 20 | Figure 1a, 2b |
| DAb 20/50 | Disc-shaped Anvil with a beveled culet | 20 | 50 | Figure 1b |
| TAf 10/60 | Toroidal Anvil with a flat culet | 10 | 60 | Figure 1c |
| TAs 2/60 | Toroidal Anvil with a semi-spherical culet featuring a cavity of 0.5 µm in depth on the top | ca. 2 | 60 | Figure 1d |
| DA 20/20 | Disc-shaped Anvil | 20 | 20 | Figure 1e |
| TAf/c 10/40 | Toroidal Anvil with a flat culet featuring a cavity of 0.5 µm in depth and ~5 µm in diameter | 10 | 40 | Figure 1f |

An example of a 3D model of a conical frustum anvil CA 10/20 and the corresponding FIB-milled anvil is shown in Figure 2.

In this section we describe the experiments, in which secondary anvils were used as *single indenters* forced against the primary anvil of a DAC. The goal of the experiments is to investigate if the size and shape of the secondary anvils used in such a mode of operation influences the maximum pressure achievable under the indenter. A scheme of the DAC assembly featuring a single secondary anvil is shown in Figure 3. As the secondary anvil is confined within paraffin oil in the primary DAC chamber, the pressure in this chamber is called confining pressure ($P_{conf.}$). The pressure imposed by the single indenter on the metallic sample, squeezed between its culet and the culet of the upper primary diamond anvil, is called sample pressure ($P_{samp.}$). To determine $P_{conf.}$, a Raman spectrum is taken from the off-sample point on the culet of the primary diamond anvil (the direction of the laser beam is shown by the red arrow in Figure 3a. $P_{conf.}$ is then calculated as described in *Methods* (ref. (*24*)). To determine $P_{samp.}$, Raman spectra are also taken from the culet

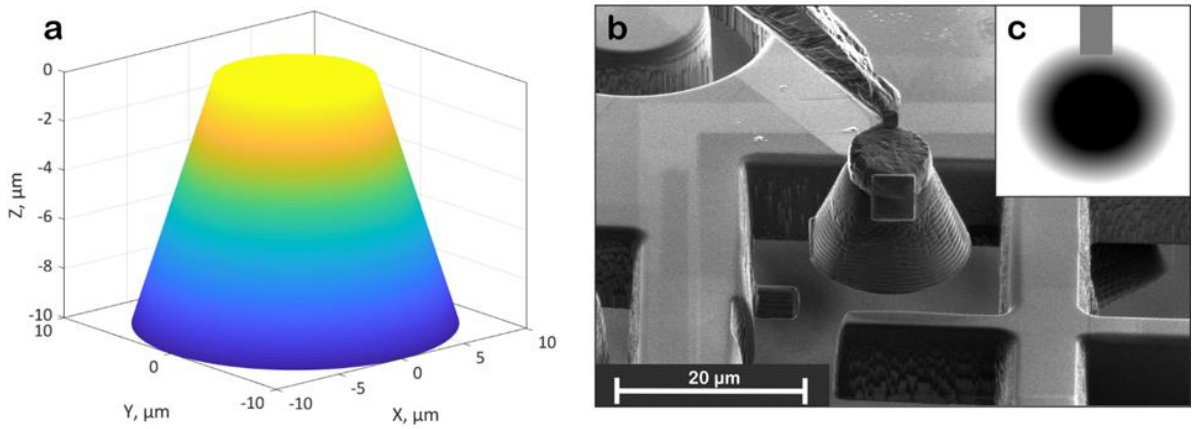


***Figure 2.*** *Conical frustum anvil CA 10/20. (a) A 3D model of the conical frustum (top and bottom diameters are 10 and 20 µm, respectively); (b) SEM image of the anvil milled from a diamond plate according to the model using FIB. A disc-shaped iridium sample was placed on the top. The sample was made by compaction of Ir powder into a pellet. The latter was fixed on the top of the anvil by a FIB-deposited Pt layer (seen as a square in front); (c) 24-bit grayscale bitmap used for fabricating the anvil.*

of the primary diamond anvil, but in the on-sample points (the directions of the laser beam are shown by the green arrows in Figure 3a). Figure 4a presents the results of such measurements in a DAC with CA 10/20 (250/250 µm primary anvils). Further, the sizes of primary

anvil's culets are given in brackets. The Raman spectrum on the bottom of Figure 4a (purple curve) is the one taken from the off-sample point of the primary diamond anvil. It gives $P_{conf.}$=31(1) GPa. The other spectra, shown in Figure 4a in different colors, are those taken from four different on-sample points. They give four different values of $P_{samp.}$ (137(1), 152(1), 156(2), and 182(2) GPa). Pressure on the sample under the indenter is considerably enhanced in comparison to confining pressure, but it is not evenly distributed across the culet of the secondary CA 10/20 anvil (with gradients up to 45 GPa in this particular example). Figure 4b illustrates the correlation between $P_{conf.}$ and $P_{samp.}$. The spectra shown in Figure 4b were taken from the same on-sample point upon pressurization of the cell. Whereas $P_{conf.}$ increased from 15(1) to 31(1) GPa, $P_{samp.}$ raised from 120(2) to 182(2) GPa, thus the higher $P_{conf.}$ the larger $P_{samp.}$.

Quantitative linear pressure profiles (Figures 5a-c) were obtained in further experiments on the results of XRD linear scans. For this purpose, at each point along a line across the pressure

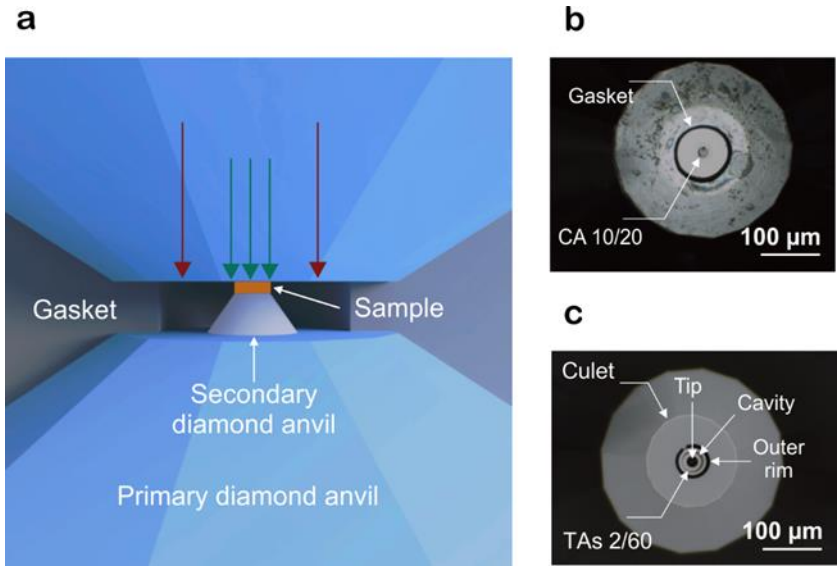


***Figure 3.*** *Elements of the dsDAC assembly with a single secondary anvil. (a) Schematic diagram of the pressure chamber of DAC with a single conical frustum-shaped secondary anvil (not scaled). Red and green arrows show the directions of the laser beam for Raman measurements from off-sample and on-sample points, respectively. (b) An image of the real pressure chamber of the DAC with the single conical (CA 10/20) secondary anvil (the culet diameter of the primary anvil is 120 µm) taken under an optical microscope; the black circle outlines the external rhenium gasket. (c) An image of the toroidal (TAs 2/60) secondary anvil placed on the primary diamond culet; the black circle and the black dot outline the outer rim and the semispherical tip, respectively.*

chamber, the pressure was determined on the EoS of the metallic sample, Ir (ref. (*38*)) or Au (ref. (*39*)), thus, providing the linear pressure profile (Figs. 5a-c).

The analysis of the pressure profiles (Figure 5) allows to conclude that the pressure distribution across all kinds of the secondary anvils is uneven, deformation of culets increases with an increase of confining pressures, and the convex deformation of culets is well pronounced for both CA 10/20 and DAb 20/50 anvils (Figure 5a, b). The TAs 2/60 appeared to be the most efficient in achieving the highest pressures (Figure 5c). The quite even distribution of pressure over the very small culet with the maximum in the middle is due to the relatively large bottom diameter of TAs 2/60, which prevents indenter's inclination, and the small size of the tip, which reduces its convex deformation.

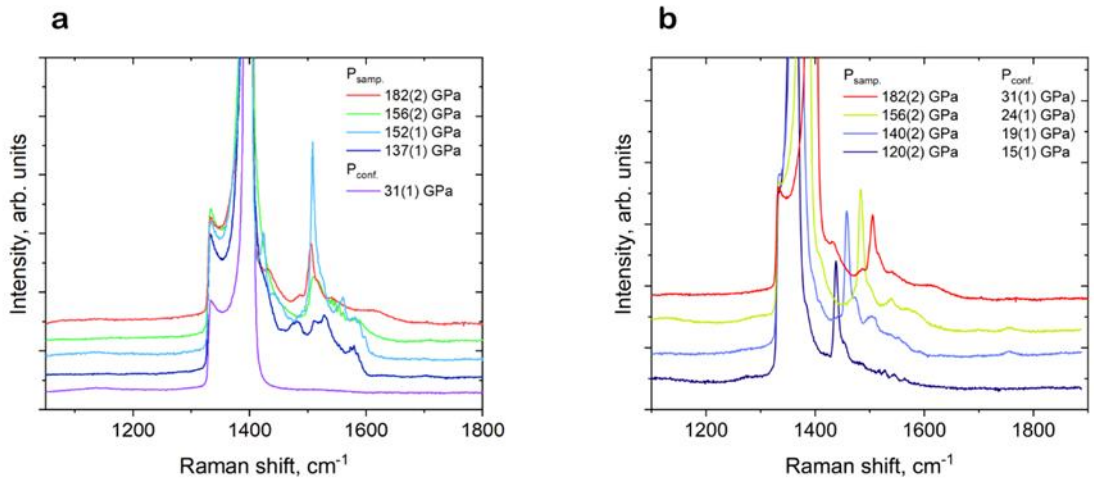


***Figure 4.*** *An example of Raman spectra of diamond used for pressure determination in the DAC with a single conical anvil CA 10/20. (a) The Raman spectrum taken from the off-sample point of the primary diamond anvil (purple curve, $P_{conf.}$=31(1) GPa) and those taken from four different on-sample points (see the schematic in Figure 3a). The shift of the high frequency edge of the Raman mode[24] gives evidence of an uneven $P_{samp.}$ distribution across the sample: $P_{samp.}$=137(1), 152(1), 156(2), and 182(2) GPa, as determined on four different spectra. (b) Spectra taken from the same on-sample point upon pressurization of the cell up to $P_{conf.}$ =31 GPa: the higher $P_{conf.}$, the larger $P_{samp.}$.*

The results of testing the pressure generation efficiency of the secondary anvils of various designs are summarized in Table 2. It is clear that the higher $P_{conf.}$, the larger $P_{samp.}$(max.) can be achieved. There are only two examples of deviations from this regularity: the results for CA 10/20 (250/250) and DA(20/20), but they have clear explanations considering peculiarities of the real experiments. In the first case, the seemingly too high $P_{samp.}$(max.)=182(2) GPa at the relatively low $P_{conf.}$=31(1) GPa was achieved in a single point at the rim of the culet because of the extreme inclination of the flat culet of the secondary anvil. In the case of DA 20/20, the lower pressure multiplication factor was due to a larger thickness of the primary gasket (~15 μm) compared to 12-13 μm in other experiments. This is why the DA(20/20) indenter faced the primary anvil at confining pressure of about 30 GPa that reduced the efficiency of the assembly in general.

As seen in Table 2, TAs 2/60 in the DAC with 120-μm primary diamond anvils enabled achieving maximal pressure of 264(8) GPa (Figure 6b), as determined on the Ir EoS (ref.(*38*)). This pressure value is comparable to those reported for dsDAC assemblies introduced by Sakai et al. (2015) (*30*) and Lobanov et al. (2015) (*44*). Despite similar pressures can be achieved in

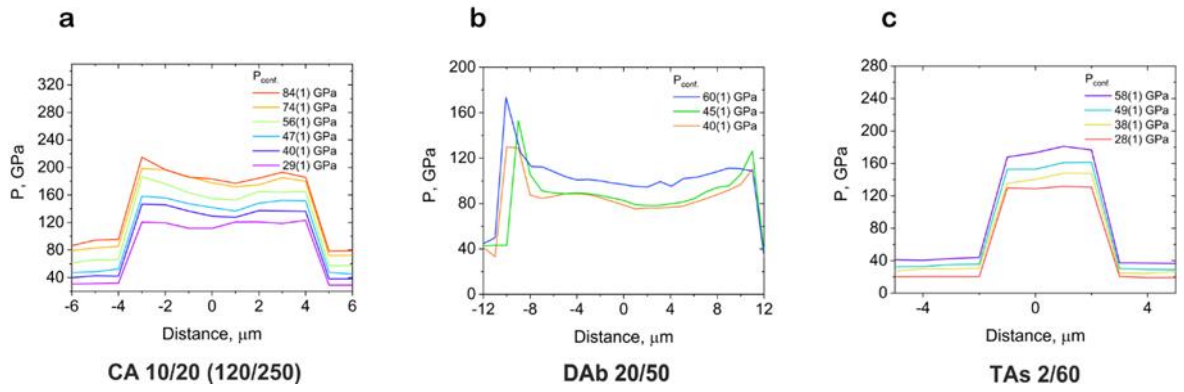


***Figure 5.*** *Linear pressure profiles for different types of secondary anvils used as single indenters in DACs.* *The pressure distribution profiles for (a) CA 10/20 (120/250), (b) DAb 20/50, and (c) TAs 2/60 anvils were retrieved from X-ray diffraction linear scans recorded with the step of 1μm across the secondary anvils.*

conventional DACs equiped with beleved diamonds with culets smaller than 50 μm, the process of alignment and preparation of such conventional DACs is laborious and requires certain skills from the researcher  Experiments with a single indenter are significantly simpler and pressures above 250 GPa can be successfully achieved with primary anvils of 120- and 250-μm culets.

***Table 2.*** *The results of testing of the secondary anvils of various designs in dsDACs. Here, $P_{samp.}$(max.) is the maximum pressure achieved on the sample and $P_{conf.}$ is the corresponding confining pressure in the primary chamber of dsDAC*

| Anvil name | Size of the primary anvils (top/bottom), μm | $P_{conf.}$, GPa | $P_{samp.}$ (max.), GPa |
|---|---|---|---|
| TAs 2/60 | 120/120 | 112(3) | 264(8) |
| CA 10/20 | 120/250 | 86(2) | 212(5) |
| CA 10/20 | 250/250 | 31(1) | 182(2) |
| DAb 20/50 | 250/250 | 60(1) | 174(5) |
| TAf 10/60 | 250/250 | 56(1) | 148(4) |
| DA 20/20 | 250/250 | 47(1) | 105(3) |

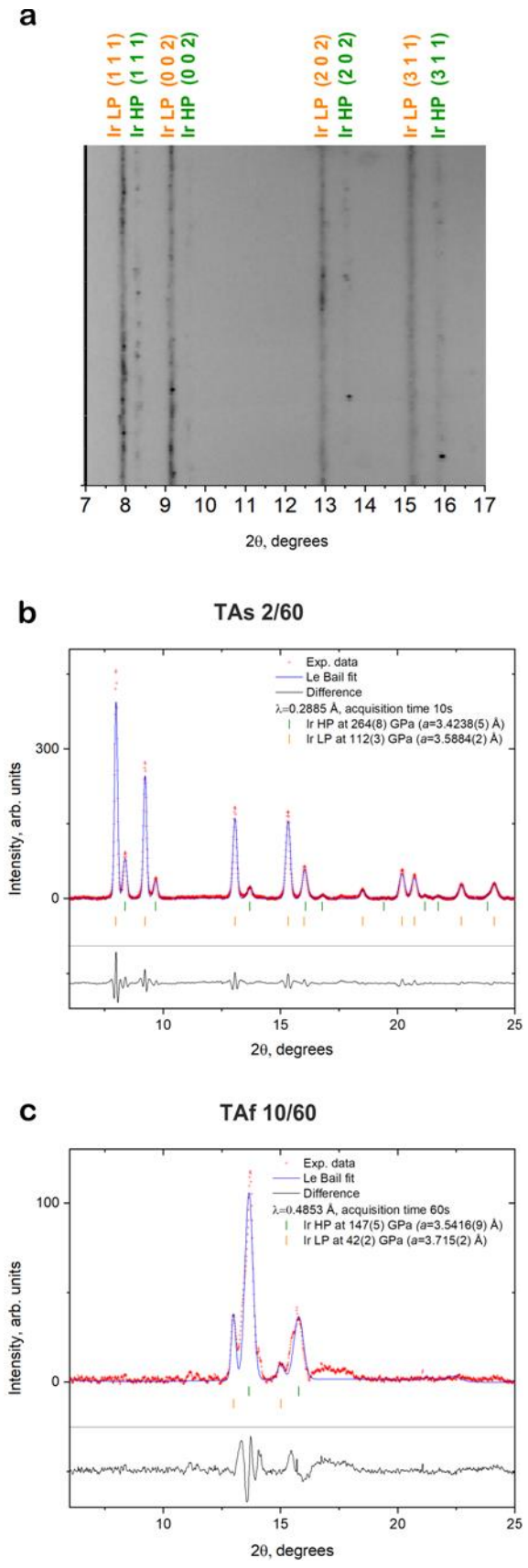


***Figure 6.*** *X-ray diffraction patterns of Ir samples in DACs. (a) Unwrapped 2D XRD pattern from a DAC with TAs 2/60 secondary and 120-μm primary diamond anvils (λ=0.2885 Å, beam size ~2x2 μm² at FWHM). The output of the Le Bail refinement using powder diffraction data for the same sample (b) and for a sample in a DAC with TAf 10/60 (c) secondary and 250-μm primary anvils (λ=0.4853 Å, beam size ~0.8x0.8 μm² at FWHM). Red crosses show the experimental data, the dark blue curve is the simulated powder diffraction pattern, black curve shows the difference; orange and green ticks correspond to the diffraction lines of Ir at low pressure (Ir LP) and high pressure (Ir HP), respectively. Pressure was determined using the equation of state from Yusenko et al. (2019).*

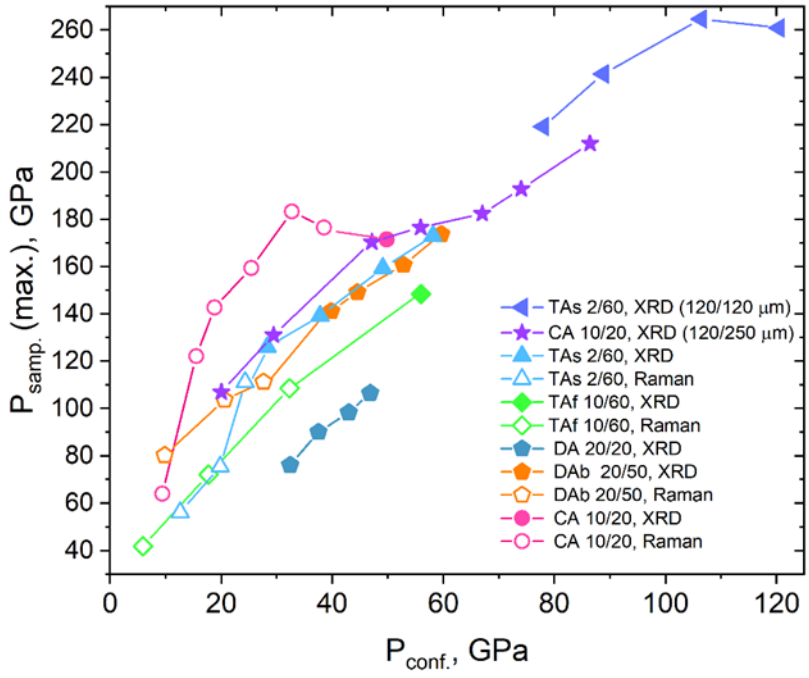


***Figure 7**. The relationship between the maximum pressures measured on the sample ($P_{samp.}$ (max) and corresponding confining pressures ($P_{conf.}$) in DACs with single secondary anvils (single indenters). Pressure values obtained from Raman spectroscopy and synchrotron X-ray diffraction are shown by open and filled symbols, respectively. Different colours designate types of indenters, according to Table 1. The size of primary anvils is indicated in brackets if it is different from (250/250).*

Moreover, if a pressure multiplication factor in a DAC with a single indenter appears to be insufficient, the DAC can be re-loaded, and the experiment repeated with the same primary anvils, as they are usually not damaged.

To compare the efficiency of secondary anvils for pressure multiplication, we plotted the values of maximal pressures achieved with different kinds of indenters, $P_{samp.}$(max.), *versus* confining pressures, $P_{conf.}$ (Figure 7). It turned that all curves have similar slopes, which means that all kinds of tested secondary anvils provide similar multiplication factors, which practically do not depend on anvils' design. Our experiments with secondary anvils acting as single indenters were terminated at about 250 GPa mainly due to the plastic deformation of the primary anvil under indenter.

*Performance of pairs of secondary anvils in dsDACs*

In this section we describe only the feasibility tests, because the performance of anvils working in pairs was not so extensively studied as that of single indenters in the current work.

To test the performance of pairs of secondary anvils in dsDAC, we first started with those of the simplest shape (DA 20/20, Figure 1e). The second-stage assembly, consisting of two diamond disks (DA 20/20) and a gasket with a sample in between, was prepared in the chamber of the FIB instrument (Figure 8a). The lower diamond disk was attached to the original diamond plate with a tiny bridge, leftover after its milling (Figure 8a,b). The gasket was made of a ~2-3-μm thick Re foil using the Ga-beam double-side polishing technique in order to avoid its thickness variation. It had a shape of a disc with a hole of ~5 μm in diameter (Figure 8a, left). The ready gasket was mounted on a standard copper grid holder, which was placed in the FIB chamber perpendicularly to the electron gun column. A disc-shaped piece of an Au foil served as a sample. It was made of a pre-compressed metal powder and had a thickness of ~2 μm (Figure 8a, middle). Both the gasket and the sample were placed on the top of the anvil using the Easy-lift needle, and the miniature gasket was fixed at its place by Pt deposition. After that, the second diamond disk was precisely aligned upon the gasket and fixed by Pt deposition (Figure 8a, right). Thus, micro-manufacturing using a dual-beam FIB enables us to choose the desired anvils shape, to put a sample exactly between the secondary anvils, and to complete assembling of the secondary stage anvils inside the FIB chamber that provides such a precise alignment which would be very difficult to realize otherwise. After cutting the bridge connecting the bottom secondary anvil to the diamond plate, the whole assembly, which is ~22-23 μm in height, could be transferred to an SEM-holder and then placed on the culet of the primary anvil in the primary chamber of the dsDAC using a micromanipulator (Micro Support Co., Ltd.).

The primary chamber of the dsDAC was then loaded with the paraffin oil that served as a pressure transmitting medium. *In situ* high-pressure XRD studies showed that dsDACs equipped with pairs of DA 20/20 secondary anvils were able to generate pressures of 186(2) GPa, as determined on the Au pressure scale(*39*) ($a_{Au}$=3.596(2) Å, $V_{Au}$=46.50(2) Å$^3$) at the confining pressure of 42(2) GPa (Figure 10a). The ($P_{samp.}$*(max.) vs* $P_{conf.}$) curves for two runs involving

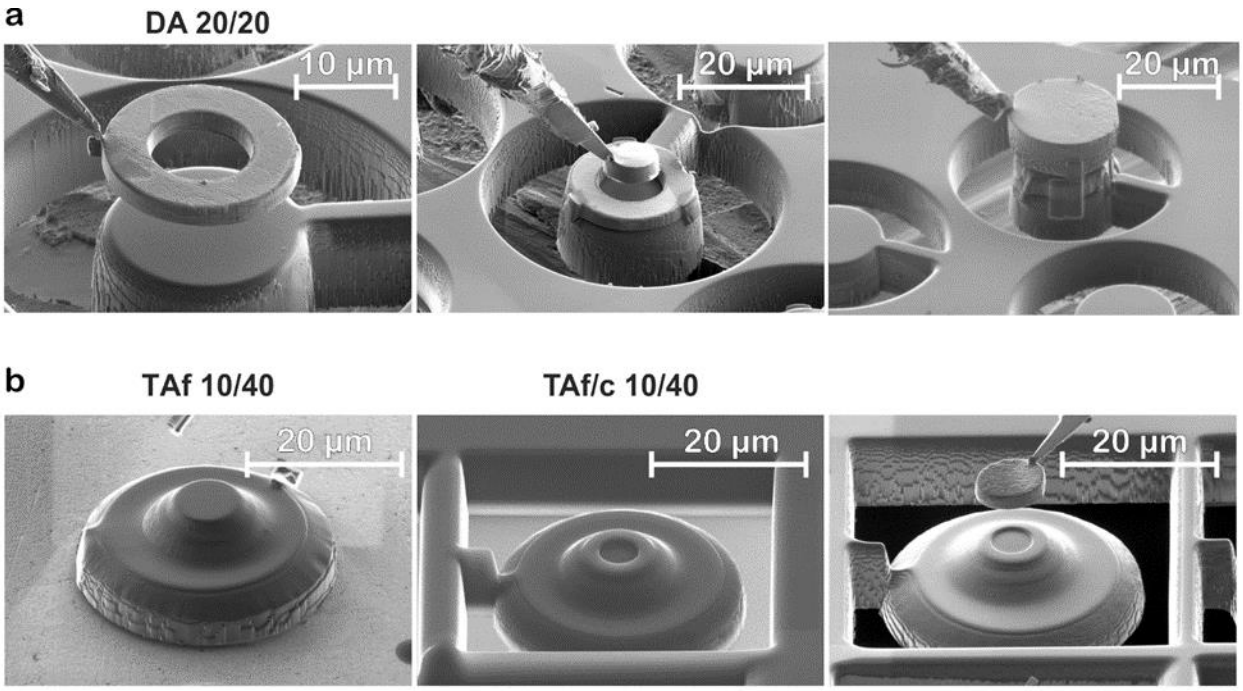


***Figure 8.*** *SEM images taken in situ in the chamber of the FIB instrument upon mounting the second-stage assemblies including two secondary anvils. (a) From the left to the right: DA 20/20 anvil at the bottom and a Re secondary gasket with a hole for a sample (left); placement of an Au sample into the hole using the Easy-lift needle (middle); completed assembly with the second DA 20/20 anvil on the top (right). (b) TAf 10/40 type anvil (left); TAf/c 10/40 anvil featuring a cavity with the depth of ~0.5 µm and the diameter of ~5 µm, which prevented the sample from complete outflow upon compression (middle); placement of an Ir sample using the Easy-lift needle directly on the top, as there was no a secondary gasket in this dsDAC assembly (right). Sketches with the dimensions of the anvils are provided in Figure 5.1.*

similar sets of two disc-shaped anvils (2 DA 20/20) (indicated by purple squares and green triangles in Figure 9a) look differently, because each DAC experiment is unique. There are a large number of parameters, which can significantly affect the rate of success of the high-pressure experiments and their results, but hardly can be standardized: small difference in thicknesses or positions of elements, sizes of samples, skills of researchers preparing a DAC, and others. In this particular case, the initial thicknesses of the primary Re gaskets (i. e. the heights of the primary sample chambers) were not identical. Nevertheless, Figure 9a shows principally different capabilities of dsDACs with two secondary anvils in comparison to DACs with single indenters

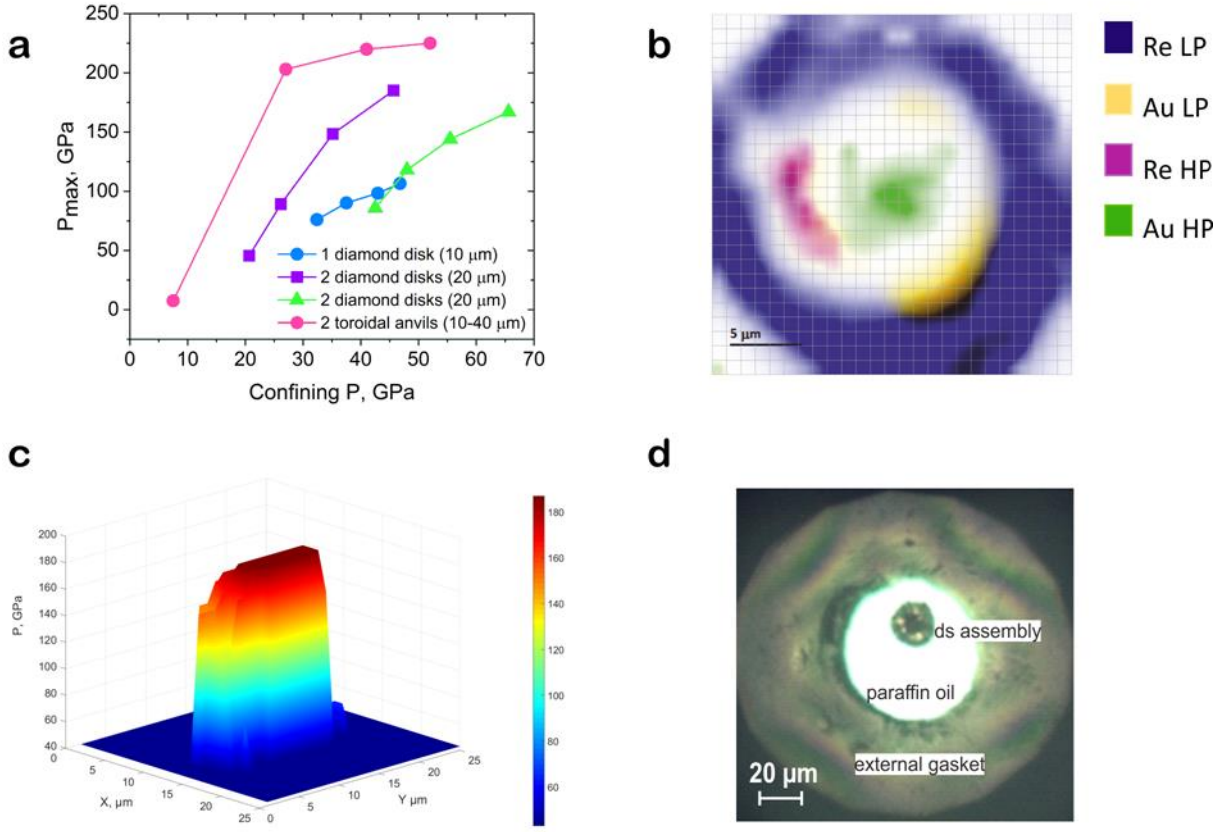


***Figure 9.*** *The results of feasibility experiments in dsDACs with pairs of secondary anvils. (a) The relationship between the maximum pressures measured on the sample ($P_{samp.}$(max.)) and corresponding confining pressures ($P_{conf.}$) for pairs of disc-shaped anvils (2 DA 20/20) in two different dsDACs experiments (purple squares and green triangles), for a pair of toroidal anvils (TAf 10/40 and TAc 10/40; pink circles), and for a DAC with a single indenter (1 DA 20/20; blue circles). (b) A 2D map showing the distribution of Au (sample material) and Re (gasket material) between the two DA 20/20 anvils obtained on the basis of XRD mapping; yellow and green regions for gold under lower (Au LP) and higher pressure (Au HP), correspondingly; dark violet and purple regions - for Re LP and Re HP; the colours' intensity is proportional the intensity of the following XRD reflections: the (100) and (101) of Re, (111) and (002) of Au; white color indicates the areas where neither Re nor Au was detected. (c) A 3D schematic showing pressure distribution over the pressure chamber imaged in (b); the colour scale to the right indicates pressures in GPa. (d) An optical image of the assembly, consisting of a pair of secondary DA 20/20 anvils loaded inside the DAC with paraffin oil as a pressure transmitting medium at confining $P_{conf.}$=42(2) GPa ($P_{samp.(max.)}$=186(2) GPa). Dark spot inside the secondary sample chamber is the Au-sample enclosed into the secondary gasket.*

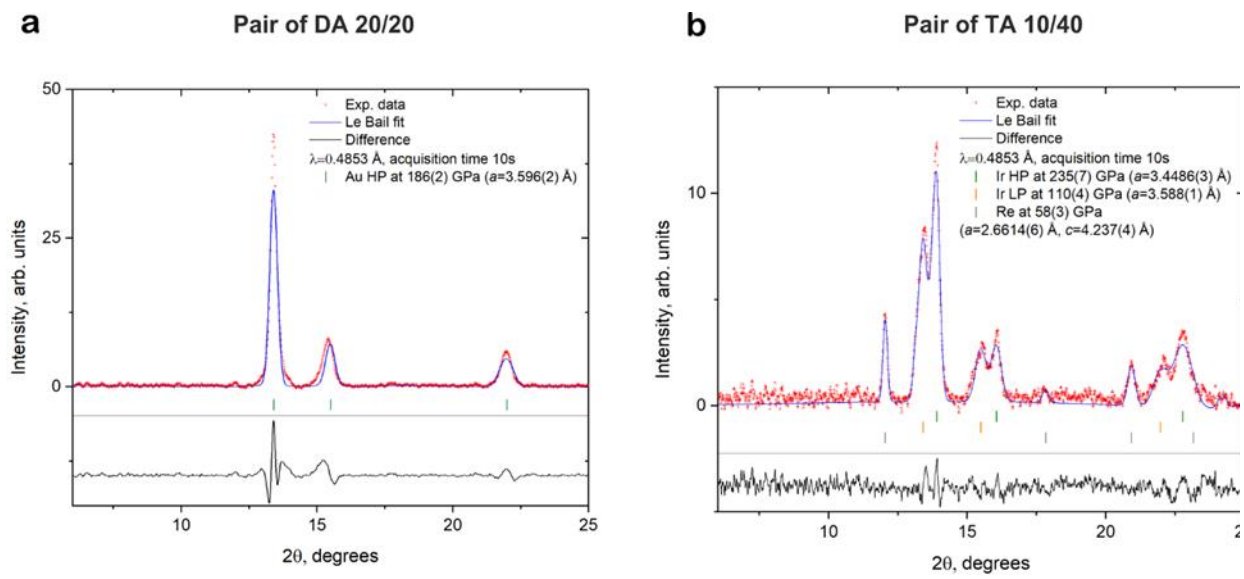


***Figure 10.*** *X-ray diffraction patterns from the samples loaded into dsDACs with pairs of secondary anvils: (a) DA20/20 and (b) TA 10/40 (b). The output of the Le Bail refinement based on powder diffraction data: red crosses are the experimental data, the blue curve is the simulated powder diffraction pattern, black curve shows the difference, orange and green ticks correspond to the diffraction lines of the sample at low pressure (Ir LP) and at high pressure (Au/Ir HP), respectively. Pressure was determined using the equations of state of Au from Fei et al.*[39] *and of Ir from Yusenko et al.*[38]

(blue circles in Figure 9a). Two secondary anvils (contrary to a single indenter) provide a higher "pressure multiplication factor".

A 2D map of the phases' distribution (Figure 9b), based on the 2D XRD mapping across the pressure chamber featuring the "2 DA 20/20" assembly, reveals that both Au and Re were smeared while the two secondary anvils bridged, but the major part of Au still remained in the middle of the chamber under high pressure (shown in green in the 2D map). Figure 9c shows a 3D schematic of the pressure distribution over the pressure chamber imaged in Figure 9b. Notably, that assembly, consisting of the two DA 20/20 remains transparent as it was made of single-crystalline diamond (Figure 9d), which enables optical measurements and spectroscopic studies.

For the next test, we used two toroidal anvils, one of which was of the TAf 10/40 type, while the second one (TAf/c 10/40, see Figure 1f) featured a cavity with the depth of ~0.5 μm and the diameter of ~5 μm (Figure 8b, middle), which prevented the sample from complete outflow upon compression. There was no secondary gasket in this dsDAC assembly, and the sample (~2 μm thick Ir foil of ~10 μm in diameter) was placed directly on the culet (Figure 8b, right) and fixed

by Pt deposition inside the FIB chamber. Primary anvils were made of beveled diamonds with 150-μm culets. The primary Re gasket was indented to a thickness of ~25 μm and a hole of ~45 μm in diameter was drilled in its center. XRD studies, conducted at the P02.2 beamline at PETRA III (see Methods), have shown that such design enables achieving pressures as high as 205(3) GPa (according to the Ir EoS(*38*)) at the confining pressure of ~30 GPa (see the straight part of the pink curve in Figure 9a). Although the pressure multiplication factor of ~7 is very promising, further compression of the dsDAC resulted in the misalignment (flow) of the secondary anvils. The maximum pressure generated in the experiment was 235(7) GPa based on Ir EOS(*38*) ($a$=3.4486(3) Å, $V$=41.015(4) Å$^3$) at the confining pressure of 58(3) GPa (Figure 10b). Remarkably, the culets of primary anvils under TA 10/40 stayed fully intact after the cell decompression that happens rarely after experiments aiming at pressures above 200 GPa.

## Summary

The FIB technique enables fabricating microanvils of a given size and shape that significantly improves the technique of dsDACs preparation. Our experiments have shown that maximal pressures achievable in DACs with a single secondary anvil do not significantly depend on the shape of the anvils (conical frustum or disc) and their culets'profiles (flat, toroidal, or spherical). However, toroidal anvils demonstrate higher stability in the assembly, more uniform pressure distribution over the sample chamber, and improve the reproducibility of experiments in DACs with a single indenter. Feasibility tests confirm high pressure multiplication efficiency of pairs of toroidal secondary anvils fabricated by FIB for applications in dsDACs.

## Acknowledgements

We thank Dr. Sylvain Petitgirard (ETH Zürich, Zürich, Switzerland), Dr. Katharina Marquardt (Imperial College London, London, UK) for kind help in the FIB preparation of sample. N. D. and L. D. thank the Federal Ministry of Education and Research, Germany (BMBF, grant No. 05K19WC1) and the Deutsche Forschungsgemeinschaft (DFG projects DU 954-11/1, DU 393-9/2, and DU 393-13/1) for financial support. N. D. thanks the Swedish Government Strategic

Research Area in Materials Science on Functional Materials at Linköping University (Faculty Grant SFO-Mat-LiU No. 200900971). We acknowledge DESY (Hamburg, Germany), a member of the Helmholtz Association HGF, for the provision of experimental facilities.

## References

1. I. G. Austin, N. F. Mott, Metallic and Nonmetallic Behavior in Transition Metal Oxides. *Science (80-. ).* **168**, 71–77 (1970).

2. M. P. Pasternak, G. K. Rozenberg, W. M. Xu, R. D. Taylor, in *High-Pressure Crystallography* (Springer Netherlands, Dordrecht, 2004; http://link.springer.com/10.1007/978-1-4020-2102-2_19), pp. 311–320.

3. A. P. Drozdov, M. I. Eremets, I. A. Troyan, V. Ksenofontov, S. I. Shylin, Conventional superconductivity at 203 kelvin at high pressures in the sulfur hydride system. *Nature*. **525**, 73–76 (2015).

4. A. P. Drozdov, P. P. Kong, V. S. Minkov, S. P. Besedin, M. A. Kuzovnikov, S. Mozaffari, L. Balicas, F. F. Balakirev, D. E. Graf, V. B. Prakapenka, E. Greenberg, D. A. Knyazev, M. Tkacz, M. I. Eremets, Superconductivity at 250 K in lanthanum hydride under high pressures. *Nature*. **569**, 528–531 (2019).

5. E. Snider, N. Dasenbrock-Gammon, R. McBride, M. Debessai, H. Vindana, K. Vencatasamy, K. V. Lawler, A. Salamat, R. P. Dias, Room-temperature superconductivity in a carbonaceous sulfur hydride. *Nature*. **586**, 373–377 (2020).

6. M. Millot, S. Hamel, J. R. Rygg, P. M. Celliers, G. W. Collins, F. Coppari, D. E. Fratanduono, R. Jeanloz, D. C. Swift, J. H. Eggert, Experimental evidence for superionic water ice using shock compression. *Nat. Phys.* **14**, 297–302 (2018).

7. A. F. Goncharov, N. Goldman, L. E. Fried, J. C. Crowhurst, I.-F. W. Kuo, C. J. Mundy, J. M. Zaug, Dynamic Ionization of Water under Extreme Conditions. *Phys. Rev. Lett.* **94**, 125508 (2005).

8. E. Kim, M. H. W. Chan, Probable observation of a supersolid helium phase. *Nature*. **427**, 225–227 (2004).

9. M. Miao, Y. Sun, E. Zurek, H. Lin, Chemistry under high pressure. *Nat. Rev. Chem.* **4**, 508–527 (2020).

10. M. Bykov, S. Chariton, H. Fei, T. Fedotenko, G. Aprilis, A. V. Ponomareva, F. Tasnádi, I. A. Abrikosov, B. Merle, P. Feldner, S. Vogel, W. Schnick, V. B. Prakapenka, E. Greenberg, M. Hanfland, A. Pakhomova, H.-P. Liermann, T. Katsura, N. Dubrovinskaia, L. Dubrovinsky, High-pressure synthesis of ultraincompressible hard rhenium nitride pernitride Re2(N2)(N2) stable at ambient conditions. *Nat. Commun.* **10**, 2994 (2019).

11. A. Friedrich, B. Winkler, E. A. Juarez-Arellano, L. Bayarjargal, Synthesis of binary transition metal nitrides, carbides and borides from the elements in the laser-heated diamond anvil cell and their structure-property relations. *Materials (Basel).* **4**, 1648–1692 (2011).

12. D. Laniel, B. Winkler, E. Koemets, T. Fedotenko, M. Bykov, E. Bykova, L. Dubrovinsky, N. Dubrovinskaia, Synthesis of magnesium-nitrogen salts of polynitrogen anions. *Nat. Commun.* **10**, 4515 (2019).

13. N. Dubrovinskaia, L. Dubrovinsky, Crystallography taken to the extreme. *Phys. Scr.* **93**, 062501 (2018).

14. E. Bykova, G. Aprilis, M. Bykov, K. Glazyrin, M. Wendt, S. Wenz, H.-P. Liermann, J. T. Roeh, A. Ehnes, N. Dubrovinskaia, L. Dubrovinsky, Single-crystal diffractometer coupled with double-sided laser heating system at the Extreme Conditions Beamline P02.2 at PETRAIII. *Rev. Sci. Instrum.* **90**, 073907 (2019).

15. T. Fedotenko, L. Dubrovinsky, G. Aprilis, E. Koemets, A. Snigirev, I. Snigireva, A. Barannikov, P. Ershov, F. Cova, M. Hanfland, N. Dubrovinskaia, Laser heating setup for diamond anvil cells for in situ synchrotron and in house high and ultra-high pressure studies. *Rev. Sci. Instrum.* **90**, 104501 (2019).

16. M. I. Eremets, Megabar high-pressure cells for Raman measurements. *J. Raman Spectrosc.* **34**, 515–518 (2003).

17. I. Kupenko, L. Dubrovinsky, N. Dubrovinskaia, C. McCammon, K. Glazyrin, E. Bykova, T. B. Ballaran, R. Sinmyo, A. I. Chumakov, V. Potapkin, A. Kantor, R. Rüffer, M. Hanfland, W. Crichton, M. Merlini, Portable double-sided laser-heating system for

Mössbauer spectroscopy and X-ray diffraction experiments at synchrotron facilities with diamond anvil cells. *Rev. Sci. Instrum.* **83**, 124501 (2012).

18. G. Aprilis, C. Strohm, I. Kupenko, S. Linhardt, A. Laskin, D. M. Vasiukov, V. Cerantola, E. G. Koemets, C. McCammon, A. Kurnosov, A. I. Chumakov, R. Rüffer, N. Dubrovinskaia, L. Dubrovinsky, Portable double-sided pulsed laser heating system for time-resolved geoscience and materials science applications. *Rev. Sci. Instrum.* **88**, 084501 (2017).

19. A. D. Rosa, O. Mathon, R. Torchio, J. Jacobs, S. Pasternak, T. Irifune, S. Pascarelli, Nano-polycrystalline diamond anvils: key devices for XAS at extreme conditions: their use, scientific impact, present status and future needs. *High Press. Res.* **40**, 65–81 (2020).

20. S. Petitgirard, G. Spiekermann, C. Weis, C. Sahle, C. Sternemann, M. Wilke, Miniature diamond anvils for X-ray Raman scattering spectroscopy experiments at high pressure. *J. Synchrotron Radiat.* **24**, 276–282 (2017).

21. A. F. Goncharov, E. Gregoryanz, H. Mao, Z. Liu, R. J. Hemley, Optical Evidence for a Nonmolecular Phase of Nitrogen above 150 GPa. *Phys. Rev. Lett.* **85**, 1262–1265 (2000).

22. Z. Konôpková, R. S. McWilliams, N. Gómez-Pérez, A. F. Goncharov, Direct measurement of thermal conductivity in solid iron at planetary core conditions. *Nature*. **534**, 99–101 (2016).

23. Y. Akahama, N. Hirao, Y. Ohishi, A. K. Singh, Equation of state of bcc-Mo by static volume compression to 410 GPa. *J. Appl. Phys.* **116**, 1–6 (2014).

24. Y. Akahama, H. Kawamura, Pressure calibration of diamond anvil Raman gauge to 410 GPa. *J. Phys. Conf. Ser.* **215**, 012195 (2010).

25. A. L. Ruoff, H. Xia, H. Luo, Y. K. Vohra, Miniaturization techniques for obtaining static pressures comparable to the pressure at the center of the earth: X-ray diffraction at 416 GPa. *Rev. Sci. Instrum.* **61**, 3830–3833 (1990).

26. R. H. Telling, C. J. Pickard, M. C. Payne, J. E. Field, Theoretical Strength and Cleavage of Diamond. *Phys. Rev. Lett.* **84**, 5160–5163 (2000).

27. W. A. Bassett, E. A. Skalwold, Diamond cleavage: importance to high pressure research. *High Press. Res.* **37**, 46–58 (2017).

28. L. Dubrovinsky, N. Dubrovinskaia, V. B. Prakapenka, A. M. Abakumov, Implementation of micro-ball nanodiamond anvils for high-pressure studies above 6 Mbar. *Nat. Commun.* **3**, 1163–1167 (2012).

29. N. Dubrovinskaia, L. Dubrovinsky, N. A. Solopova, A. Abakumov, S. Turner, M. Hanfland, E. Bykova, M. Bykov, C. Prescher, V. B. Prakapenka, S. Petitgirard, I. Chuvashova, B. Gasharova, Y.-L. Mathis, P. Ershov, I. Snigireva, A. Snigirev, Terapascal static pressure generation with ultrahigh yield strength nanodiamond. *Sci. Adv.* **2**, e1600341 (2016).

30. T. Sakai, T. Yagi, H. Ohfuji, T. Irifune, Y. Ohishi, N. Hirao, Y. Suzuki, Y. Kuroda, T. Asakawa, T. Kanemura, High-pressure generation using double stage micro-paired diamond anvils shaped by focused ion beam. *Rev. Sci. Instrum.* **86**, 033905 (2015).

31. T. Sakai, T. Yagi, T. Irifune, H. Kadobayashi, N. Hirao, T. Kunimoto, H. Ohfuji, S. Kawaguchi-Imada, Y. Ohishi, S. Tateno, K. Hirose, High pressure generation using double-stage diamond anvil technique: problems and equations of state of rhenium. *High Press. Res.* **38**, 107–119 (2018).

32. L. Dubrovinsky, N. Dubrovinskaia, E. Bykova, M. Bykov, V. Prakapenka, C. Prescher, K. Glazyrin, H.-P. Liermann, M. Hanfland, M. Ekholm, Q. Feng, L. V Pourovskii, M. I. Katsnelson, J. M. Wills, I. A. Abrikosov, The most incompressible metal osmium at static pressures above 750 gigapascals. *Nature*. **525**, 226–229 (2015).

33. S. Anzellini, A. Dewaele, F. Occelli, P. Loubeyre, M. Mezouar, Equation of state of rhenium and application for ultra high pressure calibration. *J. Appl. Phys.* **115**, 043511 (2014).

34. A. Dewaele, P. Loubeyre, F. Occelli, O. Marie, M. Mezouar, Toroidal diamond anvil cell for detailed measurements under extreme static pressures. *Nat. Commun.* **9**, 2913 (2018).

35. Z. Jenei, E. F. O'Bannon, S. T. Weir, H. Cynn, M. J. Lipp, W. J. Evans, Single crystal toroidal diamond anvils for high pressure experiments beyond 5 megabar. *Nat. Commun.* **9**, 3563 (2018).

36. P. Loubeyre, F. Occelli, P. Dumas, Synchrotron infrared spectroscopic evidence of the probable transition to metal hydrogen. *Nature*. **577**, 631–635 (2020).

37. I. Kantor, V. Prakapenka, A. Kantor, P. Dera, A. Kurnosov, S. Sinogeikin, N. Dubrovinskaia, L. Dubrovinsky, BX90: A new diamond anvil cell design for X-ray diffraction and optical measurements. *Rev. Sci. Instrum.* **83**, 125102 (2012).

38. K. V. Yusenko, S. Khandarkhaeva, T. Fedotenko, A. Pakhomova, S. A. Gromilov, L. Dubrovinsky, N. Dubrovinskaia, Equations of state of rhodium, iridium and their alloys up to 70 GPa. *J. Alloys Compd.* **788**, 212–218 (2019).

39. Y. Fei, A. Ricolleau, M. Frank, K. Mibe, G. Shen, V. Prakapenka, High-Pressure Geoscience Special Feature: Toward an internally consistent pressure scale. *Proc. Natl. Acad. Sci.* **104**, 9182–9186 (2007).

40. J. Gonzalez-Platas, M. Alvaro, F. Nestola, R. Angel, EosFit7-GUI : a new graphical user interface for equation of state calculations, analyses and teaching. *J. Appl. Crystallogr.* **49**, 1377–1382 (2016).

41. C. Prescher, V. B. Prakapenka, DIOPTAS : a program for reduction of two-dimensional X-ray diffraction data and data exploration. *High Press. Res.* **35**, 223–230 (2015).

42. R. Hrubiak, J. S. Smith, G. Shen, Multimode scanning X-ray diffraction microscopy for diamond anvil cell experiments. *Rev. Sci. Instrum.* **90**, 025109 (2019).

43. V. Petříček, M. Dušek, L. Palatinus, Crystallographic Computing System JANA2006: General features. *Zeitschrift für Krist. - Cryst. Mater.* **229**, 345–352 (2014).

44. S. S. Lobanov, V. B. Prakapenka, C. Prescher, Z. Konôpková, H. P. Liermann, K. L. Crispin, C. Zhang, A. F. Goncharov, Pressure, stress, and strain distribution in the double-stage diamond anvil cell. *J. Appl. Phys.* **118** (2015), doi:10.1063/1.4927213.

# Chapter 4.2. Sub-micron focusing setup for high-pressure crystallography at the Extreme Conditions Beamline of PETRA III

*K. Glazyrin[1], S. Khandarkhaeva[2,3], T. Fedotenko[1,3], W. Dong[1], D. Laniel[3], F. Seiboth[4], A. Schropp[4,5], J. Garrevoet[1], D. Brückner[1,6,7], G. Falkenberg[1], A. Kubec[8,9], C. David[8], M. Wendt[1], S. Wenz[1], L. Dubrovinsky[2], N. Dubrovinskaia[3,10], H.-P. Liermann[1]*

[1]*Deutsches Elektronen-Synchrotron DESY, Notkestr. 85, 22607 Hamburg, Germany*

[2]*Bayerisches Geoinstitut, University of Bayreuth, Universitätsstr. 30, 95440 Bayreuth, Germany*

[3]*Material Physics and Technology at Extreme Conditions, Laboratory of Crystallography, University of Bayreuth, Universitätsstr. 30, 95440 Bayreuth, Germany*

[4]*Center for X-ray and Nano Science CXNS, Deutsches Elektronen-Synchrotron DESY, Notkestr. 85, 22607 Hamburg, Germany*

[5]*Helmholtz Imaging Platform, Deutsches Elektronen-Synchrotron DESY, Notkestr. 85, 22607 Hamburg, Germany* [6]*Department Physik, Universität Hamburg, Luruper Chaussee 149, 22761 Hamburg, Germany*

[7]*Ruhr-Universität Bochum, Universitätsstr. 150, 44801 Bochum, Germany*

[8]*Laboratory for Micro- and Nanotechnology, Paul Scherrer Institut, Forschungsstr. 111, 5232 Villigen-PSI, Switzerland*

[9]*Current affiliation: XRnanotech GmbH, Forschungsstr. 111, 5232 Villigen-PSI, Switzerland*

[10]*Department of Physics, Chemistry and Biology (IFM), Linköping University, Campus Valla, Fysikhuset, F310, SE-581 83, Linköping, Sweden*

*J. Synchrotron Radiat.* **2022**, *29* (3). https://doi.org/10.1107/S1600577522002582.

## Abstract

Scientific tasks aiming at decoding and characterizing complex systems and processes at high pressures set new challenges to modern X-ray diffraction instrumentation in terms of X-ray flux, focal spot size and sample positioning. Here, we present new developments at the Extreme Conditions Beamline (P02.2, PETRA III, DESY, Germany) that enable considerable

improvements for data collection at very high pressures and small scattering volumes. Particularly, we describe the focusing of the X-ray beam to the sub-micron level with controlled aberrations of the focusing compound refractive lenses due to the implementation of a correcting phase plate. This device provides a significant enhancement of the signal-to-noise ratio by conditioning the beam shape profile at the focal spot. A new sample alignment system with a small sphere of confusion enables single-crystal data collection from grains of micron to sub-micron dimensions subjected to pressures as high as 200 GPa. The combination of the technical development of the optical path and the sample alignment system contributes to research and benefits on various levels, including rapid and accurate diffraction mapping of the samples with the sub-micron resolution at multimegabar pressures.

## Introduction

Exploration of systems subjected to high-pressure conditions using a combination of various pressurizing devices and a great number of sensing techniques enables great progress in the fields of geo- and planetary-sciences, material science, solid-state physics and chemistry. In particular, the diamond anvil cell (DAC), where two opposing anvils compress the sample, has been widely used for the characterization of samples in single crystalline form up to 2 Mbar (Khandarkhaeva et al., 2020) and powder at multiple Mbars (Dorfman et al., 2012; Dubrovinskaia et al., 2016; L. Dubrovinsky et al., 2015; Tateno et al., 2010). More recently, newly developed DAC designs such as the toroidal anvils (Dewaele et al., 2018; Jenei et al., 2018; McMahon, 2018) and the double stage DAC technique (Dubrovinskaia et al., 2016; Dubrovinsky et al., 2015; Dubrovinsky et al., 2012) have reached pressures up to 0.6 and 1 TPa, respectively. In addition, it has become apparent that the new synthesis products in high-pressure chemistry experiments can only be evaluated efficiently if one can map and effectively isolate the grain of interest from the surroundings, e.g. unreacted precursor material, pressure medium, other products of synthesis.

Thus, one of the major challenges of structural studies at conventional and ultra-high pressures is the reduction of sample sizes, which often requires probes with very X-ray small beam size and high flux. As X-ray diffraction is the most critical and one of the most powerful probes, the demand for sub-micron X-ray diffraction capabilities has increased significantly over the last

decade. Developments at large scale facilities are at the forefront of the state-of-art studies employing small beams and enable the determination of crystal structures and their evolution at extreme conditions, using either single crystals (SCXRD), e.g. (Bykov et al., 2019; Bykova et al., 2016; Friedrich et al., 2020; Laniel et al., 2020) or powders (PXRD) (Anzellini et al., 2019; Errandonea et al., 2020; Kawamura et al., 2002).

Review of the available literature shows that in comparison to powder diffraction techniques, high pressure SCXRD often provides a more reliable pathway for an accurate and precise structure solution, though the process of data acquisition can be more complex. Indeed, submicron-size samples, e.g. synthesized in a DAC after a laser heating, have to stay illuminated by the X-ray beam upon rotation of ±38º or higher angles. At the same time, the signal of interest should not be spoiled by a possible overlay from other phases or grains of the same phase, but of different orientations. The centering of micron-sized samples requires the implementation of more precise and accurate sample positioning systems at dedicated high-pressure beamlines. Thus, only a combination of precise motorization with the sub-micron beam capability of an instrument enables successful experiments; significantly improving the quality and usability of the data.

Here, we report the development of a sub-micron focusing setup at the general-purpose experiment table of the beamline P02.2 at PETRA III, DESY, Hamburg, Germany (Liermann et al., 2015). The new setup has a sub-micron focusing achieved by compound refractive lenses (CRLs) supplemented with a phase plate reducing the spherical aberrations of the CRLs at 25.6 keV. The implementation of a correcting phase plate is reducing the beam tails at the focal spot (Seiboth et al., 2017). This new development significantly improves capability of the beamline enabling users to collect data with the beam size at the focal spot of 0.9 x 0.9 $\mu m^2$ (H x V at full width at half maximum, FWHM) and the photon flux higher than that without the correcting phase plate.

In addition, we describe an improved sample positioning system with the implementation of a modern air bearing rotation stage operating in a combination with piezo actuator XY stages, enabling a spherical confusion on the order of a micron or below and a position accuracy of 0.1-0.2 μm. We demonstrate the capability of the new setup as an instrument by performing a test using micron-size single crystals of $CoSb_3$ and $(Mg_{1.93}Fe_{0.06})(Si_{1.93},Al_{0.06})O_6$ (orthoenstatite) prepared by a focused ion beam technique (FIB). Our studies, conducted at pressures above 150

GPa, characterize $Fe_3O_4$ and Fe-bearing perovskite $Mg_{0.91(2)}Fe_{0.09(2)}SiO_3$ measured in a multigrain matrix after their laser-heating in diamond anvil cells. These state-of-the-art examples highlight the full potential of the setup with the application to high-pressure crystallographic studies.

## Implementation of CRLs and a phase plate

A detailed description of the Extreme Conditions Beamline, P02.2, at the 3rd generation light source PETRA III can be found in Liermann et al., (2015). In order to improve the focusing capabilities of the beamline, e.g. 2 x 2 $\mu m^2$ obtained by using a Kirkpatrick-Baez (KB) mirror system, 136 2D parabolic Be CRLs with a radius of curvature at their apex of 50 µm and a geometrical aperture of 360 µm were installed at around 70.5 m from the source for X-ray diffraction experiments at 25. 6 keV. Using the full X-ray acceptance of the CRLs, a focused beam of 3 x 1.2 $\mu m^2$ (H x V) was achieved at a focal distance of 395 mm. Here and below, the values are provided for the full width at half maximum (FWHM). In order to achieve a smaller beam size at the focal spot, we reduced the incident beam to 50 x 50 $\mu m^2$ at the position of the high heat load slits system (SLT) located in the middle of the beamline at ca. 35 m from the source (just before the double crystal monochromator, DCM installed at 40.4 m). Thus, a small central area of the incident X-ray beam was used for focusing, resulting in a focal spot of ~0.9 x 0.9 $\mu m^2$ as determined with sharp-edge scans at the sample position (scans of absorbing cylindrical rods of 6 mm diameter made from hardened steel in horizontal and vertical directions in transmission mode).

Unfortunately, the size reduction of the incident beam at the position of SLT also resulted in a significant loss of the focused beam intensity. In order to improve the photon flux at the focal spot, but at the same time reduce the beamsize to sub-micron level, we reduced the spherical aberration of the lenses (Celestre et al., 2020; Seiboth et al., 2016) by implementing a customized phase plate downstream from the CRLs. Prior to the phase plate production, a stack of 136 lenses was pre-characterized at the Hard X-ray Micro/Nano-Probe Beamline P06 at PETRA III via ptychography in order to achieve optimal lateral coherence in the horizonal direction at 25.6 keV (G. Falkenberg et al. 2020, Seiboth et al., 2020). The calculated radial phase shift compensating

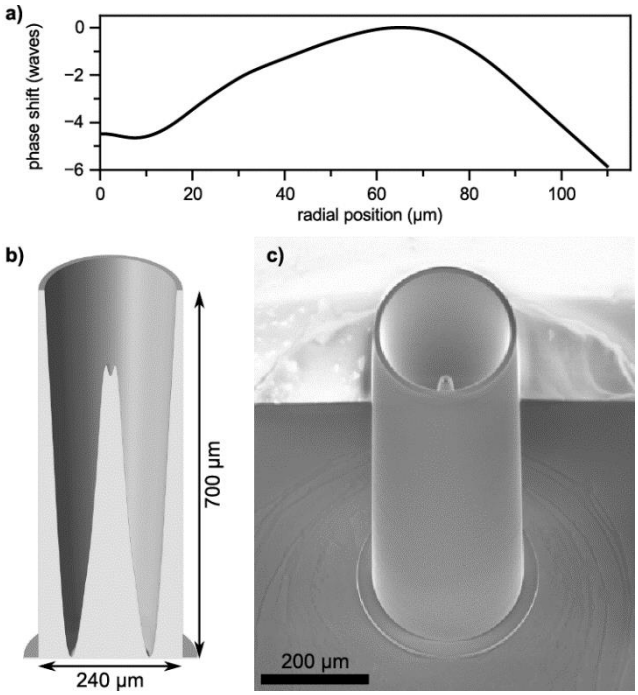


***Figure 1.*** *The correcting phase plate and its design: (a) the phase shift was quantified for the 136 CRLs at the P06 beamline by means of ptychography; (b) corresponding cross-section of a 3D model of the phase plate providing appropriate aberration corrections for this specific CRL stack; and (c) SEM image of the phase plate produced on a silicon nitride substrate.*

for spherical aberrations is shown in **Figure 1a**. A polymer structure with a height profile that matches the necessary phase correction was fabricated by a two-photon polymerization method. A cross-section of the three-dimensional model of the phase plate is shown in **Figure 1b**. The structure was created on a silicon nitride membrane with a Nanoscribe™ Photonic Professional GT using a "dip-in" lithography mode with a 25x objective (NA = 0.8; numerical aperture). In Figure 1c, we show an SEM image of the phase plate tailored to reduce the characteristic spherical aberration of the Be CRL-stack used at P02.2.

Considering the setup of P02.2, the phase plate was placed 29 mm downstream from the edge of the lens stack installed into the housing of a V-grooved CRL holder (Lengeler et al., 2005). The CRL holder provides an inert He environment protecting the CRLs from oxidation. The phase

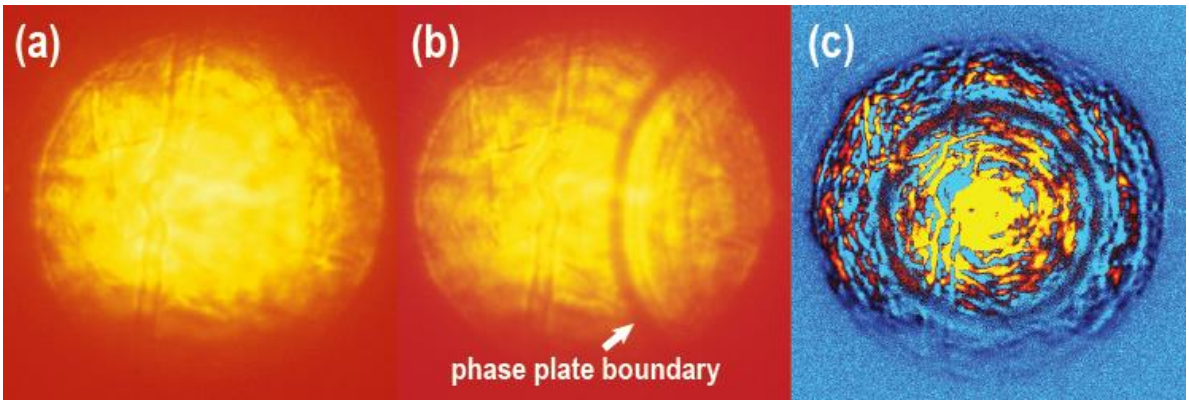


***Figure 2*** *Phase plate aligning procedure. The phase plate is located between the CRLs and the microscope installed downstream from the focal spot position. (a) Image of a defocused X-ray beam without the phase plate; (b) the phase plate is moving in the field of view approaching the central position from the right side; (c) the phase plate is centered, the image is produced by subtracting the background, e.g. (a), from the image with the phase plate centered. At the final steps of alignment and with the sharp-edge position placed to the position of the optimal focus, we make small displacement of the phase plate perpendicular to the incident beam and scan the sharp edge in order to achieve the best beam shape.*

plate was installed externally. To align the custom-made correcting phase plate to the optical axis of the CRL stack in the horizontal and vertical directions, a motorized positioning system

consisting of 2 MFA-PP micro steppers from Newport was mounted to the CRL V-groove housing. A high-resolution scintillator-based Optique Peter™ microscope (PCO.edge 4.2 CLHS camera, 20x objective, 10 μm thick YAG:Ce scintillator) was used to observe and control the alignment of the phase plate (**Figure 2**).

The lenses of the CRL stack were numbered during our measurement at P06 and were installed at the beamline in the same order. This step is important, since the phase shift of the correcting phase plate was calculated for a specific lens configuration. After the CRLs and the correcting phase plate alignment, further optimization steps were made in a search of a compromise between the photon flux and the beam size at the focal spot. This included iterative adjustments of the SLT opening and the tracking of the resulting beam size at the optimal focal spot. We measured the latter by means of sharp-edge scans at different focal distances. In the end,

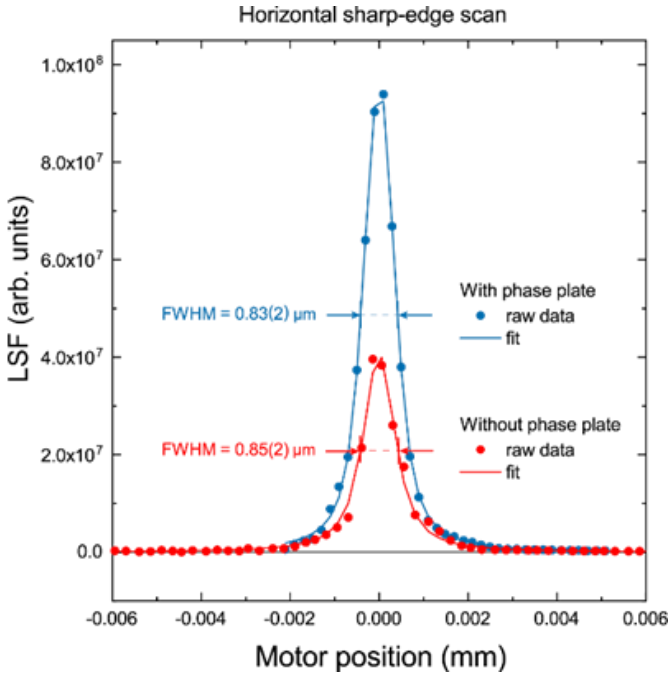


***Figure 3*** *Comparison of the horizontal focal size with (blue data) and without (red data) the correcting phase plate. The curves correspond to the derivative signal of the sharp-edge scans, linear spread function (LSF). The analysis of the curves confirms the similar size of X-ray beam in the horizontal direction. Given the same acquisition time per point, the higher values for the blue data indicate higher flux values for the setup when corrected with the correcting phase plate. With the phase plate (blue), one can employ a larger opening of SLT installed in front of the DCM position. Implementation of the phase plate enabled higher intensity X-ray beam while maintaining a small beam size with similar, or even slightly smaller beam tails, at the focal spot.*

the incident beam size at the SLT had dimensions of ~150 x 150 $\mu m^2$ and the corresponding optimal focal distance was of 400-402 mm (center of CRL stack to the focal point).

By scanning X-ray beam at the focal spot using an absorbing edge we measure a transmission curve with a sigmoidal-like shape which corresponds to an edge-spread function (ESF) (Wang et al. 2016 and the references within). By derivation of ESF we produce a linear spread function (LSF) response enabling determination of a focal spot size. In order to assess the situation before and after the installation of the phase plate as well as the advantage of using the latter, we collected data which is presented in **Figure 3**. The (a) red line depicts the beam shape at the focal spot without the phase plate and with a smaller opening of SLT (50 x 50 $\mu m^2$), while (b) the blue line corresponds to the case with the phase plate installed and a larger opening of SLT

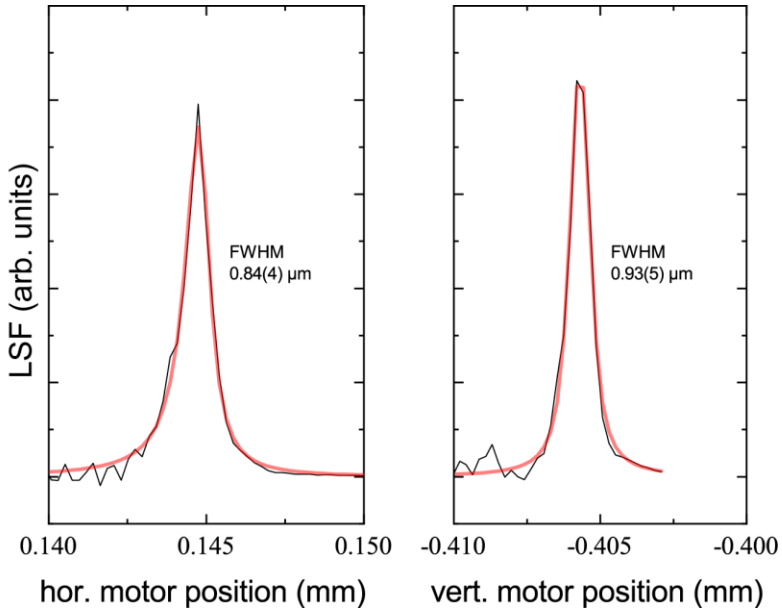


***Figure 4*** *1st order derivative of sharp-edge scans (LSF) collected during horizontal (left) and vertical (right) motors movement. We show the FWHM together with the corresponding error bar estimates.*

(~150 x 150 µm$^2$). Considering the case (a), we add that further SLT opening without installation of the phase plate increases the focal spot beyond 1 µm. Raw data for the curves was measured using the same pin-diode acquisition time, thus, the installation of the phase plate produced a gain with a factor of ~2.2. Comparing (a) and (b), we conclude that a similar focal size in the horizontal direction was achieved in both cases, including similar or lower beam tail contribution, but installation of the phase plate enabled higher photon flux.

In one of the final steps, the sample stack position was readjusted in order to bring the position of the sample stack rotation axis (controlling the sample-to-detector distance; SDD) to the position of the focal spot. **Figure 4** illustrates the horizontal and the vertical beam profiles at the focal spot used for the measurement of the single crystal data reported below. The optimization of the X-ray optical path included the installation of a Pt-based pinhole, ranging from 15-40 µm in diameter depending on the application. The photon flux for the "sub-micron" setup at the beam position with 40 µm pinhole was measured to be around $3.7 \cdot 10^9$ ph/s using a calibrated passivated implanted planar silicon (PIPS) diode.

The opening of the SLT does have several effects for the X-ray optical path. On one hand, it controls the total energy dissipating at the DCM crystals (e.g. heat bump, non-ideal surface of

crystals). On the other hand, the closing of the SLT effectively introduces a secondary source. It is hard to give a quantitative description of the realistic and non-ideal system, an analysis which goes beyond the current publication. However, we note that after further opening the SLT, an increase of flux by at least of a factor 3-5 was observed. At the same time the beam size at the focal spot increased to 1.3 x 1 $\mu m^2$ (H x V) FWHM. This option may be of interest to user groups working with low Z materials, where the compromise between the illuminating beam intensity and the beam size at the focal spot is shifted towards the higher photon flux at the sample position.

## Sample positioning system with “sub-micron” resolution

Accurate sample positioning is a crucial aspect of a high-pressure DAC experimental setup. Along with the improved focusing, it was necessary to update the existing sample positioning system (Liermann et al., 2015). We indicate the new parts in **Figure 5**. A XY PILine® piezo positioning stage (1) and a PIglide® RM air bearing rotation stage (2) were acquired from Physik Instrumente™ (PI™) GmbH & Co. They replace the top portion of the standard sample 6-motor positioning system (Liermann et al. 2015). In addition, we exchanged the motor (3) controlling the position of the rotation axis and moving it in the horizontal plane perpendicular to the X-ray beam. It was upgraded through an HPS-170 high-precision linear stage also manufactured by PI. The factory characteristics of these positioning units are listed in **Table 1**.

As indicated in **Figure 5,** the sample stack is set up on the kinematic mounting plate. It has three cavities matching the three ball point joints mounted on the base granite installed at the beamline. After the installation, the kinematic plate is fixed to the underlaying granite by means of several M12 screws. The change from a standard setup (also based on the kinematic stage approach) to the “sub-micron” configuration takes a few hours, including motor reconnection and reconfiguration. Optimal operation parameters of the motors were determined during the commissioning, e.g. the XY cross-roller stage were optimized for 0.2 nm reproducibility of movement together with PI company representatives. Loading capacities given in **Table 1** indicate that the “sub-micron” sample stack is not compatible with heavy DAC environments, e.g. a

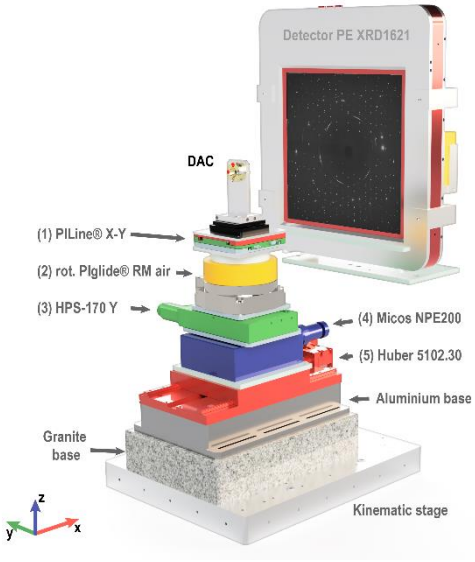


***Figure 5*** *A schematic illustration of the “sub-micron” motor sample stack. “DAC” indicates the position of a sample mounted in a DAC. For clarity, individual components are represented by different colors and are numbered. The corresponding coordinate system employed at the beamline is shown at the bottom of the figure. The x-axis is parallel to the X-ray beam direction. The Perkin Elmer XRD1621 detector is shown as reference.*

***Table 1*** *Factory characteristics of the individual positioning parts used for the “sub-micron” setup at the Extreme Conditions Beamline (ECB).*

| | |
|---|---|
| (1) XY stage with PILine® piezo motors | - 25 mm × 25 mm travel range<br>- 100 nm min. incremental motion<br>- 10 nm sensor resolution<br>- 7 N drive force, max. load capacity 50N |
| (2) PIglide® RM air bearing rotation stage | - 150 mm motion platform diameter<br>- 50 mm travel length<br>- 0.0015 µrad sensor resolution<br>- absolute angle-measuring system<br>- slot-less, brushless 3-phase torque motor |
| (3) HPS-170 high-precision linear stage | - 170 mm width, 52 mm travel range<br>- 50 nm minimum incremental motion<br>- stepper motor<br>- linear encoder with sin/cos signal transmission<br>- optical limit switches<br>- 350 N load capacity |

vacuum chamber, which is typical for the standard setup. However, the “sub-micron” sample stack can easily hold DACs of various popular designs (e.g. symmetric, BX90, Boehler-Almax, etc),

including a membrane connected to a pressure controller. The positioning of the samples by means of the “sub-micron” motor stack is fully integrated into beamline software. It is fully compatible with our standard setup (e.g. synchronization of sample positions by means of offline and online microscopes available for the users). Below we discuss the performance of the “sub-micron” instrument setup from a user’s perspective with several examples of single crystal studies at ambient and high-pressure conditions.

## Performance of the “sub-micron” experimental setup with samples at ambient conditions

Two single crystals with different absorption length (high and low Z) were used to test the accuracy and the precision of the sample positioning system: orthenstatite $(Mg_{1.93},Fe_{0.06})(Si_{1.93},Al_{0.06})O_6$, *Pbca*, $a$ = 18.2391(3), $b$ = 8.8117(2), $c$ = 5.18320(10) Å), and $CoSb_3$ ($Im\bar{3}$, $a$ = 9.0357(3) Å) measured at Bayerisches Geoinstitute using the 8-position centering procedure (Angel & Finger, 2011). Both materials are stable at ambient conditions and have large unit cells that produce a considerable number of reflections, which is ideal for testing.

Tiny single crystals of orthoenstantite and $CoSb_3$ were prepared using a focused ion beam (FIB, FEI™ SCIOS Dual beam) instrument located at DESY NanoLab. The pre-cut single crystalline lamellas were reduced to smaller size with lateral dimensions of 2-4 μm (**Figure 6**). These grains were transferred by means of a Microsupport™ Axis Pro micromanipulator into DACs used as sample holders and ensuring sample safety during transportation. We employed a Re gasket with a ~10 μm thickness indented by 40 μm culet diamond anvils of Boehler Almax design. These test crystals were measured at ambient conditions.

Single crystal samples were measured using a Perkin Elmer XRD1621 amorphous silicon detector bonded to a CsI scintillator. During the data acquisition, the crystals were rotated by ±32° and ±38° with a step size of 0.5° for $CoSb_3$ and orthoenstatite, respectively. The wavelength of the X-ray beam was tuned to 0.4830 Å (25.67 keV). Alignment of the sample to the center of the “sub-

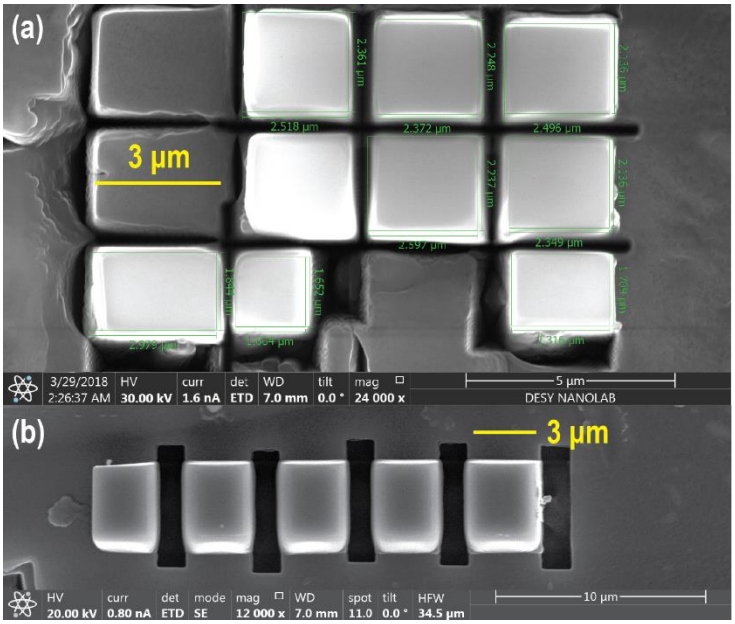


***Figure 6*** *SEM images produced by the SCIOS Dual beam FIB of the NanoLab. (a) Prepared pieces of orthoenstatite and (b) $CoSb_3$ single crystals.*

micron” motor stack rotation was performed with the help of X-ray transmission scans. We used the $CoSb_3$ absorption signal as a reference, while in the case of orthoenstatite (separate DAC, low Z material) we had to use the absorption signal from a thin gasket and then locate the orthoenstatite crystal using a visible light microscope of the beamline.

Data were processed using the CrysalisPro software package (Rigaku Crysalis Pro v. 171.40, 2020), including the SCALE3 ABSPACK routine for empirical absorption correction and conventional single crystal data treatment. The output of the program demonstrates the exceptional sample stability during the data collection of $CoSb_3$ (**Figure 7**). A minor deviation was detected in the case of the orthoenstatite sample, and we attribute it to the difficulty of sample centering for this poor X-ray scattering material.

Structure solution and refinement were conducted using OLEX2 (Dolomanov et al., 2009) with the SHELX backend (Sheldrick, 2008, 2015) and the JANA2006 package (Petricek et al., 2006). The refinement parameters and the corresponding structural information are summarized in **Table 2**. Additional information, including CIFs, is provided in the supplementary materials. Illustrations of the crystal structure in **Figure 8** were prepared with the CrystalMaker software (Palmer, 2014).

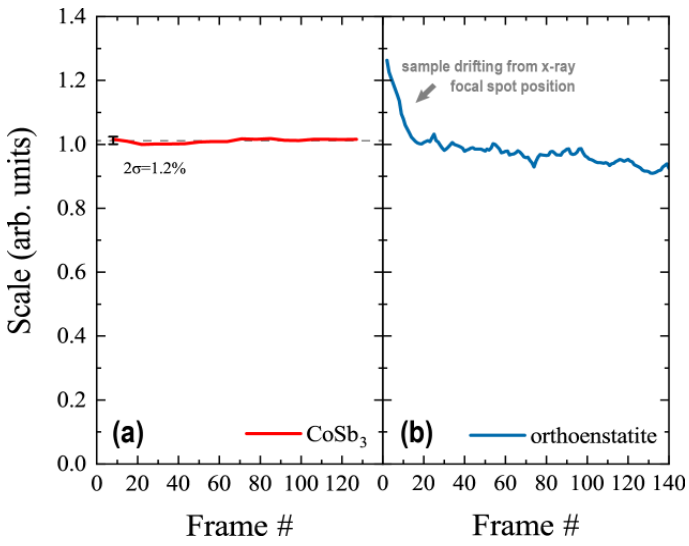


***Figure 7*** *Output of SCALE3 ABSPACK empirical absorption correction routine of Rigaku™ CrysalisPro. It indicates the amount of scaling which had to be applied on each frame in order to compensate the intensity mismatch between different Friedel equivalents. Each frame corresponds to a physical angle with a step size of 0.5° per frame. (a) Flat red line with 2·σ=1.2 % is attributed to an average value of 1.011 (grey dashed line). It indicates the excellent stability of the $CoSb_3$ sample with respect to the X-ray beam during single crystal data acquisition. (b) Our analysis shows that the orthoenstatite single crystal was slightly moving out of the X-ray beam in the angular range corresponding to the frames # 0-20. We consider that the centering procedure involving the gasket absorption profile combined with visible light observations was not perfect enough. The difference with point scatter between the red and the blue lines can be attributed to the difference of scattering factors. For (a) we had to use 50 µm Pt absorber foil in order to reduce the intensity of the diffraction signal coming from the sample. A much stronger scattering of $CoSb_3$ in comparison to ortho-enstatite is the reason for noise difference between the red and the blue curves.*

The data quality reported in **Table 2** is exceptional and in very good agreement with the literature data, even though the energy of the X-ray beam was very low (25.67 keV) which significantly limits our access to the reciprocal space due to the finite aperture of DACs. Future developments and enhancements expected for diffraction limited storage rings (DLSR) such as the ESRF-EBS, APS-U and PETRA-IV, will boost these types of studies. Considering the ECB at PETRA III, the upgrade to PETRA-IV (Schroer et al., 2019) promises improved capabilities. The upgrade will result in photon flux improvement at all photon energies interesting for high-pressure research and in combination with sub-micron focusing it will exceed the capabilities of the 3$^{rd}$ generation sources.

**Table 2** Details of the crystal structure refinements of test samples orthoenstatite $(Mg_{1.93},Fe_{0.06})(Si_{1.93},Al_{0.06})O_6$ and $CoSb_3$. Atomic displacement parameters of cations were refined with anisotropic approximation. For additional information about crystal structures and refinement parameters we refer to the supplementary materials (CIFs).

| **Crystallographic data** | | |
|---|---|---|
| **Chemical formula** | $(Mg_{1.94}Fe_{0.067})(Si_{1.93}Al_{0.067})O_6$ | $CoSb_3$ |
| $M_r$ | 202.9 | 424.2 |
| **Crystal system, space group** | Orthorhombic, *Pbca* | Cubic, *Im*3 |
| **Temperature (K)** | 293 | 293 |
| ***a*, *b*, *c* (Å)** | 5.1815 (2), 18.2321 (11), 8.8085 (5) | 9.0360 (1) |
| ***V* (Å$^3$)** | 832.14 (8) | 737.78 (1) |
| ***Z*** | 8 | 8 |
| **Radiation type** | Synchrotron, λ = 0.483 Å | Synchrotron, λ = 0.483 Å |
| **μ (mm$^{-1}$)** | 0.44 | 8.83 |
| **Crystal size (μm$^3$)** | 4 × 4 × 2 | 3 × 3 × 2 |
| **Data collection** | | |
| **Diffractometer** | Single circle (ω) diffractometer | |
| **Absorption correction** | Multi-scan. *CrysAlis PRO* 1.171.40.67a (Rigaku Oxford Diffraction, 2020) Empirical absorption correction using spherical harmonics, implemented in SCALE3 ABSPACK scaling algorithm. | |
| $T_{min}$, $T_{max}$ | 0.824, 1 | 0.888, 1 |
| **No. of measured, independent and observed [$I > 2\sigma(I)$] reflections** | 1072, 454, 409 | 490, 133, 121 |
| $R_{int}$ | 0.017 | 0.016 |
| **(sin θ/λ)$_{max}$ (Å$^{-1}$)** | 0.652 | 0.645 |
| **Refinement** | | |
| **$R[F^2 > 2\sigma(F^2)]$, $wR(F^2)$** | 0.025, 0.039 | 0.012, 0.043 |
| **No. of reflections** | 454 | 133 |
| **No. of parameters** | 61 | 9 |
| **$\Delta\rho_{max}$, $\Delta\rho_{min}$ (e Å$^{-3}$)** | 0.58, −0.62 | 1.28, −1.03 |

## Applications to materials compressed above ~150 GPa in laser heated diamond anvil cells

A successful crystallographic solution for the test cases described below would not be possible with our standard motor setup. The implementation of the new motorization enabled more accurate and reproducible sample positioning in 3D space, including sample positioning at the center of rotation of the highly accurate rotation stage. Due to the improvements of the motorization and the implementation of the correcting phase plate, which reduces the overload of the sample signal in the reciprocal space, the resulting user experience was greatly improved, especially from the data quality point of view. Each of the described cases represents an important challenge for various fields of science, such as crystal chemistry, mineral physics or planetary sciences, etc.

Iron oxides are closely related to planetary evolution (Bykova et al., 2016; Dobson & Brodholt, 2005), but also play a significant role in thermal energy storage as indicated in various studies (Grosu et al., 2017; Huang & Xu, 2019). High-pressure high-temperature treatment of the Fe-O system at elevated pressures induces various phases and structural transformations. Below we report on the observation of the *Pnma* phase of $Fe_3O_4$ at ~200 GPa. The starting material, α-$Fe_2O_3$ (hematite), was loaded in the sample chamber of a BX90 diamond anvil cell (Kantor et al., 2012) together with Ne as the pressure transmitting medium (Kurnosov et al., 2008). The starting material was laser heated at the Bayerisches Geoinstitut using a laser heating system recently developed by Fedotenko et al. (2019). It was is a pulsed laser heating system operating in continuous mode (NIR laser beam, 1070 nm, 5 μm at FWHM in diameter). Pressure was measured using the equation of state of Ne (Y. Fei et al., 2007). Single crystal datasets were collected using the Perkin-Elmer XRD1621 detector with a wavelength of 0.483 Å. The complete description of the structure of *Pnma* $Fe_3O_4$ observed at 200 GPa, including a CIF, is provided in the supplementary materials. The small X-ray beam size was crucial as it constrained the number of illuminated grains and the overlay of scattered intensity in the reciprocal space originating from various sources of the high-pressure environment.

The laser heating of the compressed hematite produced a polycrystalline mixture. Analysis of 2D scanning map data of the laser heated area indicated several larger single crystal grains that are potential candidates for structural solution. The indexing of the reflections belonging to two

**Table 3**. Detailed information of the crystal structure refinements of oP-$Fe_3O_4$ and $Mg_{0.91(2)}Fe_{0.09(2)}SiO_3$ performed on laser heated samples at ultra-high pressures. Samples were measured at ambient temperature after a laser heating procedure. For additional information about crystal structures and refinement parameters we refer to the supplementary materials (CIF).

| **Crystal data** | | |
|---|---|---|
| **Chemical formula** | $Fe_3O_4$ | $Mg_{0.91(2)}Fe_{0.09(2)}SiO_3$ |
| **Pressure (GPa)** | ~200 | ~155 |
| $M_r$ | 231.5 | 103.3 |
| **Crystal system, space group** | Orthorhombic, *Pnma* | Orthorhombic, *Pbnm* |
| **Temperature (K)** | 293 | 293 |
| ***a*, *b*, *c* (Å)** | 7.932 (10), 2.5881 (13), 8.321 (3) | 4.194 (2), 4.525 (1), 6.1910 (1) |
| ***V* (Å$^3$)** | 170.8 (2) | 117.49 (6) |
| ***Z*** | 4 | 4 |
| **Radiation type** | Synchrotron, λ = 0.483 Å | Synchrotron, λ = 0.483 Å |
| **μ (mm$^{-1}$)** | 7.97 | 0.98 |
| **Crystal size (μm$^3$)** | 1 × 2 × 1≅ | 2 × 2 × 2≅ |
| **Data collection** | | |
| **Diffractometer** | Single circle (ω) diffractometer | |
| **Absorption correction** | Multi-scan. *CrysAlis PRO* 1.171.40.67a (Rigaku Oxford Diffraction, 2019) Empirical absorption correction using spherical harmonics, implemented in SCALE3 ABSPACK scaling algorithm. | |
| $T_{min}$, $T_{max}$ | 0.559, 1 | 0.664, 1 |
| **No. of measured, independent and observed [$I > 2\sigma(I)$] reflections** | 195, 105, 88 | 106, 56, 53 |
| $R_{int}$ | 0.029 | 0.008 |
| **(sin θ/λ)$_{max}$ (Å$^{-1}$)** | 0.643 | 0.607 |
| **Refinement** | | |
| **$R[F^2 > 2\sigma(F^2)]$, $wR(F^2)$** | 0.071, 0.075 | 0.041, 0.114 |
| **No. of reflections** | 105 | 56 |
| **No. of parameters** | 22 | 13 |
| **Δρ$_{max}$, Δρ$_{min}$ (e Å$^{-3}$)** | 2.04, −1.8 | 0.51, −0.54 |

≅ - approximate size based on X-ray diffraction 2D mapping

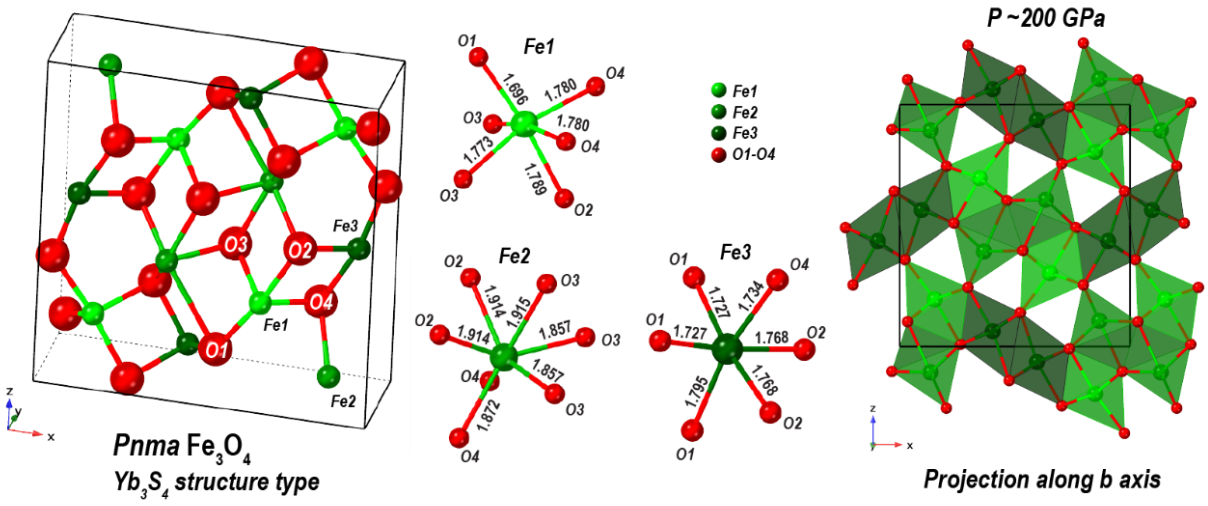


***Figure 8*** *The crystal structure of Pnma $Fe_3O_4$ formed after laser heating at 3000-3500 K. The structure is composed of layers of distorted octahedrons (Fe1 and Fe3 sites) which are interconnected through the capped trigonal prisms (Fe2 sites). The structure solution converged to $R(F^2)=7.1\%$; $wR(F^2)=7.5$ % using reflections with an intensity $I > 2\sigma(I)$. We indicate the individual building blocks and the corresponding Fe-O bonds. To the right we show a projection of the structure along the b axis providing a clear indication of edge sharing of the corresponding building blocks and an overview of the Fe-O framework.*

strongly scattering *Pnma* $Fe_3O_4$ (oP-$Fe_3O_4$) domains was identified after a careful inspection of the reciprocal space using the CrysAlisPro software. A more detailed description of the process is provided in the supplementary materials. The lateral size of the domains within the 2D map did not exceed a couple of microns. The integration of intensities for the most strongly scattering domain converged with $R_{int}=2.9$ %. The structure was solved and refined based on 195 measured reflections for 22 refined parameters with $R_1=7.1\%$ (**Table 3**). The structure of oP-$Fe_3O_4$ contains two different octahedrally coordinated positions of iron atoms (Fe1 and Fe3) with the Fe-O bond distance varying between ~1.70-1.80 Å (**Figure 8**). The distorted octahedra share edges and form ribbons, two enantiomorphic ribbons are joined with each other, hinging together along lines of the shared oxygen parallel to the *c*-axis. The Fe2 atom is surrounded by seven oxygen atoms with a Fe-O distance variation of ~1.86-1.91 Å. Its coordination can be considered as a capped trigonal prism. The structure of novel oP-$Fe_3O_4$ belongs to the $Yb_3S_4$ structure type (Chevallier et al.,

1967). It is common for warwickites, mixed metal borates of the general formula $A_xT_{4-x}B_2O_8$, where A and T are alkaline earth, lanthanide, or transition metals (Matos et al., 1996).

Charge balance considerations suggest that the Fe1 and Fe3 sites are occupied by $Fe^{3+}$. Our analysis of the Fe1-O and Fe3-O distances supplemented by the analysis of the octahedron sites volumes reveals that the Fe1 and Fe3 atoms are in the low spin state (Vasiukov, 2018). The Fe2 site is attributed to $Fe^{2+}$. It is clearly larger in comparison to the Fe1 and Fe3 sites. We suggest that the spin configuration of Fe2 should be also attributed to the low spin. However, due to the deformation of the crystallographic site we cannot fully exclude the possibility of an intermediate spin state configuration. The precise characterization of the iron atoms' electronic state in *oP*-$Fe_3O_4$ and the exploration of its phase diagram requires further investigation.

The Mg-Si-O system is equally if not more important than Fe-O for our understanding of the Earth and other planetary environments. In addition to the example of the $Fe_3O_4$ system, we show a full structure solution and a refinement of excellent quality Fe-bearing bridgmanite $Mg_{0.91(2)}Fe_{0.09(2)}SiO_3$. The data was obtained after laser heating and collected at the pressure of ~155 GPa (Ne pressure scale, Y. Fei et al. 2007). Accurate measurements of the physical properties of bridgmanite and post-perovskite, including density as a function of pressure, temperature, and composition, have always been a focus of solid-earth investigations. The studies continue with a doubled effort today involving static and dynamic compression methods (e.g. Y. Fei et al., 2021). However, information characterizing the density alone can rightfully be considered insufficient.

It must be supplemented with a thorough understanding of the crystal structure, its evolution and perturbation. Here, ultra-high-pressure studies of the Mg-Si-O system by means of single crystal X-ray diffraction represent a very specific, but very important challenge. Most experimental difficulties could be tracked down to low scattering volumes of submicron-sized samples, but they become even more severe due to the low atomic scattering factor in the case of the Mg-Si-O system. Using the example of bridgmanite laser heated to 2500-3000 K, we demonstrate the power of the new sub-micron setup at P02.2 enabling structural studies of chemically complex systems at ultra-high pressures, even those containing mostly light elements in their composition (e.g. Mg, Si, O). As we show in **Table 3**, the final refinement of the structural model converges with the very low R-factor of $R_1$*=4.11 %* based on 106 measured reflections and 13 refined parameters.

## Conclusions

By applying the most recent technical developments, within the capabilities of PETRA III, we report an upgrade of the existing high-pressure micro X-ray diffraction instrument at P02.2. The upgrade involves the modification of the X-ray optical path and the implementation of a phase plate correcting the spherical aberration of the CRLs implemented at P02.2 s in the combination with the new, more accurate and precise motorization of the sample stack.

Within our test studies conducted at ambient and pressure conditions exceeding 1 Mbar, we demonstrate the pressing issues faced in the high-pressure science and present a solution addressing the challenges of single crystal refinement from grains of micron to sub-micron dimensions. We describe the 'synthetic' examples of orthoenstatite and $CoSb_3$ measured inside the DACs at ambient conditions and extend our studies to the scientific cases exploring the crystal structures of $Fe_3O_4$ and $Mg_{0.91(2)}Fe_{0.09(2)}SiO_3$. The structures of the latter materials were successfully solved at pressure conditions exceeding 1 Mbar even though the data acquisition and analysis processes were highly challenging, e.g. complicated by sample finding and signal extraction from micron-size polycrystalline aggregate. The real case studies of $Fe_3O_4$ and $Mg_{0.91(2)}Fe_{0.09(2)}SiO_3$ demonstrate the capacity of the current instrument upgrade. We hope that our study will inspire the high-pressure community and further developments at dedicated high-pressure beamlines extending the capabilities of the latter and driving high-pressure sciences beyond the boundaries of the commonly explored P-T space.

## Acknowledgements

We acknowledge DESY (Hamburg, Germany), a member of the Helmholtz Association HGF, for the provision of experimental facilities. Parts of this research were carried out at P02.2 and P06 beamlines of PETRA III and we would like to additionally thank Andreas Stierle, Satishkumar Kulkarni and Thomas Keller for assistance in using NanoLab facilities. We are grateful to Adam Kubec currently employed at XRnanotech GmbH, which can manufacture phase plates presented in this work. We acknowledge Mirtha Pillaca and Peter Gille (Ludwig-Maximilians-Universität, München, Germany) for their great help with the preparation of the

$CoSb_3$ samples. We are grateful to Tiziana Boffa-Ballaran (Bayerisches Geoinstitut, Bayreuth, Germany) for 8-circle position measurements of orthoenstatite and $CoSb_3$. N.D. and L.D. thank the Federal Ministry of Education and Research, Germany (BMBF, grant No. 05K19WC1) and the Deutsche Forschungsgemeinschaft (DFG projects DU 954-11/1, DU 393-9/2, and DU 393-13/1) for financial support. N.D. thanks the Swedish Government Strategic Research Area in Materials Science on Functional Materials at Linköping University (Faculty Grant SFO-Mat-LiU No. 2009 00971). D.L. thanks the Alexander von Humboldt Foundation for financial support.

## References

Angel, R. J., & Finger, L. W. (2011). SINGLE: A program to control single-crystal diffractometers. Journal of Applied Crystallography, 44, 247–251. doi:10.1107/S0021889810042305

Anzellini, S., Monteseguro, V., Bandiello, E., Dewaele, A., Burakovsky, L., & Errandonea, D. (2019). In situ characterization of the high pressure – high temperature melting curve of platinum. Scientific Reports 9(1), 1–10. doi:10.1038/s41598-019-49676-y

Bykov, M., Chariton, S., Fei, H., Fedotenko, T., Aprilis, G., Ponomareva, A. V., Tasnádi, F., Abrikosov, I. A., Merle, B., Feldner, P., Vogel, S., Schnick, W., Prakapenka, V. B., Greenberg, E., Hanfland, M., Pakhomova, A., Liermann, H. P., Katsura, T., Dubrovinskaia, N., & Dubrovinsky, L. (2019). High-pressure synthesis of ultraincompressible hard rhenium nitride pernitride $Re_2(N_2)(N)_2$ stable at ambient conditions. Nature Communications, 10, 1–8. doi:10.1038/s41467-019-10995-3

Bykova, E., Dubrovinsky, L., Dubrovinskaia, N., Bykov, M., McCammon, C., Ovsyannikov, S. V., Liermann, H. P., Kupenko, I., Chumakov, A. I., Rüffer, R., Hanfland, M., & Prakapenka, V. (2016). Structural complexity of simple $Fe_2O_3$ at high pressures and temperatures. Nature Communications, 7, 1–6. doi:10.1038/ncomms10661

Celestre, R., Berujon, S., Roth, T., Del Rio, M. S., & Barrett, R. (2020). Modelling phase imperfections in compound refractive lenses. Journal of Synchrotron Radiation, 27, 305–318. doi:10.1107/S1600577519017235

Chevallier, R., Laruelle, P., & Flahaut, J. (1967). Structure cristallographique $Yb_3S_4$. Bulletin de Minéralogie, 90, 564–574. doi:10.3406/BULMI.1967.6045

Dewaele, A., Loubeyre, P., Occelli, F., Marie, O., & Mezouar, M. (2018). Toroidal diamond anvil cell for detailed measurements under extreme static pressures. Nature Communications, 9, 1–9. doi:10.1038/s41467-018-05294-2

Dobson, D. P., & Brodholt, J. P. (2005). Subducted banded iron formations as a source of ultralow-velocity zones at the core–mantle boundary. Nature, 434, 371–374. doi:10.1038/nature03430

Dolomanov, O. V., Bourhis, L. J., Gildea, R. J., Howard, J. A. K., & Puschmann, H. (2009). OLEX2: A complete structure solution, refinement and analysis program. Journal of Applied Crystallography, 42, 339–341. doi:10.1107/S0021889808042726

Dorfman, S. M., Prakapenka, V. B., Meng, Y., & Duffy, T. S. (2012). Intercomparison of pressure standards (Au, Pt, Mo, MgO, NaCl and Ne) to 2.5 Mbar. Journal of Geophysical Research: Solid Earth, 117, 8210. doi:10.1029/2012JB009292

Dubrovinskaia, N., Dubrovinsky, L., Solopova, N. A., Abakumov, A., Turner, S., Hanfland, M., Bykova, E., Bykov, M., Prescher, C., Prakapenka, V. B., Petitgirard, S., Chuvashova, I., Gasharova, B., Mathis, Y. L., Ershov, P., Snigireva, I., & Snigirev, A. (2016). Terapascal static pressure generation with ultrahigh yield strength nanodiamond. Science Advances, 2, e1600341. doi:10.1126/sciadv.1600341

Dubrovinsky, L., Dubrovinskaia, N., Bykova, E., Bykov, M., Prakapenka, V., Prescher, C., Glazyrin, K., Liermann, H.-P., Hanfland, M., Ekholm, M., Feng, Q., Pourovskii, L. V., Katsnelson, M. I., Wills, J. M., & Abrikosov, I. A. (2015). The most incompressible metal osmium at static pressures above 750 gigapascals. Nature, 525, 226–229. doi:10.1038/nature14681

Dubrovinsky, Leonid, Dubrovinskaia, N., Prakapenka, V. B., & Abakumov, A. M. (2012). Implementation of micro-ball nanodiamond anvils for high-pressure studies above 6 Mbar. Nature Communications, 3, 1–7. doi:10.1038/ncomms2160

Errandonea, D., Burakovsky, L., Preston, D. L., MacLeod, S. G., Santamaría-Perez, D., Chen, S., Cynn, H., Simak, S. I., McMahon, M. I., Proctor, J. E., & Mezouar, M. (2020). Experimental and theoretical confirmation of an orthorhombic phase transition in niobium at high pressure and temperature. Communications Materials, 1, 1–11. doi:10.1038/s43246-020-00058-2

Falkenberg, G., Seiboth, F., Kock, F., Falch, K. V., Schropp, A. Bruckner, D., Garrevoet, J. (2020) CRL optics and silicon drift detector for P06 Microprobe experiments at 35 keV, Journal of Powder Diffraction, 35, S34-S37, doi: 10.1017/S0885715620000536

Fedotenko, T., Dubrovinsky, L., Aprilis, G., Koemets, E., Snigirev, A., Snigireva, I., Barannikov, A., Ershov, P., Cova, F., Hanfland, M., & Dubrovinskaia, N. (2019). Laser heating setup for diamond anvil cells for in situ synchrotron and in house high and ultra-high pressure studies. Review of Scientific Instruments, 90, 104501. doi:10.1063/1.5117786

Fei, Y., Ricolleau, A., Frank, M., Mibe, K., Shen, G., & Prakapenka, V. (2007). Toward an internally consistent pressure scale. Proceedings of the National Academy of Sciences, 104, 9182–9186. doi:10.1073/pnas.0609013104

Fei, Y., Seagle, C. T., Townsend, J. P., McCoy, C. A., Boujibar, A., Driscoll, P., Shulenburger, L., & Furnish, M. D. (2021). Melting and density of $MgSiO_3$ determined by shock compression of bridgmanite to 1254GPa. Nature Communications, 12, 1–9. doi:10.1038/s41467-021-21170-y

Friedrich, A., Collings, I. E., Dziubek, K. F., Fanetti, S., Radacki, K., Ruiz-Fuertes, J., Pellicer-Porres, J., Hanfland, M., Sieh, D., Bini, R., Clark, S. J., & Marder, T. B. (2020). Pressure-Induced Polymerization of Polycyclic Arene-Perfluoroarene Cocrystals: Single Crystal X-ray Diffraction Studies, Reaction Kinetics, and Design of Columnar Hydrofluorocarbons. Journal of the American Chemical Society, 142, 18907–18923. doi:10.1021/jacs.0c09021

Grosu, Y., Faik, A., Ortega-Fernández, I., & D'Aguanno, B. (2017). Natural Magnetite for thermal energy storage: Excellent thermophysical properties, reversible latent heat transition and controlled thermal conductivity. Solar Energy Materials and Solar Cells, 161, 170–176. doi:10.1016/j.solmat.2016.12.006

Huang, H., & Xu, J. Y. (2019). Effect of magnetite on concrete mechanics and microwave deicing performance. IOP Conference Series: Earth and Environmental Science, 267, 042019. doi:10.1088/1755-1315/267/4/042019

Jenei, Z., O'Bannon, E. F., Weir, S. T., Cynn, H., Lipp, M. J., & Evans, W. J. (2018). Single crystal toroidal diamond anvils for high pressure experiments beyond 5 megabar. Nature Communications, 9, 1–6. doi:10.1038/s41467-018-06071-x

Kantor, I., Prakapenka, V., Kantor, A., Dera, P., Kurnosov, A., Sinogeikin, S., Dubrovinskaia, N.,

& Dubrovinsky, L. (2012). BX90: A new diamond anvil cell design for X-ray diffraction and optical measurements. Review of Scientific Instruments, 83, 125102. doi:10.1063/1.4768541

Kawamura, H., Akahama, Y., Umemoto, S., Takemura, K., Ohishi, Y., & Shimomura, O. (2002). X-ray powder diffraction from solid deuterium. Journal of Physics: Condensed Matter, 14, 10407. doi:10.1088/0953-8984/14/44/301

Khandarkhaeva, S., Fedotenko, T., Bykov, M., Bykova, E., Chariton, S., Sedmak, P., Glazyrin, K., Prakapenka, V., Dubrovinskaia, N., & Dubrovinsky, L. (2020). Novel Rhenium Carbides at 200 GPa. European Journal of Inorganic Chemistry, 22, 2186–2190. doi:10.1002/ejic.202000252

Kurnosov, A., Kantor, I., Boffa-Ballaran, T., Lindhardt, S., Dubrovinsky, L., Kuznetsov, A., & Zehnder, B. H. (2008). A novel gas-loading system for mechanically closing of various types of diamond anvil cells. Review of Scientific Instruments, 79, 045110. doi:10.1063/1.2902506

Laniel, D., Winkler, B., Bykova, E., Fedotenko, T., Chariton, S., Milman, V., Bykov, M., Prakapenka, V., Dubrovinsky, L., & Dubrovinskaia, N. (2020). Novel sulfur hydrides synthesized at extreme conditions. Physical Review B, 102, 134109. doi:10.1103/PhysRevB.102.134109

Lengeler, B., Schroer, C. G., Kuhlmann, M., Benner, B., Günzler, T. F., Kurapova, O., Zontone, F., Snigirev, A., & Snigireva, I. (2005). Refractive X-ray lenses. Journal of Physics D: Applied Physics, 38, A218. doi:10.1088/0022-3727/38/10A/042

Liermann, H.-P., Konôpková, Z., Morgenroth, W., Glazyrin, K., Bednarčik, J., McBride, E. E., Petitgirard, S., Delitz, J. T., Wendt, M., Bican, Y., Ehnes, A., Schwark, I., Rothkirch, A., Tischer, M., Heuer, J., Schulte-Schrepping, H., Kracht, T., & Franz, H. (2015). The Extreme Conditions Beamline P02.2 and the Extreme Conditions Science Infrastructure at PETRA III. Journal of Synchrotron Radiation, 22, 908–924. doi:10.1107/S1600577515005937

Matos, M., Hoffmann, R., Latgé, A. and Anda, E. V. (1996). Warwickites: Electronic Structure and Bonding. Chemistry of Materials, 8, 2324–2330. doi:10.1021/CM9601392

McMahon, M. (2018). Diamond sculpting pushes extremes. In Nature Materials (Vol. 17, Issue 10, pp. 858–859). Nature Publishing Group. doi:10.1038/s41563-018-0177-3

Palmer, D. C. (2014). CrystalMaker. CrystalMaker Software Ltd.

Petricek, V., Dusek, M., & Palatinus, L. (2006). JANA2006. The crystallographic computing

system.

Rigaku Crysalis Pro v. 171.40. (2020). CrysAlis PRO.

Schroer, C., Agapov, I., Roehlsberger, R., Wanzenberg, R., Brinkmann, R., Weckert, E., & Leemans, W. (2019). PETRA IV: Upgrade of PETRA III to the Ultimate 3D X-ray Microscope - Conceptual Design Report (CDR). url:https://bib-pubdb1.desy.de/record/426140

Seiboth, F., Bruckner, D., Kahnt, M., Lyubomirskiy, M., Wittwer, F., Dzhigaev, D., Ullsperger, T., Nolte, S., Koch, F., David, C., Garrevoet, J., Falkenberg, G., & Schroer, C. G. (2020). Hard X-ray wavefront correction via refractive phase plates made by additive and subtractive fabrication techniques. Journal of Synchrotron Radiation, 27(5), 1121–1130. doi:10.1107/S1600577520007900

Seiboth, F., Kahnt, M., Scholz, M., Seyrich, M., Wittwer, F., Garrevoet, J., Falkenberg, G., Schropp, A., & Schroer, C. G. (2016). Quantitative characterization of aberrations in X-ray optics. In A. M. Khounsary, S. Goto, & C. Morawe (Eds.), Advances in X-ray/EUV Optics and Components XI (Vol. 9963, Issue 15, p. 99630P). SPIE. doi:10.1117/12.2237646

Seiboth, F., Schropp, A., Scholz, M., Wittwer, F., Rödel, C., Wünsche, M., Ullsperger, T., Nolte, S., Rahomäki, J., Parfeniukas, K., Giakoumidis, S., Vogt, U., Wagner, U., Rau, C., Boesenberg, U., Garrevoet, J., Falkenberg, G., Galtier, E. C., Ja Lee, H., Schroer, C. G. (2017). Perfect X-ray focusing via fitting corrective glasses to aberrated optics. Nature Communications, 8, 1–5. doi:10.1038/ncomms14623

Sheldrick, G. M. (2008). A short history of SHELX. In Acta Crystallographica Section A: Foundations of Crystallography, 64, 112–122. International Union of Crystallography. doi:10.1107/S0108767307043930

Sheldrick, G. M. (2015). SHELXT - Integrated space-group and crystal-structure determination. Acta Crystallographica Section A: Foundations of Crystallography, 71, 3–8. doi:10.1107/S2053273314026370

Tateno, S., Hirose, K., Ohishi, Y., & Tatsumi, Y. (2010). The Structure of Iron in Earth's Inner Core. Science, 330, 359–361. doi:10.1126/science.1194662

Vasiukov, D. (2018). Iron electronic states in minerals of the Earth's mantle. PhD Thesis.

urn:nbn:de:bvb:703-epub-3797-7

Wang, Y., Chen, Q., Li, N., Cheng, J.-M., Li, C.-G., Li, H., Long, Q.-H., Shi, J.-S., Deng, J.-J., Experimental Comparison of Various Techniques for Spot Size Measurement of High-Energy X-Ray, Chinese Phys. C 40, 086205 (2016).

# Chapter 5 Structural diversity of magnetite and products of its decomposition at extreme conditions

*Saiana Khandarkhaeva,[1,2*] Timofey Fedotenko,[2] Stella Chariton,[3] Elena Bykova,[4] Sergey Ovsyannikov,[1,5] Konstantin Glazyrin,[6] Hanns-Peter Liermann,[6] Vitali Prakapenka,[3] Natalia Dubrovinskaia[2,7] and Leonid Dubrovinsky[1]*

[1]*Bayerisches Geoinstitut, University of Bayreuth, Universitätstraße 30, 95440 Bayreuth, Germany*

[2]*Material Physics and Technology at Extreme Conditions, Laboratory of Crystallography, University of Bayreuth, Universitätstraße 30, 95440 Bayreuth, Germany*

[3]*Center for Advanced Radiation Sources, University of Chicago, 5640 S. Ellis, 60637 Chicago, Illinois, USA*

[4]*Geophysical Laboratory, Carnegie Institution of Washington, 5251 Broad Branch Road NW, 20015 Washington, District of Columbia, USA*

[5]*Institute for Solid State Chemistry of Ural Branch of Russian Academy of Sciences, 91 Pervomayskaya Str., Yekaterinburg 620219, Russia*

[5]*Deutsches Elektronen-Synchrotron, Notkestraße 85, 22607 Hamburg, Germany*

[7]*Theoretical Physics Division, Department of Physics, Chemistry and Biology (IFM), Linköping University, SE-581 83, Linköping, Sweden*

*Inorg. Chem.* **2022**, *61* (2), 1091–1101. https://doi.org/10.1021/acs.inorgchem.1c03258.

## Abstract

Magnetite, $Fe_3O_4$, is the oldest known magnetic mineral and archetypal mixed-valence oxide. Despite its recognized role in deep Earth processes, the behavior of magnetite at extreme high-pressure high-temperature (HPHT) conditions remains insufficiently studied. Here we report on single-crystal synchrotron X-ray diffraction experiments up to ~80 GPa and 5000 K in diamond anvil cells, which reveal two previously unknown $Fe_3O_4$ polymorphs, γ-$Fe_3O_4$ with the orthorhombic $Yb_3S_4$-type structure and δ-$Fe_3O_4$ with the modified $Th_3P_4$-type structure. The latter has never been predicted for iron compounds. The decomposition of $Fe_3O_4$ at HPHT conditions was found to result in the formation of exotic phases, $Fe_5O_7$ and $Fe_{25}O_{32}$, with complex structures.

Crystal-chemical analysis of iron oxides suggests the high-spin to low-spin crossover in octahedrally coordinated $Fe^{3+}$ in the pressure interval between 43 and 51 GPa. Our experiments demonstrate that HPHT conditions promote the formation of ferric-rich Fe-O compounds, thus arguing for the possible involvement of magnetite in the deep oxygen cycle.

## Introduction

Transition metal (TM) mixed valence compounds are in focus of active fundamental and applied research in solid state physics, chemistry, and materials sciences. A number of important phenomena, like high-$T_C$ superconductivity in doped copper-oxides[1], superconductivity in iron-based materials[2] , and the *giant* magneto-resistance effects in doped manganese oxides[3], have been discovered in TM complex oxides. Iron, an archetypal transition metal, is the most widespread TM element, contributing ~35% in mass to Earth's composition. Its chemistry (and geochemistry) is critical for understanding of processes of formation of Earth (and super-Earths), dynamics of core and mantle, formation and evolution of atmosphere, origin of life and development of biosphere.

Recent studies discovered a variety of complex Fe-O compounds with unusual crystal structures and intriguing properties, formed at moderate pressures and temperatures ($Fe_4O_5$[4,5], $Fe_5O_6$[6,7], $Fe_5O_7$[8], $Fe_{6.32}O_9$[9], $Fe_7O_9$[10], $Fe_7O_{10}$[9], $Fe_{13}O_{19}$[11], $Fe_{25}O_{32}$[8], $FeO_2$[12,13]). Magnetite ($Fe_3O_4$) attracts continuous attention and many aspects of its behavior at variable temperatures and pressures remain puzzling. At ambient conditions, magnetite adopts an inverse spinel structure (Figure. 1a) with $Fe^{3+}$ ions in tetrahedral sites and a mixture of the $Fe^{3+}$ and $Fe^{2+}$ ions in equal proportion in the sites with octahedral oxygen coordination[14] (Figure. 1a). At ambient conditions magnetite is semi-metal, but upon cooling below ~125 K it undergoes a phase transition into the insulator state (discovered by Verwey in 1939)[15]. As $Fe_3O_4$ contains $Fe^{2+}$ and $Fe^{3+}$ ions, its high electrical conductivity at ambient conditions and insulator state below the Verwey transition temperature was attributed[16] to the charge transfer or ordering, respectively. Only recently, more than 70 years after Verwey's discovery, the elusive charge-ordering pattern in the low-temperature phase of $Fe_3O_4$ was solved using single-crystal X-ray diffraction, and the charge ordering in magnetite was found to involve formation of trimerons[17,18]. The same effect was observed recently for high-pressure phases of $Fe_4O_5$[5] and $Fe_5O_6$[7]; in the latter, the Verwey-type transition was found

at atmospheric pressure and temperature close to ambient that opens perspectives for its practical applications.

Due to its importance as geomaterial and as typical example for TM oxides, $Fe_3O_4$ was intensively investigated at high pressures. Upon compression up to ~25 GPa at room temperature, magnetite (further also called α-$Fe_3O_4$) undergoes structural phase transition to a "post-spinel phase" (sometimes also called "HP-$Fe_3O_4$", which we designate further as β-$Fe_3O_4$, (Figure. 1b))[19]. The transition is associated with significant changes of magnetic and electrical properties[20–22]. Kinetics of the phase transition strongly depends on temperature[23–25] (Figure 4). Decades of highly controversial history of structural studies of β-$Fe_3O_4$ ended up with the general consensus that the phase adopts the $CaTi_2O_4$-type structure[8,26–28] (Figure 1b, 2a). Yet another phase transformation of β-$Fe_3O_4$ upon laser heating (between approximately 1500 to 2000 K) at pressures from 64 to 73 GPa was reported[28,29]. Powder diffraction data were interpreted as formation of an orthorhombic phase with the $CaFe_2O_4$-type structure (Figure 2b). However, assignment of a space group and interpretation of the diffraction data remain ambiguous and call for further investigations.

The stability of β-$Fe_3O_4$ at high pressure is a widely debated problem. It is especially important due to (at least) two reasons: (a) buffers involving magnetite (or its high-pressure polymorphs) are expected to control many processes in Earth's interiors, including diamonds formation[23,30]; (b) magnetite (together with hematite and some other iron-bearing minerals) is a major component of banded iron formations (BIFs) which, as believed, have been subducted into Earth's mantle and may thus play a significant role in the planetary oxygen cycle[8,31]. Lazor et al.[32] predicted breakdown of $Fe_3O_4$ into FeO and $Fe_2O_3$ at ~50 GPa based on thermodynamic calculations. It was noted that at these conditions β-$Fe_3O_4$ has lower density than the sum of volumes of cubic $Fe_xO$ and $Rh_2O_3$-II-structured ι-$Fe_2O_3$[32]. However, justification of this hypothesis is strongly dependent on equations of state used for volume determination of relevant phases and exact composition of $Fe_xO$ component. Moreover, in the case of ferric spinels, like $Fe_3O_4$, this scenario could be inconclusive due to partial reduction of $Fe^{3+}$ to $Fe^{2+}$ during the high-pressure high-temperature treatment[26]. Indeed, according to a recent report[4], laser heating of $Fe_3O_4$ at ~80 GPa and 2950 K leads to the formation of $Fe_{25}O_{32}$, a phase, containing more ferrous iron than the starting material[8]. Summarizing the brief overview of the state-of-the-art, there are two main problems associated with the behavior of $Fe_3O_4$ at high-pressures and high-temperatures: (a) not all possible phases of $Fe_3O_4$ as well as their crystal structures (and crystal chemistry) are

established, and (b) chemical stability of the oxide is insufficiently studied, as PT conditions of its decomposition and products of reactions have not been fully characterized. Here we report the results of high-pressure high-temperature studies of $Fe_3O_4$ at pressures ~80 GPa and temperatures up to 5000 K performed in a laser-heated diamond anvil cell (LHDAC). Based on single crystal X-ray diffraction (SCXRD) data we established crystal structures of two different high-pressure $Fe_3O_4$ polymorphs, including one with the modified $Th_3P_4$-type structure, never before predicted or considered for iron oxides.

We found that $Fe_3O_4$ undergoes a series of structural and chemical transformations in the studied pressure range at temperatures above ~2400 K. Our data shows that $Fe_3O_4$ demonstrates rich structural polymorphism: different structures are built of infinite octahedral ribbons comprised of the different number of adjacent rows of $FeO_6$ octahedra. Crystal-chemical analysis of $Fe_3O_4$ polymorphs, $Fe_5O_7$, and $Fe_{25}O_{32}$ (the last two compounds are products of decomposition of the starting $Fe_3O_4$ material) reveals signatures of high-spin-to-low-spin crossover in octahedrally coordinated iron in some of the phases with a significant $Fe^{3+}$ content at pressures between 43-51 GPa. Our experiments suggest involvement of magnetite in the deep oxygen cycle and promotion of the formation of ferric-rich compounds at high pressures and temperatures (potentially even in the presence of pure iron).

The paper is organized as follows: first, we describe novel phases of $Fe_3O_4$; then we report observations on phase relations and chemical transformations of $Fe_3O_4$ at high pressures and temperatures; later we consequently discuss crystal-chemistry of novel iron oxides, the spin state of iron, chemical stability of $Fe_3O_4$, and possible implications of our findings for solid state physics, chemistry, and geosciences.

## Experiment

*Sample preparation*. Single crystals of magnetite $Fe_3O_4$ ($Fd\bar{3}m$) were grown by means of HPHT technique at 9.5 GPa and 1100 °C in a 1200-t Sumitomo press at Bayerisches Geoinstitut (BGI, Bayreuth, Germany). Single crystals with an average size of $0.01^{x}0.01^{x}0.005$ $mm^3$ were preselected on a three-circle Bruker diffractometer equipped with a SMART APEX CCD detector and a high-brilliance Rigaku rotating anode (Rotor Flex FR-D, Ag-Kα radiation) with Osmic

focusing X-ray optics. Selected crystals were loaded into BX90-type DACs[33]. Neon, served as a pressure transmitting medium, was loaded at~ 1.2 kbar using the high-pressure gas-loading setup, installed at BGI[34]. The sample was laser heated from both sides using a tightly focused NIR laser beam (1070 nm, 5 μm FWHM in diameter) in a continuous mode during 3-5 seconds at temperatures of 2700(200) K and 4800(300) K[35].

*Synchrotron X-ray diffraction*. The single-crystal X-ray diffraction experiments were conducted on the Extreme Conditions Beamline P02.2 at PETRA III, Hamburg, Germany (PerkinElmer XRD1621 flat panel detector, wavelength λ=0.2895 Å, beam size ~1.5×1.7 $\mu m^2$); on the 13-IDD beamline at the Advanced Photon source (APS), Chicago, USA (λ = 0.2952 Å, beam size ~3 × 3 $\mu m^2$, Pilatus CdTe 1 M detector). For the single-crystal XRD measurements DACs were rotated around a vertical ω-axis in a range ±38˚. The diffraction images were collected with an angular step Δω = 0.5˚.

*Data analysis*. In case of powder diffraction studies, calibration of instrument model and integration of diffraction patterns were made in the DIOPTAS[36] software using $CeO_2$ powder standard (NIST SRM 674b). Integrated patterns from powder XRD experiments were processed using the Le Bail technique implemented in JANA2006[37] software. X-ray diffraction imaging of the sample chamber was reconstructed using XDI[38] program. In case of SCXRD, integration of the reflection intensities and absorption corrections were performed in CrysAlisPro software[39]. A single crystal of orthoenstatite $(Mg_{1.93},Fe_{0.06})(Si_{1.93},Al_{0.06})O_6$ (space group *Pbca*, a=8.8117(2) Å, b=5.18320(10) Å, c=18.2391(3) Å) was used as calibration standard for refinement of the instrument model of the diffractometer. Detailed information of integration parameters as well as about the data reduction output files and indicators of the XRD data quality are given in ref.[40]. The crystal structures were solved using SHELXT[41] or superfilp method in JANA2006 and Olex2[37,41,42]. Crystal structures were refined by least-squares minimization of adjustable parameters. We performed anisotropic refinement of atomic displacement parameters only for Fe atoms due to limited dataset collected in DAC. Reflections coming from parasite diffraction produced by diamonds and crystallized pressure media were eliminated during the refinement procedure. The “Diamond” software[43] was used for the visualization of molecular graphics.

## Results

### Novel high-pressure phases of $Fe_3O_4$

*Crystal structure of the γ-$Fe_3O_4$ (orthorhombic "post-post spinel") phase observed at ~80 GPa*

Previous studies reported the formation of a new orthorhombic $Fe_3O_4$ polymorph at pressures 64-73 GPa upon heating at 1500-2000 K[28,29]. Indeed, laser heating of $Fe_3O_4$ at 2700(200) K and 78(1) GPa (Supporting Information Figure S1, Table S1) resulted in formation of the orthorhombic phase (space group *Pnma*, *a*=8.574(10) Å, *b*=2.6356(13) Å, *c*=8.761(3) Å) (Figure 1c, Supporting Information Tables S2, S3). Our SCXRD data collected at room temperature reveal that at 78(1) GPa γ-$Fe_3O_4$ crystalizes in a structure which is different from the previously proposed $CaFe_2O_4$-type (Figure 2b). In γ-$Fe_3O_4$ two iron atoms, Fe(1) and Fe(3), have octahedral oxygen environment with average <Fe-O> distances ~1.84 Å and ~1.83 Å, respectively (Figure 3a, Supporting Table S4). Considering the shape of the polyhedra and interatomic distances, the Fe(1) and Fe(3) atoms may be identified as low-spin ferric[8,13]. The Fe(2) atoms, identified as ferrous, occupy capped trigonal prisms where one of the oxygen atoms is slightly further away than the other six (~2.02 Å versus ~1.97 Å at 78(1) GPa) (Figure 3a, Supporting Table S4). The distorted octahedra share edges to form "ribbons", which are one octahedron thick and four octahedra wide (Figure 2c). Ribbons are linked to each other by *a* and *n* glides in [001] and [100] directions, respectively. The structure of orthorhombic γ-$Fe_3O_4$ belongs to the $Yb_3S_4$ type[44].

*Crystal structure of tetragonal δ-$Fe_3O_4$ phase observed at ~80 GPa*

Laser heating of $Fe_3O_4$ up to 4800(300) K at 78(1) GPa was conducted at BGI (Bayreuth, Germany) (Supporting Information FigureS1, Table S1). The approximate duration of heating was ~10-15 seconds. X-ray diffraction data collected on the temperature quenched material at the P02.2 extreme condition beamline at PETRA III (DESY, Hamburg, Germany), reveal a tetragonal unit cell with the lattice parameters *a*=5.8648(1) Å and *c*=5.948(2) Å (Figure 1d, Supporting Information Table S2). For the crystalline domains of the best quality, the inspection of systematic absences (Supporting Information Figure S2a) suggests a body-centered unit cell. Integration of the data, collected from one of the single-crystalline domains, resulted in a dataset containing 403 reflections with $I > 2\sigma(I)$ and $R_{int}$=3.3%. Structure solution and refinement in the $I\bar{4}2d$ space group gave $Fe_3O_4$ stoichiometry with R1=8.8% in an anisotropic approximation for Fe atoms. Inspection

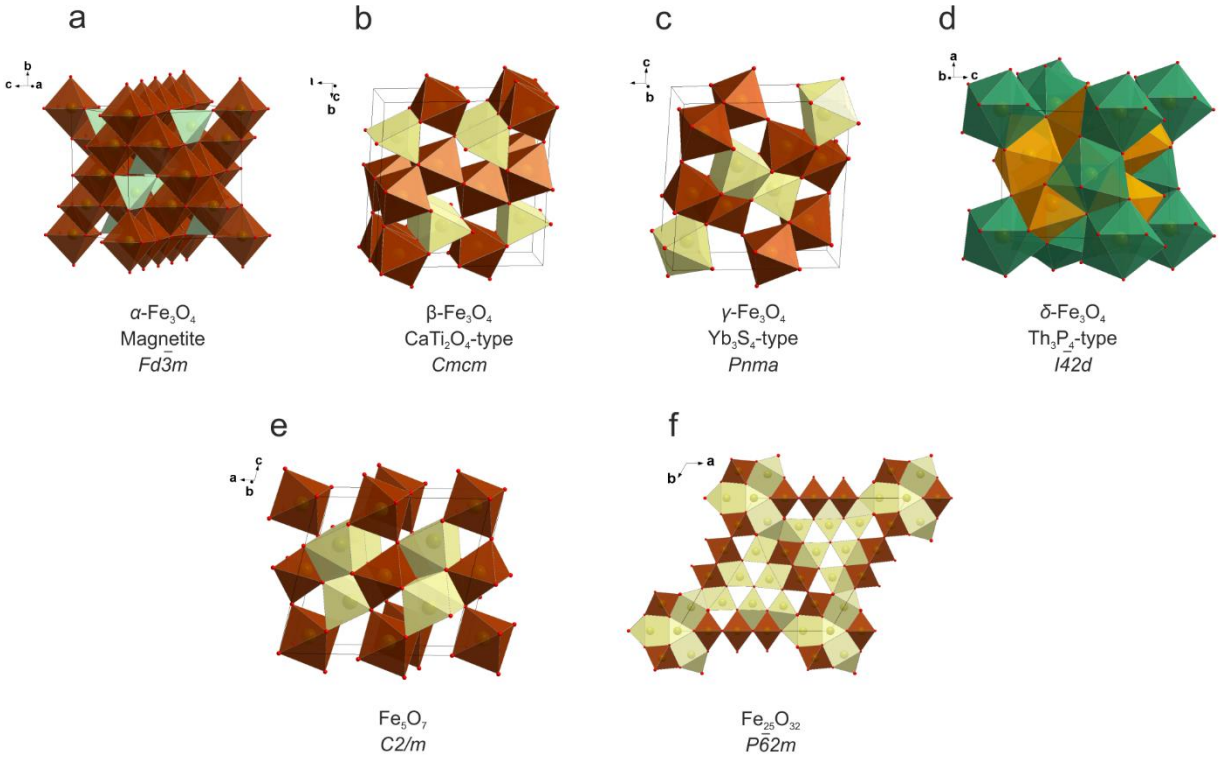


***Figure 1. Crystal structures of iron oxides observed in the present study***. *(a) α-$Fe_3O_4$, magnetite (inverse spinel type of structure, space group* $Fd\bar{3}m$*); (b) β-$Fe_3O_4$ ($CaTi_2O_4$-type, space group Cmcm); (c) γ-$Fe_3O_4$ ($Yb_3S_4$-type, space group Pnma); (d) δ-$Fe_3O_4$ ($Th_3P_4$-type, space group* $I\bar{4}2d$*) (e) $Fe_5O_7$; and (f) $Fe_{25}O_{32}$. The structure type (if known) and the space group are notated under the structure drawings. Different kinds of iron polyhedra are shown in different colors: light turquoise color designates $FeO_4$ tetrahedra; $FeO_6$ octahedra are shown by brown color; $FeO_6$ trigonal and $FeO_7$ caped trigonal prisms are designated by citron color; $FeO_8$ diagonal gyrobianticupola and snub disphenoids in the crystal structure of δ-$Fe_3O_4$ are represented by green and orange color, respectively.*

of the diffraction data from other single-crystalline grains revealed the reflections with indexes violating *I*-centering (Supporting Information Figure S2b). Although the number of such reflections, forbidden for the *I*-centered lattice, is small (within ~5-8% of all) and they all are of low intensities. For the domains of the best quality, it is still possible to solve and refine the structure in $P\bar{4}$ space group (to R1=13.7%), and confirm the $Fe_3O_4$ stoichiometry of this phase. Fractional atomic coordinates resulted from SCXRD refinements are summarized in the Supporting Information Tables S5 and S6 for $I\bar{4}2d$ and $P\bar{4}$ space groups, respectively. It is possible that $I\bar{4}2d$ and $P\bar{4}$ phases are indeed two different tetragonal $Fe_3O_4$ phases, as in a laser-

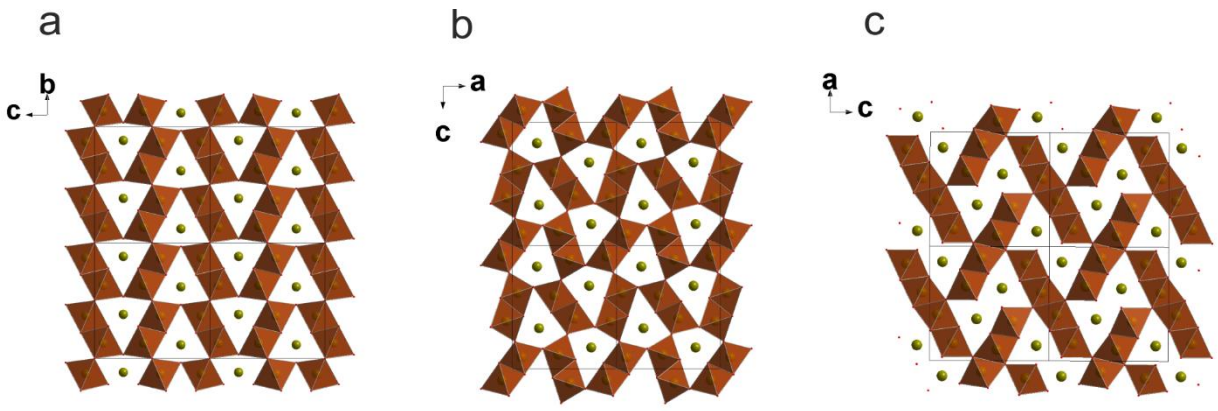


***Figure 2. Arrangement of octahedra in crystal structures of three orthorhombic high-pressure $Fe_3O_4$ polymorphs**: (a) β-$Fe_3O_4$, $CaTi_2O_4$-type, space group Cmcm [26,27], (b) hypothetic $CaFe_2O_4$-type, space group Pnma[28,29], and (c) γ-$Fe_3O_4$, $Yb_3S_4$-type, space group Pnma. $FeO_6$ octahedra are brown, green balls are iron atoms located in channels formed by octahedra, small red dots are oxygen atoms.*

heated DAC various sample spots could be heated differently. The phase with body-centered unit cell ($I\bar{4}2d$) appears upon heating at relatively low temperatures (~2400-2800 K), and another, which has more distorted primitive unit cell ($P\bar{4}$ - after heating at temperatures above ~4500 K (Supporting Information Table S1). Anyway, further on, we will designate the tetragonal iron oxide as δ-$Fe_3O_4$.

Prolonged (of about an hour) laser heating of $Fe_3O_4$ at about 3800(500) K at 78(2) GPa leads to formation of an even more distorted monoclinic phase (space group *I2*). SCXRD data, collected for this phase are not of sufficient quality to solve and refine its structure, but the lattice parameters were refined based on powder XRD data collected on the temperature-quenched sample and are equal to *a*=6.103(1) Å, b=5.787(1), *c*=5.958(1) Å, β=91.73(1)˚, and V=210.33(1) $Å^3$ at 78(1) GPa (Supporting Information Figure S3); fractional atomic coordinates of the model used for Le Bail fit of powder XRD data are given in Supporting Information Table S7. Notably, that the unit cell volume of the monoclinic phase is significantly higher than of tetragonal δ-$Fe_3O_4$, 210.33(1) $Å^3$ versus 204.34(16) $Å^3$ at 78(1) GPa. It can be associated with a partial reduction of $Fe^{3+}$ to larger-sized $Fe^{2+}$ that consequently increases the unit cell volume. Thus, this *I2*-phase is designated as δ-$Fe_3O_{4-\delta}$.

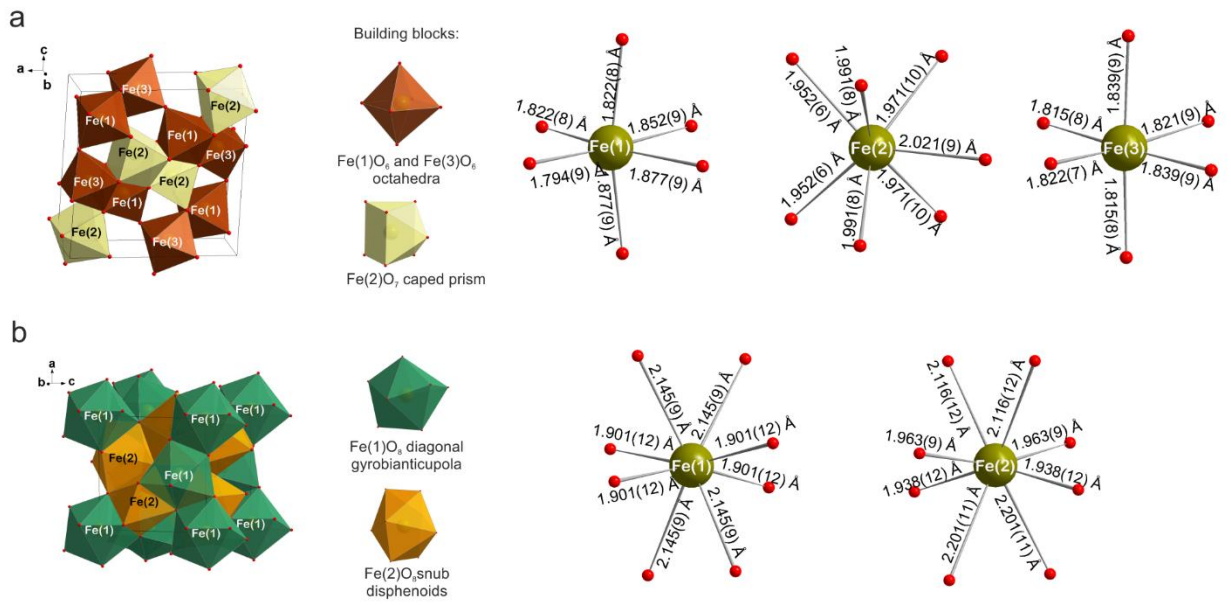


***Figure 3. Polyhedral models of the crystal structures of γ- $Fe_3O_4$ and δ-$Fe_3O_4$ and the environment of crystallographically distinct iron atoms in these polymorphs at 78(1) GPa and room temperature.*** *(a) γ-$Fe_3O_4$ with $Yb_3S_4$-type (space group Pnma); Fe(1) and Fe(3) atoms are octahedrally coordinated; Fe(2) atom occupies capped trigonal prism. (b) δ-$Fe_3O_4$ phase with the distorted $Th_3P_4$-type structure (space group $I\bar{4}2d$); two structurally distinct iron atoms form $FeO_8$ polyhedra (diagonal gyrobianticupola of Fe(1)$O_8$ and snub disphenoids of Fe(2)$O_8$).*

The structure of tetragonal δ-$Fe_3O_4$ is similar to a distorted $Th_3P_4$ -type[45] (Figure 1d). It is composed of two types of polyhedral – triangular dodecahedra $FeO_8$ of different geometry (diagonal gyrobianticupolas and snub disphenoids), whereas, in ideal cubic $Th_3P_4$, there is only one type of polyhedra (Figure 3b). Such building blocks are unusual for Fe-O compounds and potentially could be considered as intermediate forms between an octahedron and and a cube[46]. The Fe(1)$O_8$ polyhedra, connected through common edges, form zig-zag chains running along *a* and *b* directions. The chains are interconnected *via* Fe(2)$O_8$ triangular dodecahedra, which share common faces (Figure 3b). Both of the crystallographically distinct iron atoms are surrounded by four oxygen atoms at the distances of ~1.93 Å, and another four - at ~2.12 Å (the distances refer to the data at 78(1) GPa), see Figure 3b and Supporting Information Table S8. For the charge balance, it would be natural to suggest that Fe(1) (4 atoms per a unit cell) is ferrous, and Fe(2) (8

atoms per a unit cell) is ferric. However, the similarity in average Fe-O distances in both polyhedra suggests a mixed valence state for Fe in each structural position in δ-$Fe_3O_4$.

**Phase relations and stability of $Fe_3O_4$**

Summarizing our results and previous reports (see references[9,23–28,30,47,48]), we can list all $Fe_3O_4$ phases that are known to exist at pressures up to ~80 GPa: α-$Fe_3O_4$ (magnetite), β-$Fe_3O_4$ with the $CaTi_2O_4$-type structure, γ-$Fe_3O_4$ with the $Yb_3S_4$-type structure, and δ-$Fe_3O_4$ with the distorted $Th_3P_4$-type structure. Figure 4 presents a transformational phase diagram of $Fe_3O_4$ based on available literature data and the results of the present study.

The α- $Fe_3O_4$ to β-$Fe_3O_4$ transition was intensively studied (Figure 4)[23–26,28,32]. Although there are minor inconsistencies in reported P-T conditions for this transformation and departures from a correct description of the structure of β-$Fe_3O_4$, there is a consensus that β-$Fe_3O_4$ exists at pressures above ~15 GPa and up to at least 60 GPa in a wide temperature range up to ~2500 K (Figure 4). Our experiments have demonstrated the existence of the δ-$Fe_3O_4$ phase at 80 GPa and ~3700 K (*in situ* observations). The diffraction data, used to plot the data point for δ-$Fe_3O_4$ at ~4800 K and ~78 GPa, were collected from a temperature-quenched sample. Remarkably, δ-$Fe_3O_4$ was synthesized not only by direct heating of pure iron oxide, but also upon laser-heating of $(Mg_{0.3}Fe_{0.7})CO_3$ at ~61 GPa and temperatures above 2200 K (Supporting Information Table 1). In an experiment with ferromagnesite as a starting material, at pressures of ~60 GPa, δ-$Fe_3O_4$ co-exists with β-magnesio-ferrite $(Fe_{2.771}Mg_{0.229})O_4$ at temperatures up to ~2800 K (Figure 4, Supporting Information Table 9). There is no sign of Mg incorporation into the crystal structure of δ-$Fe_3O_4$. A comparison of our results with observations reported by Ricolleu and Fei[29] suggests that the phase boundary between post- and post-post-spinel phases, which they proposed, is, in fact, a boundary between the β-$Fe_3O_4$ and □-$Fe_3O_4$ phases.

Apart from phase transformations, we observed also chemical changes of $Fe_3O_4$ at P-T conditions highlighted by black rectangles in Figure 4. Annealing of $Fe_3O_4$ for a few seconds at

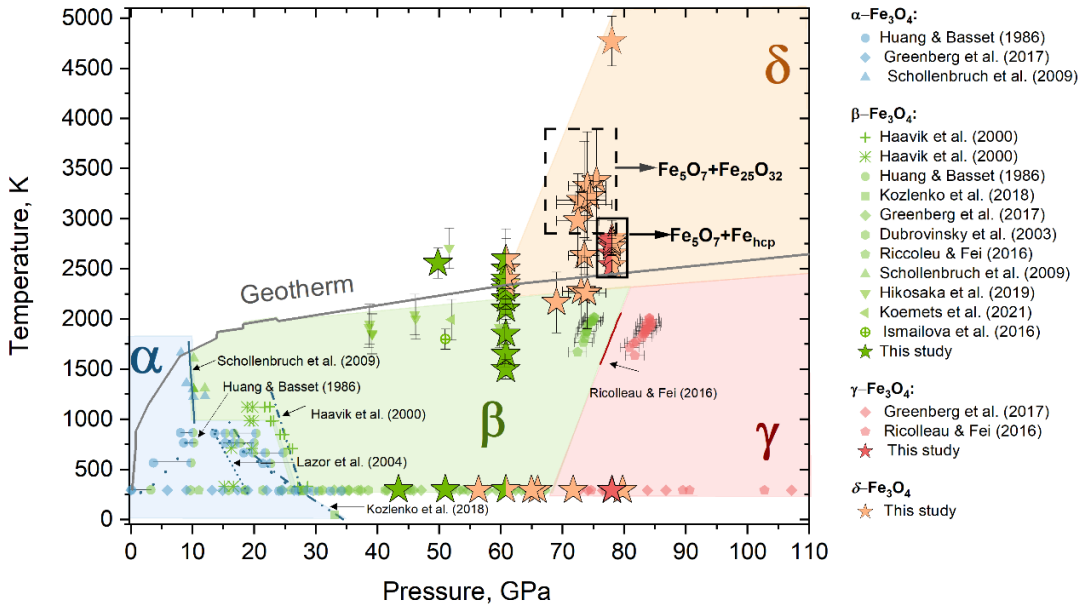


***Figure 4. Transformational phase diagram of $Fe_3O_4$ summarizing literature data (see references[9,23–28,30,47,48]) and the results of the present study (plotted as stars).*** *Grey line is the Earth's geotherm, as defined according to refs. [63,64] Dark blue lines separate the P-T fields of α-$Fe_3O_4$ and β-$Fe_3O_4$, according to refs.[23–26,32]. Solid red line is a phase boundary between β-$Fe_3O_4$ and γ-$Fe_3O_4$, determined in ref.[29]. Pressure-temperature conditions, at which different phases observed in this study, are shown by stars with error-bars (uncertainty in pressure are within the symbols' size). Colors of the stars correspond to β-$Fe_3O_4$ (green), γ-$Fe_3O_4$ (red), and δ-$Fe_3O_4$ (orange). Shared symbols represent coexisting phases. Solid and dotted rectangles show the areas where the partial decomposition of $Fe_3O_4$ was observed.*

2400–2800 K and 78(1) GPa leads to the appearance of new sharp spots on the diffraction pattern. The new peaks are indexed in the *C2/m* space group (*a*=8.646(4) Å, *b*=2.6183(5) Å, *c*=7.9508(17) Å, β=105.82(4)˚) (Supporting Information Table S10) and the structure solution results in the mixed-valence iron oxide with $Fe_5O_7$ stoichiometry[8]. Careful analysis of a 2D XRD map, which was collected from the sample area around the heated spot, reveals additional reflections corresponding to *hcp*-Fe (Supporting Information Figure S4). Full-profile analysis (Le-Bail fit) of the integrated X-ray diffraction patterns (Supporting Information Figure S4) gives the lattice parameters of *hcp*-Fe to be *a*=2.3238(8) Å, *c*=3.7001(5) Å, and V= 17.303(1) $Å^3$, that, according to the equation of state reported in ref.[49], corresponds to 83(2) GPa. Reflections of *hcp*-Fe were followed on decompression down to 65 GPa (Supporting Information Table S11).

Heating of $Fe_3O_4$ up to 4800(300) K at 78(1) GPa resulted in formation of two phases – the monoclinic $Fe_5O_7$ described above and the hexagonal $Fe_{25}O_{32}$ (space group *P*-62*m*, *a*=13.626 (3) Å, *c*=2.6598 (7) Å, Supporting Information Table S10). Continuous heating at temperatures ~3800 K resulted in an increasing amount of transformed material, while the quality of single-crystal domains of $Fe_3O_4$ phases deteriorated rapidly. These observations indicate that $Fe_5O_7$ and $Fe_{25}O_{32}$ form in expense of $Fe_3O_4$. Bykova et al.[8] reported formation of $Fe_{25}O_{32}$ as a result of heating of $Fe_3O_4$ at 80 GPa and 2950 K[8], which is probably the lowest temperature required for the synthesis of $Fe_{25}O_{32}$ at this pressure.

Once synthesized, $Fe_5O_7$ and $Fe_{25}O_{32}$ can be decompressed down to ~10 GPa (Figure 5), but for $Fe_{25}O_{32}$ single-crystal XRD data were collected only to ~40 GPa). Resulted pressure-volume (*PV*) data (Supporting Information Tables S12, S13) have been fitted with the second order Birch–Murnaghan equation of state (see Table 1) with the following parameters: up to 41 GPa - $V_0$=230.1(8) Å$^3$, $K_0$=221(9) GPa, and $V_{51GPa}$=184.4(3) Å$^3$, $K_{51GPa}$=359(12) GPa for $Fe_5O_7$; $V_{40GPa}$=457(1) Å$^3$, $K_{40GPa}$=322(15) GPa for $Fe_{25}O_{32}$ and $V_{51\,GPa}$=217.5(6) Å$^3$, $K_{51\,GPa}$=363(22) GPa for δ-$Fe_3O_4$ (Supporting Information Table S14).

## Discussion

*Crystal-chemistry of novel iron oxides.* The $CaTi_2O_4$-type of β-$Fe_3O_4$ can be considered as derived from NaCl (B1) structured FeO by introducing "periodic extended defects" or "mimetic twinning" ("chemical", "unit-cell", or "non-conservative" twinning in different terminologies) [50]. In this approach, the structure of β-$Fe_3O_4$ is a result of regular repeated "twinning" of FeO on the (113) plane (twinning operations are reflection and/or rotation around the normal to (113)) (Supporting Information Figure S6). The $Fe^{2+}$ ions are localized in trigonal prisms (or capped trigonal prisms) at the "twinning" boundary, and $Fe^{3+}$ - in chains of paired octahedra (Figure 2a, Supporting Information Figure S6). Varying "twinned" fragments and the position of twining element(s) in the parent structure, a homologous series of oxides (like $Fe_4O_5$, $Fe_5O_7$, $Fe_7O_9$, etc.) may be obtained[8]. The mimetic twinning results in different "topology" and composition of each phase. Remarkably, a comparison of the structures of β-$Fe_3O_4$ and γ-$Fe_3O_4$ phases shows that re-arrangement of octahedra and prims may result in numerous polymorphs. As mentioned above,

the structure of orthorhombic γ-$Fe_3O_4$ belongs to the $Yb_3S_4$ type[44] (Figure 2c). Characteristic feature of the structure are ribbons of edge sharing octahedra (Figure 1c, 2c), like in warwickites-type structures[51]. Ribbons are linked in "parquet" manner (Figure 2c). Assuming that octahedra are occupied by ferric iron, and prisms between them by ferrous iron (such distribution of iron agrees with observed Fe-O distances in different polyhedra, see above), we end up with the expected composition $Fe_3O_4$. The same composition may be achieved with "one octahedra ribbons" (or simply columns, like in rutile), or with "two octahedra ribbons" (Supporting Information Figure S7), etc. In other words, the case of β- $Fe_3O_4$ and γ-$Fe_3O_4$ indicates that for a certain composition an unlimited number of polymorphs is geometrically possible.

The structure of tetragonal δ-$Fe_3O_4$ is resembling that of the distorted cubic $Th_3P_4$[45] (Figure 1d, 3b): one can be transformed to the other by shift of the origin and axis renaming. In the idealized, cubic δ-$Fe_3O_4$ structure, oxygen atoms occupy Wyckoff position *16c* with the coordinate $x$~0.06. If $x$=0, oxygen atoms would form ideal *bcc* sub-lattice. In spinel-structured magnetite, α-$Fe_3O_4$, oxygen atoms form *fcc* sub-lattice. Thus, a hypothetic transformation α- $Fe_3O_4$-to-δ-$Fe_3O_4$ can be described by diffusionless Bain model[52]. Notably, transition metal (TM=Ti, Zr, Hf) nitrides, $(TM)_3N_4$, crystallize in both spinel and cubic $Th_3P_4$ type structures, and $Th_3P_4$–structured phases are higher-pressure polymorphs[53,54]. Appearance of $Th_3P_4$–like high pressure phase(s) for $A_3X_4$ compounds having spinel-type structured phases at lower pressure could be a common pattern. Recent prediction[46] of the $Mg_2SiO_4$ phase with a distorted $Th_3P_4$-type structure above 490 GPa fits well in this pattern and supports the idea that the chemically simple Fe-O system may serve as proxy for understanding the behavior of chemically more complex systems like $(Mg,Fe)(Si,Al)_2O_4$ or $(Mg,Fe)(Si,Al)O_3$ at conditions of super-Earths' mantles.

*Spin state of iron.* One of the most important parameters defining the response of iron-bearing compounds to compression is its spin state[8,13,28,47,55–58]. The best method to characterize the spin state of iron in experiments with DACs is synchrotron Mössbauer spectroscopy (SMS, or related synchrotron methods like nuclear forward spectroscopy, X-ray absorption spectroscopy, emission spectroscopy, and others).

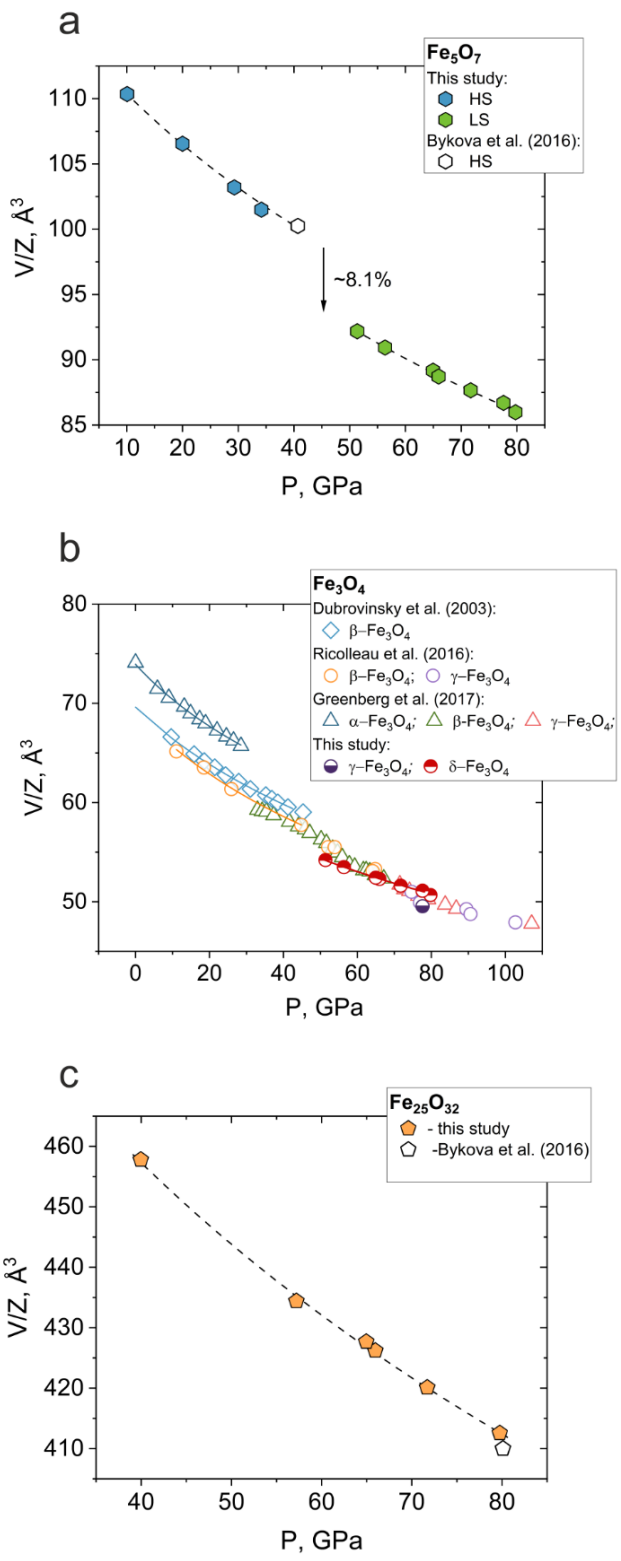


***Figure 5. Pressure-volume relations for three iron oxides.*** *V is the unit cell volume; Z is the number of formula units per a unit cell. Error bars are within the symbols' size.* ***(a) $Fe_5O_7$:*** *an isostructural spin transition in $Fe_5O_7$ between 41 and 51 GPa is manifested in the sharp reduction of the unit cell volume by ~8.1%. Dashed lines show the fit of the P-V/Z data using the second order Birch–Murnaghan EOS for HS and LS $Fe_5O_7$ phases.* ***(b) $Fe_3O_4$:*** *literature data in comparison with the data obtained in the present work. Solid lines of different colors indicate equations of state of different $Fe_3O_4$ phases: dark blue - α-$Fe_3O_4$, blue – β-$Fe_3O_4$, red – δ-$Fe_3O_4$.* ***(c) $Fe_{25}O_{32}$:*** *compressional curve does not show any sign of spin crossover, at least down to 40 GPa. Parameters of second order Birch–Murnaghan EOS of δ-$Fe_3O_4$, $Fe_5O_7$ and $Fe_{25}O_{32}$ are summarized in the Table 1, together with literature data for α-$Fe_3O_4$ and β-$Fe_3O_4$.*

Unfortunately, the kind of samples that we are dealing with are not really suitable for such studies – multi component mixtures of several phases with complex crystal structures, in which iron atoms are located in different structural environments, make interpretation of spectra ambiguous. However, single crystal diffraction data and crystal chemical considerations permit certain conclusions. Indeed, the compressional *P-V* curve of $Fe_5O_7$ (Figure 5) shows ~8.1% discontinuity between 43 and 51 GPa, which is characteristic for a spin crossover of $Fe^{3+}$ in octahedral coordination (compare, for example, with $Fe_2O_3$ with ~8.4% volume discontinuity at ~50 GPa[8,13]). In the structure of $Fe_5O_7$ (Figure 1e) there are 3 distinct iron positions– two octahedral, occupied by $Fe^{3+}$, and one in caped trigonal prism occupied by $Fe^{2+}$, according to ref. [8]. Relative changes in the volume of $FeO_6$ octahedra in $Fe_5O_7$ correspond well to the values known for other iron-bearing compounds (Figure 6, Supporting Information Figure S8); for example, at 43 GPa average volume of the octahedra is ~9.6 $Å^3$, and at 78 GPa it is of ~8.1 $Å^3$. However, octahedra volumes in $Fe_5O_7$ are larger than predicted for pure $Fe^{3+}$ (Figure 6), indicating a partial charge transfer between iron atoms in prismatic and octahedral sites (Supporting Information Figure S8). Upon spin crossover, relative volumes of $Fe^{2+}O_7$ caped prisms and $Fe^{3+}O_6$ octahedra change significantly (at 43 GPa, a ratio of the $FeO_7$ and $FeO_6$ polyhedra volumes is ~1.27, and at 78 GPa it is of ~1.33) with a notable difference between octahedra and caped prisms (Figure 6a). It indicates a spin crossover rather in ferric, than in ferrous iron in $Fe_5O_7$.

Considering structural data for γ-$Fe_3O_4$ (Figure 3a), one can find that at 78 GPa volumes of $Fe^{3+}O_6$ octahedra (8.05 and 8.14 $Å^3$ for Fe(1) and Fe(3), respectively) correspond to ferric iron in the low-spin state (Supporting Information Figure S8), while the dimensions of capped prism $Fe^{2+}O_7$ (<Fe-O> ~1.98 Å, volume is ~10.80 $Å^3$) point towards high spin $Fe^{2+}$. In the case of δ-$Fe_3O_4$, the unusual shape of $FeO_8$ polyhedra (Figure 3b) complicates the determination of the spin state of iron, but relatively long Fe-O distances (for comparison, the shortest Fe-O distance in δ-$Fe_3O_4$ is 1.91 Å, which is significantly larger than the longest 1.84 Å $Fe^{3+}$-O distance in γ-$Fe_3O_4$) and the relatively large unit cell volume (204.3 $Å^3$ for tetragonal δ-$Fe_3O_4$ *vs* 197.9 $Å^3$ for γ-$Fe_3O_4$) indicate that iron is in the high spin state. The compressional curve of $Fe_{25}O_{32}$ (Figure 5c) does not show any sign of a spin crossover.

Summarizing our observations and those described in the literature (Supporting Information Figure S8 and corresponding references), we can suggest that in iron oxides ferrous

iron in prismatic oxygen environment does not undergo spin crossover to at least 80 GPa, and ferric iron in oxygen octahedra transforms to the low spin state above ~45 GPa if $Fe^{3+}/\Sigma Fe \geq \sim 2/3$.

*Chemical stability of $Fe_3O_4$.* So far, data on chemical stability of $Fe_3O_4$ at high pressures and high temperatures have been highly inconsistent. There are reliable reports on formation of β-$Fe_3O_4$ upon decomposition of iron-bearing silicate skiagite[48], dehydration of FeOOH[9], or transformation of different iron oxides[30] at pressures of 30 to over 50 GPa and temperatures corresponding to Earth's geotherm. In this work we confirm the stablity of β-$Fe_3O_4$ at ~50 GPa and ~2500 K and formation of this phase upon decomposition of ($(Mg_{0.3}Fe_{0.7})CO_3$) observed at temperatures from 1500 K to over 2400 K and ~60 GPa (Figure 4, Supporting Information Table S1). However, above ~75 GPa upon heating of $Fe_3O_4$ between ~2000 K and ~3400 K, XRDpatterns show the presence of $Fe_5O_7$ and *hcp*-Fe (Supporting Information Table S1, Supporting Information Figure S4). The process of chemical decomposition may be then described as

$$7 \cdot Fe_3O_4 \rightarrow 4 \cdot Fe_5O_7 + Fe \qquad (1)$$

Heating at higher temperatures (up to ~4500 K) at ~78 GPa leads to formation of $Fe_{25}O_{32}$ that can be described as

$$25 \cdot Fe_3O_4 \rightarrow 3 \cdot Fe_{25}O_{32} + 2 \cdot O_2 \quad (2),$$

or

$$15 \cdot Fe_3O_4 \rightarrow Fe_{25}O_{32} + 4 \cdot Fe_5O_7 \quad (3)$$

The common feature of all processes (1)-(3) is that they reflect self-redox reactions of $Fe_3O_4$ at pressures of ~80 GPa. Uncovering details of this phenomenon and accurate determination of thermodynamic boundaries is beyond the scope of this work. However, available information permits the conclusion that there are significant changes at ~70-80 GPa and high temperature in chemistry of the Fe-O system (Figure 4, see areas highlighted with black rectangles). Cerantola et al.[47] and Bykova et al.[8] reported reduction of $Fe^{3+}$ by $O^{2-}$ in carbonates and in $Fe_2O_3$ at pressures ~70 GPa. In our experiments particularly remarkable is the possible co-existence of highly reduced (pure *hcp*-Fe) and oxidized ($Fe_5O_7$, $Fe^{3+}/\Sigma Fe$=0.75) iron species. Interestingly, a qualitatively similar conclusion may be drawn by considering the results of phase stability studies of mixed-

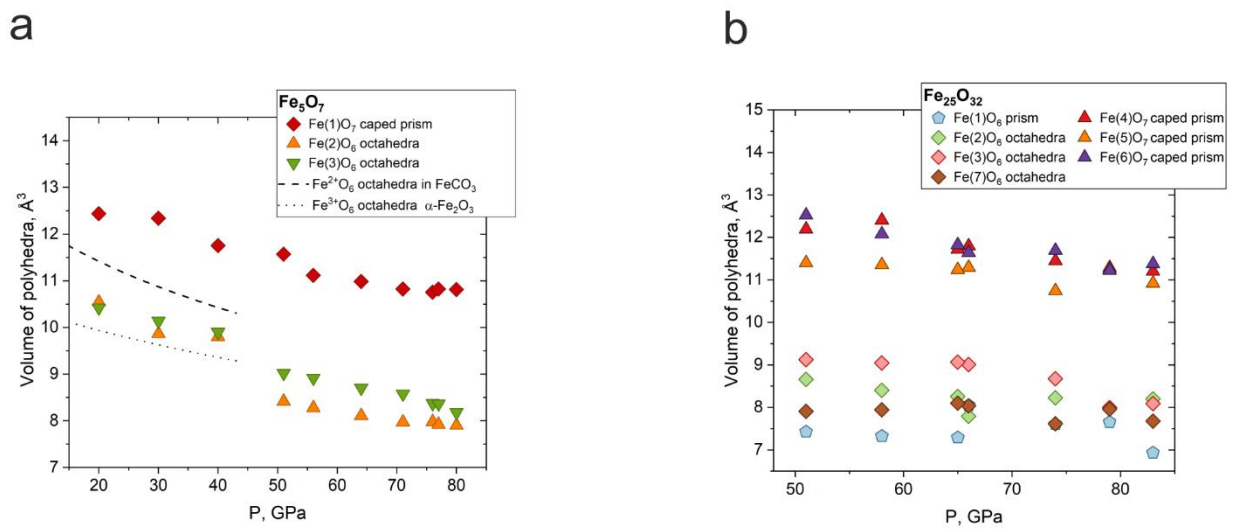


***Figure 6. Pressure dependence of the volumes of different polyhedra in $Fe_5O_7$ and $Fe_{25}O_{32}$.*** *(a) $Fe_5O_7$: volumes of octahedral are shown by triangles, and caped prisms – by diamonds. Dotted line shows the variation of the volumes of $Fe^{3+}O_6$ octhahedra in α-$Fe_2O_3$[8], and dashed line – $Fe^{2+}O_6$ octhahedra in $FeCO_3$[13]. Volumes of $FeO_6$ octahedra in $Fe_5O_7$ below ~40 GPa indicate charge transfer between iron atoms. Abrupt decrease of the volume of the octahedra suggests high-spin-to-low-spin crossover in ferric iron. (b) $Fe_{25}O_{32}$: Within studied pressure range all polyhedra in the phase contract smoothly.*

valence iron oxides in multi-anvil experiments at pressures up to about 24 GPa[59]. Linear extrapolations of pressure-oxygen fugacity phase boundaries of Fe-FeO and FeO-$Fe_5O_6$ at 1473 K suggest that at pressures between 70 and 85 GPa one may expect the equilibrium between pure iron and $Fe_5O_6$. Such changes in the behavior of the Fe-O system at ~80 GPa would affect the oxidation state and partitioning of ferrous and ferric iron in silicates and oxides. Indeed, Prescher et al.[58] reported significant changes in the partitioning coefficient of $Fe^{2+}$ and re-distribution of $Fe^{3+}$ from co-existing silicate perovskite in to ferropericlase above ~80 GPa. Bridgmanite (silicate perovskite) and ferropericlase (both containing $Fe^{2+}$ and $Fe^{3+}$) are dominant phases of Earth's lower mantle. Thus, our results on chemical instability of $Fe_3O_4$ at conditions corresponding to the depth more than 1800 km become crucial for modelling thermodynamics of mantle phases and dynamics of deep interiors, and provide additional arguments towards the possible chemical heterogeneity of the mantle[60,61].

Magnetite, hematite, and iron oxyhydroxides (like goethite) are major constituents of BIFs[31]. Accumulated on the ocean floors in early Earth history, BIFs are believed to be subducted into the deep interior. Upon subduction, oxyhydroxides are expected to lose water and transform to β-$Fe_3O_4$[9]. Our new data demonstrate that not only $Fe_2O_3$[8], but various $Fe_3O_4$ phases at conditions of Earth's lower mantle (at depth of ~1800 km) may dissociate and produce oxygen (or highly oxidized fluid). In the past, Earth's interiors were warmer[62], thus, the process of decomposition of iron oxides (i.e. $Fe_3O_4$) could occur at lower depth, thus widely contributing to global oxygen cycle and formation of oxygen-rich atmosphere.

## Conclusion

To summarize, in the present paper we report the results of high-pressure high-temperature studies of $Fe_3O_4$ up to ~80 GPa and 5000 K performed in the laser-heated diamond anvil cell. The existence of β-$Fe_3O_4$ with the $CaTi_2O_4$-type structure at geotherm temperatures and pressures over ~50 GPa was confirmed based on single-crystal X-ray diffraction. Two new high-pressure polymorphs of $Fe_3O_4$, γ-$Fe_3O_4$ and δ-$Fe_3O_4$, were synthesized above ~60 GPa. The γ-$Fe_3O_4$ is orthorhombic, resembling the $Yb_3S_4$-type structure. The δ-$Fe_3O_4$ has a modified $Th_3P_4$-type structure, not recognized until now in oxides, and never predicted for iron oxides. We found that $Fe_3O_4$, pressurized above ~75 GPa and heated above ~2000 K, becomes chemically unstable and underoes self-reduction or decomposition. Among chemical products of these processes we found pure iron and unusual iron oxides: $Fe_5O_7$ and $Fe_{25}O_{32}$. Thus, chemical instability of $Fe_3O_4$ at conditions corresponding to the depth of over 1800 km indicates significant changes in the Fe-O system and provides an additional argument in favor of possible chemical heterogeneity of Earth's lower mantle. The analysis of the compressional curves of iron oxides and variations in the volumes of Fe-O polyhedra suggests that in iron oxides at ambient temperature, ferrous iron in prismatic oxygen environment does not undergo spin crossover up to at least 80 GPa, and ferric iron in oxygen octahedra transforms from the high to the low spin state above ~45 GPa if $Fe^{3+}/\Sigma Fe \geq 2/3$.

Detailed information on the crystal data obtained from single-crystal XRD refinement of the observed phases is provided in the Supporting Information Tables S2, S9, S10. These data have been deposited at The Cambridge Crystallographic Data Centre (CCDC). CSD 2115623 contains the Supporting Information crystallographic data of β-$Fe_{2.771}Mg_{0.229}O_4$ at 58.6(5) GPa; CSD 2115631 – δ-$Fe_3O_4$ at 58.6(5) GPa; CSD 2115632 – δ-$Fe_3O_4$ at 78(1) GPa; CSD 2115639 – γ-$Fe_3O_4$ at 78(1) GPa; CSD 2115634 – $Fe_5O_7$ at 78(1) GPa; CSD 2115637– $Fe_{25}O_{32}$ at 65(1) GPa.

## Acknowledgements

N. D. and L. D. thank the Federal Ministry of Education and Research, Germany (BMBF, grant No. 05K19WC1) and the Deutsche Forschungsgemeinschaft (DFG projects DU 954-11/1, DU 393-9/2, and DU 393-13/1) for financial support. N. D. thanks the Swedish Government Strategic Research Area in Materials Science on Functional Materials at Linköping University (Faculty Grant SFO-Mat-LiU No. 200900971). We acknowledge DESY (Hamburg, Germany), a member of the Helmholtz Association HGF, for the provision of experimental facilities.

## References

(1) Bednorz, J. G.; Müller, K. A. Possible HighT c Superconductivity in the Ba-La-Cu-O System. *Zeitschrift für Phys. B Condens. Matter* **1986**, *64* (2), 189–193. https://doi.org/10.1007/BF01303701.

(2) Hosono, H.; Yamamoto, A.; Hiramatsu, H.; Ma, Y. Recent Advances in Iron-Based Superconductors toward Applications. *Mater. Today* **2018**, *21* (3), 278–302. https://doi.org/10.1016/j.mattod.2017.09.006.

(3) Salamon, M. B.; Jaime, M. The Physics of Manganites: Structure and Transport. *Rev. Mod. Phys.* **2001**, *73* (3), 583–628. https://doi.org/10.1103/RevModPhys.73.583.

(4) Lavina, B.; Dera, P.; Kim, E.; Meng, Y.; Downs, R. T.; Weck, P. F.; Sutton, S. R.; Zhao, Y. Discovery of the Recoverable High-Pressure Iron Oxide $Fe_4O_5$. *Proc. Natl. Acad. Sci.* **2011**,

*108* (42), 17281–17285. https://doi.org/10.1073/pnas.1107573108.

(5) Ovsyannikov, S. V.; Bykov, M.; Bykova, E.; Glazyrin, K.; Manna, R. S.; Tsirlin, A. A.; Cerantola, V.; Kupenko, I.; Kurnosov, A. V.; Kantor, I.; Pakhomova, A. S.; Chuvashova, I.; Chumakov, A. I.; Rüffer, R.; McCammon, C.; Dubrovinsky, L. S. Pressure Tuning of Charge Ordering in Iron Oxide. *Nat. Commun.* **2018**, *9* (1), 4142. https://doi.org/10.1038/s41467-018-06457-x.

(6) Lavina, B.; Meng, Y. Unraveling the Complexity of Iron Oxides at High Pressure and Temperature: Synthesis of $Fe_5O_6$. *Sci. Adv.* **2015**, *1* (5), e1400260. https://doi.org/10.1126/sciadv.1400260.

(7) Ovsyannikov, S. V.; Bykov, M.; Medvedev, S. A.; Naumov, P. G.; Jesche, A.; Tsirlin, A. A.; Bykova, E.; Chuvashova, I.; Karkin, A. E.; Dyadkin, V.; Chernyshov, D.; Dubrovinsky, L. S. A Room-Temperature Verwey-type Transition in Iron Oxide, $Fe_5O_6$. *Angew. Chemie Int. Ed.* **2020**, *59* (14), 5632–5636. https://doi.org/10.1002/anie.201914988.

(8) Bykova, E.; Dubrovinsky, L.; Dubrovinskaia, N.; Bykov, M.; McCammon, C.; Ovsyannikov, S. V; Liermann, H.-P.; Kupenko, I.; Chumakov, A. I.; Rüffer, R.; Hanfland, M.; Prakapenka, V. Structural Complexity of Simple $Fe_2O_3$ at High Pressures and Temperatures. *Nat. Commun.* **2016**, *7* (1), 10661. https://doi.org/10.1038/ncomms10661.

(9) Koemets, E.; Fedotenko, T.; Khandarkhaeva, S.; Bykov, M.; Bykova, E.; Thielmann, M.; Chariton, S.; Aprilis, G.; Koemets, I.; Glazyrin, K.; Liermann, H.-P.; Hanfland, M.; Ohtani, E.; Dubrovinskaia, N.; McCammon, C.; Dubrovinsky, L. Chemical Stability of FeOOH at High Pressure and Temperature, and Oxygen Recycling in Early Earth History. *Eur. J. Inorg. Chem.* **2021**, ejic.202100274. https://doi.org/10.1002/ejic.202100274.

(10) Sinmyo, R.; Bykova, E.; Ovsyannikov, S. V.; McCammon, C.; Kupenko, I.; Ismailova, L.; Dubrovinsky, L. Discovery of $Fe_7O_9$: A New Iron Oxide with a Complex Monoclinic Structure. *Sci. Rep.* **2016**, *6* (1), 32852. https://doi.org/10.1038/srep32852.

(11) Merlini, M.; Hanfland, M.; Salamat, A.; Petitgirard, S.; Müller, H. The Crystal Structures of $Mg_2Fe_2C_4O_{13}$ , with Tetrahedrally Coordinated Carbon, and $Fe_{13}O_{19}$ , Synthesized at Deep Mantle Conditions. *Am. Mineral.* **2015**, *100* (8–9), 2001–2004.

https://doi.org/10.2138/am-2015-5369.

(12) Hu, Q.; Kim, D. Y.; Yang, W.; Yang, L.; Meng, Y.; Zhang, L.; Mao, H. K. $FeO_2$ and FeOOH under Deep Lower-Mantle Conditions and Earth's Oxygen-Hydrogen Cycles. *Nature* **2016**, *534* (7606), 241–244. https://doi.org/10.1038/nature18018.

(13) Koemets, E.; Leonov, I.; Bykov, M.; Bykova, E.; Chariton, S.; Aprilis, G.; Fedotenko, T.; Clément, S.; Rouquette, J.; Haines, J.; Cerantola, V.; Glazyrin, K.; McCammon, C.; Prakapenka, V. B.; Hanfland, M.; Liermann, H.-P.; Svitlyk, V.; Torchio, R.; Rosa, A. D.; Irifune, T.; Ponomareva, A. V.; Abrikosov, I. A.; Dubrovinskaia, N.; Dubrovinsky, L. Revealing the Complex Nature of Bonding in the Binary High-Pressure Compound $FeO_2$. *Phys. Rev. Lett.* **2021**, *126* (10), 106001. https://doi.org/10.1103/PhysRevLett.126.106001.

(14) Fleet, M. E. The Structure of Magnetite. *Acta Crystallogr. Sect. B Struct. Crystallogr. Cryst. Chem.* **1981**, *37* (4), 917–920. https://doi.org/10.1107/S0567740881004597.

(15) Verwey, E. J. W. Electronic Conduction of Magnetite ($Fe_3O_4$) and Its Transition Point at Low Temperatures. *Nature*. 1939, pp 327–328. https://doi.org/10.1038/144327b0.

(16) Mott, N. F. *Metal-Insulator Transitions.*; Taylor & Francis Ltd: London, 1974. https://doi.org/10.1002/crat.19750100423.

(17) Senn, M. S.; Wright, J. P.; Attfield, J. P. Charge Order and Three-Site Distortions in the Verwey Structure of Magnetite. *Nature* **2012**, *481* (7380), 173–176. https://doi.org/10.1038/nature10704.

(18) Perversi, G.; Cumby, J.; Pachoud, E.; Wright, J. P.; Attfield, J. P. The Verwey Structure of a Natural Magnetite. *Chem. Commun.* **2016**, *52* (27), 4864–4867. https://doi.org/10.1039/c5cc10495e.

(19) Mao, H.-K.; Takahashi, T.; Bassett, W. A.; Kinsland, G. L.; Merrill, L. Isothermal Compression of Magnetite to 320 KB. *J. Geophys. Res.* **1974**, *79* (8), 1165–1170. https://doi.org/10.1029/JB079i008p01165.

(20) Mao, H.; Virgo, D.; Bell, P. M. High-Pressure $^{57}$Fe Mossbauer Data on the Phase and Magnetic Transitions Ofmagnesioferrite ($MgFe_2O4$), Magnetite ($Fe_3O_4$), and Hematite ($Fe_2O_3$). *Year B. Carnegie Inst. Washingt.* **1977**, *76*, 522–525.

(21) Pasternak, M. P.; Nasu, S.; Wada, K.; Endo, S. High-Pressure Phase of Magnetite. *Phys. Rev. B* **1994**, *50* (9), 6446–6449. https://doi.org/10.1103/PhysRevB.50.6446.

(22) Morris, E. R.; Williams, Q. Electrical Resistivity of $Fe_3O_4$ to 48 GPa: Compression-Induced Changes in Electron Hopping at Mantle Pressures. *J. Geophys. Res. Solid Earth* **1997**, *102* (B8), 18139–18148. https://doi.org/10.1029/97JB00024.

(23) Huang, E.; Bassett, W. A. Rapid Determination of $Fe_3O_4$ Phase Diagram by Synchrotron Radiation. *J. Geophys. Res.* **1986**, *91* (B5), 4697. https://doi.org/10.1029/JB091iB05p04697.

(24) Schollenbruch, K.; Woodland, A. B.; Frost, D. J.; Langenhorst, F. Detecting the Spinel–Post-Spinel Transition in $Fe_3O_4$ by in Situ Electrical Resistivity Measurements. *High Press. Res.* **2009**, *29* (4), 520–524. https://doi.org/10.1080/08957950903392092.

(25) Kozlenko, D. P.; Dubrovinsky, L. S.; Kichanov, S. E.; Lukin, E. V.; Cerantola, V.; Chumakov, A. I.; Savenko, B. N. Magnetic and Electronic Properties of Magnetite across the High Pressure Anomaly. *Sci. Rep.* **2019**, *9* (1), 4464. https://doi.org/10.1038/s41598-019-41184-3.

(26) Haavik, C.; Stølen, S.; Fjellvåg, H.; Hanfland, M.; Häusermann, D. Equation of State of Magnetite and Its High-Pressure Modification: Thermodynamics of the Fe-O System at High Pressure. *Am. Mineral.* **2000**, *85* (3–4), 514–523. https://doi.org/10.2138/am-2000-0413.

(27) Dubrovinsky, L. S.; Dubrovinskaia, N. A.; McCammon, C.; Rozenberg, G. K.; Ahuja, R.; Osorio-Guillen, J. M.; Dmitriev, V.; Weber, H. P.; Le Bihan, T.; Johansson, B. The Structure of the Metallic High-Pressure $Fe_3O_4$ Polymorph: Experimental and Theoretical Study. *J. Phys. Condens. Matter* **2003**, *15* (45), 7697–7706. https://doi.org/10.1088/0953-8984/15/45/009.

(28) Greenberg, E.; Xu, W. M.; Nikolaevsky, M.; Bykova, E.; Garbarino, G.; Glazyrin, K.; Merkel, D. G.; Dubrovinsky, L.; Pasternak, M. P.; Rozenberg, G. K. High-Pressure Magnetic, Electronic, and Structural Properties of $MFe_2O_4$ (M = Mg,Zn,Fe) Ferric Spinels. *Phys. Rev. B* **2017**, *95* (19), 195150. https://doi.org/10.1103/PhysRevB.95.195150.

(29) Ricolleau, A.; Fei, Y. Equation of State of the High-Pressure $Fe_3O_4$ Phase and a New Structural Transition at 70 GPa. *Am. Mineral.* **2016**, *101* (3), 719–725. https://doi.org/10.2138/am-2016-5409.

(30) Hikosaka, K.; Sinmyo, R.; Hirose, K.; Ishii, T.; Ohishi, Y. The Stability of $Fe_5O_6$ and Fe4O5 at High Pressure and Temperature. *Am. Mineral.* **2019**, *104* (9), 1356–1359. https://doi.org/10.2138/am-2019-7097.

(31) Dobson, D. P.; Brodholt, J. P. Subducted Banded Iron Formations as a Source of Ultralow-Velocity Zones at the Core–Mantle Boundary. *Nature* **2005**, *434* (7031), 371–374. https://doi.org/10.1038/nature03430.

(32) Lazor, P.; Shebanova, O. N.; Annersten, H. High-Pressure Study of Stability of Magnetite by Thermodynamic Analysis and Synchrotron X-Ray Diffraction. *J. Geophys. Res. Solid Earth* **2004**, *109* (B5), 1–16. https://doi.org/10.1029/2003JB002600.

(33) Kantor, I.; Prakapenka, V.; Kantor, A.; Dera, P.; Kurnosov, A.; Sinogeikin, S.; Dubrovinskaia, N.; Dubrovinsky, L. BX90: A New Diamond Anvil Cell Design for X-Ray Diffraction and Optical Measurements. *Rev. Sci. Instrum.* **2012**, *83* (125102), 125102. https://doi.org/10.1063/1.4768541.

(34) Kurnosov, A.; Kantor, I.; Boffa-Ballaran, T.; Lindhardt, S.; Dubrovinsky, L.; Kuznetsov, A.; Zehnder, B. H. A Novel Gas-Loading System for Mechanically Closing of Various Types of Diamond Anvil Cells. *Rev. Sci. Instrum.* **2008**, *79* (4), 045110. https://doi.org/10.1063/1.2902506.

(35) Fedotenko, T.; Dubrovinsky, L.; Aprilis, G.; Koemets, E.; Snigirev, A.; Snigireva, I.; Barannikov, A.; Ershov, P.; Cova, F.; Hanfland, M.; Dubrovinskaia, N. Laser Heating Setup for Diamond Anvil Cells for in Situ Synchrotron and in House High and Ultra-High Pressure Studies. *Rev. Sci. Instrum.* **2019**, *90* (10), 104501. https://doi.org/10.1063/1.5117786.

(36) Prescher, C.; Prakapenka, V. B. DIOPTAS : A Program for Reduction of Two-Dimensional X-Ray Diffraction Data and Data Exploration. *High Press. Res.* **2015**, *35* (3), 223–230. https://doi.org/10.1080/08957959.2015.1059835.

(37) Petříček, V.; Dušek, M.; Palatinus, L. Crystallographic Computing System JANA2006: General Features. *Zeitschrift für Krist. - Cryst. Mater.* **2014**, *229* (5), 345–352. https://doi.org/10.1515/zkri-2014-1737.

(38) Hrubiak, R.; Smith, J. S.; Shen, G. Multimode Scanning X-Ray Diffraction Microscopy for Diamond Anvil Cell Experiments. *Rev. Sci. Instrum.* **2019**, *90* (2), 025109. https://doi.org/10.1063/1.5057518.

(39) Rigaku Oxford Diffraction. CrysAlis Pro (v. 171.40.84). Rigaku Oxford Diffraction, Yarnton, UK 2020.

(40) Bykova, E. Single-Crystal X-Ray Diffraction at Extreme Conditions in Mineral Physics and Material Sciences, University of Bayreuth, 2015.

(41) Sheldrick, G. M. SHELXT – Integrated Space-Group and Crystal-Structure Determination. *Acta Crystallogr. Sect. A Found. Adv.* **2015**, *71* (1), 3–8. https://doi.org/10.1107/S2053273314026370.

(42) Dolomanov, O. V.; Bourhis, L. J.; Gildea, R. J.; Howard, J. A. K.; Puschmann, H. OLEX2 : A Complete Structure Solution, Refinement and Analysis Program. *J. Appl. Crystallogr.* **2009**, *42* (2), 339–341. https://doi.org/10.1107/S0021889808042726.

(43) Putz, H.; Brandenburg, K. Diamond - Crystal and Molecular Structure Visualization. Kreuzherrenstr. 102, 53227 Bonn, Germany.

(44) Chevallier, R.; Laruelle, P.; Flahaut, J. Structure Cristallographique $Yb_3S_4$. *Bull. la Société française Minéralogie Cristallogr.* **1967**, *90* (4), 564–574. https://doi.org/10.3406/bulmi.1967.6045.

(45) Zumbusch, M. Über Strukturanalogie von Uran- Und Thoriumphosphiden. *Zeitschrift für Anorg. und Allg. Chemie* **1941**, *245* (4), 402–408. https://doi.org/10.1002/zaac.19412450408.

(46) Umemoto, K.; Wentzcovitch, R. M.; Wu, S.; Ji, M.; Wang, C.-Z.; Ho, K.-M. Phase Transitions in MgSiO3 Post-Perovskite in Super-Earth Mantles. *Earth Planet. Sci. Lett.* **2017**, *478*, 40–45. https://doi.org/10.1016/j.epsl.2017.08.032.

(47) Cerantola, V.; Bykova, E.; Kupenko, I.; Merlini, M.; Ismailova, L.; McCammon, C.; Bykov, M.; Chumakov, A. I.; Petitgirard, S.; Kantor, I.; Svitlyk, V.; Jacobs, J.; Hanfland, M.; Mezouar, M.; Prescher, C.; Rüffer, R.; Prakapenka, V. B.; Dubrovinsky, L. Stability of Iron-Bearing Carbonates in the Deep Earth's Interior. *Nat. Commun.* **2017**, *8* (1), 15960. https://doi.org/10.1038/ncomms15960.

(48) Ismailova, L.; Bykova, E.; Bykov, M.; Cerantola, V.; McCammon, C.; Boffa Ballaran, T.; Bobrov, A.; Sinmyo, R.; Dubrovinskaia, N.; Glazyrin, K.; Liermann, H.-P.; Kupenko, I.; Hanfland, M.; Prescher, C.; Prakapenka, V.; Svitlyk, V.; Dubrovinsky, L. Stability of Fe,Al-Bearing Bridgmanite in the Lower Mantle and Synthesis of Pure Fe-Bridgmanite. *Sci. Adv.* **2016**, *2* (7), e1600427. https://doi.org/10.1126/sciadv.1600427.

(49) Dubrovinsky, L. S.; Saxena, S. K.; Tutti, F.; Rekhi, S.; LeBehan, T. In Situ X-Ray Study of Thermal Expansion and Phase Transition of Iron at Multimegabar Pressure. *Phys. Rev. Lett.* **2000**, *84* (8), 1720–1723. https://doi.org/10.1103/PhysRevLett.84.1720.

(50) Bakker, M.; Hyde, B. G. A Preliminary Electron Microscope Study of Chemical Twinning in the System MnS+$Y_2S_3$ , an Analogue of the Mineral System PbS+Bi 2 S 3 (Galena + Bismuthinite). *Philos. Mag. A* **1978**, *38* (6), 615–628. https://doi.org/10.1080/01418617808239260.

(51) Matos, M.; Hoffmann, R.; Latgé, A.; Anda, E. V. Warwickites: Electronic Structure and Bonding. *Chem. Mater.* **1996**, *8* (9), 2324–2330. https://doi.org/10.1021/cm9601392.

(52) Khachaturyan, A. G. *Theory of Structural Transformations in Solids*; Dover Publications, 2008.

(53) Kroll, P. Hafnium Nitride with Thorium Phosphide Structure: Physical Properties and an Assessment of the Hf-N, Zr-N, and Ti-N Phase Diagrams at High Pressures and Temperatures. *Phys. Rev. Lett.* **2003**, *90* (12), 125501. https://doi.org/10.1103/PhysRevLett.90.125501.

(54) Zerr, A.; Miehe, G.; Riedel, R. Synthesis of Cubic Zirconium and Hafnium Nitride Having Th3P4 Structure. *Nat. Mater.* **2003**, *2* (3), 185–189. https://doi.org/10.1038/nmat836.

(55) Chariton, S.; McCammon, C.; Vasiukov, D. M.; Stekiel, M.; Kantor, A.; Cerantola, V.;

Kupenko, I.; Fedotenko, T.; Koemets, E.; Hanfland, M.; Chumakov, A. I.; Dubrovinsky, L. Seismic Detectability of Carbonates in the Deep Earth: A Nuclear Inelastic Scattering Study. *Am. Mineral.* **2020**, *105* (3), 325–332. https://doi.org/10.2138/am-2020-6901.

(56) Glazyrin, K.; Sinmyo, R.; Bykova, E.; Bykov, M.; Cerantola, V.; Longo, M.; McCammon, C.; Prakapenka, V. B.; Dubrovinsky, L. Critical Behavior of $Mg_{1-x}Fe_xO$ at the pressure-induced iron spin-state crossover. *Phys. Rev. B* **2017**, *95* (21), 214412. https://doi.org/10.1103/PhysRevB.95.214412.

(57) Glazyrin, K.; Miyajima, N.; Smith, J. S.; Lee, K. K. M. Compression of a Multiphase Mantle Assemblage: Effects of Undesirable Stress and Stress Annealing on the Iron Spin State Crossover in Ferropericlase. *J. Geophys. Res. Solid Earth* **2016**, *121* (5), 3377–3392. https://doi.org/10.1002/2015JB012321.

(58) Prescher, C.; Langenhorst, F.; Dubrovinsky, L. S.; Prakapenka, V. B.; Miyajima, N. The Effect of Fe Spin Crossovers on Its Partitioning Behavior and Oxidation State in a Pyrolitic Earth's Lower Mantle System. *Earth Planet. Sci. Lett.* **2014**, *399*, 86–91. https://doi.org/10.1016/j.epsl.2014.05.011.

(59) Myhill, R.; Ojwang, D. O.; Ziberna, L.; Frost, D. J.; Ballaran, T. B.; Miyajima, N. On the P–T–FO 2 Stability of $Fe_4O_5$, $Fe_5O_6$ and $Fe_4O_5$-Rich Solid Solutions. *Contrib. to Mineral. Petrol.* **2016**, *171* (5), 1–11. https://doi.org/10.1007/s00410-016-1258-4.

(60) van der Hilst, R. D.; Widiyantoro, S.; Engdahl, E. R. Evidence for Deep Mantle Circulation from Global Tomography. *Nature* **1997**, *386* (6625), 578–584. https://doi.org/10.1038/386578a0.

(61) Zhao, D. Global Tomographic Images of Mantle Plumes and Subducting Slabs: Insight into Deep Earth Dynamics. *Phys. Earth Planet. Inter.* **2004**, *146* (1–2), 3–34. https://doi.org/10.1016/j.pepi.2003.07.032.

(62) McGovern, P. J.; Schubert, G. Thermal Evolution of the Earth: Effects of Volatile Exchange between Atmosphere and Interior. *Earth Planet. Sci. Lett.* **1989**, *96* (1–2), 27–37. https://doi.org/10.1016/0012-821X(89)90121-0.

(63) Katsura, T.; Yoneda, A.; Yamazaki, D.; Yoshino, T.; Ito, E.; Suetsugu, D.; Bina, C.; Inoue,

T.; Wiens, D.; Jellinek, M. Adiabatic Temperature Profile in the Mantle. *Phys. Earth Planet. Inter.* **2010**, *183* (1–2), 212–218. https://doi.org/10.1016/j.pepi.2010.07.001.

(64) Dziewonski, A. M.; Anderson, D. L. Preliminary Reference Earth Model. *Phys. Earth Planet. Inter.* **1981**, *25* (4), 297–356. https://doi.org/10.1016/0031-9201(81)90046-7.

## Supporting information

# Structural diversity of magnetite and products of its decomposition at extreme conditions

*Saiana Khandarkhaeva,[a,b*] Timofey Fedotenko,[b] Stella Chariton,[c] Elena Bykova,[d] Sergey Ovsyannikov,[a,e] Konstantin Glazyrin,[f] Hanns-Peter Liermann,[f] Vitali Prakapenka,[c] Natalia Dubrovinskaia [b, g] and Leonid Dubrovinsky[a]*

[a] *Bayerisches Geoinstitut, University of Bayreuth, Universitätstraße 30, 95440 Bayreuth, Germany*

[b] *Material Physics and Technology at Extreme Conditions, Laboratory of Crystallography, University of Bayreuth, Universitätstraße 30, 95440 Bayreuth, Germany*

[c] *Center for Advanced Radiation Sources, University of Chicago, 5640 S. Ellis, 60637 Chicago, Illinois, USA*

[d] *Geophysical Laboratory, Carnegie Institution of Washington, 5251 Broad Branch Road NW, 20015 Washington, District of Columbia, USA*

[e]*Institute for Solid State Chemistry of Ural Branch of Russian Academy of Sciences, 91 Pervomayskaya Str., Yekaterinburg 620219, Russia*

[f] *Deutsches Elektronen-Synchrotron, Notkestraße 85, 22607 Hamburg, Germany*

[g] *Theoretical Physics Division, Department of Physics, Chemistry and Biology (IFM), Linköping University, SE-581 83, Linköping, Sweden*

** Corresponding author's email: saiana.khandarkhaeva@uni-bayreuth.de*

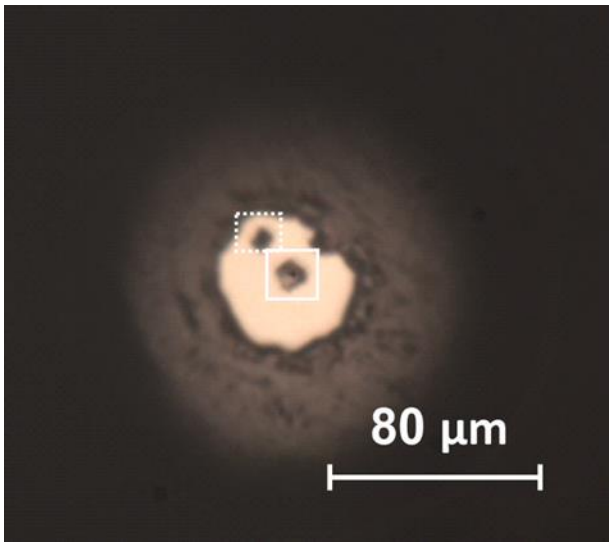


***Figure S1.*** *Optical image of the sample camber at 78(1) GPa. Crystal #1 (C1) highlighted with white solid rectangle has been heated up to 4770(250) K. Crystal #2 (C2) 1 highlighted with white dotted rectangle has been heated at lower temperatures 2700(200) K.*

**Table S1.** Summary of experimental runs, *PT* paths, and phases observed.

| **Laser-heating in home lab in BGI (starting material –$Fe_3O_4$)** | | | |
|---|---|---|---|
| Crystal | P, GPa | T, K | Phase |
| C1 | 78(1) | 4770(250) | *tP(tI)*-$Fe_3O_4$+$Fe_5O_7$+$Fe_{25}O_{32}$ |
| C2 | 78(1) | 2540(110) | *oP*-$Fe_3O_4$+*tI*-$Fe_3O_4$+$Fe_5O_7$+$Fe_{hcp}$ |
| | | 2650(210) | *oP*-$Fe_3O_4$+*tI*-$Fe_3O_4$+$Fe_5O_7$+$Fe_{hcp}$ |
| | | 2810(180) | *oP*-$Fe_3O_4$+*tI*-$Fe_3O_4$+$Fe_5O_7$+$Fe_{hcp}$ |
| | | 2720(50) | *oP*-$Fe_3O_4$+*tI*-$Fe_3O_4$+$Fe_5O_7$+$Fe_{hcp}$ |
| | | 2750(100) | *oP*-$Fe_3O_4$+*tI*-$Fe_3O_4$+$Fe_5O_7$+$Fe_{hcp}$ |
| | | 2770(50) | *oP*-$Fe_3O_4$+*tI*-$Fe_3O_4$+$Fe_5O_7$+$Fe_{hcp}$ |
| **Laser-heating at 13 IDD, GSECARS, APS (starting material –$Fe_3O_4$)** | | | |
| C1 | 77(2) | 1630(60) | *tP(tI)*-$Fe_3O_4$+$Fe_5O_7$ |
| | 74(1) | 1620(80) | *tP(tI)*-$Fe_3O_4$+$Fe_5O_7$ |
| | 77(2) | 2090(130) | *tP(tI)*-$Fe_3O_4$+$Fe_5O_7$ |
| | 76(3) | 2490(210) | *tP(tI)*-$Fe_3O_4$+$Fe_5O_7$ |
| | 76(2) | 2730(330) | *tP(tI)*-$Fe_3O_4$+$Fe_5O_7$ |
| | 76(2) | 2930(350) | *tP(tI)*-$Fe_3O_4$+$Fe_5O_7$ |

| | | | |
|---|---|---|---|
| | 76(1) | 2720(130) | *tP(tI)*-$Fe_3O_4$+$Fe_5O_7$ |
| | 78(1) | 2950(100) | *tP(tI)*-$Fe_3O_4$+$Fe_5O_7$ |
| | 75(3) | 3200(180) | *tP(tI)*-$Fe_3O_4$+$Fe_5O_7$ |
| | 76(3) | 3340(400) | *tP(tI)*-$Fe_3O_4$+$Fe_5O_7$ |
| | 77(2) | 3030(300) | *tP(tI)*-$Fe_3O_4$+$Fe_5O_7$ |
| | 77(2) | 3800(500) | *tP(tI)*-$Fe_3O_4$+$Fe_5O_7$ |
| | 76(1) | 3890(520) | *mI*-$Fe_3O_4$+$Fe_5O_7$+$Fe_{25}O_{32}$ |
| | 74(3) | 3870(540) | *mI*-$Fe_3O_4$+$Fe_5O_7$+$Fe_{25}O_{32}$ |
| | 74(5) | 3770(630) | *mI*-$Fe_3O_4$+$Fe_5O_7$+$Fe_{25}O_{32}$ |
| | 73(4) | 3450(470) | *mI*-$Fe_3O_4$+$Fe_5O_7$+$Fe_{25}O_{32}$ |
| | 73(3) | 2640(360) | *mI*-$Fe_3O_4$+$Fe_5O_7$+$Fe_{25}O_{32}$ |
| | 74(3) | 2810(180) | *mI*-$Fe_3O_4$+$Fe_5O_7$+$Fe_{25}O_{32}$ |
| | 69(1) | 2470(300) | *mI*-$Fe_3O_4$+$Fe_5O_7$+$Fe_{25}O_{32}$ |
| | 73(4) | 3100(100) | *mI*-$Fe_3O_4$+$Fe_5O_7$+$Fe_{25}O_{32}$ |
| **Laser-heating at 13 IDD, GSECARS, APS (starting material – $(Mg_{0.3}Fe_{0.7})CO_3$)** | | | |
| C1 | 61(1) | 1500(70) | carbonate+β-$Fe_{2.771}Mg_{0.229}O_4$ |
| | | 293 | carbonate+β-$Fe_{2.771}Mg_{0.229}O_4$ |
| | | 1700(70) | carbonate+β-$Fe_{2.771}Mg_{0.229}O_4$ |
| | | 293 | carbonate+ β-$Fe_{2.771}Mg_{0.229}O_4$ |
| | | 1870(70) | carbonate+ β-$Fe_{2.771}Mg_{0.229}O_4$ |
| | | 293 | carbonate+ β-$Fe_{2.771}Mg_{0.229}O_4$ |
| | | 2100(60) | carbonate+ β-$Fe_{2.771}Mg_{0.229}O_4$ |
| | | 293 | carbonate+ β-$Fe_{2.771}Mg_{0.229}O_4$ |
| | | 2260(90) | carbonate+ β-$Fe_{2.771}Mg_{0.229}O_4$+*tI*-$Fe_3O_4$ |
| | | 293 | carbonate+ β-$Fe_{2.771}Mg_{0.229}O_4$+*tI*-$Fe_3O_4$ |
| | | 2280(180) | carbonate+ β-$Fe_{2.771}Mg_{0.229}O_4$+*tI*-$Fe_3O_4$ |
| | | 293 | carbonate+ β-$Fe_{2.771}Mg_{0.229}O_4$+*tI*-$Fe_3O_4$ |
| | | 2400(270) | carbonate+ β-$Fe_{2.771}Mg_{0.229}O_4$+*tI*-$Fe_3O_4$ |
| | | 293 | carbonate+ β-$Fe_{2.771}Mg_{0.229}O_4$+*tI*-$Fe_3O_4$ |
| | | 2470(240) | carbonate+ β-$Fe_{2.771}Mg_{0.229}O_4$+*tI*-$Fe_3O_4$ |
| | | 293 | carbonate+ β-$Fe_{2.771}Mg_{0.229}O_4$+*tI*-$Fe_3O_4$ |
| | | 2600(260) | carbonate+ β-$Fe_{2.771}Mg_{0.229}O_4$+*tI*-$Fe_3O_4$ |
| | | 293 | carbonate+ β-$Fe_{2.771}Mg_{0.229}O_4$+*tI*-$Fe_3O_4$ |
| | | 2420(200) | carbonate+ β-$Fe_{2.771}Mg_{0.229}O_4$+*tI*-$Fe_3O_4$ |

**Table S2.** Details of the crystal structure refinements of novel $Fe_3O_4$ phases observed at 78(1) GPa.

| Crystal data | | |
|---|---|---|
| Chemical formula | $Fe_3O_4$ | $Fe_3O_4$ |
| $M_r$ | 231.5 | 231.5 |
| Crystal system, space group | Orthorhombic, *Pnma* | Tetragonal, $I\bar{4}2d$ |
| Temperature, K | 293 | 293 |
| *a*, Å | 8.574(10) | 5.866(3) |
| *b*, Å | 2.6356(13) | 5.866(3) |
| *c*, Å | 8.761(3) | 5.938 (3) |
| *V*, Å$^3$ | 198.0(3) | 204.34(16) |
| *Z* | 4 | 4 |
| Radiation type | λ = 0.2885 Å | X-ray, λ = 0.28850 Å |
| Radiation source | P02.2, Petra III, DESY | P02.2, Petra III, DESY |
| μ (mm$^{-1}$) | 1.60 | 1.70 |
| Crystal size (mm) | 0.003 | 0.003 |
| Diffractometer | Customized ω-circle diffractometer | |
| Absorption correction | Multi-scan<br>*CrysAlis PRO* 1.171.40.67a (Rigaku Oxford Diffraction, 2019) Empirical absorption correction using spherical harmonics, implemented in SCALE3 ABSPACK scaling algorithm. | |
| $T_{min}$, $T_{max}$ | 0.227, 1 | 0.150, 1.000 |
| No. of measured, independent and observed [$I > 2\sigma(I)$] reflections | 908, 399, 300 | 403, 222, 192 |
| $R_{int}$ | 0.043 | 0.033 |
| $(\sin\theta/\lambda)_{max}$, Å$^{-1}$ | 1.057 | 1.053 |
| Refinement | | |
| $R[F^2 > 2\sigma(F^2)]$, $wR(F^2)$, *S* | 0.076, 0.077, 1.75 | 0.088, 0.224, 1.11 |
| No. of reflections | 399 | 222 |
| No. of parameters | 31 | 12 |
| $\Delta\rho_{max}$, $\Delta\rho_{min}$, e·Å$^{-3}$ | 2.50, −1.68 | 1.78, −2.05 |

**Table S3.** Fractional atomic coordinates and isotropic (*) or equivalent isotropic displacement parameters of $\gamma$-$Fe_3O_4$ with $Yb_3S_4$ type of structure (space group *Pnma*, *a*=8.574(10) Å, *b*=2.6356(13) Å, *c*=8.761(3) Å) at 78(1) GPa.

| | ***x*** | ***y*** | ***z*** | $U_{iso}$*/$U_{eq}$ |
|---|---|---|---|---|
| **Fe1** | 0.1484(3) | 0.25 | 0.2020(2) | 0.0119(7) |
| **Fe2** | 0.3654(3) | 0.25 | 0.4001(2) | 0.0123(7) |
| **Fe3** | 0.1006(3) | 0.25 | 0.5687(2) | 0.0115(6) |
| **O1** | 0.032(2) | 0.25 | 0.3720(7) | 0.0141(1)* |
| **O2** | 0.258(2) | 0.25 | 0.0200(8) | 0.0138(1)* |
| **O3** | 0.464(2) | 0.25 | 0.6096(8) | 0.016(1)* |
| **O4** | 0.204(2) | 0.25 | 0.7504(8) | 0.0145(1)* |

**Table S4.** Selected geometric parameters of $\gamma$-$Fe_3O_4$ with $Yb_3S_4$ type of structure (space group *Pnma*, *a*=8.574(10) Å, *b*=2.6356(13) Å, *c*=8.761(3) Å) at 78(1) GPa.

| | ***distances, Å*** | | ***distances, Å*** |
|---|---|---|---|
| **Fe1—Fe1$^{i}$** | 2.636(3) | **Fe2—O3$^{viii}$** | 1.971(1) |
| **Fe1—Fe1$^{ii}$** | 2.636(3) | **Fe2—O3$^{ix}$** | 1.971(1) |
| **Fe1—Fe2** | 2.544(4) | **Fe2—O4$^{iv}$** | 1.951(6) |
| **Fe1—Fe2$^{iii}$** | 2.587(6) | **Fe2—O4$^{v}$** | 1.951(6) |
| **Fe1—O1** | 1.794(9) | **Fe3—Fe3$^{i}$** | 2.636(3) |
| **Fe1—O2** | 1.852(9) | **Fe3—Fe3$^{ii}$** | 2.636(3) |
| **Fe1—O3$^{iv}$** | 1.822(8) | **Fe3—Fe3$^{x}$** | 2.482(4) |
| **Fe1—O3$^{v}$** | 1.822(8) | **Fe3—Fe3$^{xi}$** | 2.482(4) |
| **Fe1—O4$^{iv}$** | 1.876(9) | **Fe3—O1** | 1.821(8) |
| **Fe1—O4$^{v}$** | 1.876(9) | **Fe3—O1$^{x}$** | 1.815(9) |
| **Fe2—Fe2$^{i}$** | 2.636(3) | **Fe3—O1$^{xi}$** | 1.815(9) |
| **Fe2—Fe2$^{ii}$** | 2.636(3) | **Fe3—O2$^{vi}$** | 1.839(9) |
| **Fe2—O2$^{vi}$** | 1.991(8) | **Fe3—O2$^{vii}$** | 1.839(9) |
| **Fe2—O2$^{vii}$** | 1.991(8) | **Fe3—O4** | 1.822(9) |
| **Fe2—O3** | 2.021(9) | | |

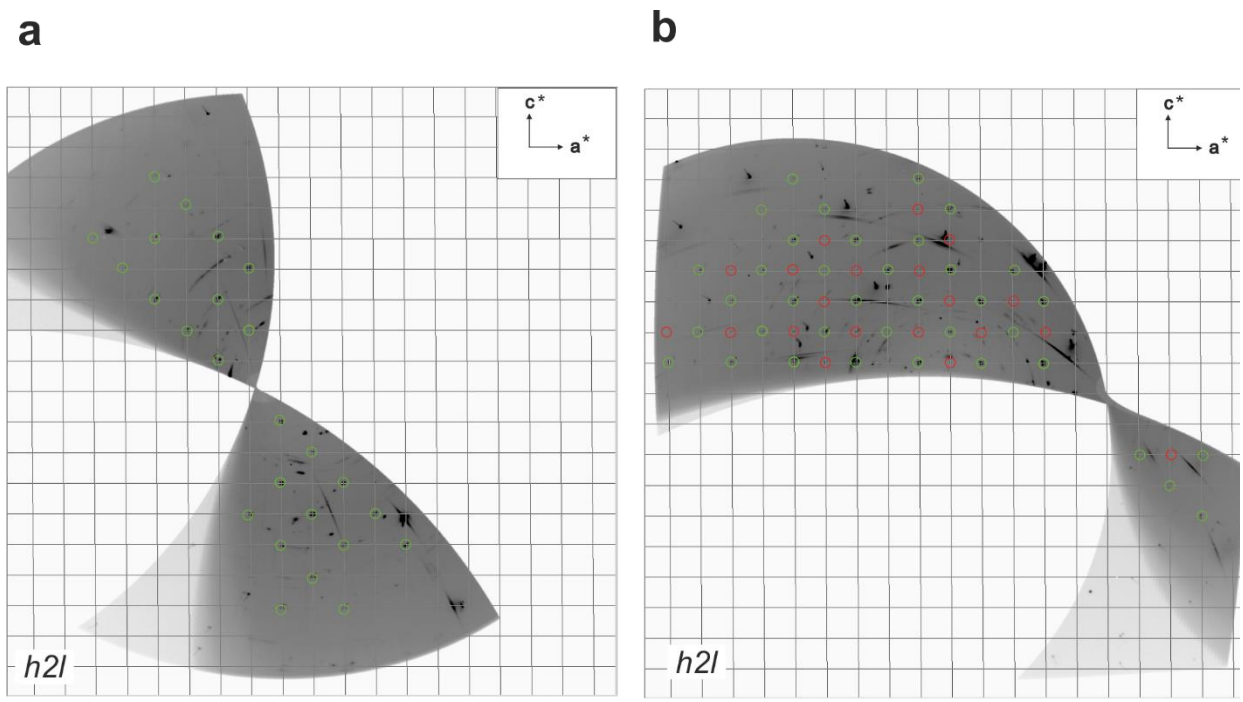


***Figure S2.*** *Reciprocal space reconstruction of (h2l) layer of two single crystal domains of tetragonal $Fe_3O_4$ phases observed in present study at 78(1) GPa after laser-heating temperatures at 4800(300 K): (a) first single-crystal domain, which crystal structure was solved and refined in space group* $I\bar{4}2d$ *(#122); (b) second single-crystal domain, which crystal structure was solved and refined in space group* $P\bar{4}$ *(#81). Green circles – reflections that are consistent with I-centering; red circles – reflections violating I-centering, suggesting* $P\bar{4}$ *space group.*

**Table S5.** Fractional atomic coordinates and isotropic (*) or equivalent isotropic displacement parameters of $\delta$-$Fe_3O_4$ with distorted $Th_3P_4$ type of structure at 78(1) GPa (space group $I\bar{4}2d$, $a$=5.8648(1) Å, $c$=5.948(2) Å).

| | ***x*** | ***y*** | ***z*** | $U_{iso}$*/$U_{eq}$ |
|---|---|---|---|---|
| **Fe1** | 0 | 0 | 0 | 0.0154(7) |
| **Fe2** | 0.3865(6) | 0.25 | 0.125 | 0.0176(6) |
| **O1** | 0.064(2) | 0.187(2) | 0.304(1) | 0.017(2)* |

**Table S6.** Fractional atomic coordinates and isotropic (*) or equivalent isotropic displacement parameters of $\delta$-$Fe_3O_4$ with distorted $Th_3P_4$ type of structure at 78(1) GPa (space group $P\bar{4}$, *a*= 5.8756(1) Å, c= 5.8984(3) Å).

| | ***x*** | ***y*** | ***z*** | $U_{iso}$*/$U_{eq}$ |
|---|---|---|---|---|
| **Fe1** | 0 | 0 | 0 | 0.0066(8) |
| **Fe2** | 0.5 | 0.5 | 0.5 | 0.113(5) |
| **Fe3** | 0 | 0.5 | 0.2469(7) | 0.0222(9) |
| **Fe4** | 0.6140 (5) | 0.2516(7) | 0.1228(5) | 0.0210(7) |
| **Fe5** | 0.2491 (5) | 0.1156(5) | 0.3760(5) | 0.0181(6) |
| **O1** | 0.3229 (18) | 0.0583(18) | 0.0514(14) | 0.005(2)* |
| **O2** | 0.175 (2) | 0.440(2) | 0.538(2) | 0.015(3)* |
| **O3** | 0.172 (7) | 0.049(4) | 0.686(6) | 0.074(11)* |
| **O4** | 0.302 (4) | 0.433(3) | 0.224(5) | 0.039(5)* |

**Table S7.** Fractional atomic coordinates of the model used for Le Bail fit of powder XRD pattern collected for *monoclinic* $Fe_3O_{4-\delta}$ phase (space group *I2*) that appeared after prolong laser heating cycle at 78(2) GPa at 13IDD, GSECARS, APS. Lattice parameters (*a*=6.103(1) Å, b=5.787(1), *c*=5.958(1) Å, β=91.73(1)˚, V=210.33(1) $Å^3$ ) were refined through Le Bail fit of powder XRD data of temperature quenched-sample at pressure of 78(1) GPa, based on Ne equation of state[1].

| | ***x*** | ***y*** | ***z*** |
|---|---|---|---|
| **Fe1** | 0.5 | 0.8440(12) | 0.5 |
| **Fe2** | 0.5 | 0.6276(10) | 1 |
| **Fe3** | 0.6286 7) | 0.2373(8) | 0.7523(9) |
| **Fe4** | 0.2429(7) | 0.4718(8) | 0.6386(10) |
| **O5** | 0.561(4) | 0.538(4) | 0.679(5) |
| **O6** | 0.684(4) | 0.162(4) | 0.444(5) |
| **O7** | 0.185(3) | 0.779(4) | 0.576(5) |
| **O4** | 0.429(4) | 0.911(5) | 0.196(6) |

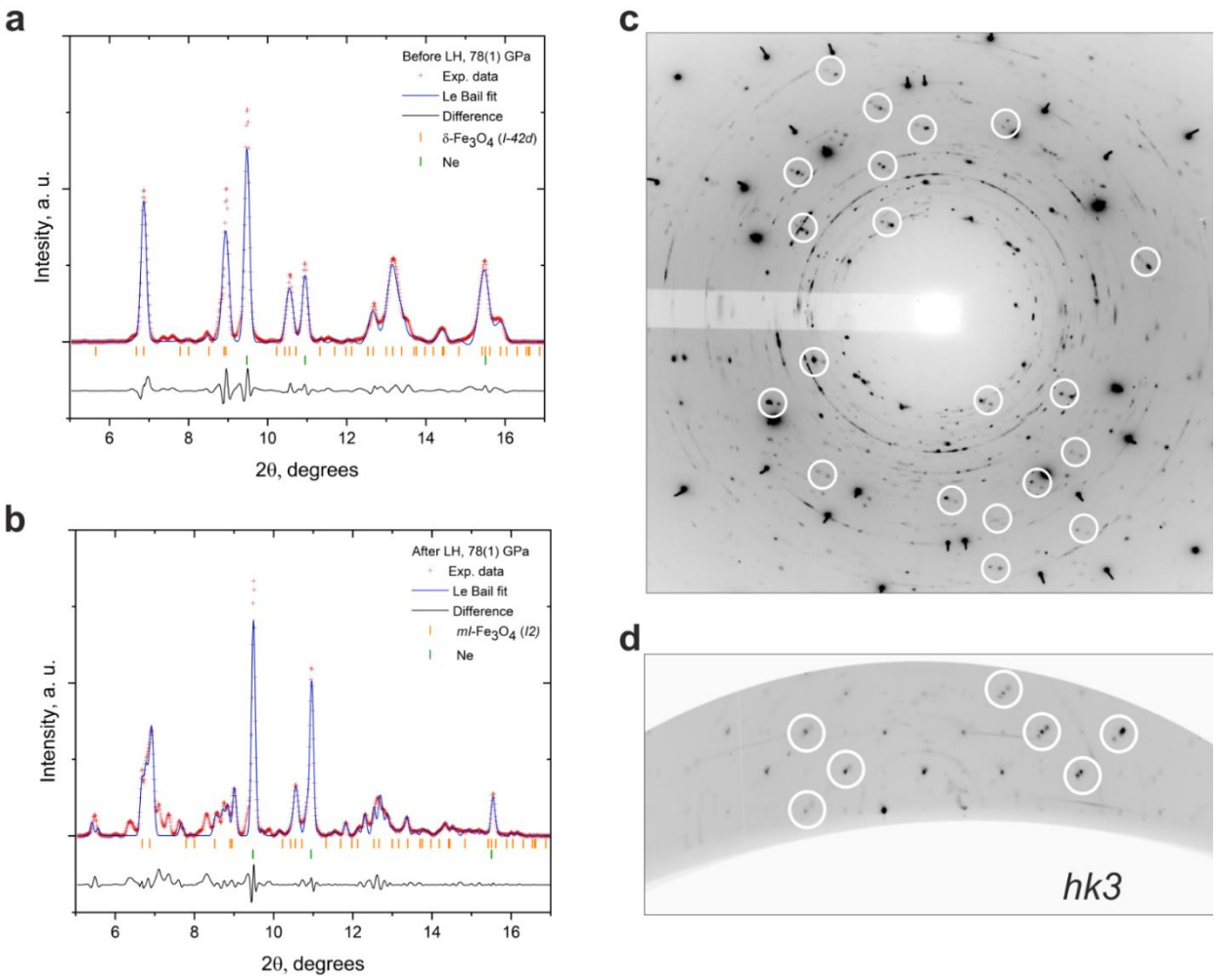


***Figure S3.*** *Powder diffraction patterns of: (a) δ-$Fe_3O_4$ (*$I\bar{4}2d$*, a=5.866(3) Å, c=5.938(3) Å, V=204.34(16) Å$^3$), $a_{Ne}$=3.032(1) Å; (b) mI-$Fe_3O_{4-\delta}$ (I2, a=6,103(1) Å, b=5.787(1), c=5.958(1) Å, β=91.73(1)°, V=210.33(1) Å$^3$), $a_{Ne}$=3.0314 (3) Å at 78(1) GPa, observed after prolong (about an hour) laser heating at ~3800 K. 2D X-ray diffraction image of mI-$Fe_3O_{4-\delta}$ (c) and reciprocal space reconstruction of (hk3) layer (d) reveal splitting of some reflections due to reduction of symmetry from* $I\bar{4}2d$ *to I2 space group. Pressure was determined by equation of state of Ne, reported in ref.* [1].

**Table S8.** Selected geometric parameters of $\delta$-$Fe_3O_4$ with distorted $Th_3P_4$ type of structure at 78(1) GPa *(*space group $I\bar{4}2d$, *a*=5.8648(1) Å, *c*=5.948(2) Å).

| | ***distances, Å*** | | ***distances, Å*** |
|---|---|---|---|
| **Fe1—Fe2$^{i}$** | 2.748(1) | **Fe2—Fe2$^{xiii}$** | 2.719(2) |
| **Fe1—Fe2$^{ii}$** | 2.748(1) | **Fe2—Fe2$^{xiv}$** | 2.719(2) |
| **Fe1—Fe2$^{iii}$** | 2.748(1) | **Fe2—O1$^{xv}$** | 2.115(1) |
| **Fe1—Fe2$^{iv}$** | 2.748(1) | **Fe2—O1$^{xiii}$** | 2.115(1) |
| **Fe1—O1** | 2.144(1) | **Fe2—O1$^{iv}$** | 1.963(9) |
| **Fe1—O1$^{v}$** | 1.903(1) | **Fe2—O1$^{viii}$** | 2.203(1) |
| **Fe1—O1$^{vi}$** | 1.903(1) | **Fe2—O1** | 2.203(1) |
| **Fe1—O1$^{vii}$** | 2.144(10) | **Fe2—O1$^{xi}$** | 1.937(1) |
| **Fe1—O1$^{viii}$** | 1.903(1) | **Fe2—O1$^{xvi}$** | 1.963(9) |
| **Fe1—O1$^{ix}$** | 2.144(10) | **Fe2—O1$^{xvii}$** | 1.937(1) |
| **Fe1—O1$^{x}$** | 2.144(10) | **O1—Fe1$^{xviii}$** | 1.903(1) |
| **Fe1—O1$^{xi}$** | 1.903(1) | **O1—Fe2$^{xix}$** | 1.963(9) |
| **Fe2—Fe2$^{iii}$** | 2.719(2) | **O1—Fe2$^{iii}$** | 2.115(1) |
| **Fe2—Fe2$^{xii}$** | 2.719(2) | **O1—Fe2$^{ii}$** | 1.937(1) |

**Table S9.** Details of the crystal structure refinements of β-$(Fe_{2.771}Mg_{0.229})O_4$ and δ-$Fe_3O_4$ phases observed at 58.6(5) GPa upon laser heating of $(Mg_{0.3}Fe_{0.7})CO_3$.

| Crystal data | | |
|---|---|---|
| Chemical formula | $Fe_3O_4$ | $Fe_{2.771}Mg_{0.229}O_4$ |
| $M_r$ | 231.5 | 224.3 |
| Crystal system, space group | Tetragonal, $I\bar{4}2d$ | Orthorhombic, *Cmcm* |
| Temperature (K) | 293 | 293 |
| *a*, Å | 5.9935 (10), | 2.658 (7), |
| *b*, Å | 5.9935 (10), | 8.861 (3), |
| *c*, Å | 5.9122 (10) | 9.063 (3) |
| *V*, Å$^3$ | 212.38 (6) | 213.5 (6) |
| *Z* | 4 | 4 |
| Radiation type | X-ray, λ = 0.2952 Å | X-ray, λ = 0.2952 Å |
| Radiation source | 13IDD, GSECARS, APS | 13IDD, GSECARS, APS |
| μ (mm$^{-1}$) | 1.58 | 1.47 |
| Crystal size (mm) | | 0.003 |
| Diffractometer | Customized ω-circle diffractometer | |
| Absorption correction | Multi-scan<br>*CrysAlis PRO* 1.171.40.63a (Rigaku Oxford Diffraction, 2019) Empirical absorption correction using spherical harmonics, implemented in SCALE3 ABSPACK scaling algorithm. | |
| $T_{min}$, $T_{max}$ | 0.646, 1 | 0.167, 1 |
| No. of measured, independent and observed [$I > 3\sigma(I)$] reflections | 602, 221, 201 | 334, 127, 89 |
| $R_{int}$ | 0.062 | 0.026 |
| $(\sin\theta/\lambda)_{max}$ (Å$^{-1}$) | 0.861 | 0.894 |
| Refinement | | |
| $R[F^2 > 3\sigma(F^2)]$, $wR(F^2)$, *S* | 0.041, 0.067, 1.77 | 0.098, 0.101, 3.30 |
| No. of reflections | 221 | 127 |
| No. of parameters | 17 | 15 |
| $\Delta\rho_{max}$, $\Delta\rho_{min}$ (e Å$^{-3}$) | 1.18, −1.30 | 3.04, −1.95 |

**Table S10**. Details of the crystal structure refinements of $Fe_5O_7$ and $Fe_{25}O_{32}$

| Chemical formula | $Fe_5O_7$ | $Fe_{25}O_{32}$ |
|---|---|---|
| P, GPa | 78(1) | 65(1) |
| $M_r$ | 391.2 | 1908.1 |
| Crystal system, space group | Monoclinic, *C*2/*m* | Hexagonal, *P*-62*m* |
| *a*, *c* (Å) | 8.646 (4) | 13.626 (3) |
| *b* | 2.6183 (5) | 13.626 (3) |
| *c* | 7.9508 (17) | 2.6598 (7) |
| α (°) | 90 | 90 |
| β (°) | 105.82 (4) | 90 |
| γ (°) | 90 | 120 |
| *V* (Å$^3$) | 173.18(10) | 427.68 (17) |
| *Z* | 2 | 1 |
| Radiation type | X-ray<br>λ = 0.2952 Å | X-ray<br>λ = 0.2895 Å |
| Radiation source | 13 IDD, GSECARS, APS | P02.2, Petra III, DESY |
| μ (mm$^{-1}$) | 1.62 | 1.55 |
| Diffractometer | Customized ω-circle diffractometer | |
| Absorption correction | Multi-scan *CrysAlis PRO* 1.171.40.67a (Rigaku Oxford Diffraction, 2019) Empirical absorption correction using spherical harmonics, implemented in SCALE3 ABSPACK scaling algorithm. | |
| $T_{min}$, $T_{max}$ | 0.343, 1 | 0.687, 1 |
| Index ranges | *h* = −10→8 | *h* = −15→15 |
| | *k* = −4→4 | k = −5→9 |
| | *l* = −13→12 | *l* = −3→2 |
| No. of measured, independent and observed [$I > 2\sigma(I)$] reflections | 249, 157, 136 | 494, 270, 242 |
| $R_{int}$ | 0.019 | 0.047 |
| $(\sin\theta/\lambda)_{max}$ (Å$^{-1}$) | 0.845 | 0.587 |
| $R[F^2 > 2\sigma(F^2)]$, $wR(F^2)$, *S* | 0.043, 0.094, 2.25 | 0.051, 0.100, 1.46 |
| No. of reflections | 157 | 270 |
| No. of parameters | 18 | 34 |
| $\Delta\rho_{max}$, $\Delta\rho_{min}$ (e Å$^{-3}$) | 1.02, −1.39 | 1.24, −1.11 |

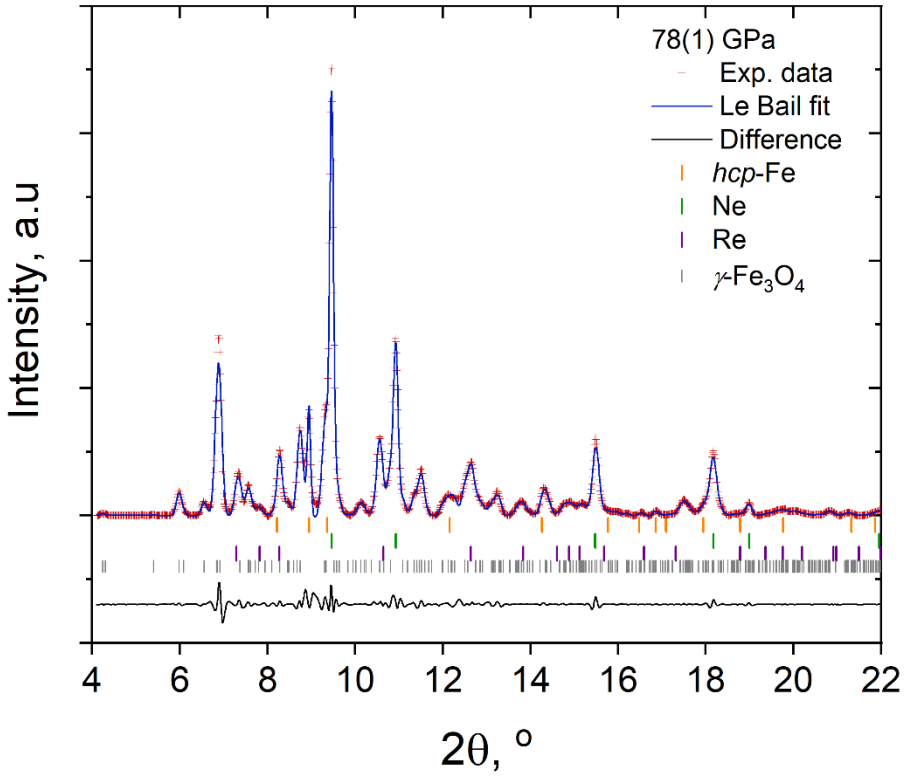


***Figure S4.*** *Le Bail fit of integrated powder XRD pattern of the sample of $Fe_3O_4$ at 78(1) GPa and after laser heating at 2700(200) K. Le bail fit was performed using Jana2006 software[2]. Orange ticks corresponds to the reflection of hcp-Fe (a=2.3238(8) Å, c=3.7001(5) Å, V=17.303(1) Å$^3$, 83(2) GPa, according to EoS from ref.[3], green ticks – Ne (a=3.030(2) (4) Å, V=27.808(2) Å$^3$, $P_{Ne}$=78(1) GPa), according to EoS from ref.[1], purple ticks represent parasitic scattering from Re gasket (a=2.6206(5) Å, c=4.229(2) Å, V=25.153(2) Å$^3$, 78(3) GPa, according to EoS from ref.[4]), grey ticks are reflections from the γ-$Fe_3O_4$ phase (a=8.574(10) Å, b=2.6356(13) Å, c=8.761(3) Å, V=198.0(3) Å$^3$).*

**Table S11.** Lattice parameters of *hcp*-Fe and Ne obtained as a result of Le Bail analysis of XRD data collected at different pressures. Pressure values are given, according to EoS of Ne[1] and *hcp*-Fe[3].

| ***a (Fe), Å*** | ***c (Fe), Å*** | ***V (Fe), Å³*** | ***P (Fe), GPa*** | ***V (Ne), Å³*** | ***P (Ne), GPa*** |
|---|---|---|---|---|---|
| 2.3238(8) | 3.7001(5) | 17.303(1) | 83(2) | 27.807(2) | 79(1) |
| 2.3324(6) | 3.7096(11) | 17.477(2) | 77(2) | 28.312 (3) | 74(1) |
| 2.3501(10) | 3.7589(27) | 17.979(30 | 63(2) | 29.140(4) | 66(1) |

**Table S12**. Lattice parameters of $Fe_5O_7$ as function of pressure. Pressure determined from the equation of state for Ne[1]

| ***P, GPa*** | ***a, Å*** | ***b, Å*** | ***c, Å*** | ***β (°)*** | ***V, Å³*** |
|---|---|---|---|---|---|
| 79.8(6) | 8.656(2) | 2.607(2) | 7.918(1) | 105.71(2) | 171.96(5) |
| 78.3(7) | 8.646(4) | 2.6183(5) | 7.951(2) | 105.82(8) | 173.2(1) |
| 71.7(6) | 8.749(7) | 2.6030(9) | 7.982(3) | 105.31(7) | 175.3(2) |
| 66.0(5) | 8.777(6) | 2.6111(9) | 8.029(4) | 105.36(6) | 177.4(2) |
| 65.0(7) | 8.808(5) | 2.6181(10) | 8.066(5) | 106.53(6) | 178.3(2) |
| 56.4(9) | 8.782(6) | 2.6536(8) | 8.097(4) | 105.44(6) | 181.9(2) |
| 51.4(8) | 8.879(4) | 2.6648(5) | 8.100(2) | 105.85(4) | 184.4(1) |
| 34.2(6) | 9.289(2) | 2.753(2) | 8.367(5) | 105.3(1) | 206.4(4) |
| 29.3(5) | 9.289(2) | 2.753(2) | 8.367(5) | 105.3(1) | 206.4(4) |
| 20.0(3) | 9.430(8) | 2.775 (1) | 8.444(3) | 105.34(7) | 213.1(2) |
| 10.1(1) | 9.526(1) | 2.805(3) | 8.570(7) | 105.42(1) | 220.7(4) |

**Table 13**. Lattice parameters of $Fe_{25}O_{32}$ as function of pressure. Pressure determined from the equation of state for Ne[1]

| ***P, GPa*** | ***a, Å*** | ***c, Å*** | ***V, Å³*** |
|---|---|---|---|
| 79.8(6) | 13.464(2) | 2.6280(7) | 412.6(2) |
| 71.7(6) | 13.565(6) | 2.6363(1) | 420.1(3) |
| 66.0(5) | 13.606(3) | 2.6587(1) | 426.2(2) |
| 65.0(5) | 13.626(3) | 2.6598(7) | 427.7(2) |
| 56.4(8) | 13.719(6) | 2.6652(7) | 434.4(3) |
| 51.4(8) | 13.786(5) | 2.6704(7) | 439.5(2) |
| 40.0(7) | 13.913(8) | 2.7309(5) | 457.8(4) |

**Table 14**. Lattice parameters of δ-$Fe_3O_4$ as function of pressure. Pressure determined from the equation of state for Ne[1]

| ***P, GPa*** | ***a, Å*** | ***c, Å*** | ***V, Å³*** |
|---|---|---|---|
| 79.8(6) | 5.853(2) | 5.917(3) | 202.72(2) |
| 78.3(7) | 5.867(3) | 5.939(3) | 204.44(2) |
| 71.7(6) | 5.872(3) | 6.010(4) | 207.2(2) |
| 66.0(5) | 5.947(3) | 5.915(5) | 209.2(3) |
| 65.0(7) | 5.991(3) | 5.841(1) | 209.7(2) |
| 56.4(9) | 5.993(4) | 5.993(4) | 215.3(2) |
| 51.4(8) | 6.060(5) | 5.905(7) | 216.8(4) |

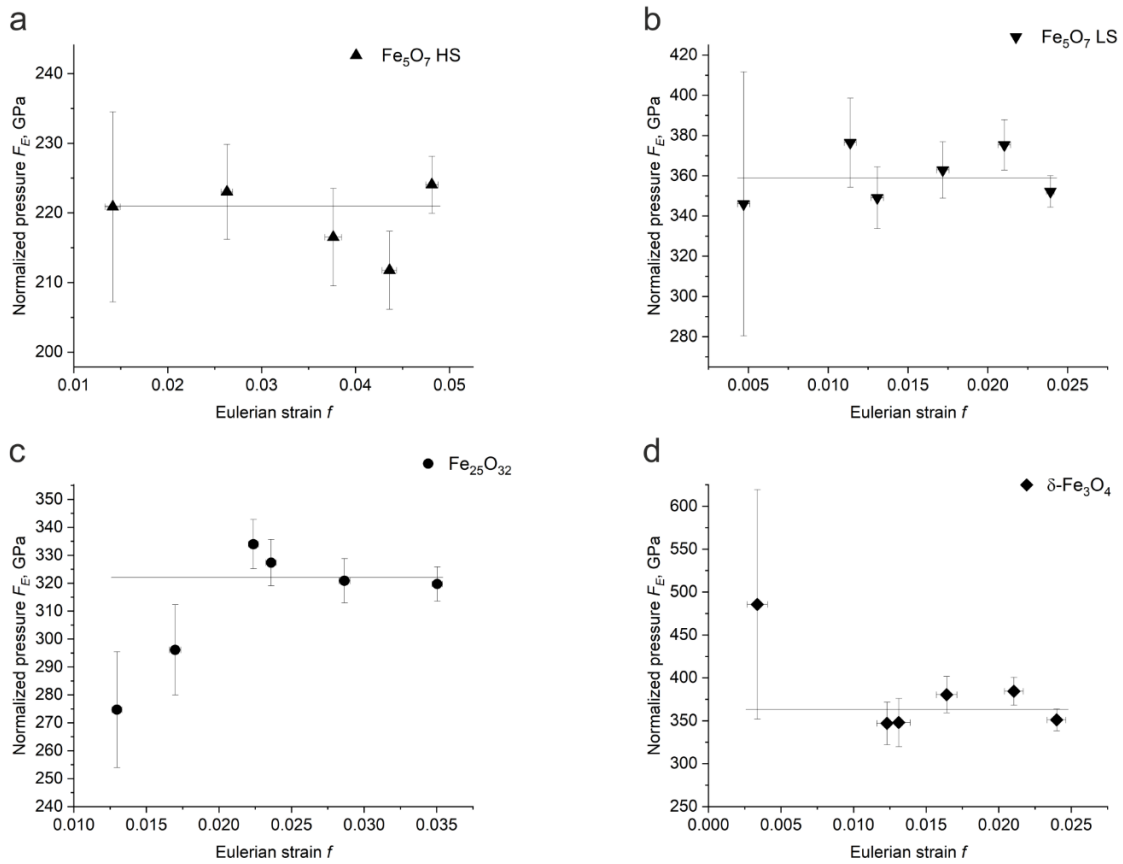


***Figure S5**. Normalized pressure - Eulerian strain ($F_E$-f) plot (b) based on 2nd order Birch-Murnaghan equation of state of $V_0$=230.1(8) Å³, $K_0$=221(9) GPa, and $V_{51GPa}$=184.4(3) Å³, $K_{51GPa}$=359(12) GPa for $Fe_5O_7$ (a, b); $V_{40GPa}$=457(1) Å³, $K_{40GPa}$=322(15) GPa for $Fe_{25}O_{32}$ (c) and $V_{51\ GPa}$=217.5(6) Å³, $K_{51\ GPa}$=363(22) GPa for δ-$Fe_3O_4$ (d).*

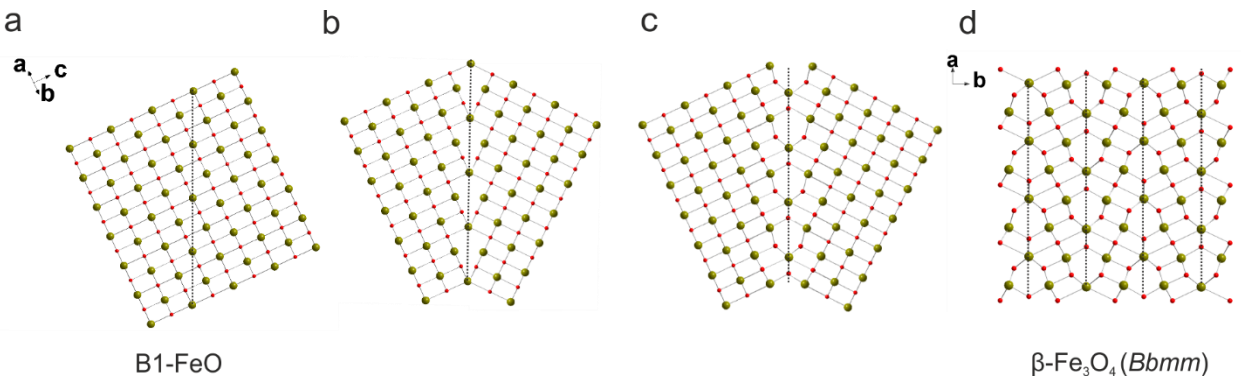


***Figure S6.*** *Twin relations between B1-structured FeO and β-$Fe_3O_4$. (a) Structure of B1-FeO projected on {110} direction, with cut on {113} shown by dotted line (green balls are Fe atoms, red balls are O atoms); (b) right-hand half rotated by 180˚ about <113>; (c) the same as (b), but the trigonal prisms are occupied by a single Fe atom on midway; (d) a crystal structure of β-$Fe_3O_4$, where $Fe^{2+}$ ions are localized in trigonal prisms (or capped trigonal prisms) at "twinning" boundary.*

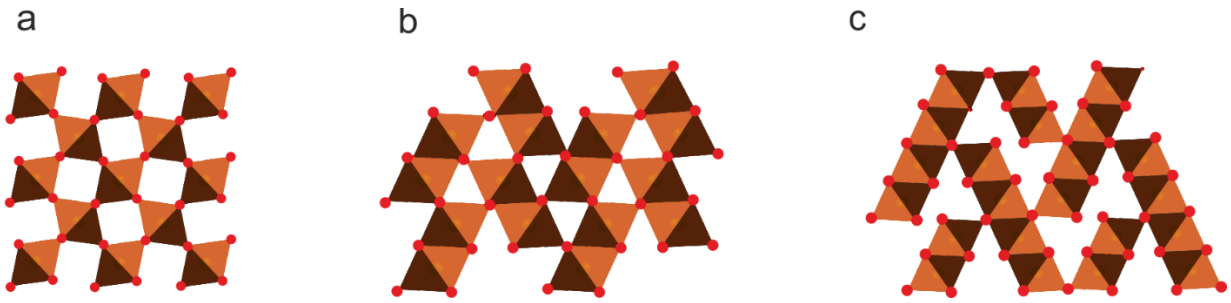


***Figure S7.*** *Different types of structure that can be achieved through the variation of octahedral packing for $Fe_3O_4$ stoichiometry: (a) a hypothetic rutile-like structure, composed of one octahedra ribbon (octahedral columns); (b) octahedral arrangement in β-$Fe_3O_4$ ($CaTi_2O_4$-type of structure) build of two-octahedra ribbons; (c) packing of four octahedra ribbons in the crystal structure of γ-$Fe_3O_4$ ($Yb_3S_4$-type of structure).*

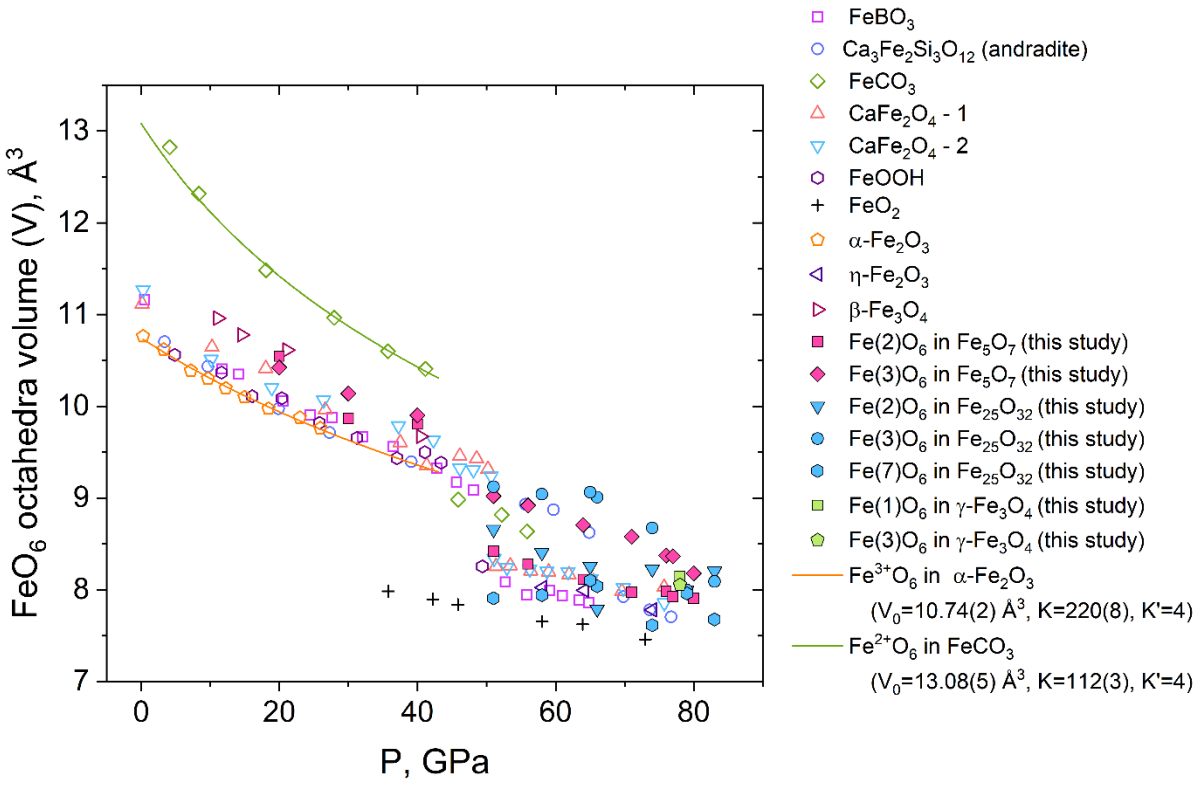


***Figure S8.*** *Pressure dependence of volumes of the $FeO_6$ octahedra in various compounds (extended and modified after ref.[5]). The compressional behavior of $Fe^{3+}O_6$ octahedra in $\alpha$-$Fe_2O_3$; $Fe^{2+}O_6$ octahedra in $FeCO_3$ in high spin state can be described by second-order Birch–Murnaghan equations of state (green and orange lines, parameters are given in figure's capture). Relative changes in volume of $FeO_6$ octahedra in $Fe_5O_7$ well corresponds to values known for other iron-bearing compounds; for example, at 43 GPa average volume of the octahedra is ~9.6 Å$^3$, and at 78 GPa - ~8.1 Å$^3$). However, octahedral volumes in $Fe_5O_7$ are higher than considered for pure $Fe^{3+}$, indicating a partial charge transfer on iron atoms in this compound between prismatic and octahedral sites*

## References

(1) Fei, Y.; Ricolleau, A.; Frank, M.; Mibe, K.; Shen, G.; Prakapenka, V. High-Pressure Geoscience Special Feature: Toward an Internally Consistent Pressure Scale. *Proc. Natl. Acad. Sci.* **2007**, *104* (22), 9182–9186. https://doi.org/10.1073/pnas.0609013104.

(2) Petříček, V.; Dušek, M.; Palatinus, L. Crystallographic Computing System JANA2006: General Features. *Zeitschrift für Krist. - Cryst. Mater.* **2014**, *229* (5), 345–352. https://doi.org/10.1515/zkri-2014-1737.

(3) Dubrovinsky, L. S.; Saxena, S. K.; Tutti, F.; Rekhi, S.; LeBehan, T. In Situ X-Ray Study of Thermal Expansion and Phase Transition of Iron at Multimegabar Pressure. *Phys. Rev. Lett.* **2000**, *84* (8), 1720–1723. https://doi.org/10.1103/PhysRevLett.84.1720.

(4) Anzellini, S.; Dewaele, A.; Occelli, F.; Loubeyre, P.; Mezouar, M. Equation of State of Rhenium and Application for Ultra High Pressure Calibration. *J. Appl. Phys.* **2014**, *115* (043511), 043511. https://doi.org/10.1063/1.4863300.

(5) Koemets, E.; Leonov, I.; Bykov, M.; Bykova, E.; Chariton, S.; Aprilis, G.; Fedotenko, T.; Clément, S.; Rouquette, J.; Haines, J.; Cerantola, V.; Glazyrin, K.; McCammon, C.; Prakapenka, V. B.; Hanfland, M.; Liermann, H.-P.; Svitlyk, V.; Torchio, R.; Rosa, A. D.; Irifune, T.; Ponomareva, A. V.; Abrikosov, I. A.; Dubrovinskaia, N.; Dubrovinsky, L. Revealing the Complex Nature of Bonding in the Binary High-Pressure Compound $FeO_2$. *Phys. Rev. Lett.* **2021**, *126* (10), 106001. https://doi.org/10.1103/PhysRevLett.126.106001.

# Chapter 6.1. Novel rhenium carbides at 200 GPa

Saiana Khandarkhaeva[1*], Timofey Fedotenko[2], Maxim Bykov[3], Elena Bykova[3], Stella Chariton[4], Pavel Sedmak[5], Konstantin Glazyrin[6], Vitali Prakapenka[4], Natalia Dubrovinskaia[2,7] and Leonid Dubrovinsky[1]

[1] *Bayerisches Geoinstitut, University of Bayreuth, Universitätstraße 30, 95440 Bayreuth, Germany*

[2] *Material Physics and Technology at Extreme Conditions, Laboratory of Crystallography University of Bayreuth, Universitätstraße 30, 95440 Bayreuth, Germany*

[3] *Geophysical Laboratory, Carnegie Institution of Washington, 5251 Broad Branch Road NW, 20015 Washington, District of Columbia, USA*

[4] *Center for Advanced Radiation Sources, University of Chicago, 5640 S. Ellis, 60637 Chicago, Illinois, USA*

[5] *European Synchrotron Radiation Facility, BP 220, 38043 Grenoble Cedex, France*

[6] *Photon Science, Deutsches Elektronen-Synchrotron, Notkestraße 85, 22607 Hamburg, Germany*

[7] *Theoretical Physics Division, Department of Physics, Chemistry and Biology (IFM) Linköping University, SE-581 83, Linköping, Sweden*

*Corresponding author: Saiana.Khandarkhaeva@uni-bayreuth.de

*Eur. J. Inorg. Chem.* **2020**, *2020* (22), 2186–2190. https://doi.org/10.1002/ejic.202000252.

## Abstract

Laser heating of rhenium in a diamond anvil cell to 3000±300 K at about 200 GPa results in formation of two previously unknown rhenium carbides, hexagonal WC-type structured ReC and orthorhombic $TiSi_2$-type structured $ReC_2$. The shortest C-C distances (1.758(3) Å at 219(5) GPa and 1.850(4) Å at 180(7) GPa) found in honeycomb-like carbon nets in the structure of $ReC_2$

are quite unusual. The Re-C solid solution formed at multimegabar pressure has the carbon content of ~20 at%.

## Introduction

Chemical compounds of 5d transition metals and carbon or other first-row elements, as B and N, often possess interesting properties attributed to strong covalent bonding.[1] Many of carbides, borides, and nitrides reveal very high melting points (for example, over 3500 K for ZrC, NbC, HfC, TaC),[2] large bulk moduli ($K_0$>390 GPa for $Re_2C$,[3] $Re_2N$,[4] $ReN_2$,[5] $IrN_2$,[6] OsB,[7] $Os_2B_3$,[7] $OsB_2$[7]), and very high hardness ($H_v$>35 GPa for $ReN_2$,[5] $WB_4$[7]). Transition-metal carbides belong to a large group of industrially important materials.

The rhenium-carbon system provides a striking example of the pressure effect on elements reactivity and the binary phase diagram. At ambient pressure, rhenium does not form stoichiometric carbides; carbon dissolves into rhenium up to 28.45 at% at the eutectic temperature (2778 K).[8] However, even very moderate pressure, just above 6 GPa (and high temperatures) was reported to promote formation of a Re-C compound.[9,10] Its correct chemical composition ($Re_2C$) and crystal structure of anti-$MoS_2$ type (hexagonal primitive, *hP*, space group $P6_3/mmc$) were established relatively recently on the basis of X-ray powder diffraction, Raman spectroscopy data and DFT calculations.[11,12] No other stoichiometric carbides apart of *hP*-$Re_2C$ have been observed at pressures up to ~70 GPa and temperatures ~4000 K.[3]

The *hP*-$Re_2C$ was found to be isostructural with $Re_2N$.[11] This analogy and the recently observed very complex and unexpected behavior of the Re-N system, featuring numerous nitrogen-rich compounds,[5,13] stimulated the study of potential reactions between Re and C at multimegabar pressures. Awareness of these reactions is also of a primary interest for the development of the methodology of ultra-high pressure high temperature experiments, in which Re gaskets are commonly used. The range of currently achievable static pressures has been extended to ~1000 GPa due to implementation of double-stage diamond anvil cells (dsDAC) and to ~600 GPa with toroidal type anvils (tDAC).[14–17] In order to achieve such extreme pressures, the linear size of samples and sample chambers should be drastically decreased. At pressures above ~150 GPa, a pressure chamber's diameter (made, as a rule, of Re) is usually smaller than 50 μm, and in dsDACs above 300 GPa it is less than 10 μm. Meanwhile, the size of a laser beam in typical

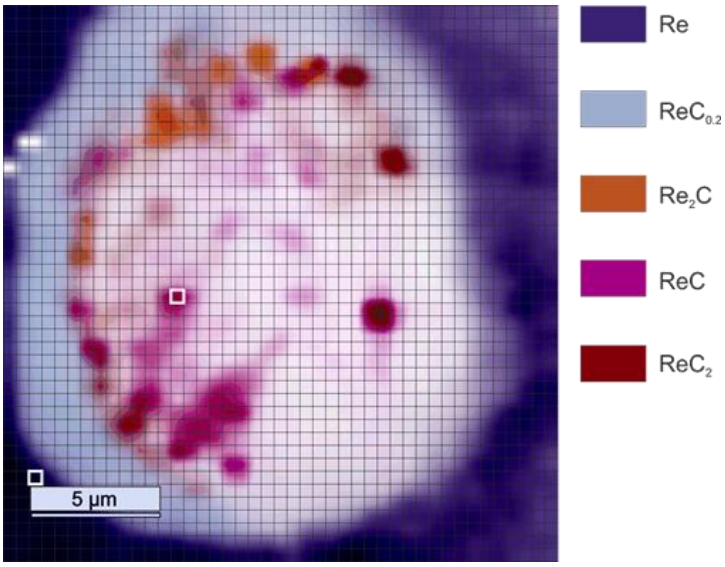


***Figure 1.*** *2D map of X-ray diffraction patterns. The color intensity is proportional to the intensity of the following reflections: the (100) and (101) reflections of the Re gasket for the violet region; the (100) and (101) reflections of $ReC_{0.2}$ for the light blueish-gray region; the (105) reflection of $Re_2C$ for the orange region; the (101) reflection of ReC with the WC-type structure for the purple region; the (002), (111), (020) reflections of $ReC_2$ for the dark red region. Characteristic diffraction images highlighted with white rectangles are shown in Figure S2.*

laser heating (LH) setups used in DAC experiments varies from 15 to 50 µm at FWHM.[18,19] As a result, irradiation of, at least the edge of a Re-gasket, by the laser beam during laser heating becomes unavoidable and may lead to a chemical reaction between Re and carbon of the diamond anvils. Therefore, correct interpretation of the results of experiments with laser-heating at ultra-high static pressures requires knowledge about possible products of rhenium and carbon interaction.

Here, we report on the *in situ* study of Re-C compounds formed due to chemical interactions between diamond anvils and the rhenium gasket after pulsed laser heating in DACs at about 200 GPa. The structures of all of the synthesized rhenium carbides, $Re_2C$, $ReC_2$, ReC, and $ReC_{0.2}$ were solved and refined using single-crystal X-ray diffraction (SCXRD) providing direct and unequivocal data to judge on both the atomic arrangement and chemical composition of the crystalline matter.

## Experiment

Two DACs have been prepared, dsDAC for Experiment #1 and conventional assembly for Experiment #2 (for details see Supporting Information, DAC preparation). Secondary anvils for Experiment #1 were made from nano-crystalline diamond (NCD) spheres of about 15-20 μm in diameter. The dsDAC in Experiment #1 was compressed up to ~415 GPa (according to the diamond Raman shift on the secondary anvil),[20] then the sample (Re flakes) was laser heated until the first bright flash of light that held for less than a second (temperature was not measured). After the first heating attempt pressure dropped down to ~200 GPa probably due to failure of the secondary anvils. However, the DAC remained intact and rhenium in the central area was again carefully laser heated in a pulsed mode (1 μs pulses, 25 kHz repetition rate, and maximum temperature of 3000±300 K).[21] Pressure did not change upon the repeated laser heating (Supporting Information, Figure S1) and the DAC with the temperature-quenched material was investigated using powder and single crystal X-ray diffraction (for details see the Supporting Information). A 2D diffraction map collected across the sample chamber revealed the presence of not only Re, but four additional phases (Figure 1). All of them have been identified and are described in detail below.

## Results and discussion

The XRD patterns collected from the edge of the Re-gasket show typical continuous powder diffraction rings of rhenium (Supporting Information, Figure S2a) not exposed to the laser beam. The unit cell volume of Re determined from the Le Bail fit varies from 22.000(5) $Å^3$ to 21.978(7) $Å^3$ for different patterns (Supporting Information, Figure S3). This corresponds to pressures of ~230-240 GPa according to equation of state (EOS) from Dubrovinsky et al.,[14] or ~190-195 GPa, according to Anzellini et al.[22] (Supporting Information, Table S1).

One of the crystalline phases we found within the laser-heated area is the hexagonal *hP*-$Re_2C$ (*P6₃/mmc*, #194) (Figure 2a).[11,12,23] The parameters of the unit cell were found to be *a*=2.5860(9) Å, *c*=9.272(3) Å, V=53.70(3) $Å^3$ (Supporting Information, Table S2, S3, Figure S4a). As written above, in this experiment the pressure, as determined from the Raman shift of the diamond anvil (Supporting Information, Figure S1), was of about 200 GPa, whereas the Re EOS

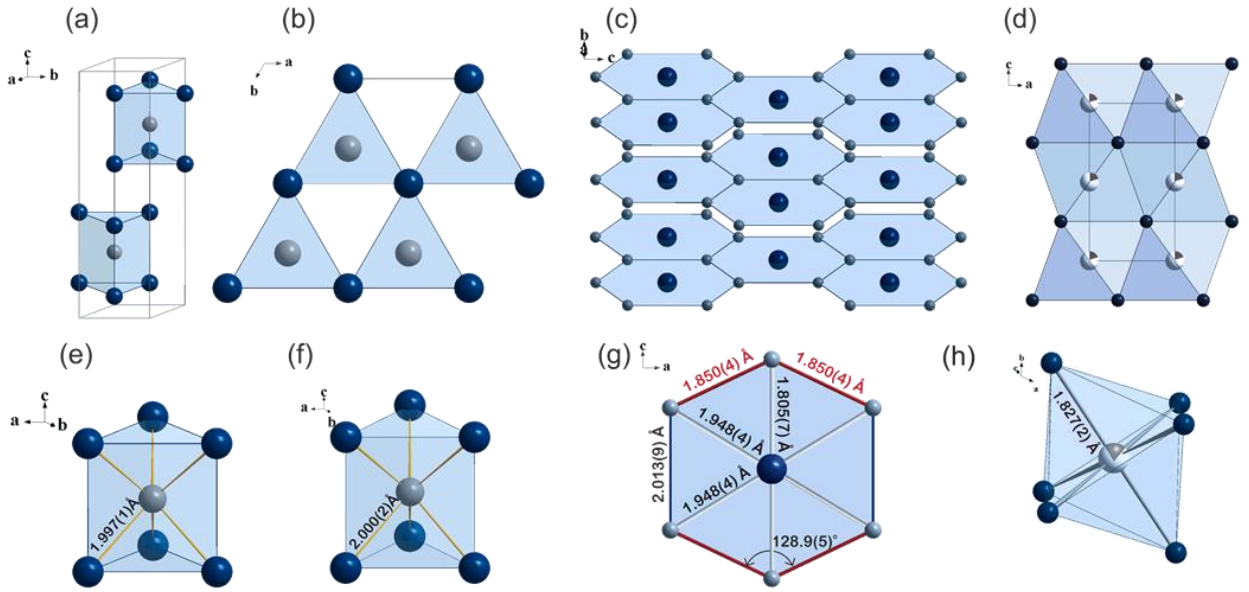


***Figure 2***. *Crystal structures of Re-C compounds observed in Experiment #1 at 180(7) GPa. (a) hP-$Re_2C$, (b) WC-type structured ReC, (c) $TiSi_2$-type structured oF-$ReC_2$; and (d) B8-type structured interstitial solid solution $ReC_{0.2}$. Dark blue balls designate Re atoms; dark gray balls – carbon atoms; white balls with a dark gray sector symbolize a partial occupancy of the position by carbon atoms. Carbon coordination polyhedra in the crystal structures of $Re_2C$ (e) and ReC (f) are strikingly similar with the Re-C bond length ~2 Å (shown by yellow color). (g) A single hexagon in the honeycomb-like web of carbon atoms, which coordinate each Re atom in the structure of $ReC_2$. (The shortest C-C distances of 1.850(4) Å are highlighted by red color. (h) A single octahedron formed by Re atoms in the structure of $ReC_{0.2}$, which incorporates carbon atoms with the occupancy of 20 %. The Re-C distances are relatively short (1.827(2) Å)*

gave up to 240 GPa. These values do not match the pressure of 172(13) GPa, determined for the given unit cell volume of *hP*-$Re_2C$ according to the EOS reported by Juarez-Arellano et al.[3] The EOS of $Re_2C$ in ref.[3] was determined on the basis of powder XRD from a sample in hard pressure transmitting medium that led to a significant uncertainty in the bulk modulus: K=405(30) GPa (K´=4.6).[3] Comparison of our data with literature motivated us to make an independent measurement to establish the EOS of *hP*-$Re_2C$ on the basis of SCXRD. In the experiment described in Supporting Information, Experimental Procedures, the P-V data were obtained up to 50 GPa from a single crystal of *hP*-$Re_2C$ pressurized in a soft (Ne) pressure transmitting medium (Supporting Information, Table S11, Figure S5). The parameters of the 3rd order Birch-Murnaghan equation of state of *hP*-$Re_2C$ ($V_0$=69.18(4) $Å^3$/unit cell, K=375(15) GPa, K´=5.0(1)) we obtained

only slightly (within uncertainties) differ from the values reported by Juarez-Arellano et al.[3] According to our EOS *hP*-$Re_2C$ synthesized in Experiment #1 was under the pressure of 180(7) GPa (Figure 3a). The structure of *hP*-$Re_2C$ (Figure 2a, Supporting Information, Table S3) determined from SCXRD is in a good agreement with model described by Friedrich et al.[11] It is characterized by the stacking sequence AABB of layers of Re atoms (with four Re atoms per a unit cell). Carbon atoms occupy the *2d* Wyckoff position in trigonal prisms formed by Re atoms with the Re-C distances of 1.997(1) Å (Figure 2e, Supporting Information, Table S4).

The structure of another phase, identified as ReC, has a hexagonal unit cell with the lattice parameters *a*=2.5510(9) Å, *c*=2.7048(11) Å, and *V*=15.24(1) $Å^3$ (Figure 1b) (Supporting Information, Table S2, S5, Figure S4b). The structure solution and refinement revealed that *hP*-ReC belongs to the WC structure type (*P-6m2*, #187) with characteristic *c/a* ratio (~0.94). Like in $Re_2C$, carbon atoms are located in trigonal prisms formed by Re atoms with the Re-C distances equal to 2.000(2) Å (Figure 2f, Supporting Information, Table S6).

One more carbide, $ReC_2$, with the orthorhombic structure found in Experiment #1 (Figure 2c, Supporting Information, Table S2, S7, Figure S4c) has the lattice parameters *a*=3.3367(10) Å, *b*=4.3155(16) Å, *c*=5.6220(13) Å, and V=80.95(4) $Å^3$ at 180(7) GPa, and a space group *Fmmm* (#69). Remarkably, the same orthorhombic phase (*a*=3.2880(9) Å, *b*=4.2088(9) Å, *c*=5.5645(8) Å, and V= 77.00(3) $Å^3$) was found in Experiment #2, in which iron oxide (FeO) in a Ne pressure medium was compressed to 219(5) GPa and pulsed-laser heated up to 2500±300 K.[19] The relatively large beam (of about 25 μm at FWHM) irradiated the Re gasket used in Experiment #2 and $ReC_2$ was found at the border of the pressure chamber.

The structure solution and refinement of the orthorhombic phase, in both Experiment #1 and #2, resulted in the chemical composition $ReC_2$. The structure shown in Figure 2c can be described as stacking of flat honeycomb-like nets of carbon atoms along the *b* direction with a translation (½, 0, ½). The “honeycomb” hexagons are not ideal (Figure 2g), they have two longer and four shorter sides (Supporting Information, Table S8). Rhenium atoms are located in the center of each of carbon hexagons (Figure 2g). Thus, in the same *ac*-plane each Re has 6 closest carbon neighbors, four of which are at a distance of 1.948(4) Å and two at 1.805(7) Å, as determined at 180(7) GPa (Supporting Information, Table S8). Note that whereas the description in terms of stacking of the Re-C nets obviously helpful to give a clear geometrical presentation of the atomic

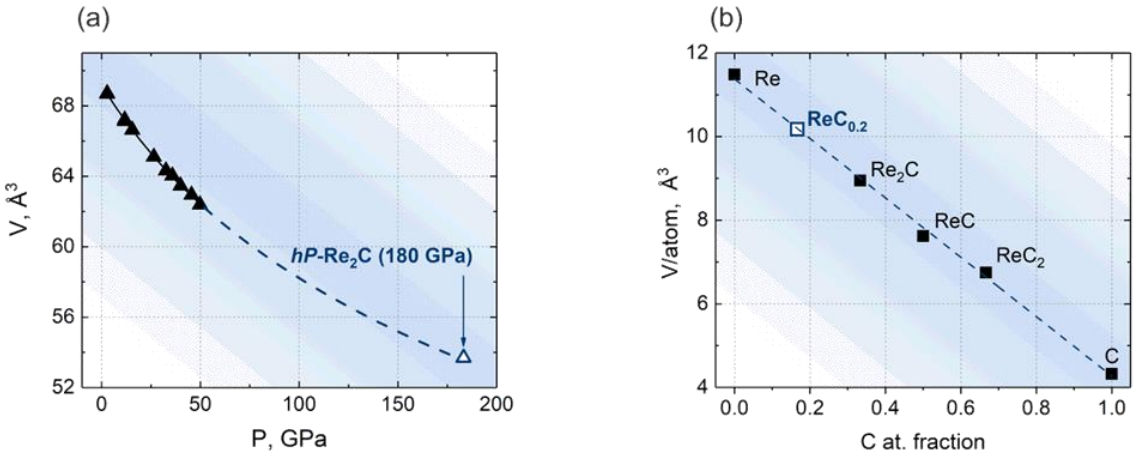


***Figure 3.*** *The unit cell volume of hP-$Re_2C$ as a function of pressure (a) and the dependence of the unit cell volumes per atom on the atomic fraction of carbon for various $Re_xC_y$ compounds at 180(7) GPa (b). Black triangles are experimental data points obtained using SCXRD on compression of hP-$Re_2C$ up to ~50 GPa in a soft (Ne) pressure transmitting medium. Solid black line is a fit of the P-V experimental data using the 3rd order Birch-Murnaghan EOS ($V_0$=69.18(4) Å$^3$/unit cell, K=375(15) GPa, K´=5.0(1)) and the dashed line is its extrapolation. Open triangle (corresponds to the volume obtained for hP-$Re_2C$ in one pressure point in Experiment #1 (see text). Black squares are experimental data points for observed Re-C compounds; open square designates $ReC_{0.2}$, in which the atomic fraction of carbon was determined in accordance with this empiric 'V/atom vs C at. fraction' relationship.*

arrangement in *oF*-$ReC_2$, the structure is not layered, as the shortest Re-Re distances between the "layers" (~2.72 Å) are similar to those in non-layered structures of *hP*-$Re_2C$ (~2.5-2.6 Å) and *hP*-ReC (~2.55-2.70 Å) at the same pressure.

It is worth noticing that in *oF*-$ReC_2$ the shortest C-C distances (1.758(3) Å at 219(5) GPa and 1.850(4) Å at 180(7) GPa) are up to 30%, or 20% larger than in $sp^2$- (~1.42 Å in graphite[24]) or $sp^3$- (~1.54 Å in diamond[25]) bonded carbon, correspondingly. This may suggest the absence of the chemical bonding between carbon atoms, but still, the latter should be proven by theoretical computations, which are out of scope of the present study. Some crystal-chemical analogy can be considered also, but it does not allow to make any definite conclusion regarding the chemical bonding in this particular case. Indeed, *oF*-$ReC_2$ is isostructural to one of the polymorphs of titanium disilicide ($TiSi_2$) (space group *Fmmm*, #69), a=4.428 Å, b=4.779 Å, c=9.078 Å, V=192.1 Å$^3$).[26] The shortest Si-Si distance in *oF*-$TiSi_2$ at ambient conditions is ~2.57 Å that is ca. 9% larger than in diamond-structured Si (~2.35 Å).[27] Any direct analogy is difficult to draw, as there

is no data on chemical bonding in *oF*-$TiSi_2$. Although *ab initio* simulations for one other polymorph of *oF*-$TiSi_2$ and a Zintl phase CaSi suggest a significant covalent interaction between Si atoms in zig-zag chains geometrically similar to the C-C chains in our *oF*-$ReC_2$ carbide, their Si-Si distances, of about 2.53 Å and 2.54 Å, correspondingly, are of only 8% larger than those in diamond-structured Si.[28,29]

Remarkably, there is a strong diffuse scattering, especially evident in the reciprocal space, suggesting a disorder along the *b*-axis in the structure of *oF*-$ReC_2$ (Supporting Information, Figure S6a). Those defects might help to stabilize the structure. In fact, the titanium disilicide *oF*-$TiSi_2$[26], which is isostructural to *oF*-$ReC_2$ (discussed above), is calculated to have the energy of about 0.3 eV/atom higher, than other titanium disilicide polymorphs[26. However, further studies are required to elaborate this hypothesis.

In the phase map built on the basis of powder XRD data (Figure 1), the light blueish-gray region indicates the phase filling the outer rim of the pressure chamber at the border with the Re gasket. On the basis of only powder XRD, it could be interpreted exclusively as Re at about 100 GPa, according to the EOS of Anzellini et al.[22] or at about 115 GPa, according to the EOS of Dubrovinsky et al.[14] that would be inconsistent with the pressure of 180(7) GPa determined previously. In a few points of this region it was possible to collect single-crystal data sets (Supporting Information, Figure S4d). Indexing of the single-crystal data gave the same result as that of powder XRD data: a hexagonal unit cell with the lattice parameters *a*=2.6028(12) Å, *c*=4.161(2) Å, *V*= 24.41(2) $Å^3$, and a space group *P6₃/mmc* (#194) (Supporting Information, Figure S4d, Table S2, S9). However, single-crystal data revealed the electron density, localized in the octahedral voids of the hcp-Re like in the B8 (NiAs)-type structure (Figure 2d) that suggests this phase to be a Re-C interstitial solid solution based on the B8-type structure (Figure 2d, h). Single-crystal diffraction data at hands are not sufficient to refine the site occupancies for carbon atoms, especially taking into account a huge difference in X-ray scattering factors of Re and C. Fortunately, we noticed that the unit cell volumes per atom for $Re_xC_y$ compounds (Re,[14] *hP*-$Re_2C$, *hP*-ReC, *oF*-$ReC_2$, and C (diamond)[30]) at 180(7) GPa, if plotted as a function of carbon content, all appear along the common straight line (Figure 3b). Considering the volume of the B8 rhenium-carbon solid solution, we have estimated its composition as $ReC_{0.2}$.

A comparison of our data for Re-C compounds and recent reports on the Re-N system demonstrates obvious crystal-chemical similarities in the two systems for compositions Re:C ≥1.

Two carbides, $Re_2C$ and ReC, are isostructural to $Re_2N$ and ReN. They are built up of $CRe_6$ or $NRe_6$ trigonal prisms, and even Re-C and Re-N interatomic distances at the same pressures are very similar.[4,5] Contrary, the structures of $ReC_2$ and $ReN_2$[5] have nothing in common and there are no signs of formation of rhenium polycarbides with more than two carbon atoms per a formula unit at least up to 180(7) GPa and 3000±300 K, unlike to the rhenium-nitrogen system.[13] Such differences can be linked a tendency of nitrogen to form di-nitrogen and poly-nitrogen anions (based on N4 units[13,31–33]) at high-pressures and high-temperatures (HPHT), whereas rhenium carbides do not reveal formation of polycarbon anions at such conditions.

Nevertheless, there is a number of experimental works and theoretical predictions that suggest progressive polymerization of carbon atoms at high pressures.[34–39] In all cases polymerization results in formation of short (~1.6 Å or shorter) C-C bonds for single bonded carbon atoms. For hexagonal carbides *hP*-$Re_2C$ or *hP*-ReC at ~200 GPa, the C-C distances are longer than 2.5 Å, which suggest the absence of chemical bonding between carbon atoms in the crystal structure. In case of rhenium dicarbide, *oF*-$ReC_2$, we observed formation of honeycomb-like carbon layers, in which the shortest C-C distances (~1.76-1.85 Å) are much longer than expected for $sp^2$- or $sp^3$-bonded carbon atoms in inorganic compounds; still, in alkanes the C-C bond length as long as 1.704 Å has been detected.[40]

## Conclusion

To summarize, we have extended the knowledge about the chemical interaction between rhenium and carbon to ~200 GPa. Two novel carbon-rich rhenium carbides – WC-type structured *hP*-ReC and $TiSi_2$-type structured *oF*-$ReC_2$ – were synthesized (hitherto only $Re_2C$ was known in the Re-C system). The fact that rhenium and carbon can produce numerous compounds at HPHT conditions should be taken into account upon planning of experiments in LHDACs at multimegabar pressures.

## Acknowledgements

N.D. and L.D. thank the Federal Ministry of Education and Research, Germany (BMBF, grants No. 5K16WC1 and No. 05K19WC1) and the Deutsche Forschungsgemeinschaft (DFG projects DU 954-11/1, DU 393-9/2, and DU 393-13/1) for financial support. N.D. thanks the Swedish Government Strategic Research Area in Materials Science on Functional Materials at Linköping University (Faculty Grant SFO-Mat-LiU No. 2009 00971). We acknowledge DESY (Hamburg, Germany), a member of the Helmholtz Association HGF, for the provision of experimental facilities. Parts of this research were carried out at Petra III and we would like to thank Dr. H.-P. Liermann for assistance in using photon beamline P02.2. We thank Dr. Alexander Kurnosov (Bayerisches Geoinstitut, Bayreuth) for assistance during the preparation of DACs.

**Keywords:** Rhenium • carbon • carbides • single-crystal X-ray diffraction • high-pressure chemistry

Detailed information on the crystal data obtained from single-crystal XRD refinement of the observed rhenium carbides at 180(7) GPa is provided in the Supporting Information, Table S2. CSD 1976969, 1976970, 1976971, 1976973 contain the supplementary crystallographic data of $Re_2C$, ReC, $ReC_{0.2}$ and $ReC_2$ correspondently. These data can be obtained from The Cambridge Crystallographic Data Centre.

## References

[1] M. T. Yeung, R. Mohammadi, R. B. Kaner, *Annu. Rev. Mater. Res.* **2016**, *46*, 465–485.

[2] H. O. Pierson, *Handbook of Refractory Carbides and Nitrides*, NOYES PUBLICATION, Westwood, New Jersey, U.S.A, **1996**.

[3] E. A. Juarez-Arellano, B. Winkler, A. Friedrich, L. Bayarjargal, V. Milman, J. Yan, S. M. Clark, *J. Alloys Compd.* **2009**, *481*, 577–581.

[4] A. Friedrich, B. Winkler, L. Bayarjargal, W. Morgenroth, E. A. Juarez-Arellano, V. Milman, K. Refson, M. Kunz, K. Chen, *Phys. Rev. Lett.* **2010**, *105*, 085504.

[5] M. Bykov, S. Chariton, H. Fei, T. Fedotenko, G. Aprilis, A. V. Ponomareva, F. Tasnádi, I. A. Abrikosov, B. Merle, P. Feldner, et al., *Nat. Commun.* **2019**, *10*, 2994.

[6] A. F. Young, C. Sanloup, E. Gregoryanz, S. Scandolo, R. J. Hemley, H. K. Mao, *Phys. Rev. Lett.* **2006**, *96*, 15501.

[7] Q. Gu, G. Krauss, W. Steurer, *Adv. Mater.* **2008**, *20*, 3620–3626.

[8] A. M. Kharkova, T. Y. Velikanova, *Poroshkovaya Metall.* **1988**, *12 (300)*, 994–997.

[9] S. V. Popova, L. G. Boiko, *High Temp. - High Press.* **1971**, *3*, 237–238.

[10] S. V. Popova, L. N. Fomicheva, L. G. Khvostantsev, *Sov. J. Exp. Theor. Phys. Lett.* **1972**, *16*, 429.

[11] A. Friedrich, B. Winkler, K. Refson, V. Milman, *Phys. Rev. B - Condens. Matter Mater. Phys.* **2012**, *86*, 014114.

[12] Z. Zhao, L. Cui, L. M. Wang, B. Xu, Z. Liu, D. Yu, J. He, X. F. Zhou, H. T. Wang, Y. Tian, *Cryst. Growth Des.* **2010**, *10*, 5024–5026.

[13] M. Bykov, E. Bykova, E. Koemets, T. Fedotenko, G. Aprilis, K. Glazyrin, H. Liermann, A. V Ponomareva, J. Tidholm, F. Tasn, et al., *Angew. Chemie - Int. Ed.* **2018**, *57*, 9048–9053.

[14] L. Dubrovinsky, N. Dubrovinskaia, V. B. Prakapenka, A. M. Abakumov, *Nat. Commun.* **2012**, *3*, 1163–1167.

[15] N. Dubrovinskaia, L. Dubrovinsky, N. A. Solopova, A. Abakumov, S. Turner, M. Hanfland, E. Bykova, M. Bykov, C. Prescher, V. B. Prakapenka, et al., *Sci. Adv.* **2016**, *2*, e1600341.

[16] A. Dewaele, P. Loubeyre, F. Occelli, O. Marie, M. Mezouar, *Nat. Commun.* **2018**, *9*, 2913.

[17] Z. Jenei, E. F. O'Bannon, S. T. Weir, H. Cynn, M. J. Lipp, W. J. Evans, *Nat. Commun.* **2018**, *9*, 3563.

[18] I. Kupenko, L. Dubrovinsky, N. Dubrovinskaia, C. McCammon, K. Glazyrin, E. Bykova, T. B. Ballaran, R. Sinmyo, A. I. Chumakov, V. Potapkin, et al., *Rev. Sci. Instrum.* **2012**, *83*,

124501.

[19] G. Aprilis, C. Strohm, I. Kupenko, S. Linhardt, A. Laskin, D. M. Vasiukov, V. Cerantola, E. G. Koemets, C. McCammon, A. Kurnosov, et al., *Rev. Sci. Instrum.* **2017**, *88*, 084501.

[20] N. Dubrovinskaia, L. Dubrovinsky, R. Caracas, M. Hanfland, *Appl. Phys. Lett.* **2010**, *97*, 1–4.

[21] T. Fedotenko, L. Dubrovinsky, G. Aprilis, E. Koemets, A. Snigirev, I. Snigireva, A. Barannikov, P. Ershov, F. Cova, M. Hanfland, et al., *Rev. Sci. Instrum.* **2019**, *90*, DOI 10.1063/1.5117786.

[22] S. Anzellini, A. Dewaele, F. Occelli, P. Loubeyre, M. Mezouar, *J. Appl. Phys.* **2014**, *115*, 043511.

[23] E. A. Juarez-Arellano, B. Winkler, A. Friedrich, D. J. Wilson, M. Koch-Müller, K. Knorr, S. C. Vogel, J. J. Wall, H. Reiche, W. Crichton, et al., *Z. Kristallogr.* **2008**, *223*, 492–501.

[24] P. Trucano, R. Chen, *Nature* **1975**, *258*, 136–137.

[25] T. Yamanaka, S. Morimoto, *Acta Crystallogr. Sect. B Struct. Sci.* **1996**, *52*, 232–238.

[26] P. L. Smith, R. Ortega, B. Brennan, *MRS Proc.* **1998**, *481*, 605–610.

[27] D. M. Többens, N. Stüßer, K. Knorr, H. M. Mayer, G. Lampert, *Mater. Sci. Forum* **2001**, *378–381*, 288–293.

[28] I. M. Kurylyshyn, T. F. Fässler, A. Fischer, C. Hauf, G. Eickerling, M. Presnitz, W. Scherer, *Angew. Chemie - Int. Ed.* **2014**, *53*, 3029–3032.

[29] M. Mizuno, I. Tanaka, H. Adachi, *Phys. Rev. B - Condens. Matter Mater. Phys.* **1999**, *59*, 15033–15047.

[30] F. Occelli, P. Loubeyre, R. Letoullec, *Nat. Mater.* **2003**, *2*, 151–154.

[31] D. Laniel, B. Winkler, E. Koemets, T. Fedotenko, M. Bykov, E. Bykova, L. Dubrovinsky, N. Dubrovinskaia, *Nat. Commun.* **2019**, *10*, 4515.

[32] M. Bykov, E. Bykova, G. Aprilis, K. Glazyrin, E. Koemets, I. Chuvashova, I. Kupenko, C. McCammon, M. Mezouar, V. Prakapenka, et al., *Nat. Commun.* **2018**, *9*, 1–8.

[33] M. Bykov, S. Khandarkhaeva, T. Fedotenko, P. Sedmak, N. Dubrovinskaia, L. Dubrovinsky, *Acta Crystallogr. Sect. E Crystallogr. Commun.* **2018**, *74*, DOI 10.1107/S2056989018012161.

[34] X. Q. Chen, C. L. Fu, C. Franchini, *J. Phys. Condens. Matter* **2010**, *22*, 292201.

[35] P. Srepusharawoot, A. Blomqvist, C. M. Araújo, R. H. Scheicher, R. Ahuja, *Phys. Rev. B - Condens. Matter Mater. Phys.* **2010**, *82*, 125439.

[36] Y. L. Li, S. N. Wang, A. R. Oganov, H. Gou, J. S. Smith, T. A. Strobel, *Nat. Commun.* **2015**, *6*, 6974.

[37] D. H. Wang, H. Y. Zhou, C. H. Hu, A. R. Oganov, Y. Zhong, G. H. Rao, *Phys. Chem. Chem. Phys.* **2014**, *16*, 20780–20784.

[38] T. A. Strobel, O. O. Kurakevych, D. Y. Kim, Y. Le Godec, W. Crichton, J. Guignard, N. Guignot, G. D. Cody, A. R. Oganov, *Inorg. Chem.* **2014**, *53*, 7020–7027.

[39] D. Benson, Y. Li, W. Luo, R. Ahuja, G. Svensson, U. Häussermann, *Inorg. Chem.* **2013**, *52*, 6402–6406.

[40] P. R. Schreiner, L. V. Chernish, P. A. Gunchenko, E. Y. Tikhonchuk, H. Hausmann, M. Serafin, S. Schlecht, J. E. P. Dahl, R. M. K. Carlson, A. A. Fokin, *Nature* **2011**, *477*, 308–311.

## Supplementary Information

# Novel rhenium carbides at 200 GPa

Saiana Khandarkhaeva[1*], Timofey Fedotenko[2], Maxim Bykov[3], Elena Bykova[3], Stella Chariton[4], Pavel Sedmak[5], Konstantin Glazyrin[6], Vitali Prakapenka[4], Natalia Dubrovinskaia[2,7] and Leonid Dubrovinsky[1]

[1] *Bayerisches Geoinstitut, University of Bayreuth, Universitätstraße 30, 95440 Bayreuth, Germany*

[2] *Material Physics and Technology at Extreme Conditions, Laboratory of Crystallography University of Bayreuth, Universitätstraße 30, 95440 Bayreuth, Germany*

[3] *Geophysical Laboratory, Carnegie Institution of Washington, 5251 Broad Branch Road NW, 20015 Washington, District of Columbia, USA*

[4] *Center for Advanced Radiation Sources, University of Chicago, 5640 S. Ellis, 60637 Chicago, Illinois, USA*

[5] *European Synchrotron Radiation Facility, BP 220, 38043 Grenoble Cedex, France*

[6] *Photon Science, Deutsches Elektronen-Synchrotron, Notkestraße 85, 22607 Hamburg, Germany*

[7] *Theoretical Physics Division, Department of Physics, Chemistry and Biology (IFM) Linköping University, SE-581 83, Linköping, Sweden*

*Corresponding author: Saiana.Khandarkhaeva@uni-bayreuth.de

## Experimental Procedures

DAC preparation

To shape secondary anvils for Experiment #1, we used the focused ion beam (FIB), the procedure of dsDAC alignment is described in detail in ref.[1]. A BX-90-type DAC[2] equipped with Boehler-Almax beveled diamonds with 40-μm culets was used for high pressure generation in the primary sample chamber. The secondary sample chamber of dsDAC was loaded with Re powder particles and neon served as a pressure-transmitting medium.[3] Secondary gasket was made of a Re foil indented to ~7 μm thickness with a hole of ~10 μm in diameter. In Experiment #2 we used BX-90-type DAC[2] equipped with Boehler-Almax beveled diamonds with 40-μm culets. Cell was loaded with FeO and Ne (pressure transmitting medium), compressed up to ~220 GPa and laser heated up to ~2500 K.

In order to study the compressional behavior of $Re_2C$, single crystals of $Re_2C$ were synthesized by means of HPHT technique in a multi-anvil press at the Bayerisches Geoinstitut (Bayreuth, Germany). Single crystals with an average size of $0.01^x0.01^x0.01$ mm$^3$ were preselected on a three-circle Bruker diffractometer equipped with a SMART APEX CCD detector and a high-brilliance Rigaku rotating anode (Rotor Flex FR-D, Mo-$K_\alpha$ radiation) with Osmic focusing X-ray optics. Crystals of $Re_2C$ were loaded in BX-90 DAC equipped by diamonds with 250 μm culets' size. Ne was loaded as pressure medium. The samples were studied by means of single-crystal X-ray diffraction (SCXRD) on the synchrotron beamline 13IDD at the Advanced Photon Source (APS), Argonne, USA (Pilatus CdTe 1M detector, $\lambda$ = 0.2952 Å). At each pressure step we have collected the data with a narrow 0.5° scanning step in the range from −38° to +38° with exposure time 0.5s/step. For first two pressure steps rotational datasets were collected twice. Until Ne has been solidified pressure has been measured by Ruby fluorescence.[4] Later Ne EOS reported by Fei et. al.[5] was used for pressure determination in the sample chamber.

Data acquisition

The single-crystal X-ray diffraction (SCXRD) experiments were conducted at the materials science (nano-) beamline ID11 at the European synchrotron radiation facility (ESRF) (Grenoble, France) (Frelon4M detector; $\lambda$=0.30996 Å; spot size $0.45^x0.45$ μm$^2$ at FWHM). 2D mapping of still XRD-images (without ω-oscillations) with exposure time 5s was performed around the sample

chamber in order to find the best spots for the data collection. SCXRD datasets were collected via DAC-rotation around ω-axis from -38˚ to 38˚ with angular step 0.5˚ and acquisition time 10 s/step.

Data analysis

In case of powder diffraction studies, calibration of instrument model and integration of diffraction patterns were made in the DIOPTAS software[6] using $CeO_2$ powder standard (NIST SRM 674b). Integrated patterns from powder XRD experiments were processed using the Le Bail technique implemented in JANA2006 software.[7] X-ray diffraction imaging of sample chamber was reconstructed using XDI[8] program and map of still-images converted from 'edf' to 'tif' format. In case of SCXRD, integration of the reflection intensities and absorption corrections were performed in CrysAlisPro software[9] using a single crystal of orthoenstatite $(Mg_{1.93},Fe_{0.06})(Si_{1.93},Al_{0.06})O_6$ (space group *Pbca*, a=8.8117(2) Å, b=5.18320(10) Å, c=18.2391(3) Å) as calibration standard for refinement of instrument model. Diffraction images were converted from 'edf' to the native CrysAlisPro format 'ESPERANTO' with Freac software.[10] Detailed information of integration parameters as well as about data reduction output files and indicators of the XRD data quality are given in ref.[11] The crystal structures were solved using Superfilp method in JANA2006, as starting model we used Patterson superposition map showing the best performance for elements with high Z. The coordinates of heavy (Re) atoms were calculated using an inverse Fourier transformation of structure factor $F_{hkl}$ of the specific (for each phase) diffracted waves. The positions of carbon atoms were defined with manual analysis of residual electron density distribution. Crystal structures were refined by least-squares minimization of adjustable parameters. We performed isotropic refinement of atomic displacement parameters due to limited dataset collected in DAC. Reflections coming from parasite diffraction produced by diamonds and crystallized pressure media were omitted during the refinement procedure. Diamond 3.2 software was used for visualization of molecular graphics.[12]

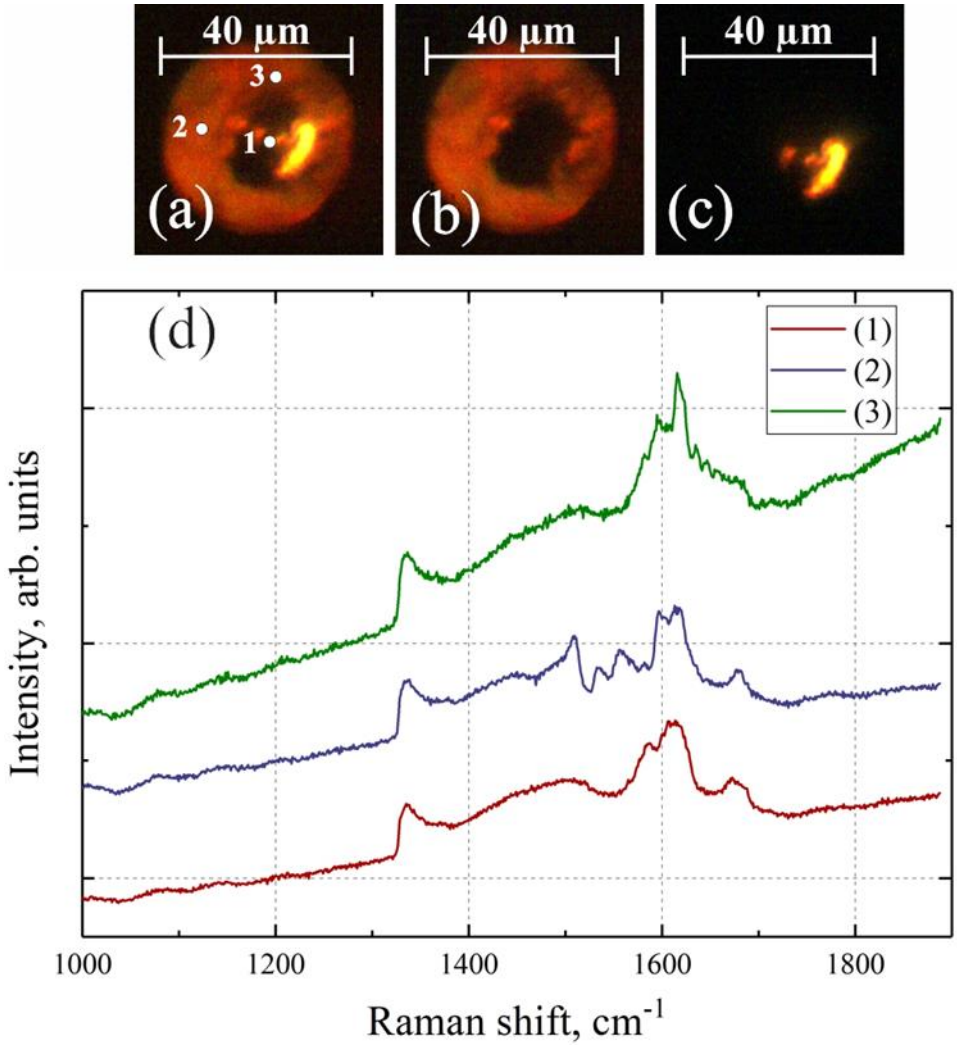


***Figure S1.*** *Photographs of the sample chamber in Experiments #1 taken after pulsed-laser heating at ~3000 K (a – front and back light illumination, b – front illumination, c – back illumination) and Raman spectra of diamond anvil collected at different locations in pressure chamber (d). Image in reflected light (b) shows that secondary Re-gasket has lost characteristic metallic luster as result of chemical reaction with anvil. Semi-transparent NCD secondary anvil is visible in transmitted light (c). Transparent area visible in transmitted light (a, c) is either due to direct contact between anvils or thin layer of Ne. Pressure determined from the Raman shift of the diamond anvil is 200(10) GPa in the center of the culet (spectrum #1), and 196(10) GPa and 199(10) GPa at the edges (#2 and #3).*[13] *Raman spectra were recorded on LabRam system equipped with He-Ne (λ=632 nm) laser source.*

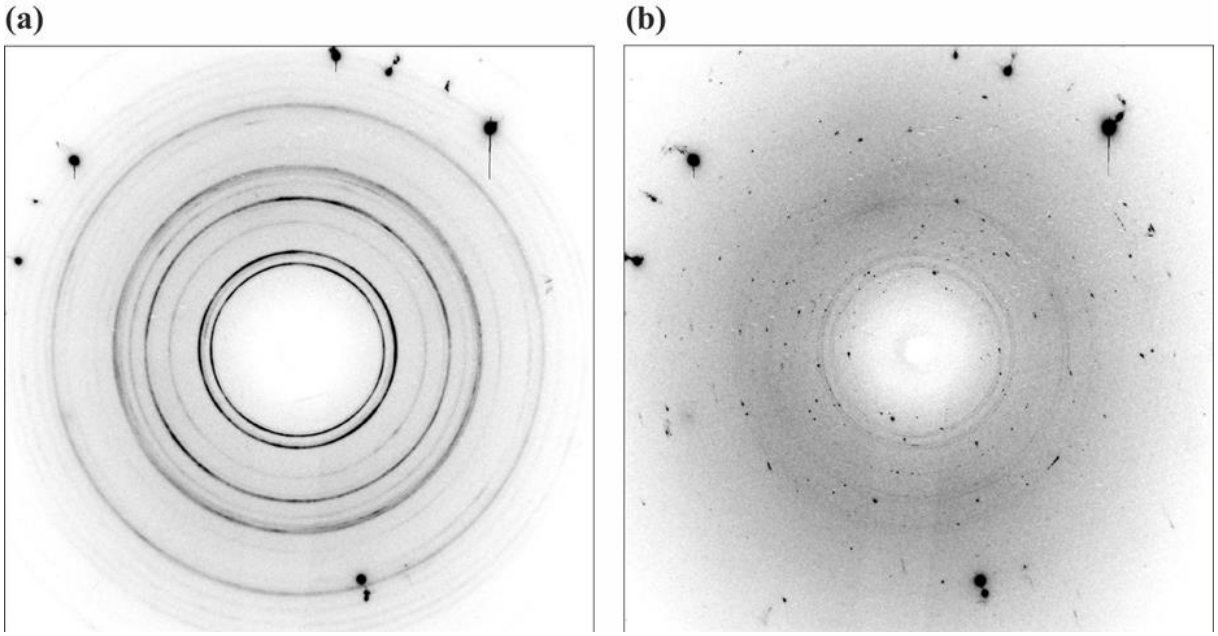


***Figure. S2.*** *Diffraction images (highlighted by white rectangles on Figure 1) collected on the edge of the Re-gasket (a) and closer to the center of the sample chamber (b) in Experiment #1. Continuous powder diffraction rings (a) come from a non-laser-irradiated part of the Re gasket. The spots (b) belong to new rhenium carbide phases. Intense diffraction spots on the both images are from the diamond anvils.*

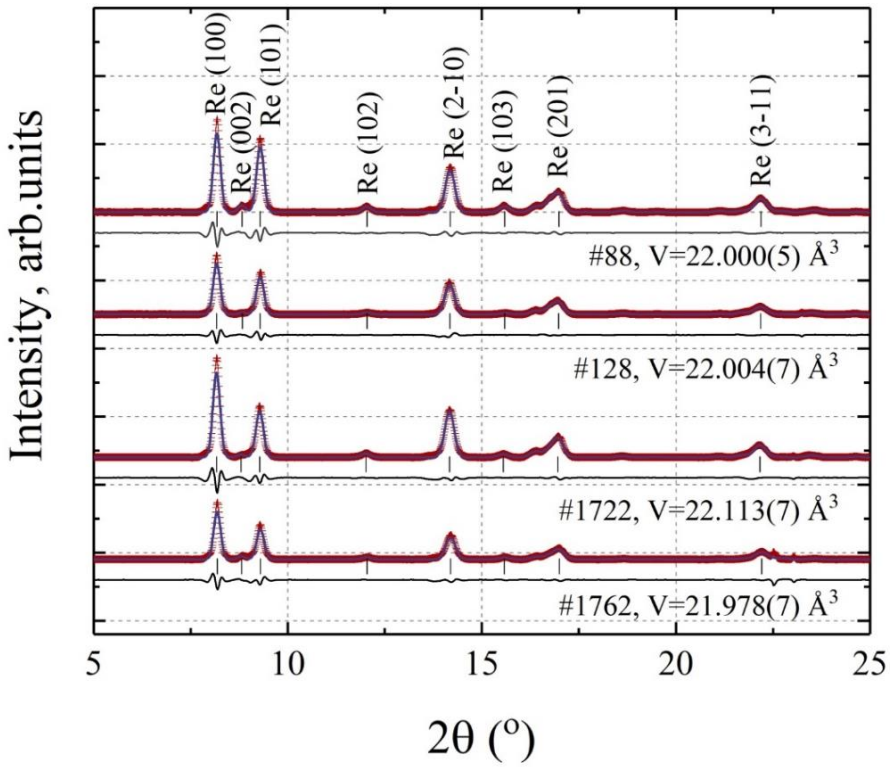


***Figure. S3***. *Representative X-ray diffraction patterns collected from the Re-gasket on the periphery of the sample chamber (wavelength λ=0.30996 Å) on ID11 at the ESRF. Powder diffraction data was processed using JANA2006 software. Red crosses are the experimental data, the blue curve is the simulated diffraction data, the black line shows the residual difference, and the vertical ticks - the positons of Re reflections. Numbers designate the diffraction frames in accordance to the 2D map shown in Figure 1. Corresponding lattice parameters are provided in Table S1.*

**Table S1.** Refined lattice parameters of Re obtained from diffraction data for a few experimental points on the gasket. Pressure was determined using the two EOS, reported in Dubrovinsky et al.[1] and Anzellini et al.[14]

| **Frame** | **a, Å** | **c, Å** | **V, Å$^3$** | **P, GPa (EOS[1])** | **P, GPa (EOS[14])** |
|---|---|---|---|---|---|
| **#88** | 2.51064(18) | 4.0301(9) | 22.000(5) | 239(1) | 196(1) |
| **#128** | 2.51182(19) | 4.0271(12) | 22.004(7) | 238(1) | 196(1) |
| **#1722** | 2.51358(17) | 4.0413(12) | 22.113(7) | 231(1) | 189(1) |
| **#1762** | 2.5086(2) | 4.0328(12) | 21.978(7) | 240(1) | 197(1) |

**Table S2.** Details of the crystal structure refinements of rhenium carbide phases observed in Experiment #1 at 180(7) GPa.

| **Composition** | **$Re_2C$** | **$ReC_{0.2}$** | **ReC** | **$ReC_2$** |
|---|---|---|---|---|
| $M_{r,.}$ g/mol | 384.4 | 188.6 | 198.2 | 210.2 |
| Crystal system, | Hexagonal | Hexagonal | Hexagonal | Orthorhombic |
| Space group | *P*6$_3$/*mmc* | *P*6$_3$/*mmc* | *P*-6*m*2 | *Fmmm* |
| Temperature (K) | 293 | 293 | 293 | 293 |
| *a* (Å) | 2.5860(9) | 2.6028(12) | 2.5510(9) | 3.3367(10) |
| *b* (Å) | 2.5860(9) | 2.6028(12) | 2.5510(9) | 4.3155(16) |
| *c* (Å) | 9.272(3) | 4.161(2) | 2.7048(11) | 5.6220(13) |
| *α* (˚) | 90 | 90 | 90 | 90 |
| *β* (˚) | 90 | 90 | 90 | 90 |
| *γ* (˚) | 120 | 120 | 120 | 90 |
| *V* (Å$^3$) | 53.70(3) | 24.41(2) | 15.24(1) | 80.95(4) |
| *Z* | 2 | 2 | 1 | 4 |
| F(000) | 312 | 152 | 81 | 348 |
| Dx (g·cm$^{-3}$) | 23.775 | 25.657 | 21.593 | 17.249 |
| Radiation type | Synchrotron, λ = 0.30996 Å | | | |
| μ (mm$^{-1}$) | 25.68 | 28.23 | 22.63 | 17.06 |
| Diffractometer | ID11 @ ESRF | | | |
| Absorption correction | Multi-scan (ABSPACK, *CrysAlis PRO* 1.171.40.53) | | | |
| No. of measured, independent and observed [$I > 3\sigma(I)$] reflections | 187, 46, 40 | 89, 29, 26 | 71, 35, 35 | 91, 36, 36 |
| $R_{int}$ | 0.065 | 0.016 | 0.007 | 0.021 |
| θ range values (˚) | 4.0 to 15.1 | 3.9 to 14.5 | 4.0 to 17.3 | 3.7 to 16.7 |
| Range of h, k, l | $h = -4 \rightarrow 4$<br>$k = -3 \rightarrow 2$<br>$l = -14 \rightarrow 14$ | $h = -4 \rightarrow 4$<br>$k = -3 \rightarrow 3$<br>$l = -4 \rightarrow 5$ | $h = -3 \rightarrow 3$<br>$k = -3 \rightarrow 3$<br>$l = -3 \rightarrow 3$ | $h = -4 \rightarrow 4$<br>$k = -5 \rightarrow 5$<br>$l = -8 \rightarrow 8$ |
| Refinement method | Full matrix least squares on $F^2$ | | | |
| $R[F^2 > 2\sigma(F^2)]$, $wR(F^2)$, *S* | 0.039, 0.067, 1.54 | 0.043, 0.097, 3.72 | 0.045, 0.106, 3.97 | 0.043, 0.116, 3.43 |
| No. of parameters | 4 | 3 | 3 | 4 |
| No. of restrains | 0 | 0 | 0 | 0 |
| $\Delta\rho_{max}$, $\Delta\rho_{min}$ (e·Å$^{-3}$) | 4.59, −7.15 | 4.13, −7.5 | 6.47, −6.87 | 5.62, −5.54 |

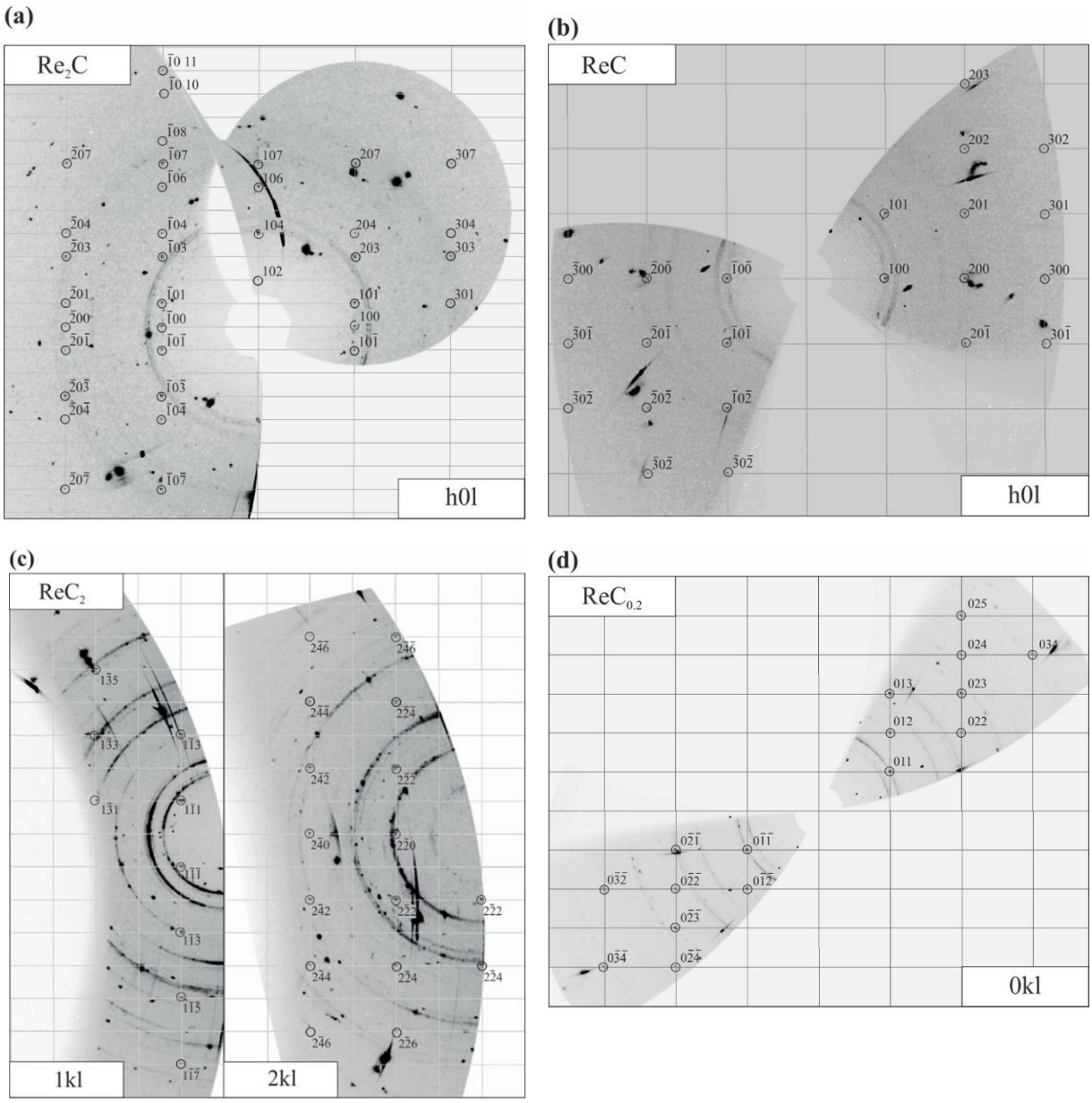


***Figure. S4.*** *(a) Reconstructed reciprocal lattice planes of Re-C compounds observed in Experiment #1: (a) – hP-$Re_2C$, (b) – WC-type structured ReC, (c) – oF-$ReC_2$ and (d) – hP-$ReC_{0.2}$. Intense powder diffraction rings on (c) are due to parasitic scattering from Re-gasket, whereas weaker rings (d) represent the formation of an interstitial solid solution $ReC_{0.2}$.*

**Table S3.** Fractional atomic coordinates and isotropic displacement parameters (Å$^2$) of $Re_2C$ at 180(7) GPa.

| | ***x*** | ***y*** | ***z*** | ***Occupancy*** | ***Wyckoff osition*** | $U_{iso}$*/$U_{eq}$ |
|---|---|---|---|---|---|---|
| **Re1** | 0.666667 | 0.333333 | 0.60693 (16) | 1 | 4f | 0.0075 (4)* |
| **C1** | 0.333333 | 0.666667 | 0.75 | 1 | 2d | 0.06 (3)* |

**Table S4.** Selected geometric parameters of $Re_2C$ at 180(7) GPa.

| **Distances:** | | | |
|---|---|---|---|
| **Re1—Re1$^{i}$** | 2.586(3) | **Re1—Re1$^{viii}$** | 2.482(2) |
| **Re1—Re1$^{ii}$** | 2.5860(18) | **Re1—Re1$^{ix}$** | 2.482(2) |
| **Re1—Re1$^{iii}$** | 2.5860(18) | **Re1—Re1$^{x}$** | 2.653(3) |
| **Re1—Re1$^{iv}$** | 2.5860(18) | **Re1—C1$^{iii}$** | 1.997(16) |
| **Re1—Re1$^{v}$** | 2.5860(18) | **Re1—C1** | 1.9972(12) |
| **Re1—Re1$^{vi}$** | 2.586(3) | **Re1—C1$^{v}$** | 1.9972(16) |
| **Re1—Re1$^{vii}$** | 2.482(2) | | |

Symmetry codes: (i) *x*−1, *y*−1, *z*; (ii) *x*−1, *y*, *z*; (iii) *x*, *y*−1, *z*; (iv) *x*, *y*+1, *z*; (v) *x*+1, *y*, *z*; (vi) *x*+1, *y*+1, *z*; (vii) *y*, *x*−1, −*z*+1; (viii) *y*, *x*, −*z*+1; (ix) *y*+1, *x*, −*z*+1; (x) −*y*+1, −*x*+1, −*z*+3/2; (xi) −*y*, −*x*+1, −*z*+3/2; (xii) −*y*+1, −*x*+2, −*z*+3/2

**Table S5.** Fractional atomic coordinates and isotropic displacement parameters (Å$^2$) of WC-type structured ReC at 180(7) GPa.

| | *x* | *y* | *z* | *Occupancy* | *Wyckoff position* | $U_{iso}$*/$U_{eq}$ |
|---|---|---|---|---|---|---|
| **Re1** | 0.333333 | 0.666667 | 0.5 | 1 | 1d | 0.0076(7)* |
| **C1** | 0.666667 | 0.333333 | 1 | 1 | 1e | 0.005(10)* |

**Table S6.** Selected geometric parameters of WC-type structured ReC at 180(7) GPa.

| **Distances:** | | | |
|---|---|---|---|
| **Re1—Re1$^{i}$** | 2.551(3) | **Re1—Re1$^{viii}$** | 2.551(3) |
| **Re1—Re1$^{ii}$** | 2.5510(18) | **Re1—C1$^{ix}$** | 1.9995(13) |
| **Re1—Re1$^{iii}$** | 2.5510(18) | **Re1—C1$^{ii}$** | 1.9995(13) |
| **Re1—Re1$^{iv}$** | 2.705(2) | **Re1—C1$^{iv}$** | 1.9995(8) |
| **Re1—Re1$^{v}$** | 2.705(2) | **Re1—C1** | 1.9995(8) |
| **Re1—Re1$^{vi}$** | 2.5510(18) | **Re1—C1$^{x}$** | 1.9995(13) |
| **Re1—Re1$^{vii}$** | 2.5510(18) | **Re1—C1$^{vi}$** | 1.9995(13) |

Symmetry codes: (i) *x*−1, *y*−1, *z*; (ii) *x*−1, *y*, *z*; (iii) *x*, *y*−1, *z*; (iv) *x*, *y*, *z*−1; (v) *x*, *y*, *z*+1; (vi) *x*, *y*+1, *z*; (vii) *x*+1, *y*, *z*; (viii) *x*+1, *y*+1, *z*; (ix) *x*−1, *y*, *z*−1; (x) *x*, *y*+1, *z*−1; (xi) *x*, *y*−1, *z*+1; (xii) *x*+1, *y*, *z*+1.

**Table S7.** Fractional atomic coordinates and isotropic displacement parameters (Å$^2$) of $ReC_2$ at 180(7) GPa.

| | *x* | *y* | *z* | *Occupancy* | *Wyckoff position* | $U_{iso}$*/$U_{eq}$ |
|---|---|---|---|---|---|---|
| **Re1** | 0 | 0 | 0 | 1 | 4a | 0.0055(7)* |
| **C1** | 0 | 0 | −0.321(12) | 1 | 8i | 0.022(11)* |

**Table S8.** Geometric parameters (Å, º) of $ReC_2$ at 180(7) GPa.

| **Distances:** | | | |
|---|---|---|---|
| **Re1—C1** | 1.805(7) | **Re1—C1$^{v}$** | 1.948(4) |
| **Re1—C1$^{i}$** | 1.948(4) | **C1—C1$^{vi}$** | 2.013(9) |
| **Re1—C1$^{ii}$** | 1.948(4) | **C1—C1$^{iv}$** | 1.850(4) |
| **Re1—C1$^{iii}$** | 1.805(7) | **C1—C1$^{v}$** | 1.850(4) |
| **Re1—C1$^{iv}$** | 1.948(4) | | |
| **Angles:** | | | |
| **C1—Re1—C1$^{i}$** | 121.0(13) | **Re1—C1—Re1$^{vii}$** | 121.0(13) |
| **C1—Re1—C1$^{ii}$** | 121.0(13) | **Re1—C1—Re1$^{viii}$** | 121.0(13) |
| **C1—Re1—C1$^{iii}$** | 180.0(5) | **Re1—C1—C1$^{vi}$** | 180.0(5) |
| **C1—Re1—C1$^{iv}$** | 59.0(13) | **Re1—C1—C1$^{iv}$** | 64(2) |
| **C1—Re1—C1$^{v}$** | 59.0(13) | **Re1—C1—C1$^{v}$** | 64(2) |
| **C1$^{i}$—Re1—C1$^{ii}$** | 118.1(18) | **Re1$^{vii}$—C1—Re1$^{viii}$** | 118(3) |
| **C1$^{i}$—Re1—C1$^{iii}$** | 59.0(13) | **Re1$^{vii}$—C1—C1$^{vi}$** | 59.0(13) |
| **C1$^{i}$—Re1—C1$^{iv}$** | 61.9(18) | **Re1$^{vii}$—C1—C1$^{iv}$** | 56.8(14) |
| **C1$^{i}$—Re1—C1$^{v}$** | 180.0(5) | **Re1$^{vii}$—C1—C1$^{v}$** | 175(3) |
| **C1$^{ii}$—Re1—C1$^{iii}$** | 59.0(13) | **Re1$^{viii}$—C1—C1$^{vi}$** | 59.0(13) |
| **C1$^{ii}$—Re1—C1$^{iv}$** | 180.0(5) | **Re1$^{viii}$—C1—C1$^{iv}$** | 175(3) |
| **C1$^{ii}$—Re1—C1$^{v}$** | 61.9(18) | **Re1$^{viii}$—C1—C1$^{v}$** | 56.8(14) |
| **C1$^{iii}$—Re1—C1$^{iv}$** | 121.0(13) | **C1$^{vi}$—C1—C1$^{iv}$** | 116(2) |
| **C1$^{iii}$—Re1—C1$^{v}$** | 121.0(13) | **C1$^{vi}$—C1—C1$^{v}$** | 116(2) |
| **C1$^{iv}$—Re1—C1$^{v}$** | 118.1(18) | **C1$^{iv}$—C1—C1$^{v}$** | 128(3) |

Symmetry codes: (i) *x*, *y*−1/2, *z*+1/2; (ii) *x*, *y*+1/2, *z*+1/2; (iii) *x*−1/2, *y*, *z*+1/2; (iv) *x*+1/2, *y*, *z*+1/2; (v) −*x*, *y*, −*z*; (vi) −*x*, *y*−1/2, −*z*−1/2; (vii) −*x*, *y*+1/2, −*z*−1/2; (viii) −*x*−1/2, *y*, −*z*−1/2; (ix) −*x*+1/2, *y*, −*z*−1/2; (x) −*x*, *y*, −*z*−1; (xi) *x*, *y*−1/2, *z*−1/2; (xii) *x*, *y*+1/2, *z*−1/2; (xiii) *x*−1/2, *y*, *z*−1/2; (xiv) *x*+1/2, *y*, *z*−1/2.

**Table S9.** Fractional atomic coordinates and isotropic displacement parameters (Å$^2$) of $ReC_{0.2}$ at 180(7) GPa.

| | *x* | *y* | *z* | *Occupancy* | *Wyckoff position* | $U_{iso}$*/$U_{eq}$ |
|---|---|---|---|---|---|---|
| **Re1** | 0.666667 | 0.333333 | 0.25 | 1 | 2d | 0.0085 (7)* |
| **C1** | 1 | 0 | 0 | 0.2 | 2a | 0.01 (3)* |

**Table S10.** Selected geometric parameters of $ReC_{0.2}$ at 180(7) GPa.

| **Distances:** | | | |
|---|---|---|---|
| **Re1—Re1$^{i}$** | 2.603(4) | **Re1—Re1$^{x}$** | 2.5666(17) |
| **Re1—Re1$^{ii}$** | 2.603(2) | **Re1—Re1$^{xi}$** | 2.567(2) |
| **Re1—Re1$^{iii}$** | 2.603(2) | **Re1—Re1$^{xii}$** | 2.567(2) |
| **Re1—Re1$^{iv}$** | 2.603(2) | **Re1—C1$^{ii}$** | 1.8277(17) |
| **Re1—Re1$^{v}$** | 2.603(2) | **Re1—C1** | 1.8277(8) |
| **Re1—Re1$^{vi}$** | 2.603(4) | **Re1—C1$^{iv}$** | 1.8277(17) |
| **Re1—Re1$^{vii}$** | 2.567(2) | **Re1—C1$^{viii}$** | 1.8277(17) |
| **Re1—Re1$^{viii}$** | 2.567(2) | **Re1—C1$^{xiii}$** | 1.8277(8) |
| **Re1—Re1$^{ix}$** | 2.5666(17) | **Re1—C1$^{xii}$** | 1.8277(17) |

Symmetry codes: (i) *x*−1, *y*−1, *z*; (ii) *x*−1, *y*, *z*; (iii) *x*, *y*−1, *z*; (iv) *x*, *y*+1, *z*; (v) *x*+1, *y*, *z*; (vi) *x*+1, *y*+1, *z*; (vii) −*x*+1, −*y*, *z*−1/2; (viii) −*x*+1, −*y*, *z*+1/2; (ix) −*x*+1, −*y*+1, *z*−1/2; (x) −*x*+1, −*y*+1, *z*+1/2; (xi) −*x*+2, −*y*+1, *z*−1/2; (xii) −*x*+2, −*y*+1, *z*+1/2; (xiii) −*x*+2, −*y*, *z*+1/2; (xiv) −*x*+2, −*y*, *z*−1/2.

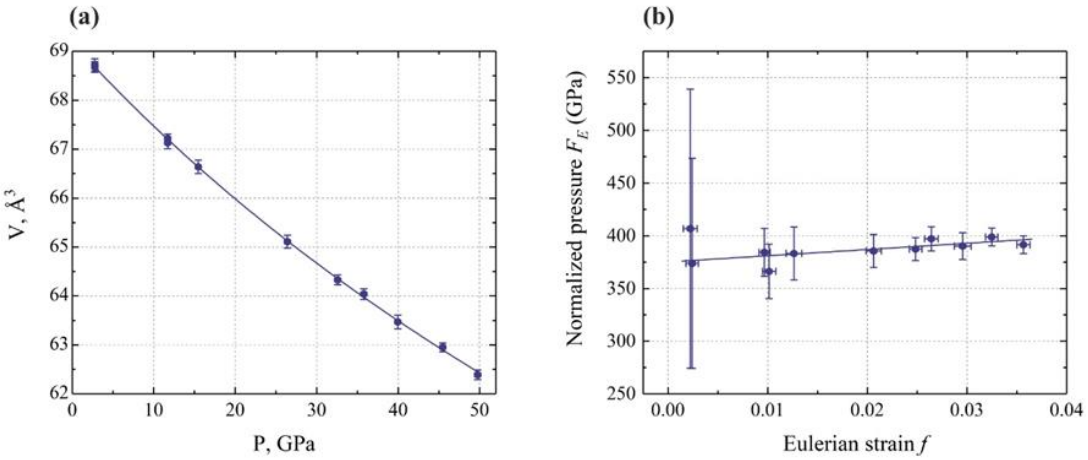


***Fig. S5.*** *Pressure dependence of the unit cell volume of hP-$Re_2C$ (a) (blue circles represent experimental data, solid blue line - fitted EOS). Normalized pressure - Eulerian strain ($F_E$-$f$) plot (b) based on 3rd order Birch-Murnaghan equation of state of $Re_2C$ ($V_0$=69.18(4), K=375 (15) GPa, K'=5.0(1)*

**Table S11.** Experimental lattice parameters of $Re_2C$ obtained during compression in diamond anvil cell (DAC).

| | **V(Ne), Å³** | **P, GPa** | **a, Å** | **c, Å** | **V, Å³** |
|---|---|---|---|---|---|
| **1** | – | 2.76 (Ruby) | 2.8355(4) | 9.864(16) | 68.68(11) |
| **2** | | | 2.8379(6) | 9.853(19) | 68.72(13) |
| **3** | 43.956(6) | 11.71(1) | 2.8146(4) | 9.798(14) | 67.22(9) |
| **4** | | | 2.8160(5) | 9.775(15) | 67.13(12) |
| **5** | 41.335(7) | 15.45(2) | 2.8079(5) | 9.76(2) | 66.64(14) |
| **6** | 36.520(6) | 26.41(2) | 2.7823(4) | 9.71(2) | 65.11(13) |
| **7** | 34.720(7) | 32.58(2) | 2.7714(4) | 9.671(15) | 64.33(10) |
| **8** | 33.942(9) | 35.79(4) | 2.7683(5) | 9.649(16) | 64.04(11) |
| **9** | 33.040(9) | 39.96(5) | 2.7573(6) | 9.64(2) | 63.47(14) |
| **10** | 31.999(8) | 45.48(5) | 2.7502(4) | 9.611(13) | 62.95(9) |
| **11** | 31.289(9) | 49.76(6) | 2.7443(4) | 9.566(16) | 62.39(10) |

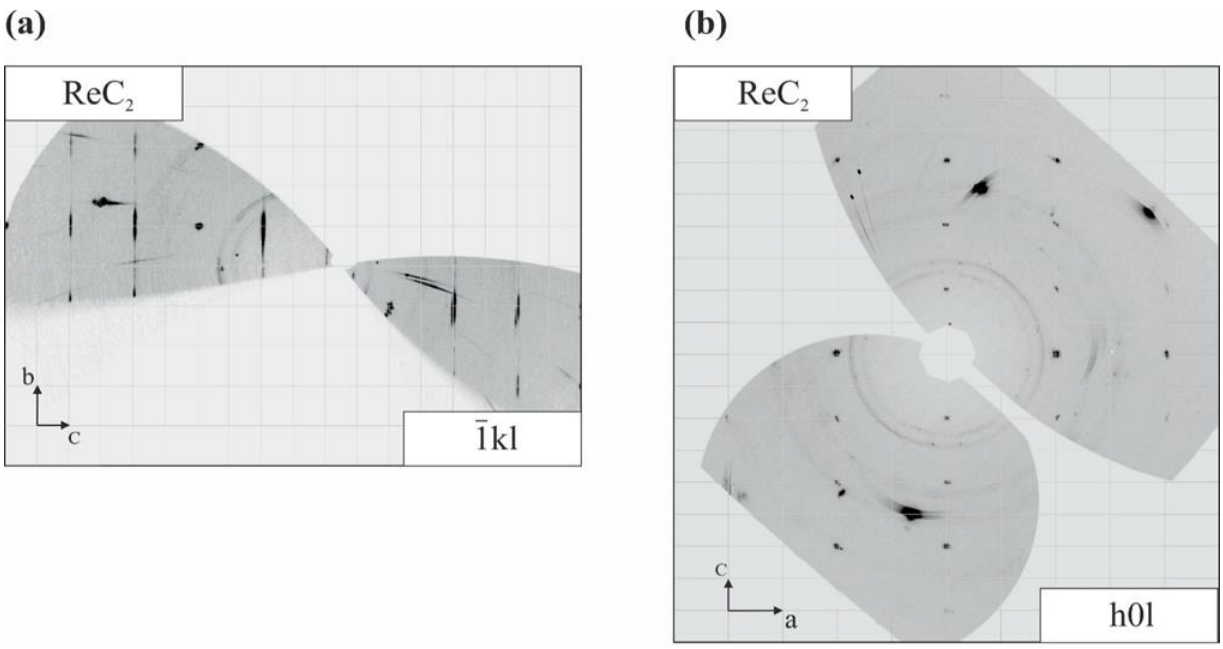


***Fig. S6****. Reconstructed reciprocal lattice planes: (-1k1) (a) and (h0l) of $TiSi_2$-type structured oF-$ReC_2$ showing strong diffuse scattering along b-axis (a).*

References

[1] L. Dubrovinsky, N. Dubrovinskaia, V. B. Prakapenka, A. M. Abakumov, *Nat. Commun.* **2012**, *3*, 1163–1167.

[2] I. Kantor, V. Prakapenka, A. Kantor, P. Dera, A. Kurnosov, S. Sinogeikin, N. Dubrovinskaia, L. Dubrovinsky, *Rev. Sci. Instrum.* **2012**, *83*, 125102.

[3] A. Kurnosov, I. Kantor, T. Boffa-Ballaran, S. Lindhardt, L. Dubrovinsky, A. Kuznetsov, B. H. Zehnder, *Rev. Sci. Instrum.* **2008**, *79*, 045110.

[4] H. K. Mao, J. Xu, P. M. Bell, *J. Geophys. Res.* **1986**, *91*, 4673.

[5] Y. Fei, A. Ricolleau, M. Frank, K. Mibe, G. Shen, V. Prakapenka, *Proc. Natl. Acad. Sci.* **2007**, *104*, 9182–9186.

[6] C. Prescher, V. B. Prakapenka, *High Press. Res.* **2015**, *35*, 223–230.

[7] V. Petrícek, M. Dušek, L. Palatinus, *Zeitschrift fur Krist.* **2014**, *229*, 345–352.

[8] R. Hrubiak, J. S. Smith, G. Shen, *XDI*, **2017**, High Pressure Collaborative Access Team, Geophysical Laboratory, Carnegie Institution of Washington, Argonne, Illinois 60439, USA.

[9] O. D. Rigaku, CrysAlisPro Software System, Version 1.171. 40.53, Rigaku Coorporation, **2018**.

[10] V. Dyadkin, *Freac*, SNBL ESRF, **2018**.

[11] E. Bykova, *Single-Crystal X-Ray Diffraction at Extreme Conditions in Mineral Physics and Material Sciences*, University of Bayreuth, 2015.

[12] H. Putz, K. Brandenburg, Diamond 3.2- Crystal and Molecular Structure Visualization.

[13] Y. Akahama, H. Kawamura, *J. Phys. Conf. Ser.* **2010**, *215*, 0–4.

[14] S. Anzellini, A. Dewaele, F. Occelli, P. Loubeyre, M. Mezouar, *J. Appl. Phys.* **2014**, *115*, 043511.

Author Contributions

L. D., N. D. and S. K. designed the research, S. K., N. D. and L. D. wrote the paper, S. K., T. F., P. S., S. C., K. G., V. P. and L. D. performed X-ray diffraction experiments, S. K., M. B., E. B. and L. D. analyzed the X-ray diffraction data, S. C. performed synthesis in the large volume press. All authors contributed to the discussion of the results.

# Chapter 6.2. High-pressure synthesis of $CaC_2$ and $Ca_3C_7$ with deprotonated polyacene- and *para*-poly(indenoindene)-like nanoribbons

*Saiana Khandarkhaeva[1,2], Timofey Fedotenko[3], Alena Aslandukova[1], Maxim Bykov[4], Dominique Laniel[2], Andrii Aslandukov[2], Björn Winkler (?), Uwe Ruschewitz[4], Christian Tobeck[4], Stella Chariton[5], Vitali Prakapenka[5], Konstantin Glazyrin[3], Hanns-Peter Liermann[3], Carlotta Giacobbe[6], Eleanor Lawrence Bright[6], Natalia Dubrovinskaia[2,7] and Leonid Dubrovinsky[1]*

[1]*Bayerisches Geoinstitut, University of Bayreuth, Universitätstraße 30, 95440 Bayreuth, Germany*

[2]*Material Physics and Technology at Extreme Conditions, Laboratory of Crystallography University of Bayreuth, Universitätstraße 30, 95440 Bayreuth, Germany*

[3]*Deutsches Elektronen-Synchrotron DESY, Notkestr. 85, 22607 Hamburg, Germany*

[4]*Institute of Inorganic Chemistry, University of Cologne, Greinstrasse 6, 50939 Cologne, Germany*

[5]*Center for Advanced Radiation Sources, The University of Chicago, 5640 S. Ellis, 60637 Chicago, Illinois, USA*

[6]*European Synchrotron Radiation Facility, BP 220, 38043 Grenoble Cedex, France*

[7]*Theoretical Physics Division, Department of Physics, Chemistry and Biology (IFM), Linköping University, SE-581 83 Linköping, Sweden*

**Corresponding author: saiana.khandarkhaeva@uni-bayreuth.de*

*To be submitted to Nature Chemisty*

## Abstract

Here we report on the synthesis of a high-pressure (HP) polymorph of $CaC_2$ and a novel compound $Ca_3C_7$. The synthesis was realized at high-pressure high-temperature conditions, and the structures of the both phases (at 44(1) and 147((2) GPa for HP-$CaC_2$ and at 38 GPa for $Ca_3C_7$) were solved and refined using single-crystal synchrotron X-ray diffraction analysis. The structures

of HP-$CaC_2$ and $Ca_3C_7$ contain deprotonated polyacene-like and *para*-poly(indenoindene)-like nanoribbons, respectively, which have never been observed before.

## Introduction

Richness of carbon chemistry and the existence of the vast number of organic compounds in nature are due to unlimited carbon catenation. Polycyclic aromatic hydrocarbons (PAHs) consisting of the finite number of fused aromatic rings give rise to various classes of polymeric compounds, if a PAH is extended into a polymer. For example, a particular class of fully conjugated ladder polymers (CLPs) is represented by an extension of indenofluorene into a polymer, that is poly(indenoindene) (PInIn)[1], where the alternation of five- and six-member rings gives rise to a ladder structure. Although its targeted synthesis has remained elusive so far, very recently on-surface synthesis of *para*-type oligo(indenoindene) (*p*-OInIn) was realised through a sequence of thermally activated reactions from an organic precursor[2]. If CLPs can be obtained through inorganic synthesis and if they can be synthesised in a crystalline form are the questions of interest *per se*, as they are fundamental for carbon chemistry. To explore this problem a suitable model system should be found. Why metal carbides are likely to be the systems of choice is explained below.

Known metal carbides contain the simplest carbon anions: isolated carbon atoms $C^{4-}$or $[C_2]^{2-}$-dumbbells ($CaC_2$, $SrC_2$, $BaC_2$, $YC_2$, $LaC_2$, $La_2C_3$, $CeC_2$, $TbC_2$, $YbC_2$, and $LuC_2$[3–6]) and linear trimers $[C_3]^{4-}$ ($Mg_2C_3$, $Me_4C_7$ (Me = Y, Ho, Er, Tm, Lu), $Sc_3C_4$ , and $Ln_3C_4$ (Ln = Ho - Lu)[7–10]), which have the same carbon skeleton as methane, acetylene, and allene. High pressure alters the bonding patterns in carbides, leading to new compounds with unusual structural units and interesting properties. Considering that for the binary systems Mg-C[11], Ca-C[12], Y-C[13], and La–C[14] *ab initio* structure search predicts the formation of unusual metal carbides with exotic $[C_4]$, $[C_5]$ units, $[C_6]$ rings, graphitic carbon sheets, and a number of structural transitions, studying them under compression might enable exploring the catenation of carbon.

Calcium carbides have been in focus of high-pressure research during recent years. $CaC_2$ is of a particular interest, as it is characterised by rich polymorphism. Three polymorphs of $CaC_2$ known at ambient conditions[15] ($CaC_2$-I, $CaC_2$-II, $CaC_2$-III) feature common for acetylides $[C_2]$-dumbbells, but carbon starts to polymerize at relatively low pressures, and at about 7 GPa $CaC_2$

transforms into a metallic phase (space group *Cmcm*) featuring 1D zig-zag polymeric carbon chains, as established using Raman spectroscopy and X-ray diffraction (XRD)[16]. Theory predicts further structural transformations in $CaC_2$ upon pressure increase coupled with the progressive polymerization of carbon atoms. According to calculations by Li et al.[17], above 20 GPa the structure of $CaC_2$ should have $P\bar{1}$ symmetry and contain infinite carbon strips built of interconnected pairs of fused five-member rings. This phase should be thermodynamically stable up to 37 GPa[17]. Above this pressure, according to the calculation, metallic $P\bar{1}$ -$CaC_2$ transforms into metallic *Immm*-$CaC_2$[17,18], in which carbon atoms are polymerized to form infinite quasi-1D ribbons built of fused 6-member rings. The latter prediction is of a particular interest, as the suggested carbon catenation in *Immm*-$CaC_2$[17,18] resembles deprotonated polyacene-like nanoribbons.

Here, we report the results of high-pressure high-temperature (HPHT) studies of $CaC_2$ in laser-heated diamond anvil cells (LHDACs) performed using synchrotron single-crystal X-ray diffraction (SCXRD) up to ~150 GPa at temperatures up to ~3000 K. For the first time, the predicted *Immm*-$CaC_2$[17,18] polymorph of $CaC_2$ was synthesized, its crystal structure was solved and refined on the basis of SCXRD data. A novel $Ca_3C_7$ compound, never anticipated or observed before, with the orthorhombic crystal structure (space group *Pnma*), featuring infinite, fully deprotonated *para*-poly-indenoindene (*p*-PInIn)-like chains, was synthesized and characterized using SCXRD. Experimental results of the present study were supported by DFT calculations, in which full structure optimization was performed for the both compounds, $CaC_2$ and $Ca_3C_7$. The optimized crystal structures are in a very good agreement with the experimentally determined ones.

## Methods

*Sample preparation*. Calcium carbide in form of pieces (thickness <10 mm, typically, technical grade, ~80%) was purchased from Sigma-Aldrich. Single crystals with an average size of ~0.05×0.05×0.01 $mm^3$ were preselected in house, on a three-circle Bruker diffractometer (SMART APEX CCD detector, Ag-Kα radiation, wavelength λ=0.5594 Å) installed in Bayerisches Geoinstitut (BGI, Bayreuth, Germany). The XRD showed a phase purity of the selected samples, no other phases except $CaC_2$-I[15] were detected during the preselection of crystals. All manipulations with the $CaC_2$-I pieces were conducted in paraffin oil to avoid their

contamination by the air moisture. Further, the single crystals of $CaC_2$ were loaded into the BX-90 diamond anvil cell[19] (DAC) equipped with pairs of Boehler-Almax diamonds with culets' diameters of 250 μm or 120 μm. The gasket was made of chemically pure Re-foil indented to ~25 μm thickness with a hole in the center of the indent of ~110 or ~60 μm in diameter. Paraffin oil was used as a pressure-transmitting medium. In house, laser heating was performed in a continuous mode using double-sided laser-heating setup at the BGI[20]. The NIR laser beam (λ=1070 nm) was focused to ~ a 5-μm spot, temperature was determined according to the grey body approximation of Planck's law.

*Synchrotron X-ray diffraction studies.* High-pressure SCXRD experiments were conducted on the Extreme Conditions Beamline P02.2 at PETRA III, Hamburg, Germany (λ=0.2895 Å, beam size ~1.5×1.7 $\mu m^2$ at FWHM, PerkinElmer XRD1621 detector); on the 13-IDD beamline at the Advanced Photon Source (APS), Chicago, USA (λ = 0.2952 Å, beam size ~3×3 $\mu m^2$, Pilatus CdTe 1 M detector); on material science beamline ID11, ESRF, Grenoble, France (λ = 0.2852 Å, beam size ~0.5×.5 $\mu m^2$, Eiger 4M CdTe detector). Prior to collection of SCXRD datasets, a 2D X-ray mapping was performed over the heated area in order to find the best spots for the data acquisition. During the SCXRD measurements, the DACs were rotated about the vertical ω-axis in a range of ±38˚, and the diffraction images were recorded with an angular step of Δω = 0.5˚.

*XRD data processing*. The analysis of powder diffraction patterns was done using the DIOPTAS software; a $CeO_2$ powder standard (NIST SRM 674b) was used for adjustment of the instrument model. 2D XRD mapping data were processed using XDI program. The SCXRD data analysis, including the indexing of diffraction peaks, data integration, frame scaling, and absorption correction, was performed using CrysAlisPro software package[21]. A crystal of orthoenstatite $(Mg_{1.93},Fe_{0.06})(Si_{1.93},Al_{0.06})O_6$ (space group *Pbca*, a=8.8117(2) Å, b=5.18320(10) Å, c=18.2391(3) Å) was used as a calibration standard for refinement of the instrumental parameters of the diffractometer (the sample-to-detector distance, the detector's origin, offsets of the goniometer angles and rotations of the X-ray beam and the detector around the instrument axis). The structures of novel phases were solved with the SHELXT[22] structure solution program using intrinsic phasing and refined with the Jana2006 program[23]. Crystal structure visualization was made with the VESTA software[24].

*Raman spectroscopy.* The spectra were collected using DilorXY system equipped with the Ar (the excitation wavelength 638 nm) laser source. The laser power in the range of 15–50 mW was applied. Raman spectra were collected in the region 1100 – 2000 $cm^{-1}$ by means of 5 accumulations for 30 seconds each. The frequency resolution was 2 $cm^{-1}$.

*DFT calculations.* The properties of the systems were determined via the first-principles calculations using Kohn-Sham density functional theory (DFT) with the generalized gradient approximation (GGA) by Perdew–Burke–Ernzerhof (PBE)[25] for the exchange–correlation energy implemented within the projector-augmented wave (PAW) method[26] for describing the interaction between the core and the valence electrons in the Vienna *ab initio* simulation package (VASP)[27]. We used the Monkhorst–Pack scheme with 4×6×6 k-points for Brillouin zone sampling and energy cutoff for the plane wave expansion of 800 eV, with which total energies are converged to better than 2 meV/atom. Computations were performed for eight volumes that cover the pressure range of 0-100 GPa for $Ca_3C_7$ and of 0-150 GPa for HP-$CaC_2$. Harmonic lattice dynamics calculations were performed with the Phonopy software using the finite displacement method[28].

## Results

Six diamond anvil cells with the samples were prepared as described above. Each of these DACs was used in a few, up to 3, experiments. DACs #1 through #5 were pressurized to ~40-50 GPa, and DAC #6 to ~90 GPa. All DACs were laser heated in home laboratory at the BGI. Additionally, DAC#1 and DAC#4 were reheated at the synchrotron beamline at the APS in order to increase the amount of recrystallized material. A summary of all experiments presented in this work, including pressure-temperature (P-T) conditions of the synthesis and the unit cell parameters of all observed phases, is given in Supplementary Table S1.

Upon compression to the target pressure, we performed Raman spectroscopy measurements of the starting material (Supplementary Fig. S1a). The spectrum, recorded at 3.3 GPa from the sample in the DAC #1 reveals the vibrational modes which can be assigned to the

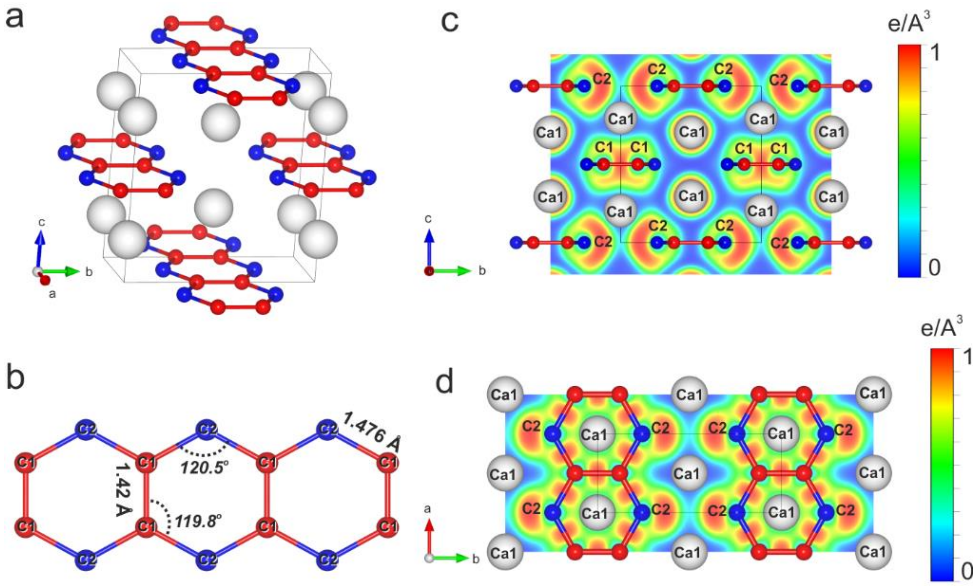


***Figure 1.*** *Crystal structure of HP-CaC2 at 44(1) GPa. (a) A ball and stick model with the unit cell outlined; calcium atoms are shown as white spheres, and carbon atoms as red and blue balls for two distinct crystallographic positions, C1 (Wyckoff site 4g) and C2 (4h), respectively. (b) The geometry of a single deprotonated poly-acene nanoribbon; the C-C distances are labeled. Cross-sections of the calculated electron localization function (ELF) are shown in the planes perpendicular (c) and parallel (d) to the polyacene nanoribbons.*

two $CaC_2$ polymorphs, tetragonal $CaC_2$-I[16,29] and monoclinic $CaC_2$-II[16,29]. Indeed, at ambient conditions, the $A_{1g}$ mode of $CaC_2$-I and the $A_g$ and $B_g$ modes of $CaC_2$-II are known to be of 1859 $cm^{-1}$, 1871 $cm^{-1}$, and 1874 $cm^{-1}$, respectively.[29] The Raman modes we observed at 3.3 GPa (1865 $cm^{-1}$ and 1875 $cm^{-1}$) are slightly shifted to the higher frequencies, as expected to happen under compression. Above ~5 GPa, $CaC_2$-II is known to transform into $CaC_2$-I, thus, the vibrational mode of $CaC_2$-II should not be present in the spectrum above this pressure. This is in accordance with our observation, as the Raman spectrum at 9.7 GPa features a single peak. At ~25 GPa Raman spectrum becomes featureless, suggesting amorphization of $CaC_2$.[16] As $CaC_2$-II was not detected by XRD in preselected crystals, we assume that only a minor amount of this phase was present in the sample loaded into the DAC.

Microphotographs taken during compression reveal changes in the sample visual appearance (Supplementary Fig. S1b): the crystal, which was initially transparent (3.3 GPa), becomes translucent at ~10 GPa and then opaque above ~25 GPa. Such changes can be attributed

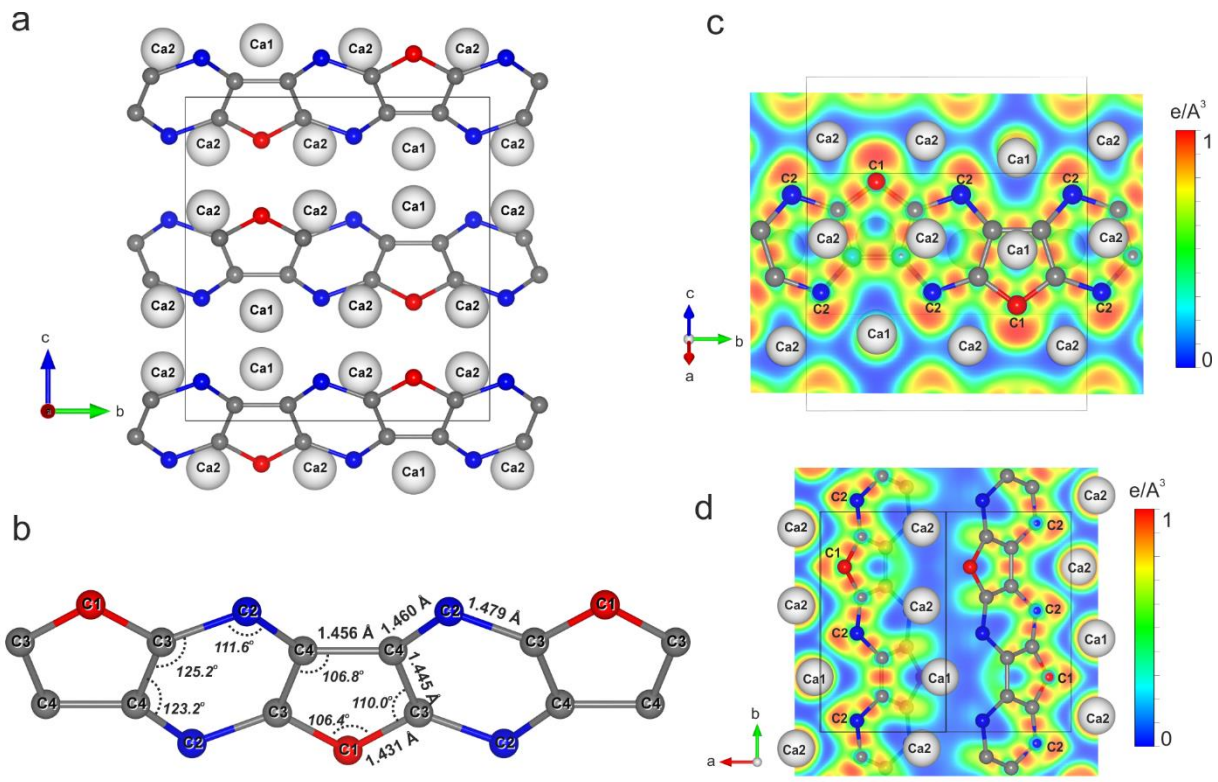


***Figure 2.*** *Crystal structure of Pnma-$Ca_3C_7$ at 38(1) GPa. (a) A projection of the $Ca_3C_7$ structure along the a-axis, emphasizing 2D chains of carbon atoms aligned along the b-axis. Calcium atoms are shown as white spheres, carbon atom as red and blue balls for two distinct crystallographic positions C1 (4c) and C2 (8d), respectively. Carbon atoms, named C3 (8d) and C4 (8d), are shown as gray balls. (b) The geometry of a single deprotonated para-poly(indenoindene) (p-PInIn) chain with the C-C distances labeled. (c) and (d) Cross-sections of the calculated electron localization function (ELF) are shown in the two different planes containing p-PInIn chains.*

to the partial band gap closure in $CaC_2$ upon compression that is supported by resistivity measurements performed by Zheng et al.[30]

After the target pressure in the DACs was achieved, the $CaC_2$ samples were laser heated that led to formation of numerous good-quality crystalline domains of new phases. That enabled room-temperature SCXRD data collection and processing using standard methods of SCXRD data analysis (see Methods and Figs. S2 and S3) that resulted in finding two previously unknown phases: a high-pressure polymorph of $CaC_2$ (we will further call it HP-$CaC_2$) and a new Ca-C compound $Ca_3C_7$. A summary of all experiments is provided in Supplementary Table S1. The

results of different experiments are mutually consistent and reproducible. The structures of the new solids were solved and refined using the best quality SCXRD datasets obtained at 38(1) GPa for $Ca_3C_7$ and at 44(1) GPa and 147(2) GPa for HP-$CaC_2$ (see Tables S2 through S5). They are described in detail below.

*Crystal structure of the high-pressure $CaC_2$ polymorph*

The structure of the novel high-pressure $CaC_2$ (HP-$CaC_2$) polymorph has an orthorhombic unit cell (space group *Immm*, Z=4) with the lattice parameters a=2.5616(3) Å, b=6.0245(17) Å, c=6.6851(15) Å at 44(1) GPa (Fig. 1a, Table S2). There are four calcium atoms in the unit cell (Fig. 1a), which occupy Wyckoff site *4i* (0,0,0.2041). The Ca-C distances to the ten nearest carbon atoms vary from ~2.44 Å to ~2.46 Å at 44(1) GPa. Carbon atoms occupy two distinct crystallographic positions (Fig. 1a, b): C1 - *4g* (0, 0.3819, 0) and C2 - *4h* (0, 0.2397, 0.5). They all are polymerized forming infinite nanoribbons of fused planar six-member rings (Fig. 1b). These planar ribbons, lying in the *ab* plane, are oriented along the *a*-axis. Thus, the structure can be described as an alternation of layers containing carbon nanoribbons, and layers of calcium atoms along the *c*-axis. The described arrangement of carbon atoms gives rise to an exotic for any known carbide poly-C entity: a $[C_4]^{4-}$ unit with a formal charge of 4−, similar to deprotonated polyacene (Supplementary Fig. S4). The refined at 44(1) GPa C-C distances in hexagons are 1.41 Å and 1.476 Å for C1-C1 and C1-C2 bonds, respectively. The two angles in in the hexagon are equal to 120.5°, while the other four are of 119.8° (Fig. 1b). 147(2) GPa. It has shown that upon compression the $C_6$-ring symmetrized: the two bond lengths, which were different at 44(1) GPa, became identical and equal to ~1.41 Å at 147(2) GPa, as predicted in ref. 28.

The pressure dependence of the unit cell volume for HP-$CaC_2$ was derived from DFT calculations as shown in Fig. 3a, and could be described by the third-order Birch–Murnaghan equation of state (EoS) with the parameters $V_0$ =127.17(2) $Å^3$, K=144.5(2) GPa, and K´=3.92(1). The experimental P-V data points, as well as the data on the pressure dependence of the unit cell parameters (see Table S1) are in a good agreement with theoretical calculations (Fig. 3a). As seen in Fig. 3, HP-$CaC_2$ experiences an anisotropic contraction upon compression with the most compressible direction along the *c*-axis and the least compressible along *a*-axis, i.e. perpendicularly and parallel to polyacene-like nanoribbons, correspondingly (Fig. 3a).

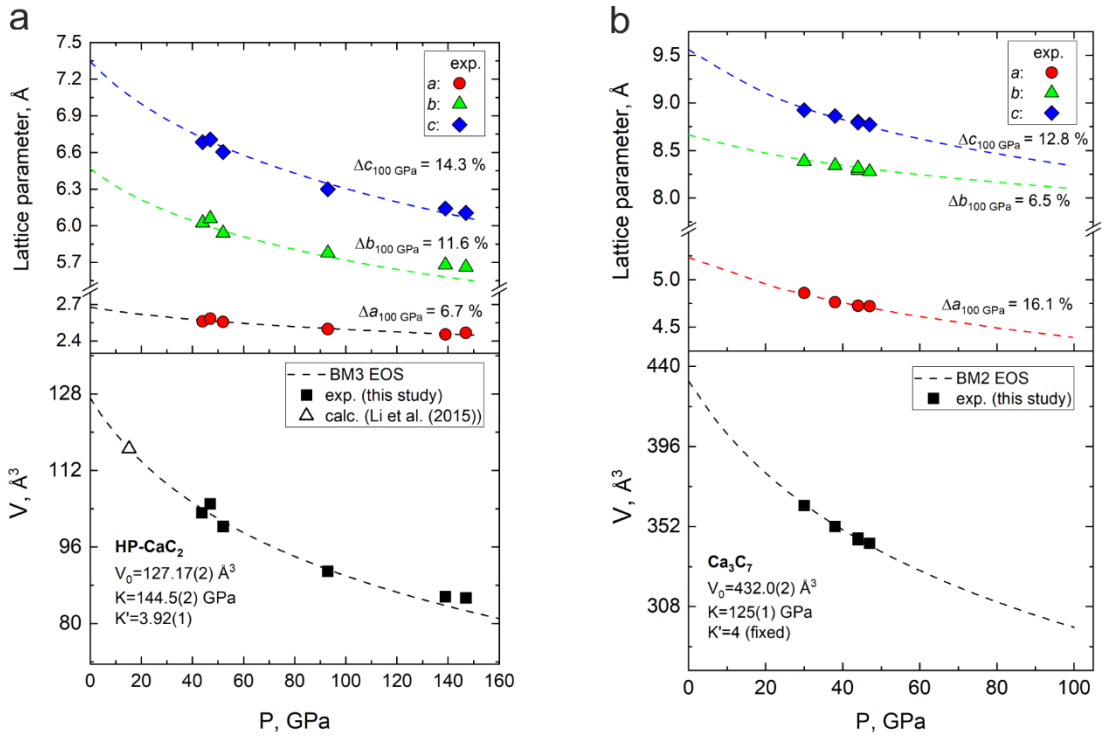


***Figure 3.*** *Pressure dependence of the lattice parameters and the unit cell volume for two Ca-C compounds. (a) HP-$CaC_2$; (b) $Ca_3C_7$. Solid symbols are experimental data points; dashed curves represent theoretical data; the black dashed lines are the fit of the calculated PV data using the Birch–Murnaghan equations of state with following parameters: $V_0$=127.17(2) Å$^3$, K=144.5(2) GPa, and K´=3.92 for HP-$CaC_2$; and $V_0$=432.0(2) Å$^3$, K=125(1) GPa, K´=4 (fixed) for $Ca_3C_7$.*

### *Crystal structure of the novel high-pressure compound $Ca_3C_7$*

Laser-heating of $CaC_2$ in paraffin oil at pressures of ~40 GPa results in the appearance of new diffraction peaks, which do belong neither to HP-$CaC_2$ nor to B1-CaO. Indexing reveals an orthorhombic unit cell with the lattice parameters a=4.762(4) Å, b=8.3411(11) Å, and c=8.8625(13) Å at 38(1) GPa (space group *Pnma*) (see Supplementary Fig. S3, Table S2). The structure solution and refinement suggest $Ca_3C_7$ stoichiometry with four formula units per a unit cell. Such a compound has never been synthesized or theoretically predicted hitherto. There are two independent crystallographic positions of calcium atoms in the crystal structure of $Ca_3C_7$: Ca1 on the Wyckoff site *4c* (0.0519, 0.25, 0.33981) and Ca2 on the Wyckoff site *8d* (0.19584, 0.57441, 0.35335). Carbon atom C1 is at the Wyckoff position *4c* (0.19090, 0.25, 0.19090). Other carbon atoms, C2 (0.2160(9), 0.0533(2), 0.1206(2)), C3 (0.1821(9), 0.6126(2), 0.0646(2)) and C4

(0.0171(9), 0.1627(2), 0.04895(19)) occupy there independent Wyckoff sites *8d (*x,y,z). In the crystal structure of $Ca_3C_7$ carbon atoms form infinite non-planar chains made of fused distorted $C_6$ and $C_5$ rings, which are isomorphous to deprotonated *para*-type poly(indenoindene) (*p*-PInIn) [2] (Fig. 2a, b). The projection on the [011] plane visualizes the alternation of layers of calcium atoms with deprotonated *p*-PInIn carbon chains (Fig. 2a). To the best of our knowledge, such type of poly-C entity has never been predicted or reported for any of metal carbides known in inorganic chemistry. There are five different C-C distances in the complex $[C_{14}]^{12-}$ polyanion (Supplementary Fig. S5), at 38(1) GPa the shortest and the longest C-C bonds are equal to 1.431 Å and 1.479 Å, correspondingly. Unlike to $C_6$-ring in deprotonated polyacene nanoribbon in HP-$CaC_2$, the hexagon in *p*-PInIn anion in $Ca_3C_7$ exhibits pronounced distortion, where two angles strongly deviate from 120˚ and are equal to 111.6˚. These modest differences underline a subtle, but recognizable dissimilarity in their chemical environment, namely the complexity of poly-C species and their coordination with the $Ca^{2+}$ ions.

The pressure dependence of the unit cell parameters and the unit cell volume of $Ca_3C_7$ has been established by theoretical calculations. The compressional behavior of $Ca_3C_7$ is highly anisotropic with least compressible direction along the *b*-axis, parallel to deprotonated *p*-PInIn chains (Fig.3b). The calculated PV-data could be fitted by the second-order Birch–Murnaghan EoS with the parameters $V_0$ =432.0(2) $Å^3$, K=125(1) GPa, and K´=4(fixed). The unit cell parameters derived from four independent SCXRD experiments, conducted at various pressures from 30 to 47 GPa (Supplementary Table 1) show a good agreement with the calculated EoS (Fig. 3b).

*Electronic structure of HP-$CaC_2$ and $Ca_3C_7$*

**HP-$CaC_2$**

The crystal structure of experimentally observed HP-$CaC_2$ is in a very good agreement with recent theoretical predictions[17,18]. Harmonic phonon dispersion calculations reveal that HP-$CaC_2$ is dynamically stable at its synthesis pressure of 44(1) GPa (Fig. 4a). The calculated electron density of states shows that HP-$CaC_2$ is metallic and the main contributions at the Fermi level come from the Ca *3d* and C *2p* states (Fig. 4c). The computed charge density was analyzed in terms of the electron localization function (ELF), which revealed a strong covalent bonding between carbon atoms within deprotonated poly-acene nanoribbons, and ionic bonds between Ca1

and C2 atoms (Fig. 1c, d). Bader charge analysis for Ca1, C1, and C2 atoms yields values of 1.191, -0.378, and -0.813 (Supplementary Table S3), respectively.

**$Ca_3C_7$**

$Ca_3C_7$ solid also remains dynamically stable at its synthesis pressure of 38(1) GPa (Fig. 4b). The calculated electron density of states suggests it to be a narrow-band *p*-type semiconductor (Fig. 4d). Computed ELF charge shows a formation of covalent bonds between carbon atoms in deprotonated *p*-PInIn carbon chains, and a strong ionic interaction between Ca and C atoms (Fig. 2c, d). Bader charge analysis for Ca1, Ca2 atoms yields values of 1.227, 1.232; for C1, C2, C3, C4 atoms: -0.718, -0.798, -0.338, -0.351, respectively (Supplementary Table S4).

## Discussion

A possibility for polymeric-carbon structures in alkali metal carbides has been suggested in a number of theoretical works on the Li-C[18], Ca-C[17,18], Mg-C[31] systems. However, complex polymeric carbon anions have never been observed experimentally. HP-$CaC_2$ is the first example. It was synthesized at pressures of ~40 GPa that is within the suggested range of its thermodynamic stability[17], which was proposed to extend to 105 GPa. At higher pressures, a $MgB_2$-type structure was predicted to be more stable[17]. However, we did not observe it. Instead, HP-$CaC_2$ was preserved to ~150 GPa, as revealed by our SCXRD data.

The C-C distances in $[C_4]^{4-}$ in HP-$CaC_2$ at 44(1) GPa are 1.42 Å and 1.476 Å. They are larger than expected for double- (~1.34 Å) and 1.5- bonded (~1.39 Å) carbon atoms, as known in ethylene and benzene, respectively. This leads us to the conclusion that the C-C bond orders in HP-$CaC_2$ are non-integer and should be in the range of 1.0–1.5 in analogy to γ-$Y_4C_5$[32].

$Ca_3C_7$ solid contains unique poly-C anion, that has never been predicted before. According to charge balance considerations the total formal charge of deprotonated *p*-PInIn-like $[C_{14}]$ anion should be -12, based on formula $6{\cdot}Ca^{2+}[C_{14}]^{12-}$. The lengths of C-C bonds at 38(1) GPa in this poly-anion (1.43-1.48 Å) suggest their order to be in the range of 1.0–1.5. Remarkably, they are close to the bond lengths in carbon pentagons in *P-1* $CaC_2$, predicted by Li et al. at 20 GPa. Also

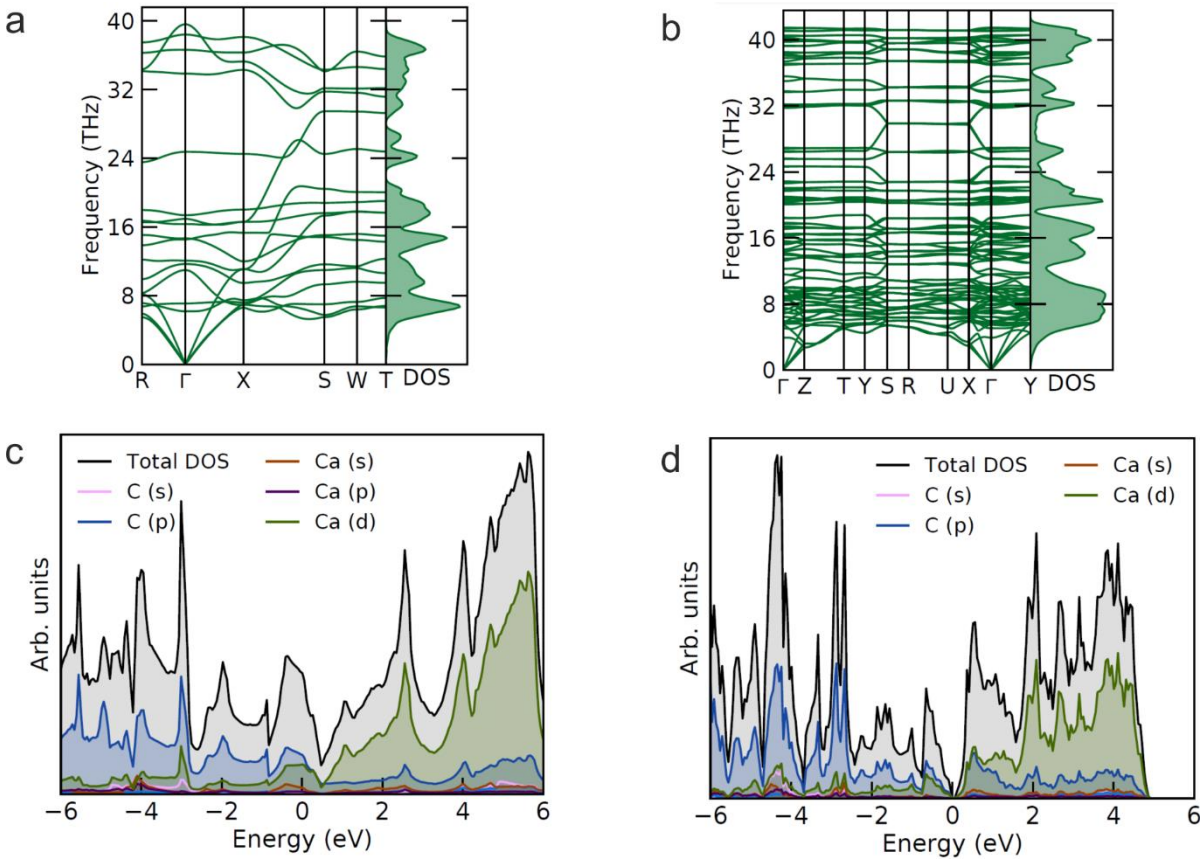


***Figure 4.*** *Results of DFT-based calculations for HP-$CaC_2$ at 44(1) and $Ca_3C_7$ at 38(1) GPa. Calculated phonon dispersion curves for HP-$CaC_2$ (a) and $Ca_3C_7$ (b). Calculated electron density of states of for HP-$CaC_2$ (c) and $Ca_3C_7$ (d); the Fermi energy level was set at 0 eV.*

the length of C-C contacts (1.46-1.57 Å at ambient conditions) in a predicted for $MgC_2$[31] poly-anionic entity containing $C_5$ pentagons, is similar to those in $Ca_3C_7$. The average length of C-C bonds in the distorted C6-ring of *p*-PInIn-like $[C_{14}]^{12-}$ anion is much longer than in fluorene[33] (~1.46 Å at 38 (1) GPa in $[C_{14}]^{12-}$ *vs* 1.40 Å at atmospheric pressure in $C_{13}H_{10}$). However, the average bonds length in the $C_5$ ring in $Ca_3C_7$ at 38(1) GPa is equal to the average bonds length in pentagon in fluorene at ambient conditions (~1.44 Å).

To explore the thermodynamic stability of HP-$CaC_2$ and $Ca_3C_7$ in comparison to other calcium carbides, a convex hull was constructed for the binary Ca-C system at pressure of ~40 GPa considering predicted phases[17]. The formation enthalpies of the compounds $Ca + x \cdot C \rightarrow CaC_x$ are calculated relative to the DFT total energies of the end-member elements Ca[34] and C as

$\Delta H_{formation} = (H_{CaC_x}\text{-}H_{Ca}\text{-}x \cdot H_c)/(1 + x)$. The both observed in the present study phases lie on the convex hull and therefore are thermodynamically stable at P =40 GPa (Fig. 5). Notably, that HP-$CaC_2$ also remains thermodynamically stable at P =140 GPa (Supplementary Fig. S6). Although an attempt to recover HP-$CaC_2$ and $Ca_3C_7$ at ambient conditions was unsuccessful, according to our calculations, the compound should be dynamically stable even at atmospheric pressure (Supplementary Fig. S7). Therefore, their stabilization can be potentially achieved through low-temperature decompression.

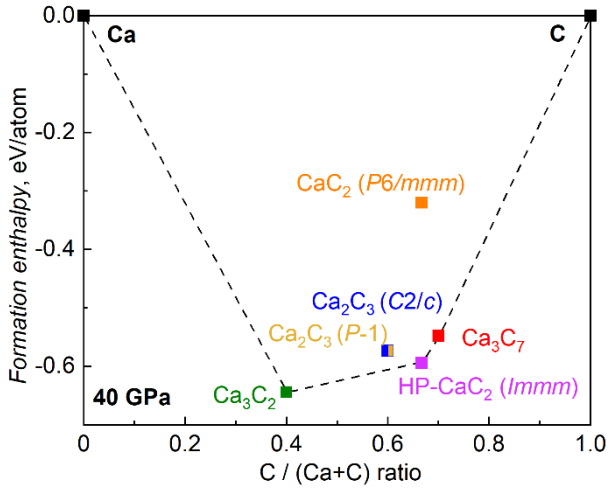


***Figure 5.*** *The calculated convex hull for the Ca-C binary joint with predicted and observed calcium carbides at 40 GPa. The phases HP-$CaC_2$ and $Ca_3C_7$ lie on the convex hull (black dashed line) and are, thus, thermodynamically stable. Phases $Ca_2C_3$ (P-1), $Ca_2C_3$ (C2/m) and $CaC_2$ (P6/mmm) are off the convex hull and, therefore, unstable.*

## Conclusions

In the present work we performed high-pressure high-temperature studies of $CaC_2$ in laser-heated diamond anvil cells using synchrotron single-crystal X-ray diffraction. They revealed two new materials with unique crystal structures. The high-pressure polymorph of $CaC_2$ with the previously predicted *Immm* structure was synthesized in the pressure range of ca. 44 through 150 GPa at temperatures between ca. 2300 and 3300 K. Its crystal structure containing infinite fully deprotonated polyacene-like nanoribbons was solved and refined, and its compressional behaviour was studied at room temperature. A novel $Ca_3C_7$ compound, never anticipated or observed before,

was synthesized and characterized using SCXRD at ca. 40 GPa. Its orthorhombic crystal structure featues infinite, fully deprotonated *para*-poly-indenoindene (*p*-PInIn)-like chains.

## References


(1) Tobe, Y. Non-Alternant Non-Benzenoid Aromatic Compounds: Past, Present, and Future. *Chem. Rec.* **2015**, *15* (1), 86–96. https://doi.org/10.1002/tcr.201402077.

(2) Di Giovannantonio, M.; Chen, Q.; Urgel, J. I.; Ruffieux, P.; Pignedoli, C. A.; Müllen, K.; Narita, A.; Fasel, R. On-Surface Synthesis of Oligo(Indenoindene). *J. Am. Chem. Soc.* **2020**, *142* (30), 12925–12929. https://doi.org/10.1021/jacs.0c05701.

(3) Louis E. Toth. *Transition Metal Carbides and Nitrides*; 1971.

(4) Spedding, F. H.; Gschneidner, K.; Daane, A. H. The Crystal Structures of Some of the Rare Earth Carbides. *J. Am. Chem. Soc.* **1958**, *80* (17), 4499–4503. https://doi.org/10.1021/ja01550a017.

(5) Sakai, T.; Adachi, G. Y.; Yoshida, T.; Shiokawa, J. Magnetic and Electrical Properties of LaC2, CeC2, PrC2, NdC2, and SmC2. *J. Chem. Phys.* **1981**, *75* (6), 3027–3032. https://doi.org/10.1063/1.442396.

(6) Atoji, M.; Medrud, R. C.; Gschneidner, K.; Daane, A. H.; Rundle, R. E.; Spedding, F. H.; Gschneidner, K.; Daane, A. H.; Sakai, T.; Adachi, G. Y.; Yoshida, T.; Shiokawa, J.; Rundle, R. E.; Baenziger, N. C.; Wilson, A. S.; McDonald, R. A. Neutron Diffraction Studies of CaC2, YC2, LaC 2, CeC2, TbC2, YbC2, LuC 2, and UC2. *J. Chem. Phys.* **1958**, *80* (6), 99–105. https://doi.org/10.1063/1.1730352.

(7) Babizhetskyy, V.; Kotur, B.; Levytskyy, V.; Michor, H. *Handbook on the Physics and Chemistry of Rare Earths*, 1st ed.; Elsevier B.V., 2017; Vol. 52. https://doi.org/10.1016/bs.hpcre.2017.09.001.

(8) Mattausch, H.; Gulden, T.; Kremer, R. K.; Horakh, J.; Simon, A. Carbide Mit C34-- Und C4_-Ionen. **1994**, 1439–1443.

(9) Fjellvaag, H.; Karen, P. Crystal Structure of Magnesium Sesquicarbide. *Inorg. Chem.* **1992**, *31* (15), 3260–3263. https://doi.org/10.1021/ic00041a018.

(10) Pöttgen, R.; Jeitschko, W. Sc3C4, a Carbide with C3 Units Derived from Propadiene. *Inorg. Chem.* **1991**, *30* (3), 427–431. https://doi.org/10.1021/ic00003a013.

(11) Strobel, T. A.; Kurakevych, O. O.; Kim, D. Y.; Le Godec, Y.; Crichton, W.; Guignard, J.; Guignot, N.; Cody, G. D.; Oganov, A. R. Synthesis of β-Mg2C3: A Monoclinic High-Pressure Polymorph of Magnesium Sesquicarbide. *Inorg. Chem.* **2014**, *53* (13), 7020–7027. https://doi.org/10.1021/ic500960d.

(12) Li, Y. L.; Wang, S. N.; Oganov, A. R.; Gou, H.; Smith, J. S.; Strobel, T. A. Investigation of Exotic Stable Calcium Carbides Using Theory and Experiment. *Nat. Commun.* **2015**, *6* (May), 1–9. https://doi.org/10.1038/ncomms7974.

(13) Gao, X.; Jiang, Y.; Zhou, R.; Feng, J. Stability and Elastic Properties of Y-C Binary Compounds Investigated by First Principles Calculations. *J. Alloys Compd.* **2014**, *587*, 819–826. https://doi.org/10.1016/j.jallcom.2013.11.005.

(14) Su, C.; Zhang, J.; Liu, G.; Wang, X.; Wang, H.; Ma, Y. Catenation of Carbon in LaC2 Predicted under High Pressure. *Phys. Chem. Chem. Phys.* **2016**, *18* (21), 14286–14291. https://doi.org/10.1039/c6cp01484d.

(15) Knapp, M.; Ruschewitz, U. Structural Phase Transitions in CaC2. *Chem. - A Eur. J.* **2001**, *7* (4), 874–880. https://doi.org/10.1002/1521-3765(20010216)7:4<874::AID-CHEM874>3.0.CO;2-V.

(16) Wang, L.; Huang, X.; Li, D.; Huang, Y.; Bao, K.; Li, F.; Wu, G.; Liu, B.; Cui, T. Pressure-Induced Structural Transformation of CaC 2. *J. Chem. Phys.* **2016**, *144* (19), 194506. https://doi.org/10.1063/1.4948705.

(17) Li, Y. L.; Wang, S. N.; Oganov, A. R.; Gou, H.; Smith, J. S.; Strobel, T. A. Investigation of Exotic Stable Calcium Carbides Using Theory and Experiment. *Nat. Commun.* **2015**, *6* (6974), 6974. https://doi.org/10.1038/ncomms7974.

(18) Benson, D.; Li, Y.; Luo, W.; Ahuja, R.; Svensson, G.; Häussermann, U. Lithium and Calcium Carbides with Polymeric Carbon Structures. *Inorg. Chem.* **2013**, *52* (11), 6402–

6406. https://doi.org/10.1021/ic4002219.

(19) Kantor, I.; Prakapenka, V.; Kantor, A.; Dera, P.; Kurnosov, A.; Sinogeikin, S.; Dubrovinskaia, N.; Dubrovinsky, L. BX90: A New Diamond Anvil Cell Design for X-Ray Diffraction and Optical Measurements. *Rev. Sci. Instrum.* **2012**, *83* (125102), 125102. https://doi.org/10.1063/1.4768541.

(20) Fedotenko, T.; Dubrovinsky, L.; Aprilis, G.; Koemets, E.; Snigirev, A.; Snigireva, I.; Barannikov, A.; Ershov, P.; Cova, F.; Hanfland, M.; Dubrovinskaia, N. Laser Heating Setup for Diamond Anvil Cells for in Situ Synchrotron and in House High and Ultra-High Pressure Studies. *Rev. Sci. Instrum.* **2019**, *90* (10), 104501. https://doi.org/10.1063/1.5117786.

(21) Rigaku Oxford Diffraction. CrysAlis Pro (v. 171.40.84). Rigaku Oxford Diffraction, Yarnton, UK 2020.

(22) Sheldrick, G. M. SHELXT – Integrated Space-Group and Crystal-Structure Determination. *Acta Crystallogr. Sect. A Found. Adv.* **2015**, *71* (1), 3–8. https://doi.org/10.1107/S2053273314026370.

(23) Petříček, V.; Dušek, M.; Palatinus, L. Crystallographic Computing System JANA2006: General Features. *Zeitschrift für Krist. - Cryst. Mater.* **2014**, *229* (5), 345–352. https://doi.org/10.1515/zkri-2014-1737.

(24) Momma, K.; Izumi, F. VESTA 3 for Three-Dimensional Visualization of Crystal, Volumetric and Morphology Data. *J. Appl. Crystallogr.* **2011**, *44* (6), 1272–1276. https://doi.org/10.1107/S0021889811038970.

(25) Perdew, J. P.; Burke, K.; Ernzerhof, M. Generalized Gradient Approximation Made Simple. *Phys. Rev. Lett.* **1996**, *77* (18), 3865–3868. https://doi.org/10.1103/PhysRevLett.77.3865.

(26) Kresse, G.; Joubert, D. From Ultrasoft Pseudopotentials to the Projector Augmented-Wave Method. *Phys. Rev. B* **1999**, *59* (3), 1758–1775. https://doi.org/10.1103/PhysRevB.59.1758.

(27) Kresse, G.; Furthmüller, J. Efficient Iterative Schemes for Ab Initio Total-Energy Calculations Using a Plane-Wave Basis Set. *Phys. Rev. B - Condens. Matter Mater. Phys.* **1996**, *54* (16), 11169–11186. https://doi.org/10.1103/PhysRevB.54.11169.

(28) Togo, A.; Tanaka, I. First Principles Phonon Calculations in Materials Science. *Scr. Mater.* **2015**, *108*, 1–5. https://doi.org/10.1016/j.scriptamat.2015.07.021.

(29) Konar, S.; Nylén, J.; Svensson, G.; Bernin, D.; Edén, M.; Ruschewitz, U.; Häussermann, U. The Many Phases of CaC2. *J. Solid State Chem.* **2016**, *239*, 204–213. https://doi.org/10.1016/j.jssc.2016.04.030.

(30) Zheng, H.; Wang, L.; Li, K.; Yang, Y.; Wang, Y.; Wu, J.; Dong, X.; Wang, C.-H.; Tulk, C. A.; Molaison, J. J.; Ivanov, I. N.; Feygenson, M.; Yang, W.; Guthrie, M.; Zhao, Y.; Mao, H.-K.; Jin, C. Pressure Induced Polymerization of Acetylide Anions in CaC 2 and 10 7 Fold Enhancement of Electrical Conductivity. *Chem. Sci.* **2017**, *8* (1), 298–304. https://doi.org/10.1039/C6SC02830F.

(31) Srepusharawoot, P.; Blomqvist, A.; Araújo, C. M.; Scheicher, R. H.; Ahuja, R. One-Dimensional Polymeric Carbon Structure Based on Five-Membered Rings in Alkaline Earth Metal Dicarbides BeC2 and MgC2. *Phys. Rev. B - Condens. Matter Mater. Phys.* **2010**, *82* (12), 125439. https://doi.org/10.1103/PhysRevB.82.125439.

(32) Aslandukova, A.; Aslandukov, A.; Yuan, L.; Laniel, D.; Khandarkhaeva, S.; Fedotenko, T.; Steinle-Neumann, G.; Glazyrin, K.; Dubrovinskaia, N.; Dubrovinsky, L. Novel High-Pressure Yttrium Carbide <math Display="inline"> <mrow> <mi>γ</Mi> <mtext>−</Mtext> <msub> <mrow> <mi Mathvariant="normal">Y</Mi> </Mrow> <mrow> <mn>4</Mn> </Mrow> </Msub> <msub> <mrow> <mi Mathvariant="normal">C</Mi> </Mrow> <mrow> <mn>5</Mn>. *Phys. Rev. Lett.* **2021**, *127* (13), 135501. https://doi.org/10.1103/PhysRevLett.127.135501.

(33) The Crystal and Molecular Structure of Fluorene. *Proc. R. Soc. London. Ser. A. Math. Phys. Sci.* **1955**, *227* (1169), 200–214. https://doi.org/10.1098/rspa.1955.0004.

(34) Anzellini, S.; Errandonea, D.; MacLeod, S. G.; Botella, P.; Daisenberger, D.; De'Ath, J. M.; Gonzalez-Platas, J.; Ibáñez, J.; McMahon, M. I.; Munro, K. A.; Popescu, C.; Ruiz-Fuertes, J.; Wilson, C. W. Phase Diagram of Calcium at High Pressure and High Temperature. *Phys. Rev. Mater.* **2018**, *2* (8), 083608. https://doi.org/10.1103/PhysRevMaterials.2.083608.

## Supporting Information

# High-pressure synthesis of $CaC_2$ and $Ca_3C_7$ with deprotonated polyacene- and *para*-poly(indenoindene)-like nanoribbons

*Saiana Khandarkhaeva[1,2], Timofey Fedotenko[3], Alena Aslandukova[1], Maxim Bykov[4], Dominique Laniel[2], Andrii Aslandukov[2], Björn Winkler (?), Uwe Ruschewitz[4], Christian Tobeck[4], Stella Chariton[5], Vitali Prakapenka[5], Konstantin Glazyrin[3], Hanns-Peter Liermann[3], Carlotta Giacobbe[6], Eleanor Lawrence Bright[6], Natalia Dubrovinskaia[2,7] and Leonid Dubrovinsky[1]*

[1]*Bayerisches Geoinstitut, University of Bayreuth, Universitätstraße 30, 95440 Bayreuth, Germany*

[2]*Material Physics and Technology at Extreme Conditions, Laboratory of Crystallography University of Bayreuth, Universitätstraße 30, 95440 Bayreuth, Germany*

[3]*Deutsches Elektronen-Synchrotron DESY, Notkestr. 85, 22607 Hamburg, Germany*

[4]*Institute of Inorganic Chemistry, University of Cologne, Greinstrasse 6, 50939 Cologne, Germany*

[5]*Center for Advanced Radiation Sources, The University of Chicago, 5640 S. Ellis, 60637 Chicago, Illinois, USA*

[6]*European Synchrotron Radiation Facility, BP 220, 38043 Grenoble Cedex, France*

[7]*Theoretical Physics Division, Department of Physics, Chemistry and Biology (IFM), Linköping University, SE-581 83 Linköping, Sweden*

**Corresponding author: saiana.khandarkhaeva@uni-bayreuth.de*

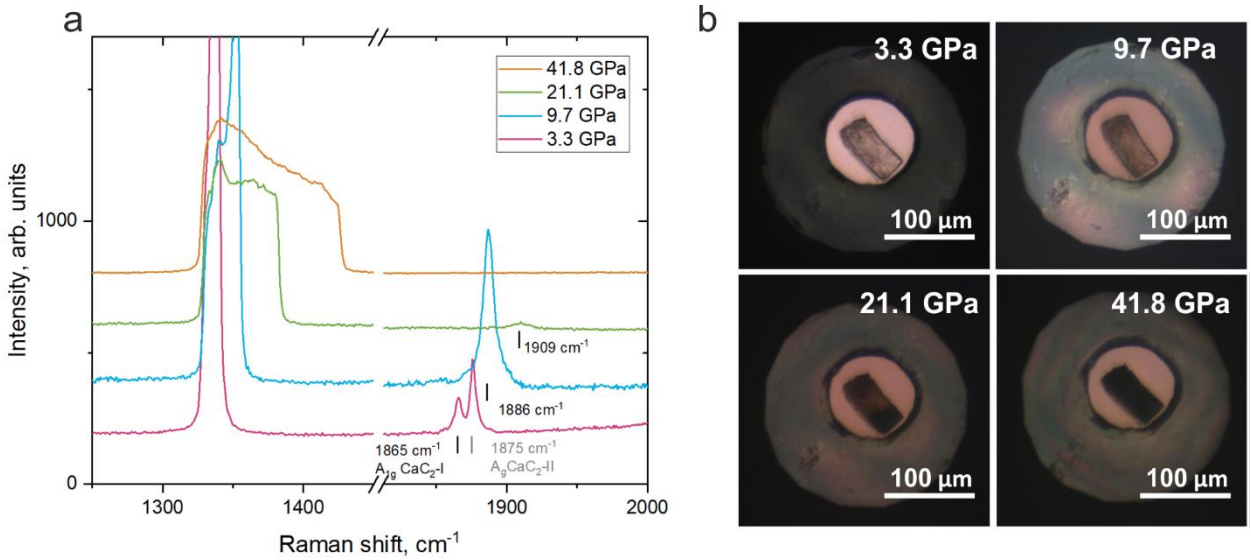


***Fig. S1.*** *Raman spectra (a) and microphotographs (b) of a $CaC_2$ sample taken upon its compression at room temperature in DAC #1. Raman spectra (a) were recorded on using DilorXY system equipped with the Ar (the excitation wavelength 638 nm) laser source. Black and gray ticks highlight vibrational modes of two polymorphs: tetragonal $CaC_2$-I and monoclinic $CaC_2$-II. Microphotographs (b) reveal changes in the visual appearance of the sample with increasing pressure: initially transparent crystal becomes translucent at ~10 GPa and then opaque above ~25 GPa.*

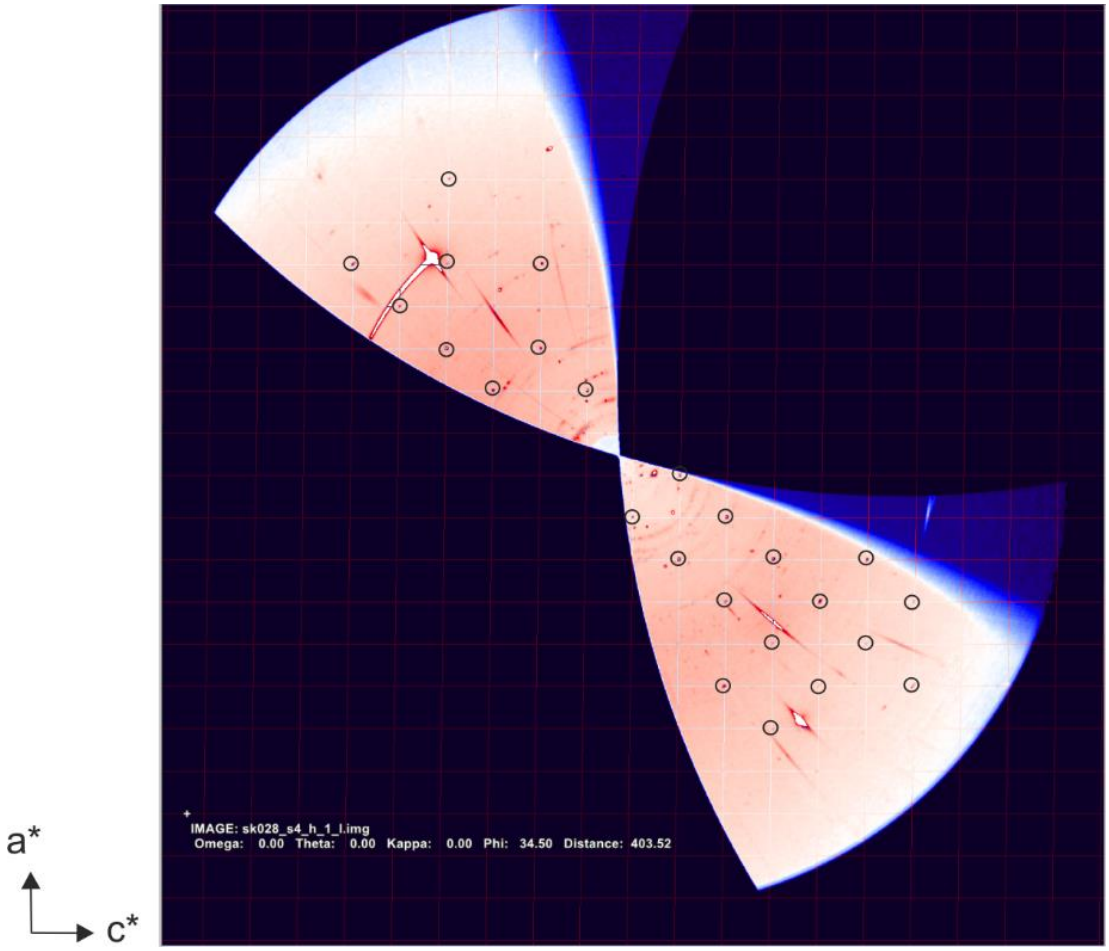


***Fig. S2***. *Reciprocal space reconstruction of the (h1l) plain fot the single-crystal domain of the high-pressure $CaC_2$ polymorph (HP-$CaC_2$, space group Immm) observed after laser heating of $CaC_2$ at 2400(100) K at 44(1) GPa. Black circles. They belong to a single grain of the best quality.*

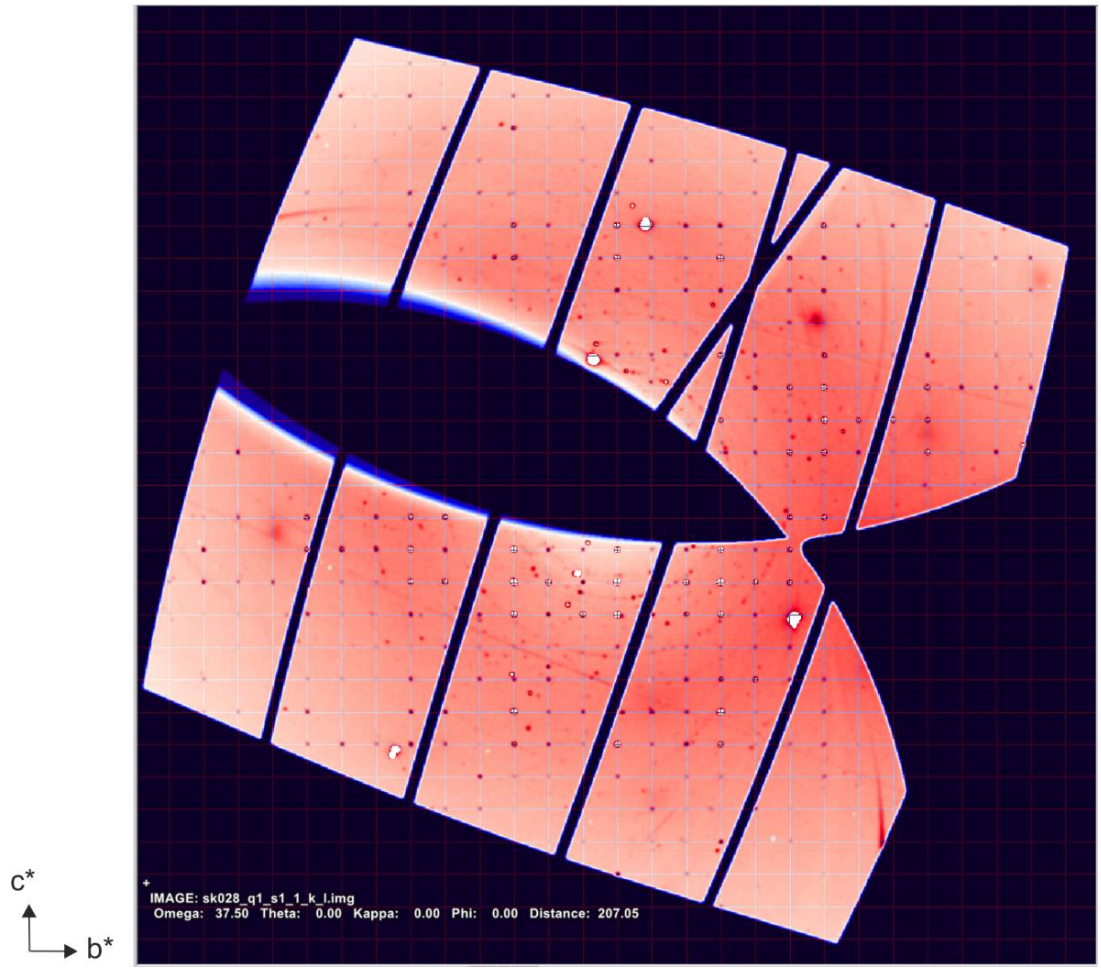


***Fig. S3***. *Reciprocal space reconstruction of the (1kl) the single-crystal domain of the* $Ca_3C_7$ *phase observed after laser-heating of* $CaC_2$ *at 2350(150) K at 38(1) GPa. Diffraction peaks, which belong to the single-crystalline grain of the best quality used for structure solution and refinement, are seen at the nodes of the reciprocal lattice.*

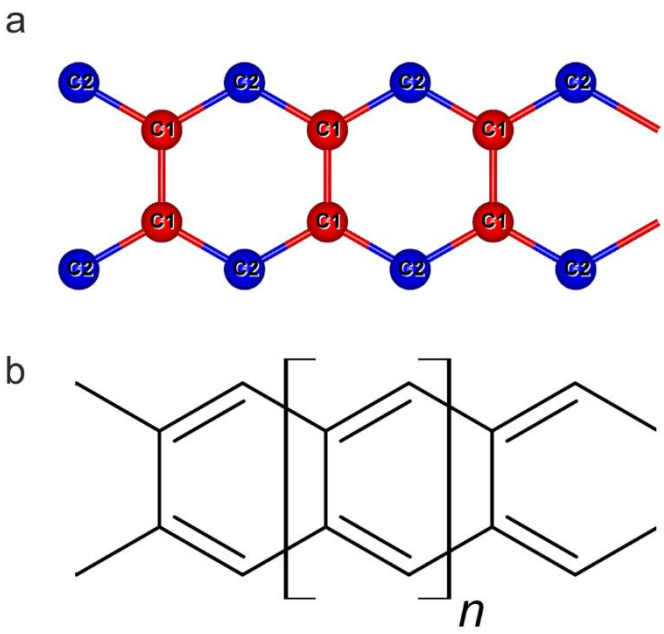


***Fig. S4.*** *A comparison of carbon poly-anion in the crystal structure of HP-$CaC_2$ (a) and polyacene (b).*

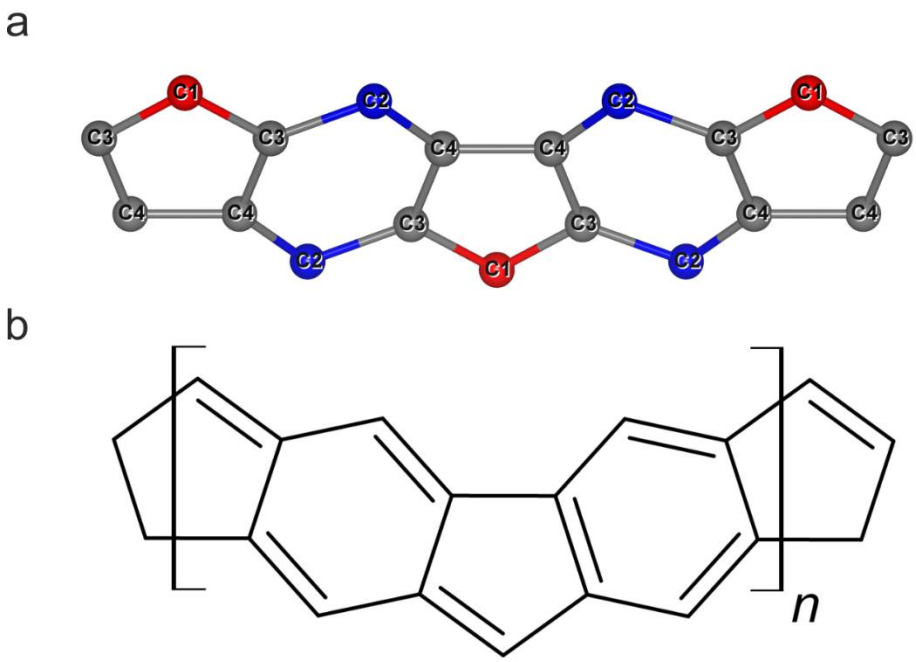


**Fig. S5.** A comparison of carbon poly-anion in the crystal structure of $Ca_3C_7$ (a) and *para*-type poly(indenoindene) (b).

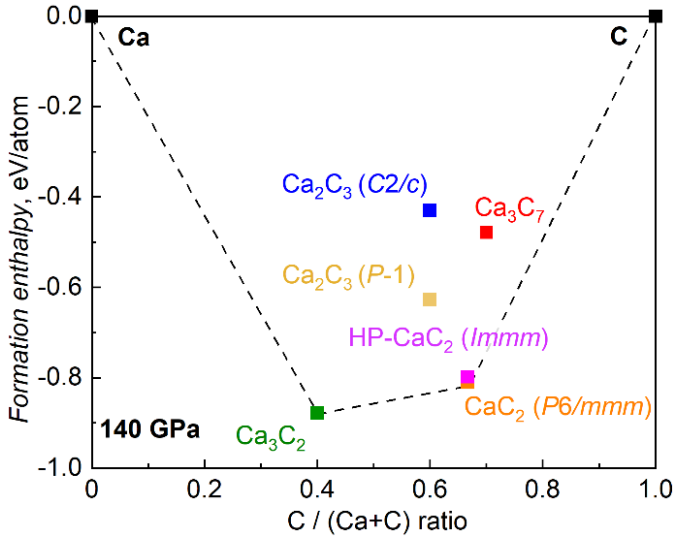


***Fig. S6.*** *The calculated convex hull in the Ca-C binary-join for predicted and observed calcium carbides at 140 GPa. The HP-$CaC_2$ phase lies on the convex hull (black dashed line) and are thus thermodynamically stable at this pressure.*

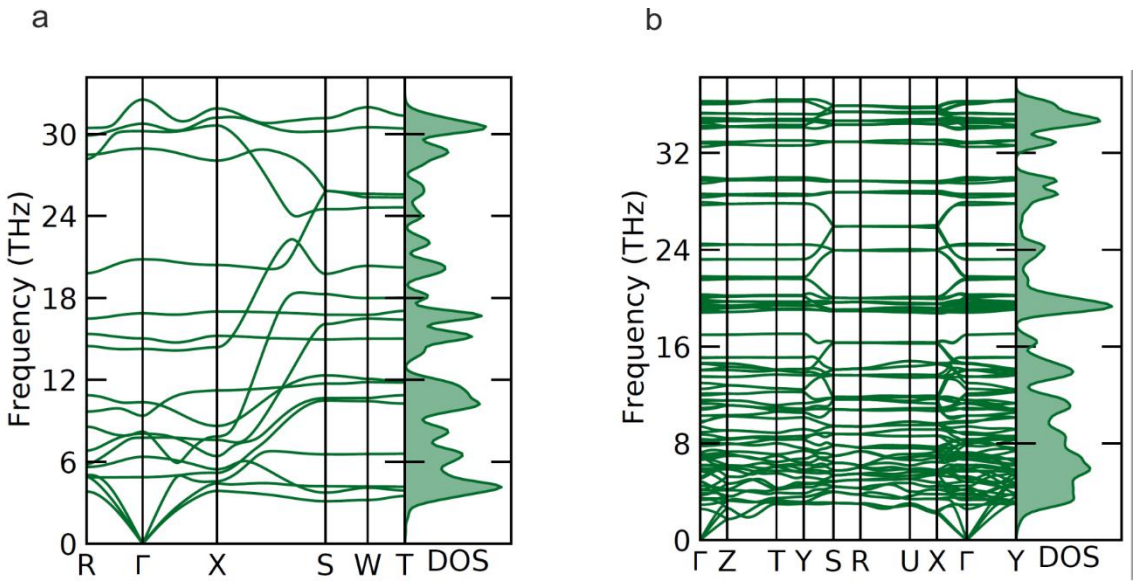


***Fig. S7.*** *Calculated phonon dispersion curves of HP-$CaC_2$ (a) and $Ca_3C_7$ (b) at 0 GPa.*

**Table S1.** Summary of experiments conducted in the present study.

| Experiment | Phase | a, Å | b, Å | c, Å | V, Å$^3$ | Pressure, GPa | Temperature, K |
|---|---|---|---|---|---|---|---|
| **#1_1** | $Ca_3C_7$ | 4.715(3) | 8.288(4) | 8.803(3) | 344.0(3) | 44(2) | 2400(100) |
| | HP-$CaC_2$ | 2.5616(3) | 6.025(2) | 6.685(2) | 103.17(4) | | |
| | B1 CaO | 4.444(1) | 4.444(1) | 4.444(1) | 87.77(5) | | |
| **#2_2*** | $Ca_3C_7$ | 4.762(4) | 8.341(1) | 8.863(2) | 352.1(3) | 38(1) | 2350(150) |
| | B1 CaO | 4.4764(4) | 4.4764(4) | 4.4764(4) | 89.70(1) | | |
| **#2_3** | $Ca_3C_7$ | 4.859(6) | 8.385(2) | 8.923(2) | 363.6 (4) | 30(2)** | |
| | B1 CaO | 4.5231(3) | 4.5231(3) | 4.5231(3) | 92.54(1) | | |
| **#3** | $Ca_3C_7$ | 4.727(5) | 8.316(2) | 8.791(2) | 345.6(3) | 44(1) | 2300(200) |
| | B1 CaO | 4.4399(4) | 4.4399(4) | 4.4399(4) | 87.53(2) | | |
| **#4** | $Ca_3C_7$ | 4.720(3) | 8.277(4) | 8.772(4) | 342.7(3) | 47(1) | 2300(300) |
| | HP-$CaC_2$ | 2.584(1) | 6.060(1) | 6.706(2) | 105.0(5) | 47(1) | |
| **#5** | HP-$CaC_2$ | 2.541(1) | 5.946(4) | 6.598(2) | 99.69(8) | 52(1) | 2400(200) |
| **#6_1*** | HP-$CaC_2$ | 2.4965(6) | 5.782(3) | 6.295(3) | 90.87(7) | 93(1) | 3000(300) |
| **#6_2*** | HP-$CaC_2$ | 2.454(2) | 5.680(2) | 6.141(5) | 85.59(10) | 139(2) | 3300(300) |
| **#6_3** | HP-$CaC_2$ | 2.4690(3) | 5.663(2) | 6.106(2) | 85.37(3) | 147(2) | |

It includes a list of phases observed in each experiment, their structural parameters, and pressure-temperature conditions of the synthesis. The first digit in the number of an experiment indicates the number of the DAC; the second digit, if given – the number of the experiment conducted in the same DAC.

All the DACs were laser heated in home laboratory at the BGI. An asterisk (*) in the number indicates that additional laser-heating was done at the extreme condition beamline 13-IDD at the Advanced Photon Source (APS, Chicago, USA). A double asterisk (**) indicates room temperature decompression. All diffraction measurements were made at room temperature on pressurized, but temperature-quenched samples after laser heating.

**Table S2.** Details of the crystal structure refinements of $CaC_2$ and $Ca_3C_7$ at 44(1) and 38(1) GPa, respectively.

| Chemical formula | $Ca_3C_7$ | $CaC_2$ |
|---|---|---|
| Pressure, GPa | 38(1) | 44(1) |
| $M_r$ | 204.3 | 64.1 |
| | 3.855 | |
| Crystal system, space group | Orthorhombic, *Pnma* | Orthorhombic, *Immm* |
| Temperature (K) | 293 | 293 |
| *a*, *b*, *c* (Å) | 4.762 (4), 8.3411 (11), 8.8625 (13) | 2.5616 (3), 6.0245 (17), 6.6851 (15) |
| *V* (Å$^3$) | 352.1 (3) | 103.17 (4) |
| *Z* | 4 | 4 |
| Radiation type | X-ray, λ = 0.29521 Å | X-ray, λ = 0.2885 Å |
| Radiation source | 13IDD, GSECARS, APS | P02.2, Petra III, DESY |
| μ (mm$^{-1}$) | 0.39 | 0.41 |
| Crystal size (mm) | 0.002×0.002×0.002 | 0.002×0.002×0.002 |
| Diffractometer | Customized ω-circle diffractometer | |
| Absorption correction | Multi-scan<br>*CrysAlis PRO* 1.171.40.84a (Rigaku Oxford Diffraction, 2020) Empirical absorption correction using spherical harmonics, implemented in SCALE3 ABSPACK scaling algorithm. | |
| $T_{min}$, $T_{max}$ | 0.547, 1 | 0.623, 1 |
| No. of measured, independent and observed [$I > 3\sigma(I)$] reflections | 888, 412, 362 | 291, 134, 96 |
| $\theta_{min}$, $\theta_{max}$ | 1.9°, 15.0° | 3.4°, 15° |
| hkl range | $h = -3\rightarrow4$<br>$k = -13\rightarrow13$<br>$l = -13\rightarrow14$ | $h = -4\rightarrow4$<br>$k = -7\rightarrow9$<br>$l = -9\rightarrow10$ |
| $R_{int}$ | 0.014 | 0.105 |
| $(\sin\theta/\lambda)_{max}$ (Å$^{-1}$) | 0.879 | 1.037 |
| $R[F^2 > 2\sigma(F^2)]$, $wR(F^2)$, $S$ | 0.026, 0.062, 1.92 | 0.059, 0.125, 1.20 |
| No. of reflections | 412 | 134 |
| No. of parameters | 31 | 9 |
| $\Delta\rho_{max}$, $\Delta\rho_{min}$ (e Å$^{-3}$) | 0.43, −0.40 | 1.05, −1.24 |

**Table S3**. Fractional atomic coordinates, isotropic* or equivalent isotropic displacement parameters (Å$^2$) and Bader charges of HP-$CaC_2$ at 44(1) GPa.

| **Experiment** | | | | |
|---|---|---|---|---|
| | x | y | z | $U_{iso}$*/$U_{eq}$ |
| **Ca1** | 0 | 0 | 0.2041 (2) | 0.0078 (5) |
| **C1** | 0 | 0.3819 (15) | 0 | 0.0071 (11)* |
| **C2** | 0 | 0.2397 (15) | 0.5 | 0.0078 (12)* |
| **Theory** | | | | |
| | *x* | *y* | *z* | *Bader charge* |
| **Ca1** | 0 | 0 | 0.20425 | 1.191 |
| **C1** | 0 | 0.37868 | 0 | -0.378 |
| **C2** | | 0.24217 | 0.5 | -0.813 |

**Table S4.** Fractional atomic coordinates, isotropic* or equivalent isotropic displacement parameters (Å$^2$) and Bader charges of $Ca_3C_7$ at 38(1) GPa.

| **Experiment** | | | | |
|---|---|---|---|---|
| | *x* | *y* | *z* | $U_{iso}$*/$U_{eq}$ |
| **Ca1** | 0.0519 (3) | 0.25 | 0.33981 (6) | 0.0055 (4) |
| **Ca2** | 0.19584 (19) | 0.57441 (5) | 0.35335 (4) | 0.0051 (2) |
| **C1** | 0.1909 (12) | 0.25 | 0.6332 (3) | 0.0052 (5)* |
| **C2** | 0.2160 (9) | 0.0533 (2) | 0.1206 (2) | 0.0063 (3)* |
| **C3** | 0.1821 (9) | 0.6126 (2) | 0.0646 (2) | 0.0055 (3)* |
| **C4** | 0.0171 (9) | 0.1627 (2) | 0.04895 (19) | 0.0050 (3)* |
| **Theory** | | | | |
| | *x* | *y* | *z* | *Bader charge* |
| **Ca1** | 0.04764 | 0.25 | 0.34161 | 1.227 |
| **Ca2** | 0.19509 | 0.57445 | 0.35355 | 1.232 |
| **C1** | 0.18986 | 0.25000 | 0.63304 | -0.718 |
| **C2** | 0.21204 | 0.05162 | 0.12032 | -0.798 |
| **C3** | 0.18233 | 0.61247 | 0.06504 | -0.338 |
| **C4** | 0.01607 | 0.16307 | 0.04999 | -0.351 |

**Table S5.** Details of the crystal structure refinements of HP-$CaC_2$ at 147(2) GPa.

| Chemical formula | $CaC_2$ |
|---|---|
| Pressure | 147(2) GPa |
| $M_r$ | 64.1 |
| Crystal system, space group | Orthorhombic, *Immm* |
| Temperature (K) | 293 |
| *a*, *b*, *c* (Å) | 2.4690 (3), 5.6625 (17), 6.1062 (15) |
| *V* (Å$^3$) | 85.37 (3) |
| *Z* | 4 |
| Radiation type | X-ray, λ = 0.2852 Å |
| Radiation source | ID11, ESRF |
| μ (mm$^{-1}$) | 0.48 |
| Crystal size (mm) | 0.0005×0.0005×0.0005 |
| Diffractometer | Customized ω-circle diffractometer |
| Absorption correction | Multi-scan<br>*CrysAlis PRO* 1.171.41.93a (Rigaku Oxford Diffraction, 2020) Empirical absorption correction using spherical harmonics, implemented in SCALE3 ABSPACK scaling algorithm. |
| $T_{min}$, $T_{max}$ | 0.624, 1 |
| No. of measured, independent and observed [$I > 3\sigma(I)$] reflections | 196, 134, 121 |
| $\theta_{min}$, $\theta_{max}$ | 2.9°, 19.4° |
| hkl range | $h = -4 \rightarrow 4$<br>$k = -11 \rightarrow 11$<br>$l = -10 \rightarrow 4$ |
| $R_{int}$ | 0.023 |
| $(\sin\theta/\lambda)_{max}$ (Å$^{-1}$) | 1.169 |
| $R[F^2 > 2\sigma(F^2)]$, $wR(F^2)$, *S* | 0.044, 0.097, 2.32 |
| No. of reflections | 134 |
| No. of parameters | 13 |
| $\Delta\rho_{max}$, $\Delta\rho_{min}$ (e Å$^{-3}$) | 1.41, −1.58 |

**Table S6.** Fractional atomic coordinates, isotropic* or equivalent isotropic displacement parameters (Å2) and Bader charges of HP-$CaC_2$ at 147(2) GPa.

| **Experiment** | | | | |
|---|---|---|---|---|
| | x | y | z | $U_{iso}$*/$U_{eq}$ |
| **Ca1** | 0 | 0 | 0.20080 (18) | 0.0078 (5) |
| **C1** | 0 | 0.3749 (6) | 0 | 0.0071 (11)* |
| **C2** | 0 | 0.2472 (6) | 0.5 | 0.0078 (12)* |
| **Theory** | | | | |
| | *x* | *y* | *z* | *Bader charge* |
| **Ca1** | 0 | 0 | 0.20286 | 1.06489 |
| **C1** | 0 | 0.37346 | 0 | -0.3378 |
| **C2** | 0 | 0.2483 | 0.5 | -0.727 |

# Chapter 7 Materials synthesis at terapascal static pressures

*Leonid Dubrovinsky[1]*, Saiana Khandarkhaeva[1,2], Timofey Fedotenko[3], Dominique Laniel[2], Maxim Bykov[4], Carlotta Giacobbe[5], Eleanor Lawrence Bright[5], Pavel Sedmak[5], Stella Chariton[6], Vitali Prakapenka[6], Alena V. Ponomareva[7], Ekaterina A. Smirnova[7], Maxim P. Belov[7], Ferenc Tasnádi[8], Nina Shulumba[8], Florian Trybel[8], Igor A. Abrikosov[8*], Natalia Dubrovinskaia[2,8]*

[1]*Bayerisches Geoinstitut, University of Bayreuth, Universitätstraße 30, 95440 Bayreuth, Germany*

[2]*Material Physics and Technology at Extreme Conditions, Laboratory of Crystallography University of Bayreuth, Universitätstraße 30, 95440 Bayreuth, Germany*

[3]*Deutsches Elektronen-Synchrotron DESY, Notkestr. 85, 22607 Hamburg, Germany*

[4]*Institute of Inorganic Chemistry, University of Cologne, Greinstrasse 6, 50939 Cologne, Germany*

[5]*European Synchrotron Radiation Facility, BP 220, 38043 Grenoble Cedex, France*

[6]*Center for Advanced Radiation Sources, The University of Chicago, 5640 S. Ellis, 60637 Chicago, Illinois, USA*

[7]*Materials Modeling and Development Laboratory, National University of Science and Technology "MISIS", Leninskiy Prospekt 4, 119991 Moscow, Russia.*

[8]*Theoretical Physics Division, Department of Physics, Chemistry and Biology (IFM), Linköping University, SE-581 83 Linköping, Sweden*

**Corresponding authors: Leonid.Dubrovinslky@uni-bayreuth.de, igor.abrikosov@liu.se*

*In press, Nature*

## Abstract

Theoretical modelling predicts very unusual structures and properties of materials at extreme pressure-temperature conditions[1,2]. Hitherto, their synthesis and investigations above 200 GPa have been hindered by both the technical complexity of ultra-high-pressure experiments and the absence of relevant methods of materials' analysis *in situ*. Here we report on the methodology that was developed to enable

experiments at static compression in terapascal regime with laser heating and on its application to the synthesis of a novel rhenium nitride, $Re_7N_3$, and a rhenium-nitrogen alloy between ca. 600 and 900 GPa in a laser-heated double-stage diamond anvil cell (ds-DAC)[3]. Theoretical analysis has shown that the extreme compression is decisive for the stabilization of $Re_7N_3$. Full chemical and structural characterization of the materials, realized using synchrotron single-crystal X-ray diffraction on microcrystals *in situ*, demonstrates the capabilities of the methodology to extend high-pressure crystallography to the terapascal regime.

## Introduction

The state of matter is strongly affected by variations in its chemical composition and the external parameters, such as pressure and temperature, allowing tuning of materials properties. This gives rise to a variety of phenomena relevant for a broad range of scientific disciplines and technological applications, from fundamental understanding of the Universe to targeted design of advanced materials. Compression is known to endorse metal-to-insulator transitions[4], superconductivity[5], and new "super"-states of matter[6]. Latest developments in the diamond anvil cell technique, and, particularly, the invention of double-stage and toroidal diamond anvil cells (ds-DACs and t-DACs)[3,7,8], enabled a breakthrough in the synthesis of materials and studying structure-properties relations at high and ultra-high pressures. Very recent examples are the discovery of a new nitrogen allotrope bp-N[9], which resolved a puzzle in understanding of the high-pressure behavior of pnictogen family elements, and the synthesis of a whole plethora of novel transition metals nitrides and polynitrides[10–15] including metal-inorganic frameworks (MIFs)[9,13]- a new class of compounds featuring open porous structures at megabar compression. Solving and refining the crystal structures of solids synthesized directly from elements in laser-heated conventional DACs[10–15] at pressures as high as up to about two megabar[12,16] became possible due to the synergy of our expertise both in generating multimegabar pressures[3,17,18] (for details see section "dsDAC technique" in Supplemental Materials) and in single-crystal X-ray diffraction (sc-XRD) at ultra-high pressures, which were pioneered a few years ago.[19,20] As the high-pressure high-temperature (HPHT) synthesis has become a well-established technique for materials discovery, extending investigations to the TPa regime has been desired for a long time.

Here, we report a new development in the methodology of the HPHT synthesis experiments that extends the limits of high-pressure crystallography to the terapascal range. To achieve the desired pressures, we combined toroidal[7,8] and double-stage[3,17,18] anvils design. A rhenium-nitrogen alloy, and a novel rhenium nitride $Re_7N_3$ were synthesized in three different experiments in the Re-N system (Supplementary

Information Table S1) in a laser-heated double-stage diamond anvil cell. Their full structural and chemical characterization was performed *in situ* using single-crystal X-ray diffraction.

## Experiment

The ds-DACs were prepared following the procedure outlined below. Conventional Boehler-Almax type single-beveled diamond anvils with 40-μm culets were milled by FIB in order to produce a toroidal profile on the surface of the culet and to shape a miniature culet of about 10 μm in diameter in its center (Extended Data Fig. 1). As a gasket we used a strip of a 200-μm thick Re foil, which was pre-indented in a few steps. The final indentation of 10 μm in diameter (made using anvils with the toroidal profile) had the thickness of about ~4 μm (the indentation procedure is described in detail in the figure caption of Extended Data Fig. 1). A hole of ~6 μm in diameter was made in the center of the indentation using FIB or by tightly focused pulsed NIR laser to form a pressure chamber. A schematic of the ds-DAC assembly, mounted into a BX-90 DAC[21] equipped with toroidal diamond anvils, is shown in Extended Data Fig. 1. To realize a ds-DAC design, two semi-balls made of transparent nanocrystalline diamond[17], FIB-milled from a single ball with a diameter of 12 to 14 μm, were placed over the tip of the miniature 10-μm culet (Extended Data Figs. 1,2). The semi-balls were small enough to stick on the toroidal anvils, but in one case (dsDAC #2, Supplementary Information Table S1) paraffin wax was used to fix them. A few grains of a rhenium powder (99.995% purity, Merck Inc.) were placed into the pressure chamber, which was then filled with nitrogen ($N_2$) at about 1.4 kbar using the high-pressure gas-loading setup[22] at the Bayerisches Geoinstitut (BGI, Bayreuth, Germany), closed, and pressurized.

Pressures in the pressure chambers after closing of the cells were of about 50 to 80 GPa (Extended Data Fig. 3); pressures on the primary anvils were below 10 GPa, as measured according to ref. 23[23]. Our experience suggests that the cell should be pressurized quickly to ~40 GPa on the primary anvils to avoid loss of nitrogen. The presence of nitrogen can be monitored on $N_2$ vibrons in the Raman spectra (Extended Data Fig. 3). However, $N_2$ vibrons were not detectable above ~150 GPa (Extended Data Fig. 3) in the pressure chamber, as at such compression nitrogen becomes non-transparent and we cannot detect the Raman signal anymore). In ds-DAC #2 we were able to observe the evolution of the Raman signal from the secondary anvil in parallel with that from the primary anvil upon pressurization (Extended Data Fig. 4). Huge stress on the secondary anvil is manifested in the large asymmetry of its corresponding Raman line, whose high-frequency edge is difficult to determine reliably (Extended Data Fig. 4). Thus, it cannot be used for characterization of pressure in the sample chamber (note also that, as a rule, Raman spectra of NCD are rather weak and broad).

In all dsDAC experiments described here, we followed the same protocol. After pressurization of the cells to about 120-140 GPa on the first-stage anvils[24], the samples were laser heated. The dsDACs #2 and #3 were heated by a pulsed laser (1 μs pulses duration, 25 kHz repetition rate, ~25 W at each side) at the BGI using the setup specially designed for ultra-high pressures: the NIR (1070 nm) laser beam is of less than 5 μm FWHM in diameter and optical magnification of about 300 times[25,26]. The entire pressure chamber of dsDAC #2 was heated at 2900(200) K during about 3 min, and dsDAC #3 at 3450(200) K during about 5 min. After laser-heating, pressure on the primary anvils of dsDAC #2 was of about 100 GPa, and dsDAC #3 – of about 120 GPa.

## Results and discussion

The dsDAC #1 was heated at 13-IDD at GSECARS (Advanced Photon Source (APS), USA) from both sides using a tightly focused NIR laser beam (of about 8 μm FWHM in diameter) in pulsed mode (1 μs pulses duration, 50 kHz repetition rate, ~20 W each side) during 5 s at a temperature of 2200(200) K. Powder diffraction data acquired before laser heating (Extended Data Fig. 5; at 13-IDD X-ray beam was of ~3x3 $\mu m^2$ FWHM) gave the following lattice parameters of Re: for the gasket they were equal to $a$=2.5606(5) Å, $c$=4.0588(12) Å, $V$=23.047(7) $Å^3$, and for the Re sample $a$=2.2214 (3) Å, $c$=3.5609 (8) Å, V=15.21 (1) $Å^3$. These parameters correspond to the pressures of 149(3) GPa on the gasket and 930(5) GPa on the sample; the conservative values are given according to the EOS from ref.[27] (Supplementary Information Table S1; the uncertainty in pressure corresponds to the statistical error in volume). X-ray powder diffraction patterns collected after laser heating show that positions of the diffraction lines of Re gasket did not change within the accuracy of the measurements, while those from Re sample changed very slightly ($a$=2.2297 (2) Å, $c$=3.5735 (5) Å, and $V$=15.38(1) $Å^3$ corresponding to pressure of 895(5) GPa[27]).

After laser heating for each dsDAC at 13-IDD at GSECARS numerous diffraction spots were observed (Extended Data Fig. 5), indicating phase transformation(s) or/and chemical reaction(s) in the samples. However, deciphering what happened based on powder diffraction data turned out to be impossible, as the patterns were dominated by the diffraction lines from the gasket and non-transformed Re, owing the relatively large X-ray beam and a small sample size. Single-crystal diffraction data were of poor quality that precluded their analysis.

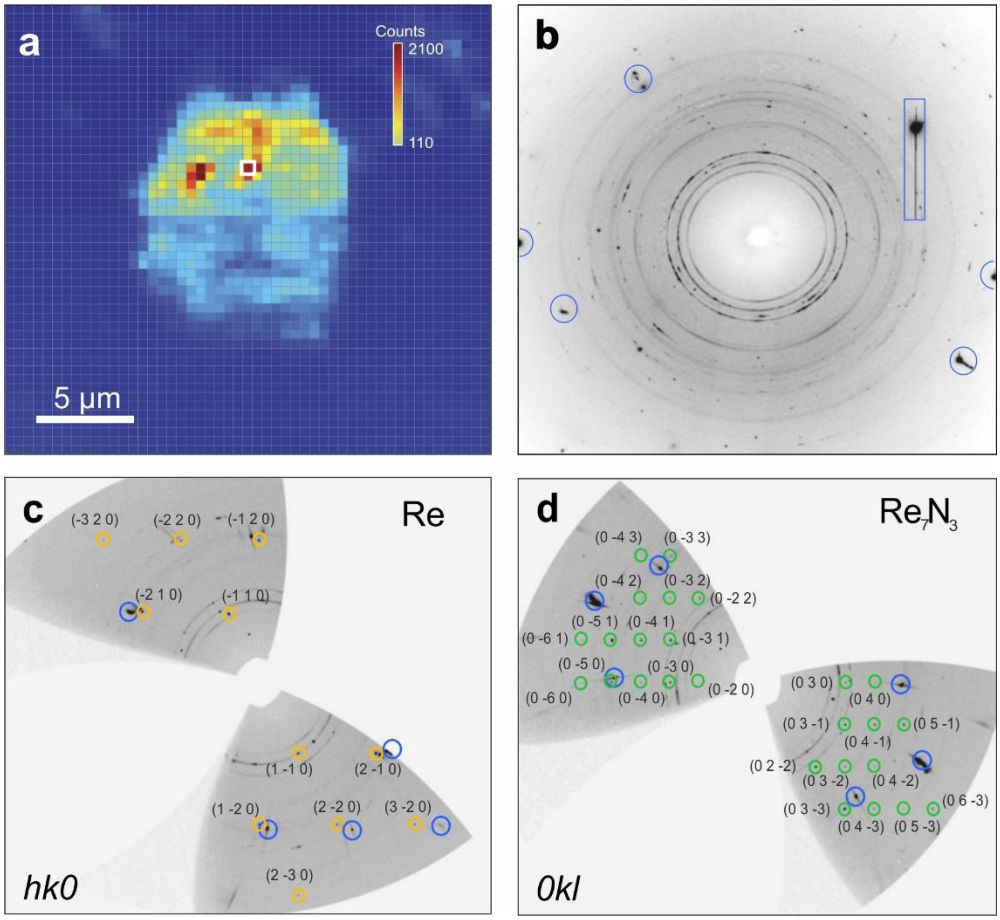


***Fig. 1. Results of X-ray diffraction measurements on the sample of Re and $N_2$ pulsed laser-heated in dsDAC #1.*** *(a) X-ray 2D map showing the distribution of different phases (re-crystallized Re and $Re_7N_3$) in the pressure chamber of dsDAC#1. Each pixel on the map corresponds to 2D X-ray diffraction pattern collected at Frelon 4M detector at ID11 beamline at ESRF (beam-size ~0.45×0.45 μm² at FWHM, λ=0.3099 Å). The map covers the whole pressure chamber (21.5×21.5 μm², steps of 0.5 μm in both directions, 10s acquisition time per frame). Total collection time was ~8 hours. The color intensity is proportional to the intensity of the following reflections: the (100) reflection of Re gasket for the dark blue region; the (101) reflection of Re for the light blue region (inside the sample chamber); the color bar on the insertion corresponds to the sum of intensities of (202) and (420) reflections of $Re_7N_3$. (b) example of as-collected diffraction image with diffraction lines and spots of Re (a= 2.2269(4) Å, c= 3.5702(15) Å) and $Re_7N_3$ (a=6.2788(2) Å, c=4.000(2) Å); reconstructed reciprocal lattice planes of Re (c) and $Re_7N_3$ (d). Characteristic diffraction image shown on (b) is highlighted with white rectangle on (a). Reflections of Re (c) and $Re_7N_3$ (d) are marked by yellow and green circles and corresponding hkl are given; reflections coming from the diamond anvil are highlighted by white circles; powder diffraction lines are due to Re gasket and not-transformed rhenium. Blue circles and the rectangular mark parasitic reflections from diamond anvils.*

The dsDACs with temperature-quenched material were transported to ID11 at the ESRF (Grenoble, France) and investigated using both powder and single-crystal X-ray diffraction (see Methods). Despite the nominally small size of the X-ray beam, the reflections from the gasket were present even in the patterns collected from the center of the sample chamber. 2D diffraction maps of still XRD-images revealed powder diffraction of the Re gasket and non-transformed material that allowed the analysis of the pressure distribution both within and around the sample (Extended Data Fig. 2). In dsDAC #1, for example, pressure at the sample/gasket boundary did not exceed ~160 GPa, while pressure at all points within the sample chamber is almost the same, of about 900 GPa (Extended Data Fig. 2). Our observations regarding the pressure distribution (Extended Data Fig. 3) in the sample chamber are consistent with previously reported for toroidal type anvils[7,8] and give the pressure magnification factor (the ratio of pressures on primary and secondary anvils) of about 6, in accordance with previous publications on ds-DACs[17,28].

Apart from powder diffraction rings, the diffraction patterns collected at ID11 from certain locations in the sample area show numerous spots (Fig. 1). At these positions we collected single-crystal datasets upon DAC-rotation around ω-axis from -38˚ to 38˚ with the angular step of 0.5˚ (*Methods*). For dsDAC #1, particularly, the analysis of sc-XRD data revealed the presence of domains of two phases (Supplementary Information Table S2). The first phase is hexagonal (space group $P6_3/mmc$) with the lattice parameters $a$= 2.2269(4) Å, $c$= 3.5702(15) Å, and $V$=15.33(1) Å$^3$, as determined using 64 reflections. It was interpreted as Re (Fig. 1,2) being under pressure of 905(5) GPa[27]. Within uncertainty, the $c/a$ ratio (1.603(5)) coincides with that reported for pure Re at lower pressures[3,27]. The structure solution and refinement showed indeed that rhenium recrystallizes upon pulsed laser heating (Fig. 2, Supplementary Information Table S2), but is not contaminated by carbon or nitrogen (at least in the quantities that could be detectable from our XRD data).

The second phase found in the pressure chamber of the dsDAC #1 after heating is also hexagonal (space group $P6_3mc$) and has the lattice parameters $a$=6.2788(2) Å, $c$=4.000(2) Å, and $V$=136.53(11) Å$^3$. Based on 394 independent reflections, the structure of this phase was solved and refined in isotropic approximation of atomic displacement parameters (Fig. 2, Supplementary Information Table S2) to $R_1$=5.7%. The chemical composition of the phase was refined as $Re_7N_3$. Considering the possibility of the reaction between rhenium and carbon from the anvils, we checked if the phase could be interpreted as carbide ($Re_7C_3$). In this case, however, the isotropic thermal parameter of carbon becomes negative, supporting the assignment of the atomic positions to nitrogen.

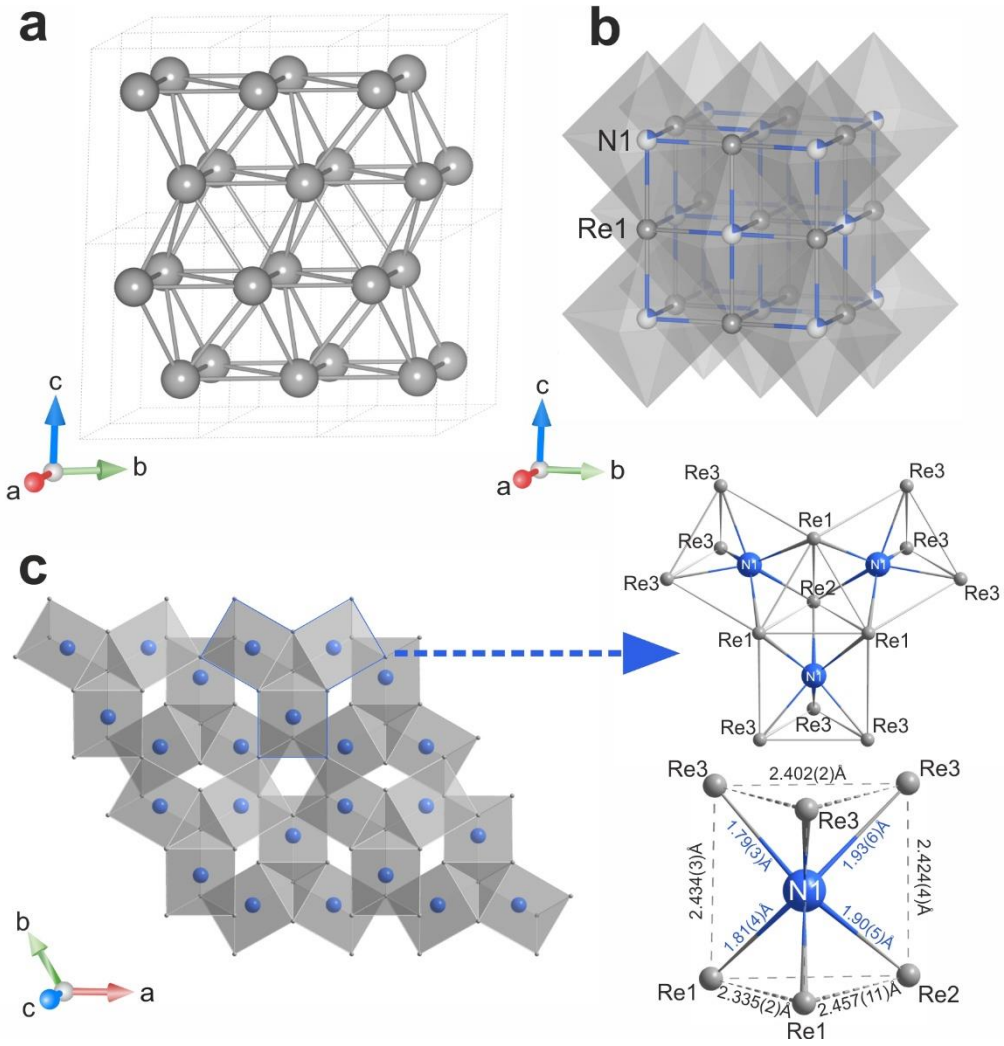


***Fig. 2. Crystal structures of phases observed in laser-heated dsDACs.*** *(a) Hexagonal rhenium at 905(5) GPa in dsDAC #1 (a= 2.2269(4) Å, c= 3.5702 (15) Å, and V=15.33(1) Å$^3$); (b) cubic (B1 NaCl-type) rhenium-nitrogen solid solution $ReN_{0.2}$ at 730(4) GPa (a=3.3994(7) Å, V=39.28(2) Å$^3$); (c) hexagonal $Re_7N_3$ (a=6.2788(2) Å, c=4.000(2) Å, and V=136.53(11) Å$^3$). In $Re_7N_3$ structural units are $NRe_6$ prisms with the nitrogen atom in the center. Rhenium atoms are grey and nitrogen atoms are blue.*

The structure units of $Re_7N_3$ are distorted $NRe_6$ trigonal prisms (Fig. 2). Three prisms are connected through shared edges forming triads, which are stacked along the $6_3$ axis. Each triad is rotated by 60° with regard to upper and lower neighbors in the columns (Fig. 2). The columns are connected to each other by prisms' common vertices. Crystal structures built of combined triads of prisms are well known among carbides, borides, phosphides, and nitrides[29]. Moreover, there are a number of binary compounds with the $A_7X_3$ stoichiometry, and especially hexagonal ones with the $Th_7Fe_3$-type structure (more than 70 entries in

the ICSD database[30]), the same as of the $Re_7N_3$ compound. We noticed that in $Re_7N_3$, the shortest and average distances between the Re-Re nearest neighbors (~2.28 Å and ~2.37 Å, respectively) are just slightly longer than the Re-Re distances in metallic rhenium (~2.23 Å), which is present in the pressure chamber along with the nitride. A comparison of the shortest and average distances between the closest A-A neighbors in the $Th_7Fe_3$-type structured compounds with the metal-metal distances in corresponding pure metals at the same pressures (Extended Data Fig. 6) shows indeed a clear similarity (in some cases, for example, in experimentally studied $Fe_7C_3$ at 158 GPa[31], or theoretically predicted $Fe_7N_3$ at 150 GPa[32], the A-A distances are even slightly shorter in compounds than in pure metals). Remarkably, the average Re-N distance in $NRe_6$ prisms in $Re_7N_3$ (<Re-N> is 1.84 Å) follows the same trend as for other $Th_7Fe_3$-type structured compounds when <A-X> is compared with <A-A> (Extended Data Fig. 6). According to our experimental data, the Re-N distances in trigonal prisms in $Re_7N_3$ vary from ~1.79 to ~1.94 Å, and, as expected for multimegabar pressures (the shortest previously reported rhenium-nitrogen distance is ~1.96 Å in $ReN_8$ $xN_2$ at 134 GPa[11]). One can note that in the TPa pressure range, the Re-Re interatomic distances become comparable with those of transition metals of the 4$^{th}$ Period (Cr, Mn, Fe, Ni), which are known to form $Th_7Fe_3$-type structured (or similar) compounds at ambient (or relatively low) pressure[30]. It may be an indication that a huge reduction of the Re size promotes formation of $Re_7N_3$ at several hundreds of GPa, but the existence of $Ru_7B_3$ at ambient pressure[30] (in ruthenium the metal-metal distance is ~2.68 Å vs ~2.75 Å in Re) suggests that the size factor may be important, but not necessarily crucial.

The synthesis of $Re_7N_3$ was reproduced in dsDAC #2. Diffraction data collected at ID11 at ESRF shows numerous diffraction spots, and the analysis of the integrated powder diffraction pattern confirmed the presence of the hexagonal phase with the lattice parameters very close to those obtained for $Re_7N_3$ in dsDAC #1 (Supplementary Tables S1, S3; Extended Data Fig. 7). Unfortunately, the quality of the diffraction was insufficient for the single-crystal data analysis; the deterioration of the quality of diffraction data may be due to a pressure drop from ~140 GPa to ~100 GPa on primary anvils upon laser heating. Still, for dsDAC #2 we were able to release pressure to ambient without total destruction of the pressure chamber and found there a particle of almost 2 μm in diameter, which consisted of Re and N in the atomic ratio of about 2:1 (Extended Data Fig. 8). This finding gives an additional evidence of the synthesis of rhenium nitride in dsDAC #2.

To elucidate the effect of the extreme compression on the stability of the novel $Re_7N_3$ compound and to characterize its physical properties, we carried out electronic structure calculations in the framework of the Density Functional Theory and studied its electronic, thermodynamic and vibrational properties (see *Methods*, Supplementary Information Computational Details).

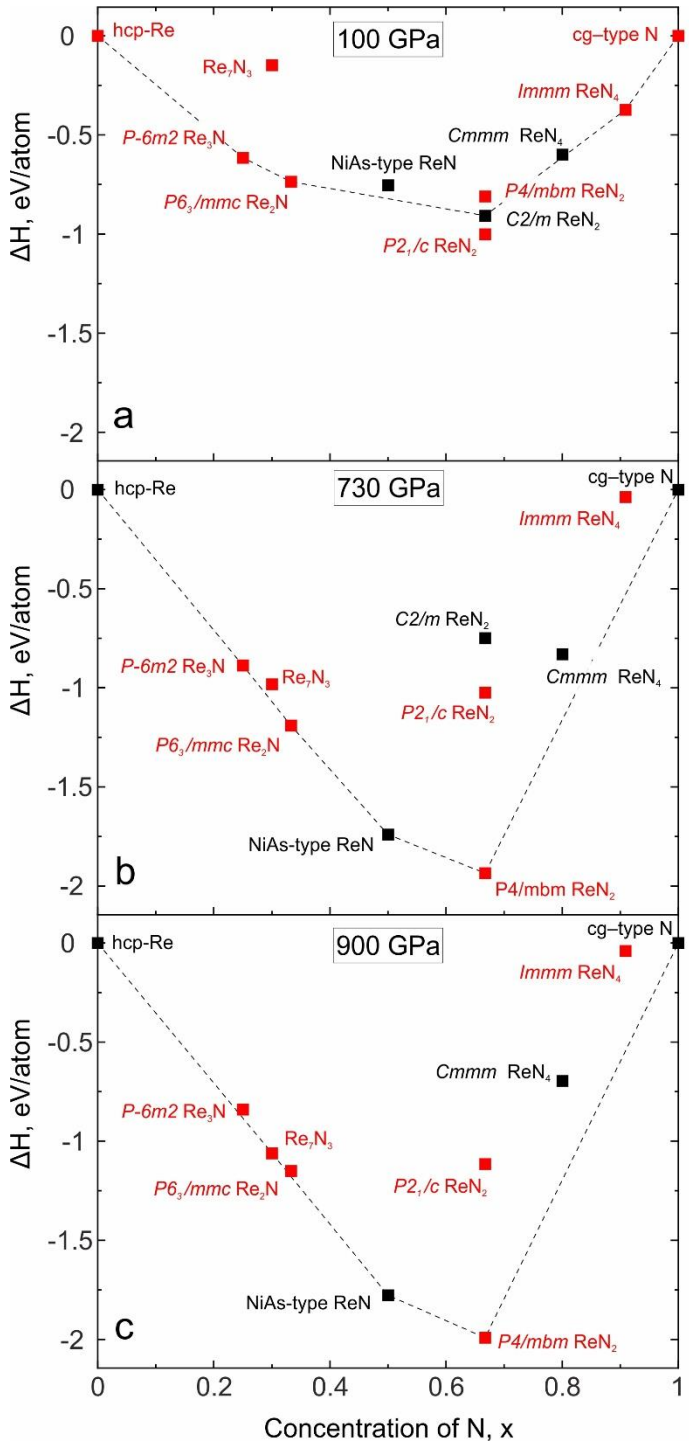


***Fig. 3. Formation enthalpy of $Re_7N_3$.*** *Data shown with respect to theoretically predicted[41] (black circles), and experimentally known (red squares, $Re_3N$ and , $ReN_2$[13] ($P2_1/c$), $ReN_2$ (P4/mbm), $ReN_{10}$[11] (Immm)) competing high-pressure phases in system Re-N calculated at pressure (a) 100 GPa, (b) 730 GPa, and (c) 900 GPa.*

The optimized lattice parameters and coordinates of atoms of $Re_7N_3$ were found to be in excellent agreement with experiment (Supplementary Information Table S4). A difference in pressure calculated at experimental volumes for $Re_7N_3$ may indicate that the calculated equation of state of Re and/or $Re_7Ne_3$ at ultra-high compressions are becoming less accurate, which is often the case in GGA calculations[17]. Examination of the electronic band structure (Supplementary Information Electronic Properties of $Re_7N_3$ and Fig. S1), electronic density of states (Supplementary Information Fig. S2, S3), electron localization function (Supplementary Information Fig. S4), and the charge density maps (Supplementary Information Figure S5) shows that $Re_7N_3$ is a metal which has a combination of metallic and ionic bonding with some covalent component.

The dsDAC #3 was laser heated to maximum temperature of 3450(200) K and the lattice parameters of Re measured after heating were found to be $a$=2.2803(3) Å, $c$=3.622(1) Å, and $V$=16.31(2) Å$^3$. According to the EOS of Re[27], the sample was under pressure of 730(4) GPa (Supplementary Information Table S1, Supplementary Information Fig. S6). The analysis of single-crystal XRD data revealed the presence of a cubic phase (space group $Fm\bar{3}m$) with the lattice parameter of ~3.40 to ~3.41 Å depending on a spot from which the XRD pattern was taken. Structural solution suggests that the phase has the NaCl (B1) type structure (Fig. 2, Supplementary Information Fig. S7) with one position occupied by Re and the other- by a light element. Attempts to refine the crystal structure assuming that the position of the light element is fully occupied by N or C led to an unreasonably high thermal parameter (~0.1 Å$^2$). For the highly symmetric NaCl-type structure containing heavy Re atoms simultaneous refinement of the occupancy and the thermal parameter of a lighter element is not reasonable, so we constrained the thermal parameters of all atoms to be equal. In this approximation, the composition of the cubic phase was $ReN_{0.20}$ (Supplementary Information Table S2). Of course, based on X-ray diffraction data alone we could not exclude that the light element might be carbon, but theoretical calculations (see Supplementary Information, Re-based solution phase) suggest that nitrogen is more plausible. A partial occupation of octahedral voids of the underlying *fcc* packing of Re atoms by nitrogen predicts negative formation enthalpies of metastable alloys (Supplementary Information Fig. S8, S9, Supplementary Information Table S5), while filling them with carbon leads to positive formation enthalpies (Supplementary Information Fig. S8, Supplementary Information Table S6).

Theoretical simulations allowed an insight into a possibility of the synthesis of $Re_7N_3$ at pressures lower than those achieved in the current study. At 100 GPa the formation enthalpy of metastable $Re_7N_3$ is well above the convex hull (Fig. 3, Supplementary Information Thermodynamic Stability of $Re_7N_3$, Extended Data Fig. 9). Even taking into account the anomalously large (~0.2 eV/atom) metastability range of nitrides[33], this compound cannot be considered as synthesizable at 100 GPa. On the contrary, at 730 GPa

the calculated formation enthalpy of $Re_7N_3$, though still above the convex hull, becomes well within the metastability range of nitrides (Fig 3, Supplementary Information Lattice Dynamics of $Re_7N_3$, Extended Data Fig. 9), and at ~900 GPa – the pressure of the realised experimental sysnthesis- it lies on the convex hull (Fig. 3).

Multimegabar pressures have been long-thought to have a profound effect on chemistry and physics of materials[1,2] and to lead to formation of phases with exotic crystal structures. In this work we have demonstrated that at pressures as high as those exceeding 600 GPa new compounds can be synthesized in laser-heated dsDACs and their structures can be solved *in situ*. By extending experimental field of high-pressure synthesis and structural studies to terapascal range, our work paves the way towards discovering of new materials and observations of novel physical phenomena.

## Methods

Diffraction data were acquired at ID11 beam-line at ESRF. Experiments with dsDAC #1 were performed using Frelon 4M detector, wavelength 0.3099 Å, beam size $0.45^{x}0.45$ $\mu m^2$ at FWHM; data for dsDAC #2 and dsDAC #3 were were collected with Eiger2 CdTe 4M detector, wavelength 0.2882 Å, beam size $0.5^{x}0.5$ $\mu m^2$ $\mu m^2$ at FWHM. 2D mappings of still XRD-images (without ω-oscillations) were performed with the explosure time up to 10 s; single crystal datasets were collected via DACs rotation around ω-axis from -38˚ to 38˚ with the angular step 0.5˚ and acquisition time 10 s/step.

In case of powder diffraction studies, calibration of instrument model and integration of diffraction patterns were made in the DIOPTAS[34] software using $CeO_2$ powder standard (NIST SRM 674b). Integrated patterns from powder XRD experiments were processed using the Le Bail technique implemented in JANA2006[35] software. X-ray diffraction imaging of the sample chamber was reconstructed using XDI[36] program and map of still-images converted from 'edf' to 'tif' format. In case of SCXRD, integration of the reflection intensities and absorption corrections were performed in CrysAlisPro software[37]. Single crystal of orthoenstatite $(Mg_{1.93},Fe_{0.06})(Si_{1.93},Al_{0.06})O_6$ (space group *Pbca*, *a*=8.8117(2) Å, *b*=5.18320(10) Å, *c*=18.2391(3) Å) was used as calibration standard for refinement of the instrument model of the diffractometer. Diffraction images were converted from 'edf' to the native CrysAlisPro format 'ESPERANTO' with Freac software[37]. Detailed information of integration parameters as well as about the data reduction output files and indicators of the XRD data quality are given in ref 5[19]. The crystal structures

were solved using SHELXT or superfilp method in JANA2006 and Olex2[35,38,39]. Crystal structures were refined by least-squares minimization of adjustable parameters. We performed isotropic refinement of atomic displacement parameters due to limited dataset collected in DAC. Reflections coming from parasite diffraction produced by diamonds and crystallized pressure media were eliminated during the refinement procedure. "Diamond" software[40] was used for visualization of molecular graphics.

The electronic structure, total energy and forces calculations of the studied rhenium nitrides were carried out in the framework of the Density Functional Theory (DFT, see Supplementary Information for Computational Details). We used supercells of different sizes with an underlying fcc crystal and and various amounts of either N or C to simulate the Re-N and Re-C cubic phases with NaCl (B1) type structure (see Supplementary Information Re-based Solution Phase). To investigate the influence of pressure on the thermodynamic stability of $Re_7N_3$, its enthaly of formation, as well as the enthalpies of formation for various phases of rhenium nitride, known experimentally[10,11,13] and predicted theoretically[41], were calculated and a thermodynamic convex hull was constructed based on the calculation results (Supplementary Information Thermodynamic Stability of $Re_7N_3$).

Phonon dispersion relations for $Re_7N_3$ were calculated in the harmonic approximation at volume 200 Å$^3$ ($a$=7.122 Å, $c$=4.553 Å) of the unit cell, corresponding to P=102 GPa, as well as at experimental volume 136.52 Å$^3$ ($a$=6.277 Å, $c$=4.001 Å) of the unit cell (Supplementary Information Table S4) that corresponded to calculated pressure 732 GPa (see Extended Data Fig. 9, Supplementary Information Computational Details). Because $Re_7N_3$ is predicted to be dynamically unstable at the synthesis pressure due to the presence of imaginary frequencies in this approximation (Extended Data Fig. 9, Supplementary Information Lattice Dynamics of $Re_7N_3$), we investigated the anharmonic effects of lattice vibrations at finite temperature employing the Temperature Dependent Effective Potential (TDEP) method[42] with effective second and third-order interatomic force constants calculated from first principles[43]. The calculations are based on modeling the potential energy surface in the vicinity of equilibrium with a Hamiltonian of the form:

$$H = U_0 + \sum_i \frac{\mathbf{p}_i^2}{2m_i} + \frac{1}{2!}\sum_{ij\alpha\beta} \Phi_{ij}^{\alpha\beta} u_i^{\alpha} u_j^{\beta} + \frac{1}{3!}\sum_{ijk\alpha\beta\gamma} \Phi_{ijk}^{\alpha\beta\gamma} u_i^{\alpha} u_j^{\beta} u_k^{\gamma} \ldots \quad (1)$$

where $\boldsymbol{\Phi}$ are interaction parameters (the effective force constants) of increasing order, and $u$ denotes the displacement of ions from their equilibrium positions.

We calculated the spectral function $S(\boldsymbol{q},E)$ at 300 K, which describes the spectrum of lattice excitations with energy $E = \hbar\Omega$ for mode $\omega_{qs}$ at wave vector $\boldsymbol{q}$[44,45]. $S(\boldsymbol{q},E)$ provides insight into the phonon frequencies as well as strength of three-phonon processes via the broadening in Extended Data Fig. 9. The

$S(\boldsymbol{q},E)$ of $Re_7N_3$ is typical of a weakly anharmonic solid with Lorentzian broadening of single peaks. Additionally, the lines are reasonably crisp, without substantial broadening, indicating that the anharmonic interaction strength is well within the range of validity for the perturbation theory. Importantly, $Re_7N_3$ is seen to be dynamically stable (there are no imaginary frequencies) at the synthesis pressure (see Supplementary Information, Lattice dynamics of $Re_7N_3$).

## Acknowledgements

We thank Dr. Sylvain Petitgirard (ETH Zürich, Zürich, Switzerland) for kind help in the FIB preparation of sample. Dr. A. Kurnosov, D. Wiesner, S. Übelhack, and S. Linhardt acknowledge for technical assistance. D.L. thanks the Alexander von Humboldt Foundation and the Deutsche Forschungsgemeinschaft (DFG, project LA-4916/1-1) for financial support. N. D. and L. D. thank the Federal Ministry of Education and Research, Germany (BMBF, grant No. 05K19WC1) and the DFG (DFG projects DU 954-11/1, DU 393-9/2, and DU 393-13/2) for financial support. N. D. thanks the Swedish Government Strategic Research Area in Materials Science on Functional Materials at Linköping University (Faculty Grant SFO-Mat-LiU No. 200900971). MB acknowledges the support of Deutsche Forschungsgemeinschaft (DFG project BY112/2-1). European Synchrotron Radiation Facility is acknowledged for beamtime provision at the Material Science beamline ID11. Portions of this work were performed at GeoSoilEnviroCARS (The University of Chicago, Sector 13), Advanced Photon Source (APS), Argonne National Laboratory. GeoSoilEnviroCARS is supported by the National Science Foundation – Earth Sciences (EAR – 1634415). This research used resources of the Advanced Photon Source, a U.S. Department of Energy (DOE) Office of Science User Facility operated for the DOE Office of Science by Argonne National Laboratory under Contract No. DE-AC02-06CH11357. Theoretical analysis of chemical bonding was supported by the Russian Science Foundation (Project No. 18-12-00492). Support from the Knut and Alice Wallenberg Foundation (Wallenberg Scholar Grant No. KAW-2018.0194), the Swedish Government Strategic Research Areas in Materials Science on Functional Materials at Linköping University (Faculty Grant SFO-Mat-LiU No. 2009 00971), the Swedish e-science Research Center (SeRC), the Swedish Research Council (VR) grant No. 2019-05600, the VINN Excellence Center Functional Nanoscale Materials (FunMat-2) Grant 2016–05156 and the Swedish Foundation for Strategic Research (SSF) Project No. EM16-0004 is gratefully acknowledged. The computations were carried out at supercomputer cluster at NUST “MISIS” and at resources provided by the Swedish National Infrastructure for Computing (SNIC) partially funded by the Swedish Research Council through grant agreement no. 2016-07213.

**Author Contributions** L.D. and N.D. designed the work. L.D., S.K., D.L. prepared high-pressure experiments. L.D., S.K., T.F., M.B., D.L., C.G., E.L.B., P.S., S.C., V.P. conducted experiments. L.D., S.K., D.L., S.C. processed experimental data. A.V.P., E.A.S., M.P.B., F.T., N.S., Fl.T. and I.A.A. performed theoretical analysis. The manuscript was written by L.D., N.D., and I.A.A. with contributions from all the authors. All the authors commented on successive drafts and have given approval to the final version of the manuscript.

## References


1. McMillan, P. F. Chemistry at high pressure. *Chem. Soc. Rev.* **35**, 855 (2006).
2. Needs, R. J. & Pickard, C. J. Perspective: Role of structure prediction in materials discovery and design. *APL Mater.* **4**, 053210 (2016).
3. Dubrovinsky, L., Dubrovinskaia, N., Prakapenka, V. B. & Abakumov, A. M. Implementation of micro-ball nanodiamond anvils for high-pressure studies above 6 Mbar. *Nat. Commun.* **3**, 1163–1167 (2012).
4. Austin, I. G. & Mott, N. F. Metallic and Nonmetallic Behavior in Transition Metal Oxides. *Science (80-. ).* **168**, 71–77 (1970).
5. Shimizu, K. *et al.* Superconductivity in the non-magnetic state of iron under pressure. *Nature* **412**, 316–318 (2001).
6. Kim, E. & Chan, M. H. W. Probable observation of a supersolid helium phase. *Nature* **427**, 225–227 (2004).
7. Dewaele, A., Loubeyre, P., Occelli, F., Marie, O. & Mezouar, M. Toroidal diamond anvil cell for detailed measurements under extreme static pressures. *Nat. Commun.* **9**, 2913 (2018).
8. Jenei, Z. *et al.* Single crystal toroidal diamond anvils for high pressure experiments beyond 5 megabar. *Nat. Commun.* **9**, 3563 (2018).
9. Laniel, D. *et al.* High-Pressure Polymeric Nitrogen Allotrope with the Black Phosphorus Structure. *Phys. Rev. Lett.* **124**, 216001 (2020).
10. Friedrich, A. *et al.* Novel Rhenium Nitrides. Phys. Rev. Lett. **105**, 085504 (2010).
11. Bykov, M. *et al.* High-Pressure Synthesis of a Nitrogen-Rich Inclusion Compound $ReN_{8^x}$ $N_2$ with

Conjugated Polymeric Nitrogen Chains. *Angew. Chemie - Int. Ed.* **57**, 9048–9053 (2018).

12. Bykov, M. *et al.* Synthesis of $FeN_4$ at 180 GPa and its crystal structure from a submicron-sized grain. *Acta Crystallogr. Sect. E Crystallogr. Commun.* **74**, 1392–1395 (2018).

13. Bykov, M. *et al.* High-pressure synthesis of ultraincompressible hard rhenium nitride pernitride $Re_2(N_2)(N_2)$ stable at ambient conditions. *Nat. Commun.* **10**, 2994 (2019).

14. Bykov, M. *et al.* Synthesis of Arsenopyrite-Type Rhodium Pernitride RhN 2 from a Single-Source Azide Precursor. *Eur. J. Inorg. Chem.* **2019**, 3667–3671 (2019).

15. Bykov, M. *et al.* High-Pressure Synthesis of Metal–Inorganic Frameworks $Hf_4N_{20}{}^xN2$ , $WN_8{}^xN_2$ , and $Os_5N_{23}{}^xN_2$ with Polymeric Nitrogen Linkers. *Angew. Chemie* **132**, 10407–10412 (2020).

16. Khandarkhaeva, S. *et al.* Novel Rhenium Carbides at 200 GPa. *Eur. J. Inorg. Chem.* **2020**, 2186–2190 (2020).

17. Dubrovinskaia, N. *et al.* Terapascal static pressure generation with ultrahigh yield strength nanodiamond. *Sci. Adv.* **2**, e1600341 (2016).

18. Dubrovinsky, L. *et al.* The most incompressible metal osmium at static pressures above 750 gigapascals. *Nature* **525**, 226–229 (2015).

19. Bykova, E. Single-crystal X-ray diffraction at extreme conditions in mineral physics and material sciences. (University of Bayreuth, 2015).

20. Dubrovinskaia, N. & Dubrovinsky, L. Crystallography taken to the extreme. *Phys. Scr.* **93**, 062501 (2018).

21. Kantor, I. *et al.* BX90: A new diamond anvil cell design for X-ray diffraction and optical measurements. *Rev. Sci. Instrum.* **83**, 125102 (2012).

22. Kurnosov, A. *et al.* A novel gas-loading system for mechanically closing of various types of diamond anvil cells. *Rev. Sci. Instrum.* **79**, 045110 (2008).

23. Akahama, Y., Hirao, N., Ohishi, Y. & Singh, A. K. Equation of state of bcc-Mo by static volume compression to 410 GPa. *J. Appl. Phys.* **116**, 1–6 (2014).

/24. Akahama, Y. & Kawamura, H. Pressure calibration of diamond anvil Raman gauge to 410 GPa. *J. Phys. Conf. Ser.* **215**, 012195 (2010).

25. Aprilis, G. *et al.* Portable double-sided pulsed laser heating system for time-resolved geoscience and

materials science applications. *Rev. Sci. Instrum.* **88**, 084501 (2017).

26. Fedotenko, T. *et al.* Laser heating setup for diamond anvil cells for in situ synchrotron and in house high and ultra-high pressure studies. *Rev. Sci. Instrum.* **90**, 104501 (2019).

27. Anzellini, S., Dewaele, A., Occelli, F., Loubeyre, P. & Mezouar, M. Equation of state of rhenium and application for ultra high pressure calibration. *J. Appl. Phys.* **115**, 043511 (2014).

28. Sakai, T. *et al.* High pressure generation using double-stage diamond anvil technique: problems and equations of state of rhenium. *High Press. Res.* **38**, 107–119 (2018).

29. Li, W.-K., Zhou, G.-D. & Mak, T. *Advanced Structural Inorganic Chemistry*. (Oxford University Press, 2008). doi:10.1093/acprof:oso/9780199216949.001.0001

30. ICSD database. Available at: https://icsd.products.fiz-karlsruhe.de/.

31. Prescher, C. *et al.* High Poisson's ratio of Earth's inner core explained by carbon alloying. *Nat. Geosci.* **8**, 220–223 (2015).

32. Sagatov, N., Gavryushkin, P. N., Inerbaev, T. M. & Litasov, K. D. New high-pressure phases of $Fe_7N_3$ and Fe $_7C_3$ stable at Earth's core conditions: evidences for carbon–nitrogen isomorphism in Fe-compounds. *RSC Adv.* **9**, 3577–3581 (2019).

33. Sun, W. *et al.* The thermodynamic scale of inorganic crystalline metastability. *Sci. Adv.* **2**, e1600225 (2016).

34. Prescher, C. & Prakapenka, V. B. DIOPTAS : a program for reduction of two-dimensional X-ray diffraction data and data exploration. *High Press. Res.* **35**, 223–230 (2015).

35. Petříček, V., Dušek, M. & Palatinus, L. Crystallographic Computing System JANA2006: General features. *Zeitschrift für Krist. - Cryst. Mater.* **229**, 345–352 (2014).

36. Hrubiak, R., Smith, J. S. & Shen, G. Multimode scanning X-ray diffraction microscopy for diamond anvil cell experiments. *Rev. Sci. Instrum.* **90**, 025109 (2019).

37. Rigaku Oxford Diffraction. CrysAlis Pro (v. 171.40.84). (2020).

38. Sheldrick, G. M. SHELXT – Integrated space-group and crystal-structure determination. *Acta Crystallogr. Sect. A Found. Adv.* **71**, 3–8 (2015).

39. Dolomanov, O. V., Bourhis, L. J., Gildea, R. J., Howard, J. A. K. & Puschmann, H. OLEX2 : a complete structure solution, refinement and analysis program. *J. Appl. Crystallogr.* **42**, 339–341

(2009).

40. Putz, H. & Brandenburg, K. Diamond - Crystal and Molecular Structure Visualization.

41. Zhao, Z. *et al*. Nitrogen concentration driving the hardness of rhenium nitrides. *Sci. Rep.* **4**, 4797 (2015).

42. Hellman, O., Abrikosov, I. A. & Simak, S. I. Lattice dynamics of anharmonic solids from first principles. *Phys. Rev. B* **84**, 180301 (2011).

43. Hellman, O. & Abrikosov, I. A. Temperature-dependent effective third-order interatomic force constants from first principles. *Phys. Rev. B* **88**, 144301 (2013).

44. Cowley, R. A. Anharmonic crystals. *Reports Prog. Phys.* **31**, 303 (1968).

45. Maradudin, A. A. & Fein, A. E. Scattering of Neutrons by an Anharmonic Crystal. *Phys. Rev.* **128**, 2589–2608 (1962).

## Extended data

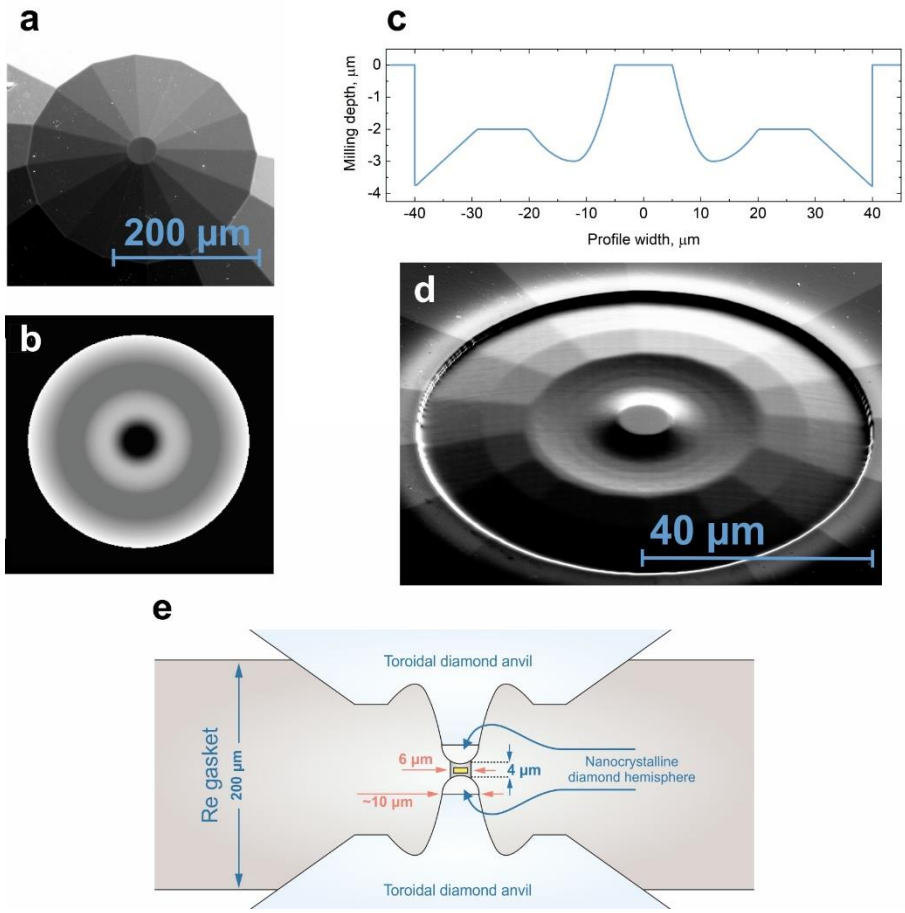


***Extended Data Fig. 1. Toroidal profile produced by FIB milling on a culet of a conventional anvil.*** *(a) Original Boehler-Almax type single-beveled diamond anvils with 40-µm culets (before milling); (b) gray-scale bitmap used for milling; (c) the milling depth profile; (d) crafted toroidal culet; (e) a schematic of the ds-DAC assembly (not scaled) in a cross-section: a gasket (grey) with the pressure chamber (dark grey; the sample is yellow) squeezed between the two toroidal diamond anvils (light blue) equipped with the semi-balls of NCD diamond (white); the pressure chamber is of 6 µm in diameter and 4 µm in height. The gasket was prepared as follows: as gaskets we used strips of a 200-µm thick Re foil. To make an indentation with a thickness of about ~4 µm, we followed a many-step procedure. First, the Re foil was pre-indented to a thickness of ~20 µm using a pair of single-beveled diamonds with 80-µm culets. Then, a hole of about 30 µm in diameter was laser-drilled in the center of the indentation, and the indentation was pressurized again between the same beveled diamonds. This led to closing of the hole and reducing the thickness of the indentation. This procedure was repeated a few times until the thickness of about 7 µm was achieved. The gasket was mounted into a BX-90 DAC equipped with toroidal diamond anvil and indented by their miniature 10-µm culets to a thickness of ~4 µm. A hole (of ~6 µm in diameter) in the center of the ~10-µm indentation was made using FIB or by tightly focused pulsed NIR laser to form a pressure chamber.*

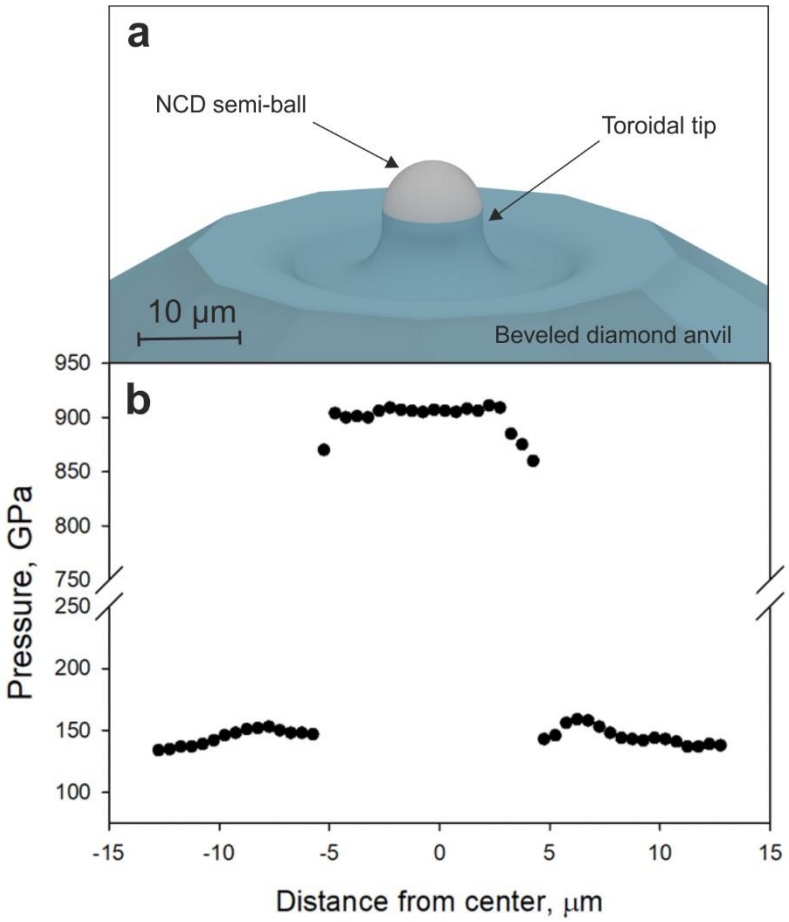


***Extended Data Fig. 2. A schematic illustration of the experimental setup.*** *(a) 3D presentation of a diamond anvil featuring a toroidal profile milled by FIB on the surface of a conventional Boehler-Almax type single-beveled diamond anvil with a 40-μm culet. A semi-ball of transparent nanocrystalline diamond (NCD)[17], FIB-milled from a single ball with a diameter of 12 to 14 μm, was placed over the tip to realise a double-stage dsDAC design. Two anvils of this kind were forced together as shown in the scheme in Extended Data Fig. 1. (b) Pressure profile along the cross-section through the center of a dsDAC #1 after pulsed laser heating. Diffraction patterns were collected at each point with a step of 0.5 μm at ID11 beam line at the ESRF, and pressure was determined according to the EOS from ref. [27] using the lattice parameters of Re found from powder diffraction data.*

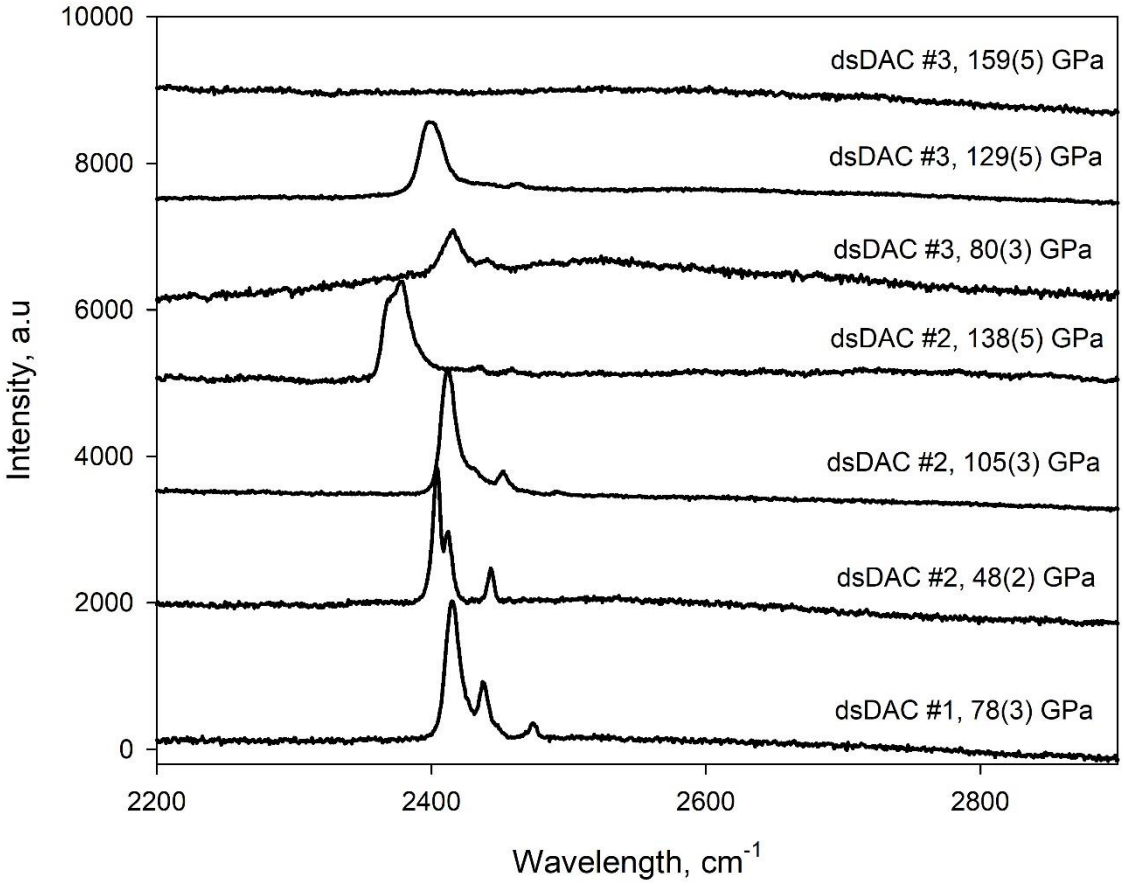


***Extended Data Fig. 3. Raman spectra taken upon compression of the dsDAC after nitrogen gas loading featuring nitrogen vibrones.*** *At pressure above ~160 GPa Raman signal of nitrogen becomes non-detectable. The pressures were determined according to ref.[24].*

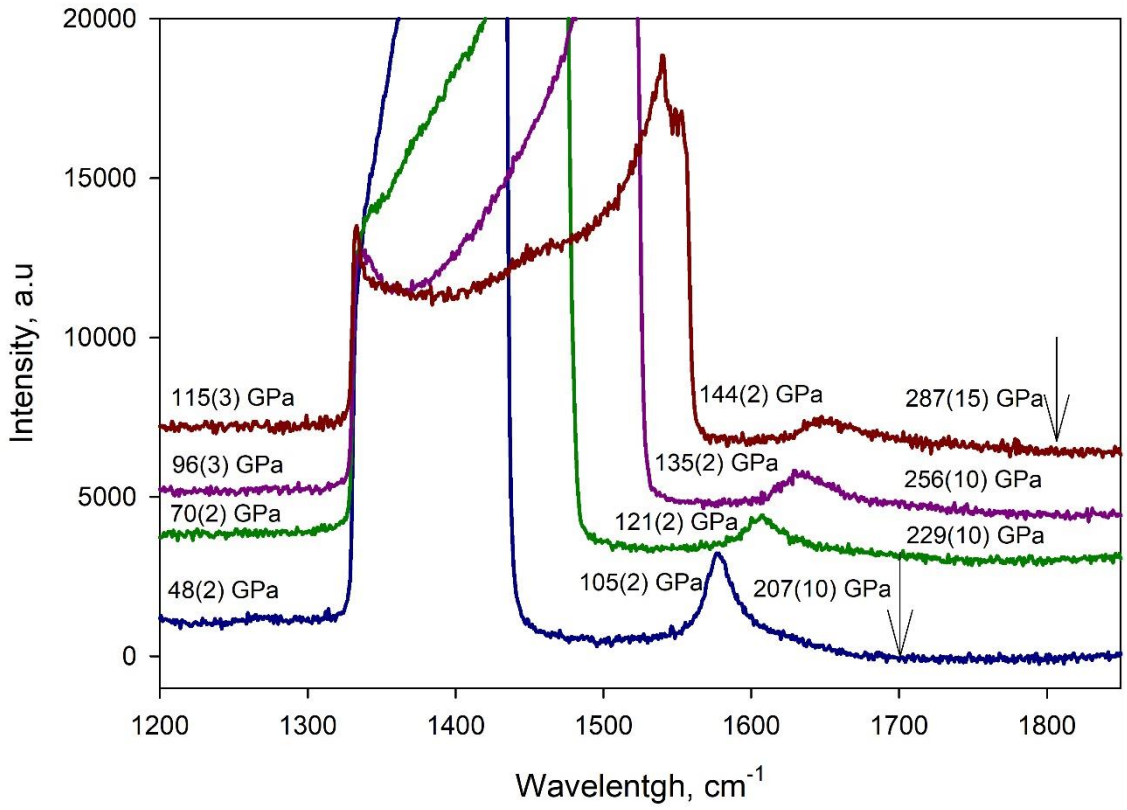


***Extended Data Fig. 4. Evolution of Raman spectra of primary and secondary anvils upon compression of dsDAC #2.*** *Pressure determined from diamond line Raman shift (ref.[24]). On the left, pressures on primary anvil. Near peaks at ~1600 cm$^{-1}$ – pressures on the body of secondary anvil. Values on the right gives estimates of pressures from boarding Raman line of secondary anvil (arrows provide examples of positions found by analysis of the first derivatives of the spectra). Reliable determination of the pressure in the chamber from Raman shift of diamond line of secondary NCD anvils is not feasibly.*

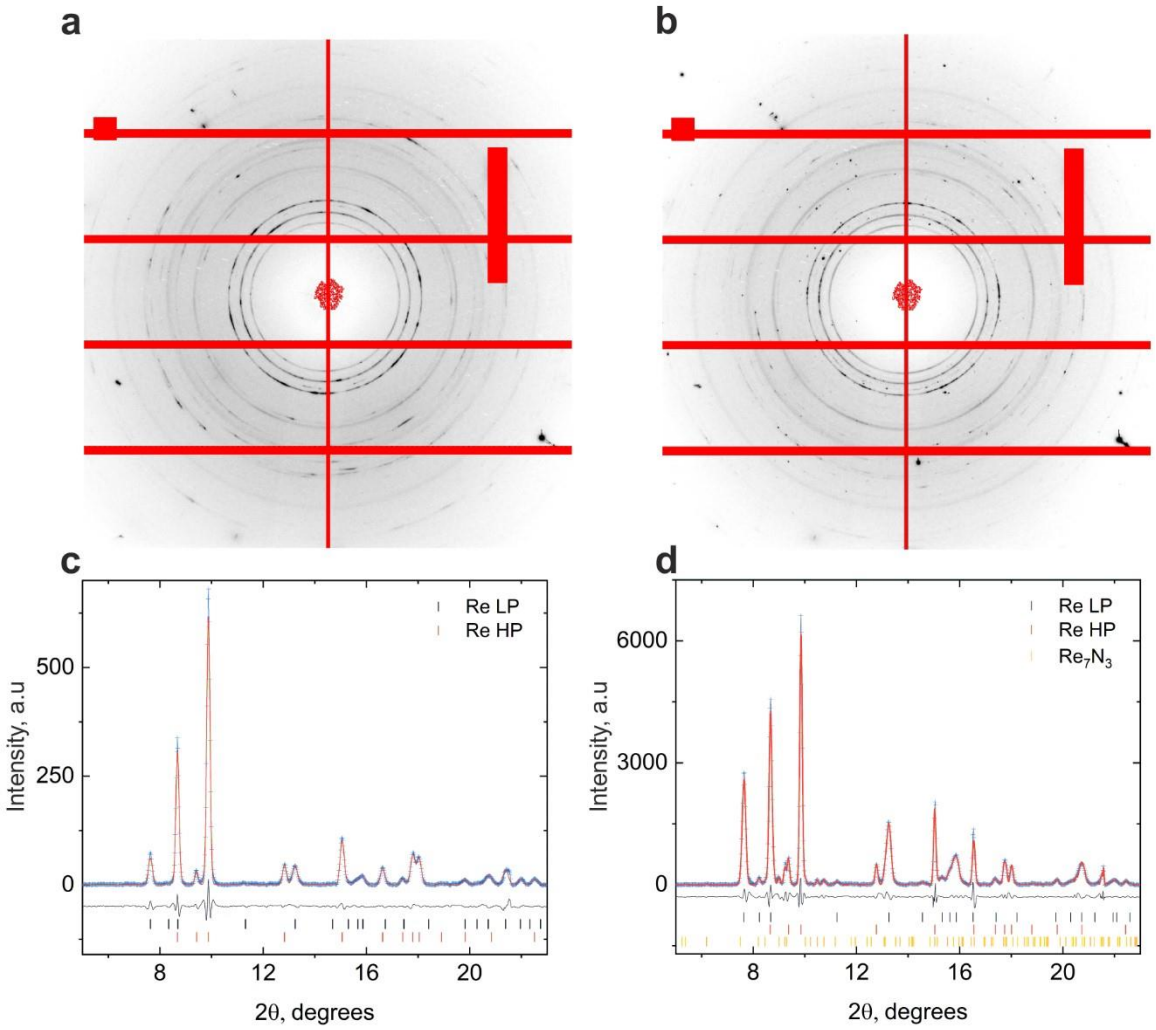


***Extended Data Fig. 5. Examples of powder diffraction patterns collected from dsDAC #1 at 13-IDD (APS, USA, the beam of 3x3 μm² HWFM).*** *(a) The center of the pressure chamber of the as-compressed ds-DAC; (c) Re LP: a=2.5606(5) Å, c=4.0588(12) Å, and V=23.047(7) Å³, that is at 149(3) GPa according to the EOS from ref.[27], or 173(3) GPa according to ref.[3]; Re HP: a=2.2214(3) Å, c=3.5609(8) Å, and V=15.21(1) Å³, that is at 930(5) GPa[27] or 1298(10) GPa[3]; (b) after pulsed laser heating at 2200(200) K during 5 s; (d) Re LP: a=2.5577(3) Å, c=4.1095(12) Å, and V=23.282(7) Å³, at 140(3) GPa[27] or 162(3) GPa[3]; Re HP: a=2.2297(2) Å, c=3.5735(5) Å, and V=15.38(1) Å³, at 895(5) GPa[27] or 1250(10) GPa[3]; $Re_7N_3$: a=6.3086(4) Å, c=4.0048(7)) Å, and V=138.04(4) Å³). Structural data for $Re_7N_3$ were taken from the results of single-crystal XRD data analysis.*

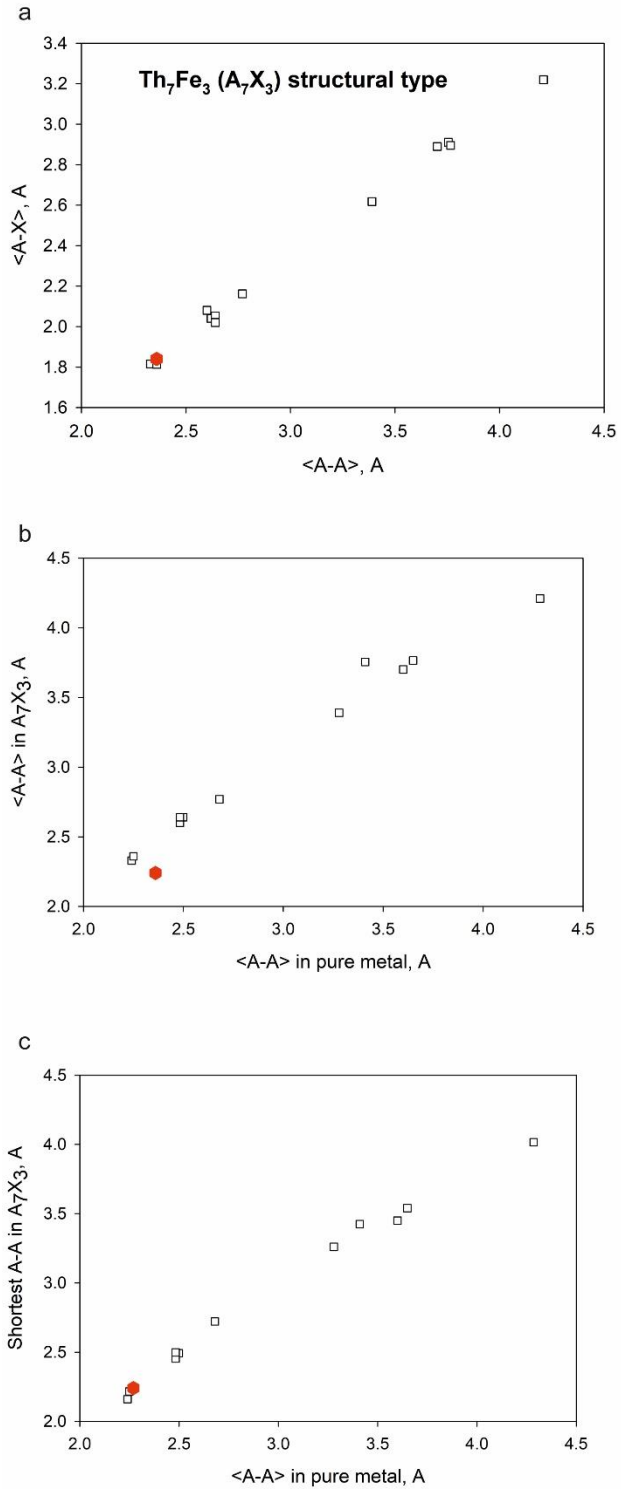


***Extended Data Fig. 6. Interatomic distances in $Th_7Fe_3$ structured and some other selected $A_7X_3$ compounds.*** *Comparison of shortest (a) and average between first neighbors (b) A-A distances in $A_7X_3$ compounds with metal-metal contacts in corresponding pure metals ("A") at the same pressures. (c) Correlation between average <X-A> distances in $XA_6$ prisms and first neighbors <A-A> distances. Red hexagons correspond to $Re_7N_3$ described in this work; data for orthorhombic $Fe_7C_3$ at 158 GPa from ref.[34]; data for predicted $Fe_7N_3$ at 150 GPa from ref. [32]; all other data are from database ref. [30].*

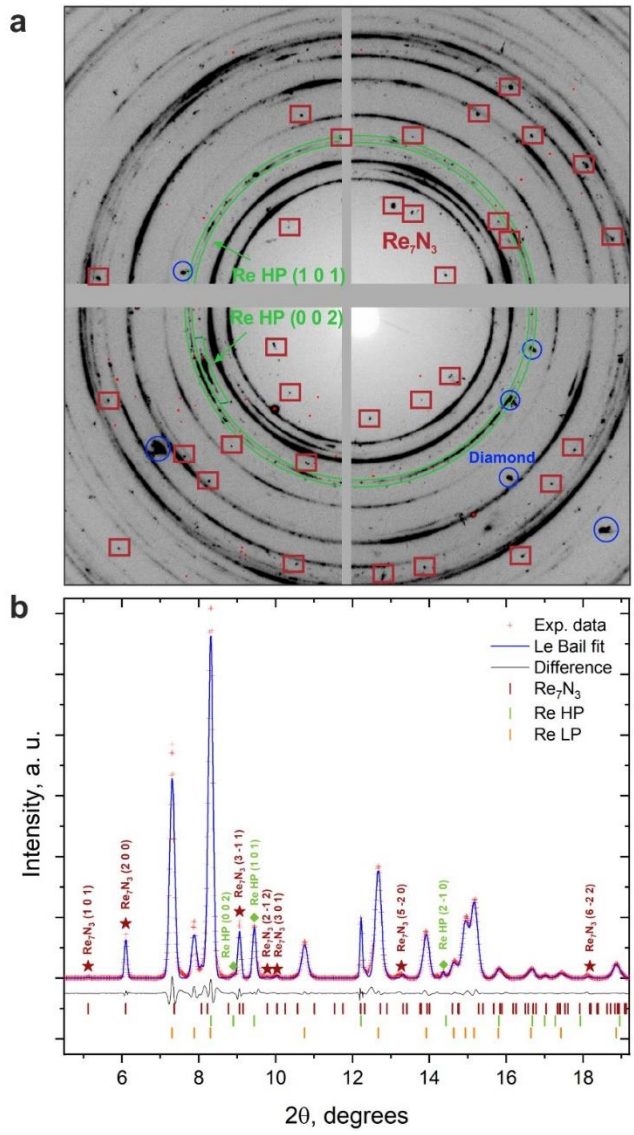


***Extended Data Fig. 7. Example of powder diffraction pattern collected from dsDAC #2.*** *Data collected at ID11 (ESRF, Grenoble, France, the beam of 0.5x.5 μm² FWHM) at 646 GPa (see Supplementary Information Table S1). (a) 2D diffraction image shows diffraction spots of $Re_7N_3$ and rings of hcp-Re at different pressures; (b) refinement of powder diffraction pattern with Le Bail fit implemented in Jana2006 software. Values of lattice parameters are given in Supplementary Information Table S3.*

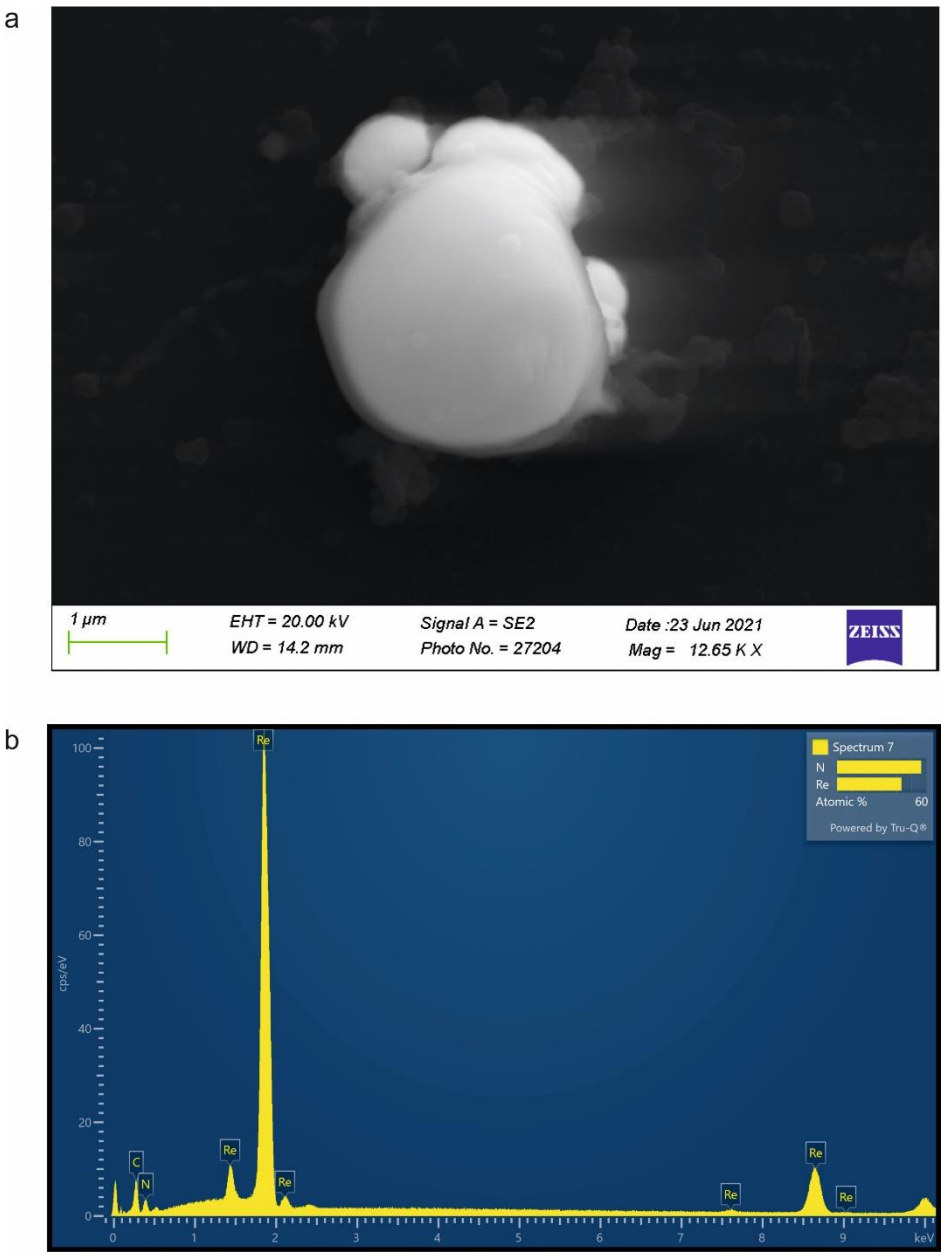


***Extended Data Fig. 8. SEM image (left) and example of EDX spectra (right) of a sample extracted from the dsDAC #2.*** *Sample contains Re and N in atomic proportions ~2:1. Images and spectra were collected on a ZEISS SEM, Leo Gemini 1530 with a Schottky field emission gun employing an accelerating voltage of 20 kV.*

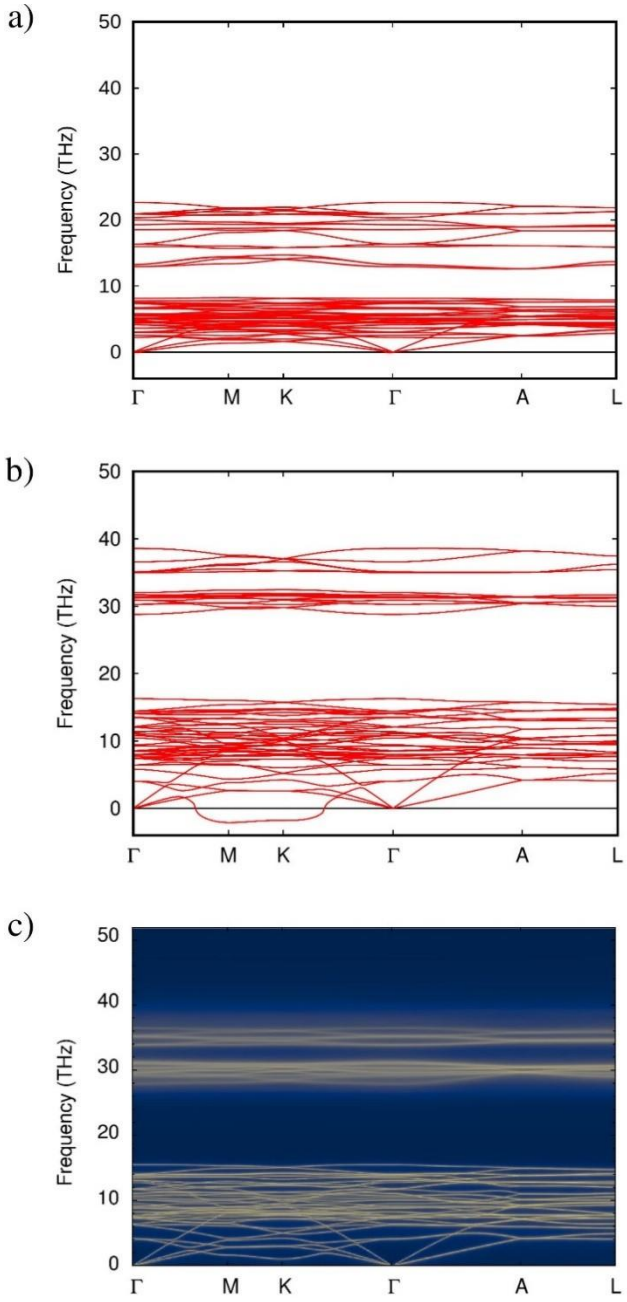


***Extended Data Fig. 9. Phonon dispersion relations for $Re_7N_3$ calculated within the harmonic approximation.*** *(a) Theoretical pressure P=102 GPa. (b) Experimental volume 136.52 Å$^3$ which corresponded to theoretical pressure ~730 GPa. (c) Vibrational spectral function at P~730 GPa and T= 300 K calculated using TDEP method. The results show that in the harmonic approximation $Re_7N_3$ is unstable at the synthesis pressure (imaginary frequencies are shown below zero frequency line). Including anharmonic effects of lattice vibrations removes the dynamical instability at P=730 GPa (all the branches are real).*

## Supplementary Information

# Materials synthesis at terapascal static pressures

*Leonid Dubrovinsky[1]*, Saiana Khandarkhaeva[1,2], Timofey Fedotenko[3], Dominique Laniel[2], Maxim Bykov[4], Carlotta Giacobbe[5], Eleanor Lawrence Bright[5], Pavel Sedmak[5], Stella Chariton[6], Vitali Prakapenka[6], Alena V. Ponomareva[7], Ekaterina A. Smirnova[7], Maxim P. Belov[7], Ferenc Tasnádi[8], Nina Shulumba[8], Florian Trybel[8], Igor A. Abrikosov[8*], Natalia Dubrovinskaia[2,8]*

[1]*Bayerisches Geoinstitut, University of Bayreuth, Universitätstraße 30, 95440 Bayreuth, Germany*

[2]*Material Physics and Technology at Extreme Conditions, Laboratory of Crystallography University of Bayreuth, Universitätstraße 30, 95440 Bayreuth, Germany*

[3]*Deutsches Elektronen-Synchrotron DESY, Notkestr. 85, 22607 Hamburg, Germany*

[4]*Institute of Inorganic Chemistry, University of Cologne, Greinstrasse 6, 50939 Cologne, Germany*

[5]*European Synchrotron Radiation Facility, BP 220, 38043 Grenoble Cedex, France*

[6]*Center for Advanced Radiation Sources, The University of Chicago, 5640 S. Ellis, 60637 Chicago, Illinois, USA*

[7]*Materials Modeling and Development Laboratory, National University of Science and Technology "MISIS", Leninskiy Prospekt 4, 119991 Moscow, Russia.*

[8]*Theoretical Physics Division, Department of Physics, Chemistry and Biology (IFM), Linköping University, SE-581 83 Linköping, Sweden*

**Corresponding authors: Leonid.Dubrovinslky@uni-bayreuth.de, igor.abrikosov@liu.se*

**Computational details**.

We employed the projector augmented wave (PAW) method[1,2] as implemented in the VASP[3]. The exchange and correlation effects were considered using generalized gradient approximation (GGA) with PBE parametrization[4]. To investigate the high-pressure phases, we used "hard" potentials with the configurations of the valence electrons of $5p^6 5d^6 6s^1$ and $2s^2 2p^6$ (Re_pv and N_h potentials) for rhenium and nitrogen, respectively. The cut-off energy was set to 870 eV. The integration over the Brillouin zone was performed using the k-points obtained by Monkhorst-Pack method[5] with the 33×33×33 points mesh for $Re_7N_3$, 30×30×20 for *hcp*-Re, 28×28×12 for $P\bar{6}m2$ $Re_3N$, 30×30×10 for *P6₃/mmc* $Re_2N$, 5×10×5 for $Re_{16}N_4$, 30×30×10 for $P\bar{6}m2$ $Re_3N_2$, 32×32×16 for NiAs-type ReN, 8×20×10 for *C/2m* $ReN_2$, 12×8×12 for *P2₁/c* $ReN_2$, 10×19×11 for *Imm2* $ReN_3$, 12×24×36 for *Cmmm* $ReN_4$, 14×8×14 for *Immm* $ReN_{10}$, 20×20×20 for diamond C, 16×16×16 for *cg*–type N. All initial configurations of the compressed crystals were optimized with respect to lattice parameters and atomic coordinates to ensure the hydrostatic pressure condition. Methfessel-Paxton algorithm[6] with broadening 0.1 eV was used for the structure optimization, electronic band structure and the enthalpies calculations. The tetrahedron method for the Brillouin zone integration with Blöchl corrections[7] was applied for calculations of the electronic density of states.

Harmonic phonons for $Re_7N_3$ were calculated using the small displacement method implemented into Phonopy software package[8,9]. Phonon dispersions have been calculated on a 2×2×2 supercell and 3×3×3 sampling of the Brillouin zone. Methfessel-Paxton algorithm[6] with broadening 0.2 eV was used for the force field calculation. Additional calculations carried out with a (2×2×3) supercell size and (3×3×3) sampling of the Brillouin zone (not shown) confirm sufficient convergence of the results obtained on the smaller supercell, which are presented in Extended Data Fig. 9.

To investigate the anharmonic effects of lattice vibrations at finite temperature we employed the Temperature Dependent Effective Potential (TDEP) method[11-13]. A calculation of force constants (see Methods, Eq. (1)) consists of creating snapshots of a supercell with thermally displaced atoms corresponding to a specified temperature, calculating forces using an *ab initio* density functional theory code such as VASP, and fitting the forces and displacements with the model Hamiltonian. Performing this procedure at given temperature renormalizes the interaction parameters, incorporating all orders of non-harmonic effects. Once force constants are obtained, we can obtain the phonon spectra, broadening and linewidth needed for calculation of the spectral function $S(\mathbf{q},E)$.

$Re_7N_3$ structure is modeled by supercell containing 260 atoms in total, with 182 Re atoms and 78 N atoms. For given experimental volume 136.52 $Å^3$ (calculated pressure 732 GPa), we performed the iterative scheme to obtain a set of forces and atomic displacements for calculation of the second and the

third order force constants using TDEP. An efficient stochastic sampling approach to prepare a set of thermalized with thermal displacements corresponding to Maxwell-Boltzmann statistics at temperature 300 K configurations for each iteration. Once the snapshots are created, we performed a series of first-principles simulations to obtain a set of force-displacement data sets.

We performed iterative scheme which consists of 6 iterations with 200 snapshots each. Note that the plane wave energy cutoff used in our VASP calculations was set to 600 eV and the Brillouin zone was sampled with a 3×3×3 k-point mesh. Using the output from the final iteration we calculated the spectral function at T=300 K shown in Extended Data Fig. 9.

**Electronic properties of $Re_7N_3$.**

The electronic band structure of $Re_7N_3$ is shown in Supplementary Information Fig. S1, while its electronic density of states (DOS) is shown in Supplementary Information Fig. S2 and compared with that of pure *hcp*-Re in Fig. S3. The nitride is metallic owing to the bands crossing the Fermi energy $E_F$ (Supplementary Information Fig. S1) leading to the finite DOS at $E_F$ (Supplementary Information Fig. S2). The main contribution to the DOS at the Fermi levet comes from 5*d* electrons of Re. The peaks in the lower energy part of the DOS (-24 eV: -20 eV) arise from 2*s* electrons of N (Supplementary Information Fig. S3). This band is separated by an energy gap of 4.5 eV from states (-16 eV: -11 eV) formed predominantly by N *p*-electrons and Re d-electrons, with some contribution from Re *s*- and *p*-states. Note that Re states could be partially related to the N states decomposed into Re-orbitals (Fig. S3). A broad band (-11 eV: 9 eV) is predominantly due to Re *d*-electros.

Due to the difference in electronegativity between Re and N, one can expect that the bonding in the system should be predominantly ionic. On the other hand, the overlap between *d*-orbitals of Re and *p*-orbitals of N can be considered as an indicator of hybridization and the covalent component of the bonding. Indeed, the presence of unoccupied N *p*-states above the Fermi energy shows that the interaction cannot be purely ionic. To better understand the nature of atomic bonding in $Re_7N_3$, we calculated the electron localization function (ELF) (Supplementary Information Fig. S4), spatial distribution of electronic density maps and total charge-density contour (Fig. S5). The low localization of electrons in the region between adjacent N and Re atoms with almost spherically distributed ELF attactors around nitrogen atoms indicates the ionic component of the interatomic bond (Supplementary Information Fig. S4). The same features can be seen from Supplementary Information Fig. S5, which shows the spatial distribution of electronic density in the range [−16 eV: -10 eV], namely high and nearly spherical charge distribution around N atoms. Next, in the energy range [-10 eV: -4 eV] there are predominantly strong Re-Re and weaker N-N interactions

(Supplementary Information Fig. 5). In the interval [-4 eV: 0 eV] an increase in electron density between Re and N atoms and directional charge redistribution are observed (Supplementary Information Fig. S5), which indicates the presence of a covalent component of the atomic bond. Finally, the total charge density plot (Supplementary Information Fig. S5) shows slightly anisotropic spherically distributed areas of charge density around Re and N atoms with bridges between them.

**Re-based solution phase**.

We use VASP to calculate the mixing enthalpies for 2×1×2 supercells with an underlying fcc crystal structure with 16 Re atoms and various amounts of either N or C ($Re_{16}(C,N)_x$ with x=2, 3, 4) occupying octapores in the supercells to simulate the Re-N and Re-C cubic phases with NaCl (B1) type structure. To calculate the formation enthalpy $\Delta H$ for Re-N solid solutions, we used hcp-rhenium and nitrogen in the cg-N structure and for Re-C carbon in the diamond structure.

Analysis of the 2×1×2 *fcc* configurations containing nitrogen shows that it is beneficial for it to be either in neighboring octopores (touching along the edge), or in the octopores that are on the third coordination sphere (that is, those which don't touch at all, but are not far away). Such configurations lead to negative formation enthalpies (Supplementary Information Fig. S8, Supplementary Information Table S5). The situation when the nitrogen octopores touch only in a single vertex (the case, where each unit cell stoichiometry is $Re_4N$) is the least energetically favorable.

We note that for each individual supercell structural relaxation leads to slight orthorhombic distortions (< 4%). However, the presence of several nearly energetically degenerate supercells (Supplementary Information Table S5) suggests that the distortions could be out in a macroscopic sample. Therefore, we perform additional structural relaxations in 2×2×2 supercells using Quantum Espresso[14]. Similar to the VASP calculations , we use the projector augmented wave (PAW) method and consider exchange and correlation effects in terms of the generalized gradient approximation (GGA) with PBE parametrization[4] . We use a kinetic energy cutoff of 80 Ry for wavefunctions and 800 Ry for the charge density and 2×2×2 *k*-points.

We generate all possible structures based on an 2×2×2 supercell of *fcc*-Re with stoichiometry $Re_{32}N_8$, which showed the most negative formation enthalpies of the probed 2×1×2 supercells (Supplementary Information Fig. S8, Supplementary Information Table S5). When occupying 8 out of 32 possible octopores in the cell, it is possible to build 10518300 structures. We reduce the number by considering only structures in which the center of gravity of the nitrogen coordinates coincides with the

center of the supercell, which reduces the data set to ~50000 structures and ensures a relatively uniform distribution of N atoms (Supplementary Information Fig. S9). From this set, we randomly choose 100 structures and perform a structural relaxation with no constraints on the lattice or cell parameters until forces are < 0.5 meV/Å$^2$ per atom. Within the data set, we obtain a small enthalpy variation, depending on the relative position of the octopores occupied by N, in agreement with the 2×1×2 unit cell calculations. All calculations maintain the *fcc*-Re host lattice with varying orthorombic distortion between 0.4% and 4% and < 0.3% variation in cell volume. Averaging over all coordinates leads to a nearly cubic structure (average orthorombic distortion is below 0.02%).

Thus, the formation of $ReN_{0.20}$ solution phase with NaCl (B1) type structure is quite plausible, even though the alloy should be metastable at the synthesis pressure as its mixing enthalpy is above the convex hull. For all ReC solid solutions the formation enthalpies are positive, making the formation of the Re-C alloys in the experiment highly unlikely (Supplementary Information Fig. 8, Supplementary Information Table S6).

**Thermodynamic stability of $Re_7N_3$.**

Investigation of the influence of pressure on the thermodynamic stability of $Re_7N_3$ is a highly non-trivial task. In the maximum pressure range 100 GPa-200 GPa that has been achieved so far, nitrides of rhenium can be found in a wide range of compositions as a consequence of the multiple oxidation states of rhenium, while the phase diagram in the TPa pressure range is unknown and an identification of all the competing phases, as well as a treatment of the off-stoichiometric phases is beyond the subject matter of the present study. Therefore, the enthalpies of formation were calculated for $Re_7N_3$ and compared to experimentally known and theoretically predicted stoichiometric high-pressure phases in Re-N system from the literature. In more details, we used hcp rhenium in the *P6$_3$/mmc* structure, and nitrogen in the *cg*-N structure. Zhao et al.[15] previously constructed a convex hull at a pressure of 100 GPa[16]. Using the evolutionary structure search method in a region with a high rhenium content, two thermodynamically stable structures, $Re_3N$ ($P\bar{6}m2$) and $Re_2N$ (*P6$_3$/mmc*), were identified by Zhao *et al.* theoretically. In fact, these two compounds were synthesized earlier by Friedrich *et al.*[10] at lower pressures (13-31 GPa). Two nitrides $Re_3N_2$ ($P\bar{6}m2$) and ReN-NiAs were found in ref. [15] to be quite close to the convex hull, both slightly above it. Thus, these four structures together with $Re_7N_3$ were considered in the present study.

In the region enriched with nitrogen we considered the following phases: $ReN_2$ (*C2/m*), $ReN_3$ (*Imm2*), $ReN_4$ (*Cmmm*), $ReN_2$ (*P2$_1$/c*), $ReN_2$ (*P4/mbm*), $ReN_{10}$ (*Immm*). The three former phases, $ReN_2$ (*C2/m*), $ReN_3$ (*Imm2*) and $ReN_4$ (*Cmmm*), were predicted theoretically as thermodynamically stable phases

at 100 GPa in ref. [15]. The three latter compounds, $ReN_2$[17] (*P21/c*), $ReN_2$ (*P4/mbm*), and $ReN_{10}$[18] (*Immm*), have been recently synthesized experimentally. Our results, summarized in Fig 3 show that an increase in pressure leads to remarkable increase of stability of $Re_7N_3$ with respect to the other competing phases.

The results of our calculations at a pressure of 730 GPa (corresponding to calculated pressure at the experimental synthesis volume) are shown in Fig. 3b. Two nitrides, $Re_3N$ and $Re_2N$, lie on a convex hull. The enthalpy of formation of $Re_7N_3$ lies slightly above the ground state line (~ 0.05 eV) between $Re_3N$ and $Re_2N$. The compound $Re_3N_2$ ($P\bar{6}m2$) lies far from the ground state line, while ReN in the NiAs-type structure becomes thermodynamically stable at this pressure (among the considered phases). In a region with a high nitrogen content, the convex hull line passes only through $ReN_2$ nitride (*P4/mbm*).

Since the enthalpy of formation for $Re_7N_3$ is very close to the ground state line, a change in pressure can affect the thermodynamic stability of this nitride. To study this further, we constructed a ground state line at higher pressure of 900 GPa (Fig. 3). In the concentration interval enriched with nitrogen the results changed very little. However, for nitrides with a high rhenium content changes were significant. It can be seen that at this pressure the $Re_2N$ and ReN phases are still thermodynamically stable, but $Re_3N$ turned out to lie slightly higher than the ground state line. Most importantly, for $Re_7N_3$ the change in pressure placed its enthalpy of formation at the convex hull line. Note that at P=100 GPa $Re_7N_3$ has formation enthalpy wich is well above the convex hull line (Fig. 3).

**Lattice dynamics of $Re_7N_3$.**

It is necessary that the $Re_7N_3$ phase is at least metastable to be synthesized in experiment. This can be evaluated theoretically in a study of the dynamical stability of a material: in a metastable phase all the frequencies of its lattice vibrations are real. To check the dynamical stability of the $Re_7N_3$, we calculated its phonon dispersion relations in the harmonic approximation. We observed that at 100 GPa the dynamical stability condition is fulfilled (Extended Data Fig. 9), despite the fact that the formation entalpy of $Re_7N_3$ is well above the convex hull (Fig. 3). Surprisingly, calculations carried out at ~730 GPa, that corresponds to volume per atom at the experimental synthesis pressures, showed the presence of imaginary frequenceis along Γ-M-K-Γ direction of the Brillouin zone (Extended Data Fig. 9). This means that in the harmonic approximation $Re_7N_3$ would be classified as dynamically unstable, impossible to synthesize compound. However, calculations of the vibrational spectral function carried out at T=300 K that take into account anharmonic effects of lattice vibrations do not show any sign of the dynamical instabiliy and confirm that $Re_7N_3$ is at least metastable at this pressure (Extended Data Fig. 9).

This effect is interesting, giving the fact that the temperature 300 K corresponds to ~25 meV, while the *PV* term at 1 TPa is ~750 eV. Moreover, $Re_7N_3$ is not a strongly anharmonic solid: phonon lifetimes are quite long, as seen from a relatively small broadening of the phonon lines in (Extended Data Fig. 9). The contribution of anharmonic effects of lattice vibrations is expected to be tiny in such materials. To understand this observation, we consider in more details the electronic structure of the $Re_7N_3$ and its interplay with lattice dynamics of this system. We recall that Re electron configuration is Xe $4f^{14}$ $5d^5$ $6s^2$. Nine electrons are transferred from seven Re atoms to three N atoms. The remaining sp- and d-electrons are weakly hybridized, leading to a nearly half-filled Re *d*-band, similar to Re metal. Indeed, comparing the Re *d*-band of $Re_7N_3$ with the DOS of pure *hcp*-Re calculated at nearly the same pressure (Supplementary Information Fig. S3). The latter, being half-filled by 5 Re *d*-electrons that occupy all the bonding states leaving all the anti-bonding states unoccupied explains very high formation energy of Re-metal in the framework of the Friedel rectangular band model[19]. Even more well-developed separation of the bonding states below the Fermi energy from antibonding states above the Fermi energy by a pseudogap located in a vicinity of $E_F$ is seen in the DOS of $Re_7N_3$.

In fact, comparing its electronic DOS at the synthesis pressure with that calculated at P~100 GPa one observes (Supplementary Information Fig. 2), besides a typical pressure induced broadening of the bands, a clear shift of the occupied peaks down in energy (relative to $E_F$, see insets in Supplementary Information Fig. 2). Such a position of the pseudogap, in general, is a characteristic of a stable system, while the pressure-induced shift of the occupied peaks reduces the one-electron contribution to the total energy contributing to the pressure-induced stabilization of $Re_7N_3$.

However, as we deal with a chemically complex compound with many atoms per unit cell, the details of the electronic structure are non-trivial. We identify the presence of a Van-Hove singularity seen as a peak of the electronic DOS at the Fermi level (inset in Supplementary Information Fig. S2), associated with rather flat bands along Γ-M line (Supplementary Information Fig. S1). Though the singularity is small, its position at the Fermi energy is quite unfavorable from an energetic point of view, contributing to the observed dynamical instability of $Re_7N_3$ in the harmonic approximation at P~730 GPa (Extended Data Fig. 9) which effectively uses the static ideal crystal lattice (with small displacements of selected ions) for calculations of the force constants. Note that at P~100 GPa the Van-Hove singularity is above $E_F$, and $Re_7N_3$ is predicted to be dynamically stable in the harmonic approximation. On the other hand, it has been established that lattice vibrations at finite temperature smear out the singularities of the electronic structure, leading to a disappearance of anomalies at the phonon dispersion relations[20]. As the Van-Hove singularity at the Fermi level observed at P~730 GPa is quite small in $Re_7N_3$, the TDEP calculations at temperature 300 K predict that the materials is dynamically stable at the synthesis pressure (Extended Data Fig. 9).

**Brief overview of the double-stage DAC (dsDAC) technique**

The ds-DAC original purpose was to generate ultra-high static pressures, those beyond the limit of a conventional DAC of about 300 to maximum 400 GPa. At first, pressures of about 600 GPa were achieved in a ds-DAC[21], as determined on the lattice parameters of gold using powder X-ray diffraction (XRD). Then static equations of states (EOSes) of several metals (platinum, osmium, tungsten, and tantalum) were cross-calibrated up to 500 GPa[22] based on the EOS of gold by Yokoo et al.[23] and the compressional behavior of Os was studied up to 774 GPa[22]. Hitherto, the highest static pressure achieved using ds-DACs is 1065 GPa[24], as determined on the gold pressure scale[23]. Modified ds-DAC designs tried by various research groups[25–27] have not led to generating pressures comparable to those reported by Bayreuth team[24]. Sakai et al.[28] conducted experiments in a ds-DAC with the secondary anvils manufactured from single crystal diamond using FIB and reported the maxim pressure of 460 GPa. Although these authors achieved the same degree of compression of rhenium as in Dubrovinsky et al.[21], they reported different pressures, as they used the Re pressure scale of Anzellini et al.[29]. There is a significant inconstancy between the data of Anzellini et al.[29] and Dubrovinsky et al.[21] and this reflects some general difficulties in the pressure characterization at multimegabar pressures. A unique estimate of pressure becomes difficult, if there are discrepancies in the literature. This is the case for Re, as the results by Sakai et al.[28] up to ~300 GPa pressure are close to those of Anzellini et al.[29], while Jenei's et al.[30] measurements in the same pressure range agree with the EOS of Dubrovinsky et al.[21].

Recently diamond anvils of a toroidal shape (t-DACs) were described by Jenei et al.[30] and Dewaele et al.[31] The both groups[30,31] were able to generate static pressures above 600 GPa, thus confirming conclusions of Bayreuth team that pressures above 0.5 TPa may be achieved using the DAC technique. As pointed out by Dewaele et al.[31], the toroidal shape of the diamond anvil of the t-DAC has similarities with the second-stage diamond anvil of the Bayreuth's ds-DAC[21,22,24].

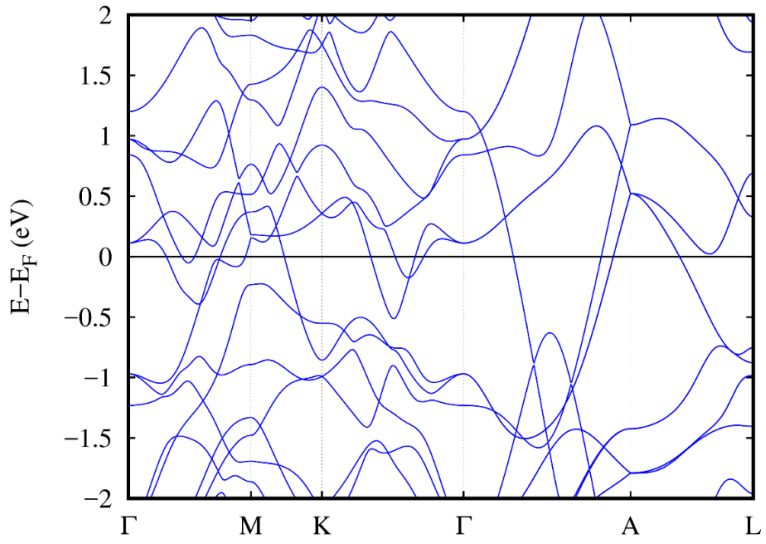


**Supplementary Information Figure S1.** Electronic band structure of $Re_7N_3$ calculated at experimental volume 136.5 $Å^3$ corresponding to calculated pressure ~730 GPa. $E_F$ denotes the Fermi energy.

a)

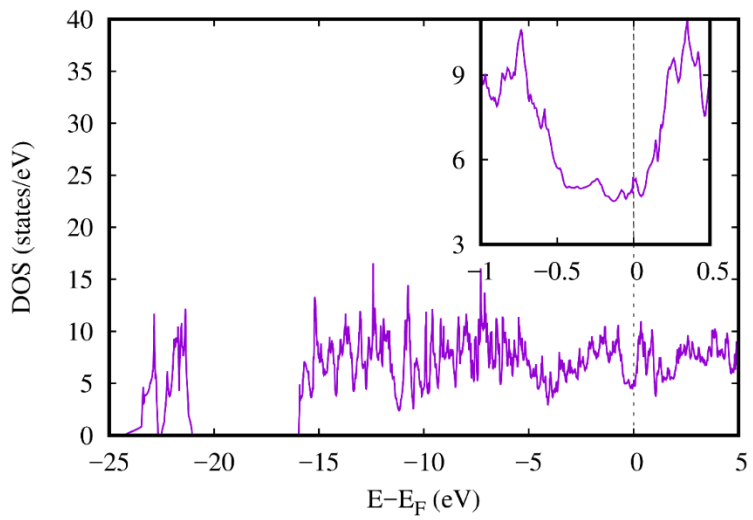


b)

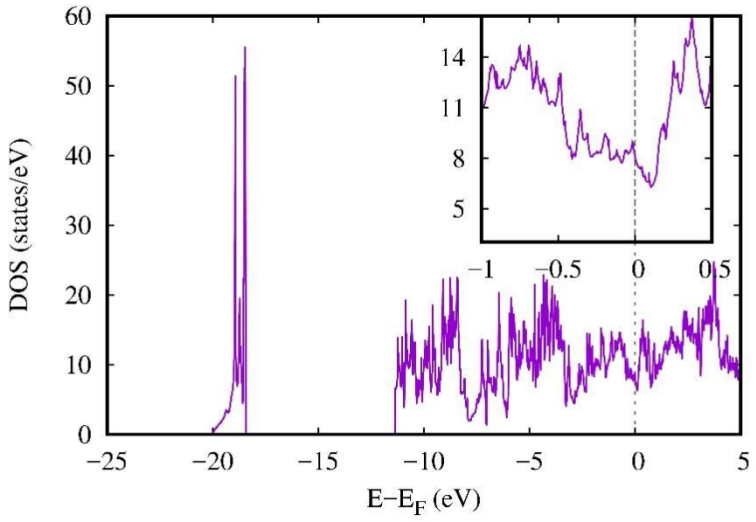


***Supplementary Information Fig. S2***. *(a) Electronic density of states (DOS) of $Re_7N_3$ calculated per formula unit as a function of energy E at experimental volume 136.5 Å$^3$ corresponding to calculated pressure ~730 GPa. The inset shows magnified image of the eDOS in a vicinity of the Fermi energy $E_F$. (b) DOS of $Re_7N_3$ calculated per formula unit at volume 200 Å$^3$ corresponding to calculated pressure ~100 GPa is shown for comparison.*

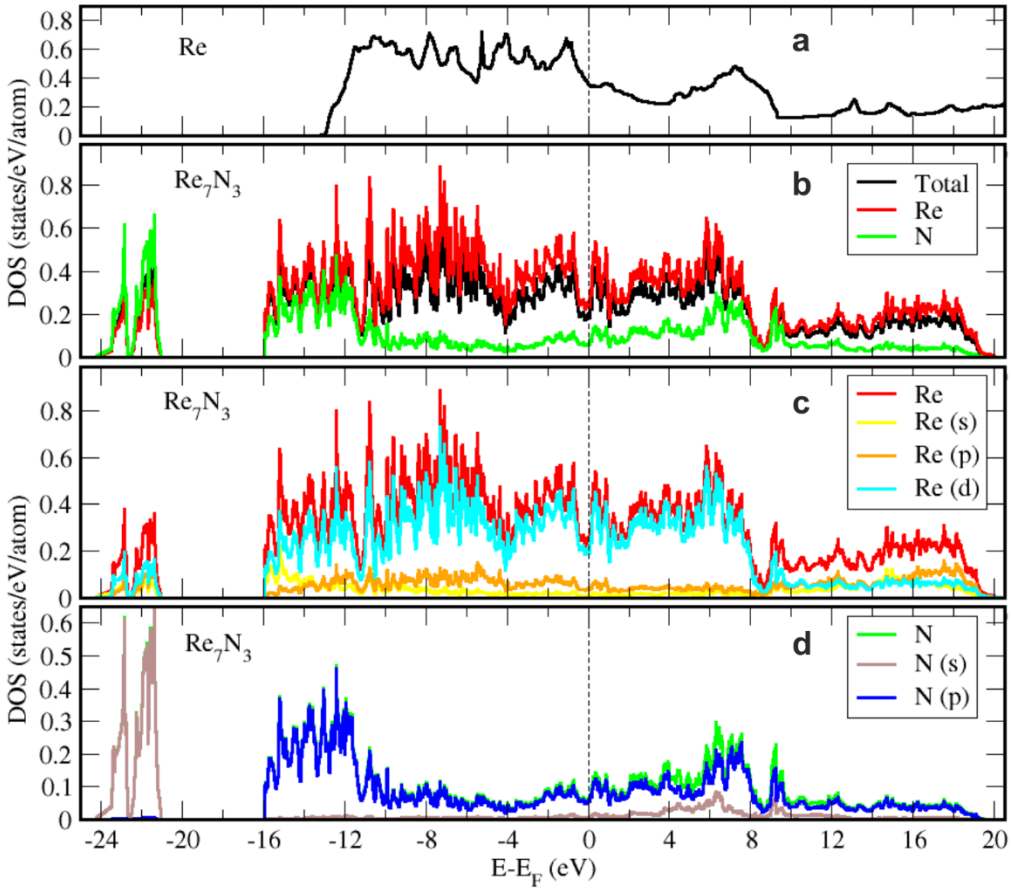


***Supplementary Information Figure S3.*** *Electronic density of states calculated as a function of energy E for hcp Re at V=16.95 Å³ (P=734 GPa) (a) and local partial eDOS of $Re_7N_3$ at V=136.5 Å³ (P=732 GPa) (b-d). (b) Total and local (atom-projected) densities of states of the $Re_7N_3$. (c) Partial (orbital-projected) local density of states at Re atoms. (d) Partial local density of states at N atoms. Energy zero is chosen at the Fermi energy $E_F$.*

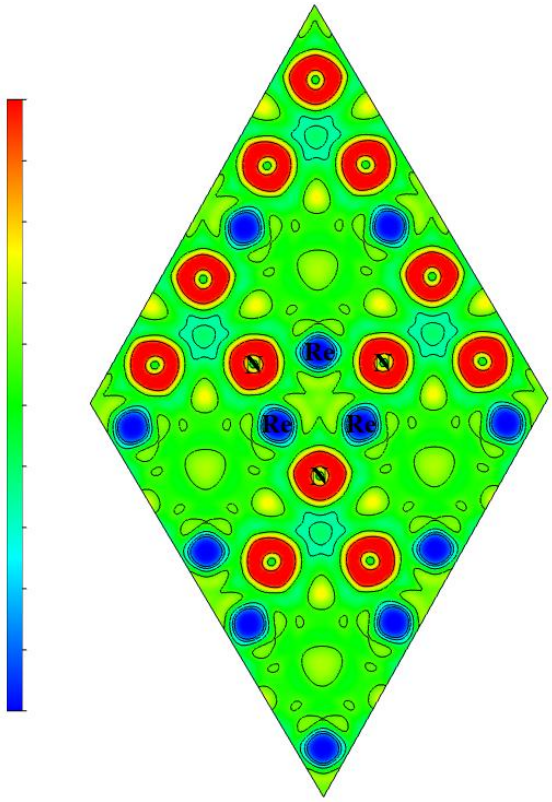


***Supplementary Information Figure S4.*** *Electron localization function of $Re_7N_3$ calculated at experimental synthesis volume 136.5 Å$^3$ corresponding to calculated pressure ~730 GPa. The saturation level value is 0.7.*

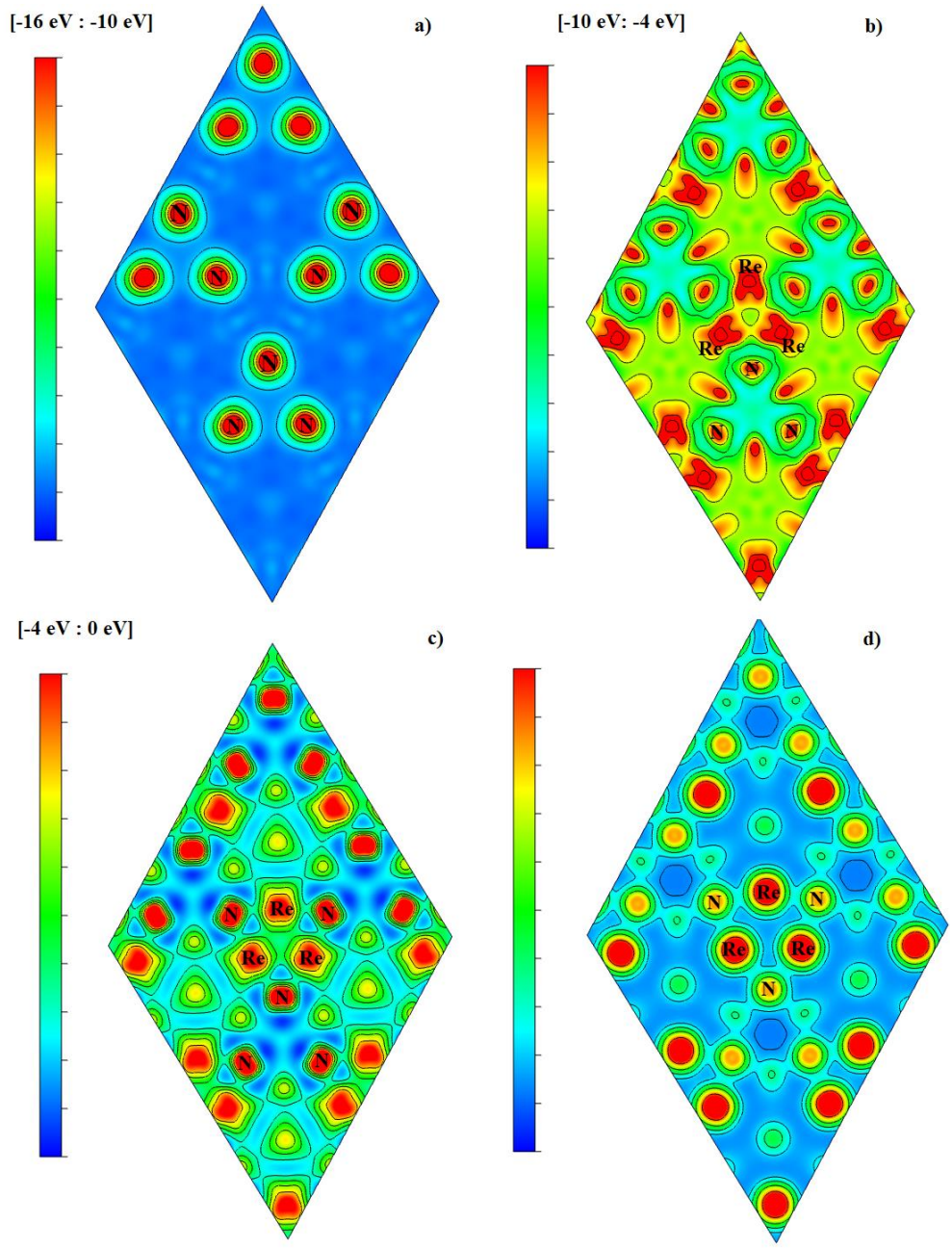


***Supplementary Information Figure S5***. *Spatial distributions of charge density of $Re_7N_3$ in energy regions [−16 eV: -10 eV] (a), [−10 eV: -4 eV] (b), and [−4 eV: -0 eV] below the Fermi energy (c), as well as total electronic density map (d) calculated at experimental synthesis volume 136.5 $Å^3$ corresponding to calculated pressure ~730 GPa.*

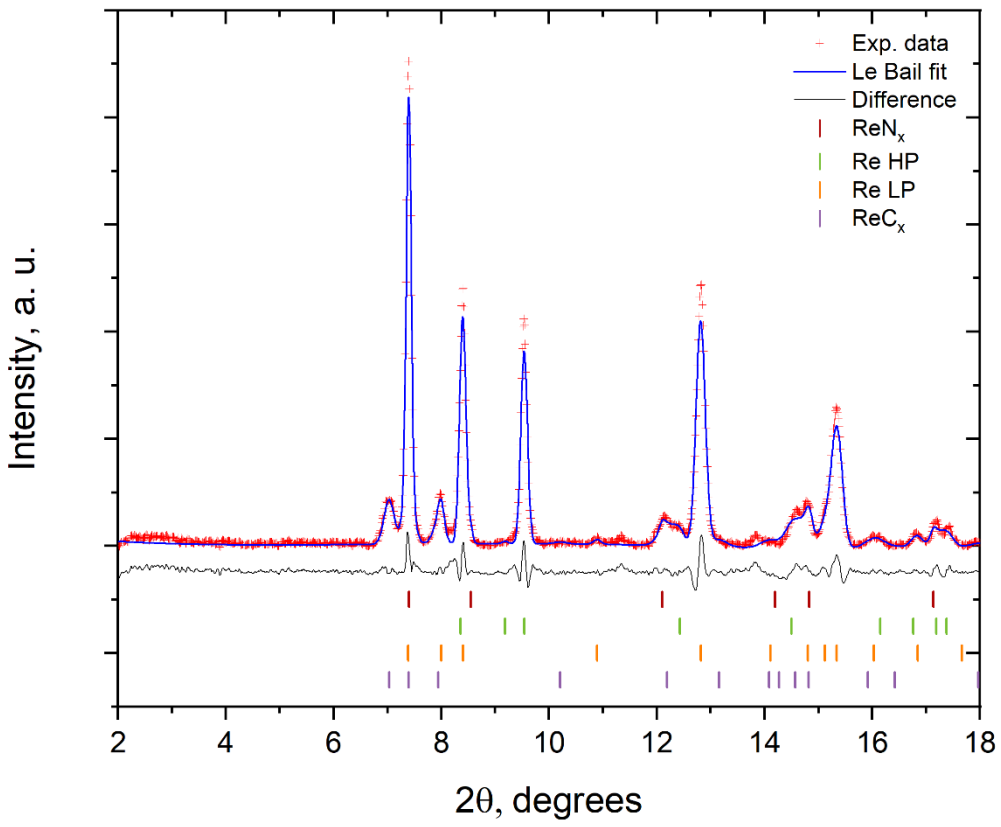


***Supplementary Information Fig. S6***. *Example of a powder diffraction pattern collected from dsDAC #3 at ID11 (ESRF, Grenoble, France, the beam of 0.5x0.5 μm² FWHM and the wavelength 0.2952 Å). Refinement performed with Le Bail fit implemented in Jana2006 software. Values of lattice parameters are given in Supplementary Information Table S7. Weak and relatively broad reflections of hexagonal phase are assigned to $ReC_x$ (x≈0.6) as far as similar phase was reported in ref.[36] as a product of chemical interaction of rhenium and carbon in the similar pressure range. Composition of the cubic $ReN_x$ phase is approximately $ReN_{0.2}$.*

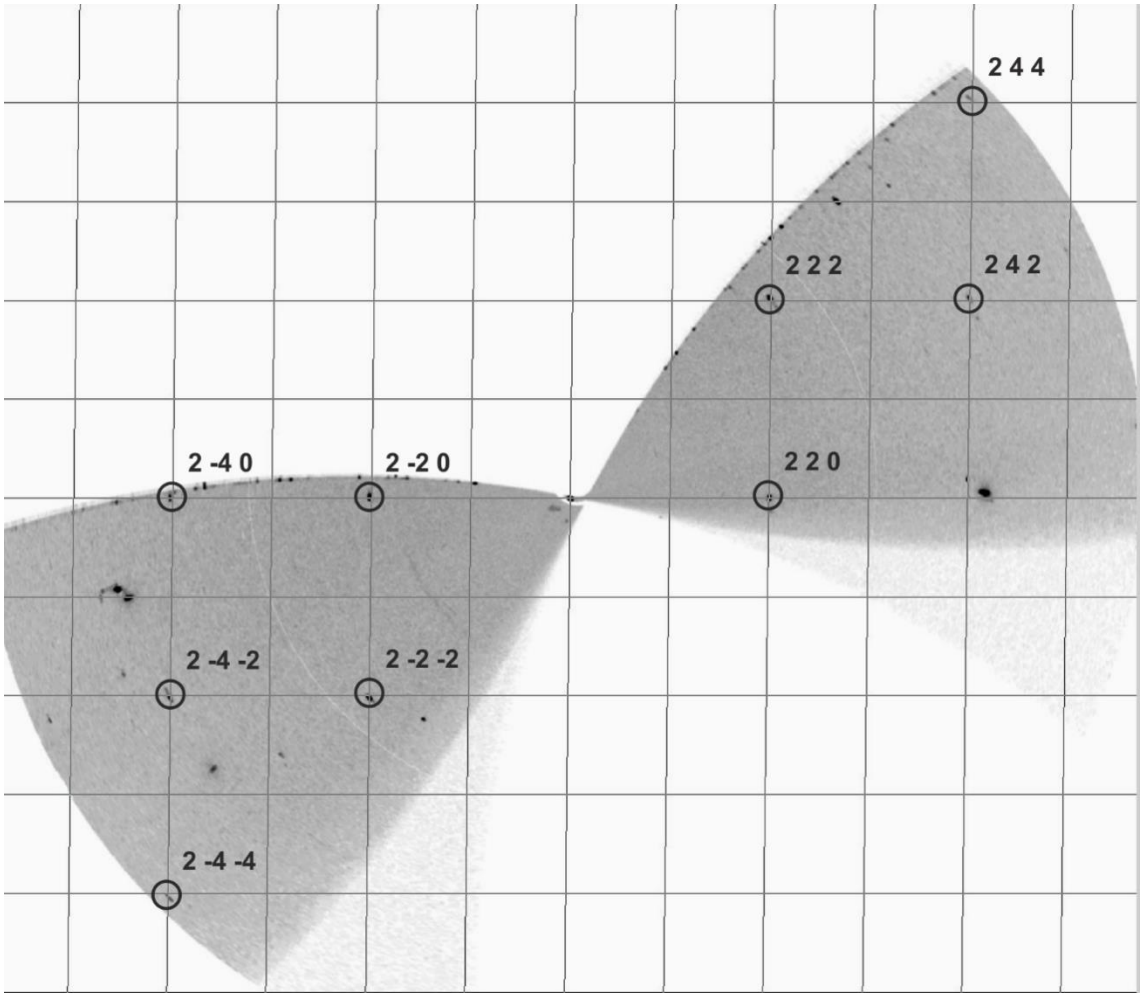


***Supplementary Information Figure S7***. *Example of reciprocal space reconstructions (2kl plane) for the cubic phase (space group* $Fm\bar{3}m$*, lattice parameter a=3.3994(7) Å) found in dsDAC #3.*

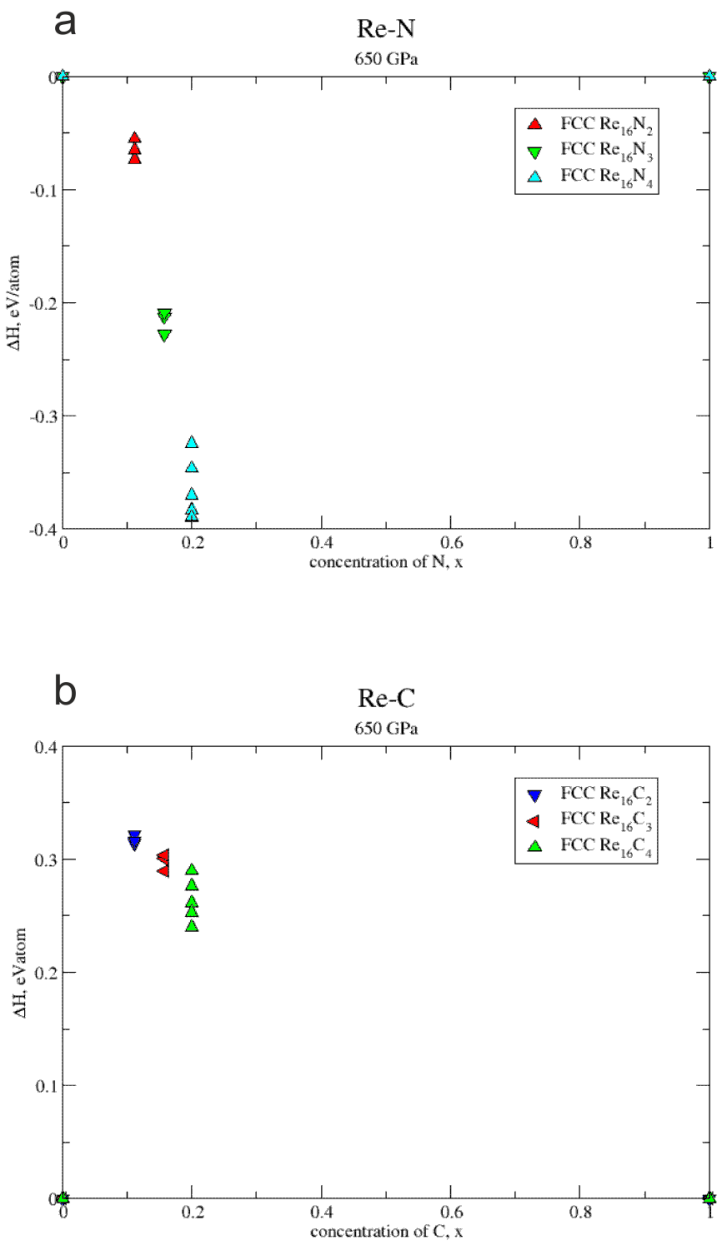


***Supplementary Information Figure S8.*** *Formation enthalpy for the most energetically favorable configurations of Re-N (a) and Re-C (b) 2×1×2 supercells simulating Re-N cubic phase with NaCl (B1) type structure. List of formation enthalpies for all 2×1×2 supercells considered in this study can be found in Supplementary Information Table S5 and Table S6 for N and C, respectively.*

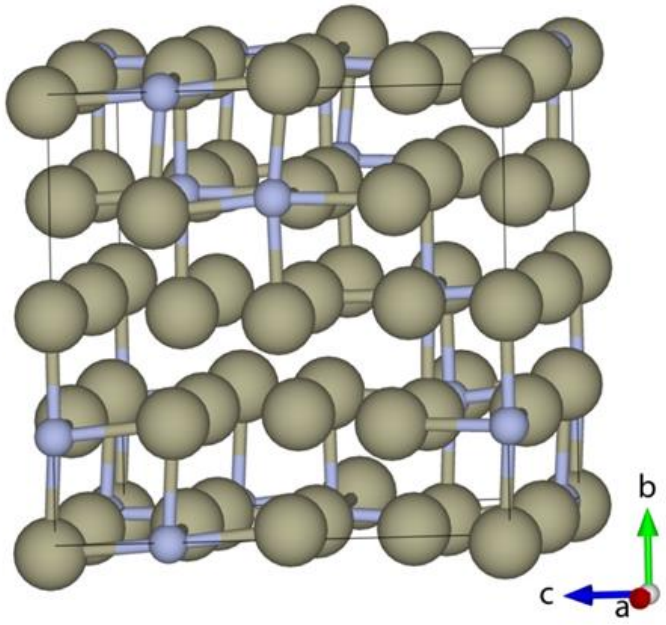


***Supplementary Information Figure S9**. Visualization of one exemplary $Re_{32}N_8$ supercell simulating Re-N cubic phase with NaCl (B1) type structure after structural relaxation.*

**Table S1**. Summary of experiments

| | **Maximal pressure, GPa P1/P2*** | | **Maximal temperature, K** | **Phases observed** |
|---|---|---|---|---|
| | ref. 21 | ref. 29 | | |
| **dsDAC #1** | 1298(10)/173(3) | 930(5)/149(3) | 2200(200) | $Re_7N_3$, re-crystallized Re |
| **dsDAC #2** | 974(2)/100(1) | 646(2)/89(1) | 2400(200) | $Re_7N_3$, re-crystallized Re |
| **dsDAC #3** | 1132(7)/134(2) | 730(4)/117(1) | 3450(200) | $ReN_x$ alloy, re-crystallized Re |

*In each column the first value (P1) is the pressure on the sample, and the next value (P2) is the pressure on primary anvils (as determined from the Re EOS according to ref. 21 or ref. 29 (in ref. 29 the EOS of Re was measured in quasihydrostatic He pressure medium).

**Table S2**. Details of the crystal structure refinements of Re, $Re_7N_3$, and $ReN_{0.2}$ phases.

| Pressure | 1240(15)[21] or 905(5)[29] GPa | | 1132(7)[21] or 730(4)[29] |
|---|---|---|---|
| Chemical formula | Re | $Re_7N_3$ | $ReN_{0.2}$ |
| $M_r$ | 186.20 | 1345.43 | 189.01 |
| Crystal system, space group | Hexagonal, $P6_3/mmc$ | Hexagonal, $P6_3mc$ | Cubic, $Fm\text{-}3m$ |
| Temperature (K) | 293 | 293 | 293 |
| $a$, $c$ (Å) | 2.2269 (4), | 6.2778 (19), | 3.3994 (7) |
| $c$ (Å) | 3.5702 (15) | 4.000 (2) | |
| $V$ (Å$^3$) | 15.33 (1) | 136.53 (11) | 39.28 (2) |
| $Z$ | 2 | 2 | 4 |
| Radiation type (synchrotron) | λ = 0.30996 Å | | 0.2882 Å |
| μ (mm$^{-1}$) | 43.22 | 35.28 | |
| Crystal size (mm) | 0.001 × 0.001 × 0.001 | | |
| Diffractometer | ID11, ESRF | | |
| Absorption correction | *CrysAlis PRO* 1.171.40.84a (Rigaku Oxford Diffraction, 2019) Spherical absorption correction using equivalent radius and absorption coefficient. Empirical absorption correction using spherical harmonics, implemented in SCALE3 ABSPACK scaling algorithm. | | |
| $T_{min}$, $T_{max}$ | | | |
| No. of measured, independent and observed [$I > 2\sigma(I)$] reflections | 54, 20, 19 | 394, 196, 148 | 66, 17, 17 |
| $R_{int}$ | 0.075 | 0.030 | 0.114 |
| $(\sin\theta/\lambda)_{max}$ (Å$^{-1}$) | 0.875 | 0.954 | 1.130 |
| $R[F^2 > 2\sigma(F^2)]$, $wR(F^2)$, $S$ | 0.086, 0.209, 1.34 | 0.057, 0.099, 1.09 | 0.050, 0.116, 1.54 |
| No. of reflections | 20 | 196 | 17 |
| No. of parameters | 2 | 12 | 1 |
| $\Delta\rho_{max}$, $\Delta\rho_{min}$ (e Å$^{-3}$) | 8.01, −10.07 | 3.03, −3.22 | 9.03, −6.68 |

**Table S3.** Lattice parameters of Re and $Re_7N_3$ obtained during Le Bail fit of the powder diffraction pattern from dsDAC #2.

| **Phase** | ***a*, Å** | ***c*, Å** | ***V*, Å$^3$** | **P, GPa ref.[29]** | **P, GPa ref.[21]** |
|---|---|---|---|---|---|
| Re LP | 2.6120(2) | 4.1942(6) | 24.782(4) | 89(1) | 100(1) |
| Re HP | 2.2945(3) | 3.6972(8) | 16.856(3) | 646(2) | 974(2) |
| $Re_7N_3$ | 6.3010(7) | 4.0469(6) | 139.15(2) | | |

**Table S4.** Crystallographic data for $Re_7N_3$ calculated at experimental volumes and temperature T=0 K.

| | **$Re_7N_3$,** ***$P6_3mc$*** **PBE** |
|---|---|
| **V, Å$^3$** | 136.5 |
| **Pressure, GPa** | 732 |
| ***a*, Å** | 6.2772 |
| ***c*, Å** | 4.0007 |
| **Fractional atomic coordinates (x/a, y/b, z/c)** | Re1 (0.3333, 0.6667; 0.8094) Re2 (0.4556; 0.54440; 0.2934) Re3 (0.1223; 0.8777; 0.9831) N (0.1897; 0.8103; 0.5616) |

**Table S5.** Formation enthalpies of 2×1×2 supercells with $Re_{16}N_x$ (x=2,3,4) stoichiometry with different occupations of octapores by N atoms simulating Re-N cubic phase with NaCl (B1) type structure at 650 GPa.

| Concentration of N | Enthalpy of formation, eV/atom | |
|---|---|---|
| 0.000000 | 0.000000 | Re HCP |
| 0.111111 | -0.055177 | $Re_{16}N_2$ |
| 0.111111 | -0.073184 | $Re_{16}N_2$ |
| 0.111111 | -0.055169 | $Re_{16}N_2$ |
| 0.111111 | -0.064662 | $Re_{16}N_2$ |
| 0.157895 | -0.212287 | $Re_{16}N_3$ |
| 0.157895 | -0.227716 | $Re_{16}N_3$ |
| 0.157895 | -0.144791 | $Re_{16}N_3$ |
| 0.157895 | -0.227759 | $Re_{16}N_3$ |
| 0.157895 | -0.208550 | $Re_{16}N_3$ |
| 0.157895 | -0.227710 | $Re_{16}N_3$ |
| 0.157895 | -0.208550 | $Re_{16}N_3$ |
| 0.200000 | -0.389473 | $Re_{16}N_4$ |
| 0.200000 | -0.346507 | $Re_{16}N_4$ |
| 0.200000 | -0.389651 | $Re_{16}N_4$ |
| 0.200000 | -0.370255 | $Re_{16}N_4$ |
| 0.200000 | -0.383485 | $Re_{16}N_4$ |
| 0.200000 | -0.370427 | $Re_{16}N_4$ |
| 0.200000 | -0.383653 | $Re_{16}N_4$ |
| 0.200000 | -0.370337 | $Re_{16}N_4$ |
| 0.200000 | -0.389473 | $Re_{16}N_4$ |
| 0.200000 | -0.389489 | $Re_{16}N_4$ |
| 0.200000 | -0.324581 | $Re_{16}N_4$ |
| 0.200000 | -0.370428 | $Re_{16}N_4$ |
| 1.000000 | 0.000000 | cg-N |

**Table S6.** Formation enthalpies of 2×1×2 supercells with $Re_{16}C_x$ (x=2,3,4) stoichiometry with different occupations of octapores by C atoms simulating Re-C cubic phase with NaCl (B1) type structure at 650 GPa.

| Concentration of N | Enthalpy of formation, eV/atom | |
|---|---|---|
| 0.000000 | 0.000000 | Re HCP |
| 0.111111 | 0.314061 | $Re_{16}C_2$ |
| 0.111111 | 0.321492 | $Re_{16}C_2$ |
| 0.111111 | 0.316490 | $Re_{16}C_2$ |
| 0.157895 | 0.300479 | $Re_{16}C_3$ |
| 0.157895 | 0.303620 | $Re_{16}C_3$ |
| 0.157895 | 0.303597 | $Re_{16}C_3$ |
| 0.157895 | 0.289469 | $Re_{16}C_3$ |
| 0.157895 | 0.289494 | $Re_{16}C_3$ |
| 0.157895 | 0.289495 | $Re_{16}C_3$ |
| 0.200000 | 0.252995 | $Re_{16}C_4$ |
| 0.200000 | 0.261154 | $Re_{16}C_4$ |
| 0.200000 | 0.276412 | $Re_{16}C_4$ |
| 0.200000 | 0.253007 | $Re_{16}C_4$ |
| 0.200000 | 0.289973 | $Re_{16}C_4$ |
| 0.200000 | 0.252827 | $Re_{16}C_4$ |
| 0.200000 | 0.240137 | $Re_{16}C_4$ |
| 0.200000 | 0.253007 | $Re_{16}C_4$ |
| 0.200000 | 0.290011 | $Re_{16}C_4$ |
| 0.200000 | 0.252822 | $Re_{16}C_4$ |
| 1.000000 | 0.000000 | Diamond-C |

**Table S7.** Lattice parameters of the phases obtained during Le Bail fit of powder diffraction pattern from dsDAC #3.

| Phase | *a*, Å | *c*, Å | *V*, Å$^3$ | P, GPa (ref.[29]) | P, GPa (ref.[21]) |
|---|---|---|---|---|---|
| Re LP | 2.5876(3) | 4.123(4) | 23.91(2) | 117(1) | 134(2) |
| Re HP | 2.2803(3) | 3.622(1) | 16.31(2) | 730(4) | 1132(7) |
| $ReC_{0.6}$ | 2.7266(8) | 4.469(3) | 28.77(3) | | |
| $ReN_{0.2}$ | 3.3994 (7) | | 39.28 (2) | | |

**Supplementary references:**


1. Blöchl, P. E. Projector augmented-wave method. *Phys. Rev. B* **50**, 17953–17979 (1994).
2. Kresse, G. & Joubert, D. From ultrasoft pseudopotentials to the projector augmented-wave method. *Phys. Rev. B* **59**, 1758–1775 (1999).
3. Kresse, G. & Furthmüller, J. Efficient iterative schemes for ab initio total-energy calculations using a plane-wave basis set. *Phys. Rev. B - Condens. Matter Mater. Phys.* **54**, 11169–11186 (1996).
4. Perdew, J. P., Burke, K. & Ernzerhof, M. Generalized Gradient Approximation Made Simple. *Phys. Rev. Lett.* **77**, 3865–3868 (1996).
5. Monkhorst, H. J. & Pack, J. D. Special points for Brillouin-zone integrations. *Phys. Rev. B* **13**, 5188–5192 (1976).
6. Methfessel, M. & Paxton, A. T. High-precision sampling for Brillouin-zone integration in metals. *Phys. Rev. B* **40**, 3616–3621 (1989).
7. Blöchl, P. E., Jepsen, O. & Andersen, O. K. Improved tetrahedron method for Brillouin-zone integrations. *Phys. Rev. B* **49**, 16223–16233 (1994).
8. Togo, A. & Tanaka, I. First principles phonon calculations in materials science. *Scr. Mater.* **108**, 1–5 (2015).
9. Cowley, R. A. Anharmonic crystals. *Reports Prog. Phys.* **31**, 303 (1968).
10. Friedrich, A. *et al.* Novel Rhenium Nitrides. Phys. Rev. Lett. **105**, 085504 (2010).]

11. Hellman, O., Abrikosov, I. A. & Simak, S. I. Lattice dynamics of anharmonic solids from first principles. *Phys. Rev. B* **84**, 180301 (2011).

12. Hellman, O., Steneteg, P., Abrikosov, I. A. & Simak, S. I. Temperature dependent effective potential method for accurate free energy calculations of solids. *Phys. Rev. B - Condens. Matter Mater. Phys.* **87**, 1–8 (2013).

13. Hellman, O. & Abrikosov, I. A. Temperature-dependent effective third-order interatomic force constants from first principles. *Phys. Rev. B* **88**, 144301 (2013).

14. Giannozzi, P. *et al.* Quantum ESPRESSO toward the exascale. *J. Chem. Phys.* **152**, 154105 (2020).

15. Zhao, Z. *et al.* Nitrogen concentration driving the hardness of rhenium nitrides. *Sci. Rep.* **4**, 4797 (2015).

16. Zhao, Z. *et al.* Bulk $Re_2C$: Crystal structure, hardness, and ultra- incompressibility. *Cryst. Growth Des.* **10**, 5024–5026 (2010).

17. Bykov, M. *et al.* High-pressure synthesis of ultraincompressible hard rhenium nitride pernitride Re2(N2)(N2) stable at ambient conditions. *Nat. Commun.* **10**, 2994 (2019).

18. Bykov, M. *et al.* High-Pressure Synthesis of a Nitrogen-Rich Inclusion Compound $ReN_8 \cdot x\ N_2$ with Conjugated Polymeric Nitrogen Chains. *Angew. Chemie - Int. Ed.* **57**, 9048–9053 (2018).

19. Pettifor, D. F. *Bonding and Structure of Molecules and Solids*. (Clarendon Press, 1995).

20. Tidholm, J. *et al.* Temperature dependence of the Kohn anomaly in bcc Nb from first-principles self-consistent phonon calculations. *Phys. Rev. B* **101**, 115119 (2020).

21. Dubrovinsky, L., Dubrovinskaia, N., Prakapenka, V. B. & Abakumov, A. M. Implementation of micro-ball nanodiamond anvils for high-pressure studies above 6 Mbar. *Nat. Commun.* **3**, 1163–1167 (2012).

22. Dubrovinsky, L. *et al.* The most incompressible metal osmium at static pressures above 750 gigapascals. *Nature* **525**, 226–229 (2015).

23. Yokoo, M. *et al.* Ultrahigh-pressure scales for gold and platinum at pressures up to 550 GPa. *Phys. Rev. B* **80**, 104114 (2009).

24. Dubrovinskaia, N. *et al.* Terapascal static pressure generation with ultrahigh yield strength nanodiamond. *Sci. Adv.* **2**, e1600341 (2016).

25. Sakai, T. *et al.* High-pressure generation using double stage micro-paired diamond anvils shaped by focused ion beam. *Rev. Sci. Instrum.* **86**, 033905 (2015).

26. Lobanov, S. S. *et al.* Pressure, stress, and strain distribution in the double-stage diamond anvil cell. *J. Appl. Phys.* **118**, (2015).

27. Vohra, Y. K. *et al.* High pressure studies using two-stage diamond micro-anvils grown by chemical vapor deposition. *High Press. Res.* **35**, 282–288 (2015).

28. Sakai, T. *et al.* High pressure generation using double-stage diamond anvil technique: problems and equations of state of rhenium. *High Press. Res.* **38**, 107–119 (2018).

29. Anzellini, S., Dewaele, A., Occelli, F., Loubeyre, P. & Mezouar, M. Equation of state of rhenium and application for ultra high pressure calibration. *J. Appl. Phys.* **115**, 043511 (2014).

30. Jenei, Z. *et al.* Single crystal toroidal diamond anvils for high pressure experiments beyond 5 megabar. *Nat. Commun.* **9**, 3563 (2018).

31. Dewaele, A., Loubeyre, P., Occelli, F., Marie, O. & Mezouar, M. Toroidal diamond anvil cell for detailed measurements under extreme static pressures. *Nat. Commun.* **9**, 2913 (2018).

32. Akahama, Y. & Kawamura, H. Pressure calibration of diamond anvil Raman gauge to 410 GPa. *J. Phys. Conf. Ser.* **215**, 012195 (2010).

33. Prescher, C. *et al.* High Poisson's ratio of Earth's inner core explained by carbon alloying. *Nat. Geosci.* **8**, 220–223 (2015).

34. Sagatov, N., Gavryushkin, P. N., Inerbaev, T. M. & Litasov, K. D. New high-pressure phases of $Fe_7N_3$ and $Fe_7C_3$ stable at Earth's core conditions: evidences for carbon–nitrogen isomorphism in Fe-compounds. *RSC Adv.* **9**, 3577–3581 (2019).

35. ICSD database. Available at: https://icsd.products.fiz-karlsruhe.de/.

36. Khandarkhaeva, S. *et al.* Novel Rhenium Carbides at 200 GPa. *Eur. J. Inorg. Chem.* **2020**, 2186–2190 (2020)

**(Eidesstattliche) Versicherungen und Erklärungen**

(§ 9 Satz 2 Nr. 3 PromO BayNAT)

*Hiermit versichere ich eidesstattlich, dass ich die Arbeit selbstständig verfasst und keine anderen als die von mir angegebenen Quellen und Hilfsmittel benutzt habe (vgl. Art. 64 Abs. 1 Satz 6 BayHSchG).*

(§ 9 Satz 2 Nr. 3 PromO BayNAT)

*Hiermit erkläre ich, dass ich die Dissertation nicht bereits zur Erlangung eines akademischen Grades eingereicht habe und dass ich nicht bereits diese oder eine gleichartige Doktorprüfung endgültig nicht bestanden habe.*

(§ 9 Satz 2 Nr. 4 PromO BayNAT)

*Hiermit erkläre ich, dass ich Hilfe von gewerblichen Promotionsberatern bzw. -vermittlern oder ähnlichen Dienstleistern weder bisher in Anspruch genommen habe noch künftig in Anspruch nehmen werde.*

(§ 9 Satz 2 Nr. 7 PromO BayNAT)

*Hiermit erkläre ich mein Einverständnis, dass die elektronische Fassung meiner Dissertation unter Wahrung meiner Urheberrechte und des Datenschutzes einer gesonderten Überprüfung unterzogen werden kann.*

(§ 9 Satz 2 Nr. 8 PromO BayNAT)

*Hiermit erkläre ich mein Einverständnis, dass bei Verdacht wissenschaftlichen Fehlverhaltens Ermittlungen durch universitätsinterne Organe der wissenschaftlichen Selbstkontrolle stattfinden können.*

…….

Ort, Datum, Unterschrift